

ABSTRACT

HORN, TIMOTHY JOSEPH. Development and Experimental Evaluation of a Novel, Patient Specific Implant for Limb Sparing Surgery. (Under the direction of Dr. Ola L.A. Harrysson and Dr. Denis J. Marcellin-Little, DEDV).

Canine osteosarcoma is a highly aggressive bone cancer affecting an estimated 8000 dogs each year. Treatment typically consists of limb amputation for tumor control and adjuvant chemotherapy because of the high rate of metastasis. For dogs with concurrent disease, amputation may not be a viable option. Limb sparing surgery is a potential alternative in which only the affected portion of the bone is removed followed by endoprosthetic reconstruction. Barriers to the successful implementation of limb sparing include; aseptic loosening, joint or prosthetic instability, infection, implant failure, and fatigue fracture. This research seeks to address the shortcomings of current limb sparing implants and procedures for the treatment of canine osteosarcoma with a novel implant manufactured using a form of additive manufacturing known as electron beam melting. Direct metal additive manufacturing facilitates unprecedented freedom of implant design and manufacture. 3-D computer models of skeletal and soft tissue features derived from computed-tomography or magnetic resonance imaging systems provide a foundation for such designs. From these models a patient-specific implant may be designed, within a CAD (computer aided design) system, which exactly fits a given individual's skeletal anatomy. Control of mechanical/material properties, surface topography, and implant structure is also afforded. Efforts related to this study have led to the development of new, patient specific bone analog models that will serve as an experimental platform for the biomechanical evaluation of multiple implant configurations. The results indicate that additively manufactured implants address many of the shortcomings associated with the commercial alternatives

Development and Experimental Evaluation of a
Novel, Patient Specific Implant for
Limb Sparing Surgery

by
Timothy Joseph Horn

A dissertation submitted to the Graduate Faculty
of North Carolina State University
in partial fulfillment of the
requirements for the Degree of
Doctor of Philosophy

Industrial Engineering

Raleigh, North Carolina

2014

APPROVED BY:

Dr. Ola L.A. Harrysson
Co-Chair of Advisory Committee

Dr. Denis J. Marcellin-Little
Co-Chair of Advisory Committee

Dr. Harvey A. West II

Dr. B. Duncan X. Lascelles

DEDICATION

For my wife, Ross

“Quel ch'ella par quando un poco sorride,
non si pò dicer né tenere a mente,
sè è novo miracolo e gentile.”

Dante Alighieri, 1295

BIOGRAPHY

Timothy Horn was born in Utica, New York. He earned the degree of A.A.S in wood science from the State University of New York at Morrisville in 2000, after which he transferred to North Carolina State University. Here, he earned a bachelor of science degree in wood and paper science engineering, focusing on machining and tooling. In 2007 he completed his Master degree through the Integrated Manufacturing Systems Engineering Institute at North Carolina State University. In 2007 he enrolled in the doctoral program in the department of industrial and systems engineering with a focus on the biomedical applications of additive manufacturing.

ACKNOWLEDGMENTS

This work has been funded in part by the Center for Additive Manufacturing and Logistics and by a grant from the Bone Cancer Dogs Inc. (Sponsored Projects Number 2011-2055)

TABLE OF CONTENTS

LIST OF TABLES	viii
LIST OF FIGURES	ix
1.0 INTRODUCTION.....	1
2.0 LITERATURE REVIEW: THE CURRENT STATE OF CANINE LIMB SPARING TECHNOLOGY FOR THE DISTAL RADIUS	5
2.1 Introduction to Canine Osteosarcoma.....	6
2.2 Limb Sparing Techniques for the Distal Radius.....	9
2.2.1 Allografts.	9
2.2.2 Autografts.	14
2.2.3 Ulnar transposition.....	18
2.2.4 Bone transport osteogenesis.....	21
2.2.5 Metallic endoprosthesis.	24
2.3 Discussion.....	31
2.4 Conclusions.....	36
3.0 DEVELOPMENT OF A PATIENT-SPECIFIC BONE ANALOG FOR THE BIOMECHANICAL EVALUATION OF CUSTOM IMPLANTS.....	38
3.1 Selection of bone Analog Materials.....	40
3.2 Methods of Testing of Bone Analog Materials.....	48
3.3 Results of Bone Analog Material Testing.....	51
3.4 Methods for the Design and Manufacture of Patient Specific Analogs.....	54
3.5 Discussion.....	64
4.0 VALIDATION OF ANALOG RADII.....	66
4.1 Analog Radii Testing Methods	67
4.1.1 Four point bending.....	69
4.1.2 Torsion tests.	71
4.1.3 Axial compression.	74
4.1.4 Screw withdrawal tests.	75
4.1.5 Cyclic Loading of a Plated Connection	76
4.2 Analog Radii Testing Results	78
4.3 Discussion on the Validation of Composite Analog Radii	88

5.0 EVALUATION OF Ti6Al4V CELLULAR STRUCTURES FABRICATED WITH EBM 94

5.1 Background..... 97
5.2 Methods..... 106
 5.2.1 Sample Design and Preparation 106
 5.2.2 Powder Measurement and Characterization 108
 5.2.3 Sample Fabrication using Electron Beam Melting 108
 5.2.3 Sample Measurement and Characterization..... 115
 5.2.4 Mechanical Testing..... 115
5.3 Results..... 118
 5.3.1 Powder Analysis 118
 5.3.2 Strut Measurement Results 118
 5.3.3 Mechanical Testing..... 121
5.4 Discussion..... 127

6.0 EXPERIMENTAL EVALUATION OF KEY IMPLANT FEATURES OF THE PROXIMAL ENDOPROTHESIS FACILITATED BY ADDITIVE MANUFACTURING..... 134

6.1 Background..... 134
6.2 Materials and Methods..... 137
 6.2.1 Fabrication of new analog radii 137
 6.2.2 Design of Test Implants and Features..... 138
 6.2.3 EBM Fabrication of Test Implants 146
 6.2.4 Drilling, Tapping and Cutting of Analog Radii 148
 6.2.5 Measurement of Plate Contact..... 152
 6.2.6 Application of Strain Gauges..... 159
 6.2.7 Mechanical Testing Apparatus 161
 6.2.7.1 Cantilever Testing..... 163
 6.2.7.2 Torsion Testing 164
 6.2.7.3 Axial Testing..... 166
6.3 Results..... 167
 6.3.1 Analog Radii 167
 6.3.2 Preliminary Four Point Flexure of Graft Segments with Ovoid Cross Section... 170
 6.3.3 Contact at the bone implant interface 171
 6.3.4 Analysis of Mechanical Testing Results..... 178
 6.3.4.1 Cantilever Test Results 179
 6.3.4.2 Axial Test Results 185
 6.3.4.3 Torsional Test Results..... 192
6.4 Discussion..... 197

**7.0 IN VITRO EVALUATION OF NOVEL, PATIENT SPECIFIC LIMB SPARING
ENDOPROSTHESES FABRICATED WITH ELECTRON BEAM MELTING 202**

7.1 Background..... 203
7.1.1 Relevant Anatomy of the Canine Forelimb 203
7.1.2 Internal Fixation..... 205
7.1.3 Pancarpal Arthrodesis 207
7.2 Methods..... 208
7.2.1 Image Acquisition..... 208
7.2.2 Patient Specific Implant Design..... 209
7.2.3 Patient Specific Implant Fabrication..... 215
7.2.4 Specimen Preparation 219
7.2.5 Surgical Placement of Endoprostheses 221
7.2.6 Mechanical Testing of Limb Sparing Constructs 229
7.3 Results..... 233
7.3.1 Implant Measurements..... 233
7.3.2 Mechanical Test Results 234
7.3.3 Surgical Duration 237
7.4 Discussion 238

8.0 SUMMARY AND FUTURE WORK 243

REFERENCES..... 249

APPENDICES 265

Appendix 1: Lists of Cadavers..... 2666
Appendix 2: Derivations 2677
Derivation of Equation 6.1:..... 2677

LIST OF TABLES

Table 3.1: Results of tensile testing of cortical bone and cancellous bone analog materials. Means with identical subscripts do not differ statistically.....	52
Table 5.1: Elemental analysis of Ti6Al4V powder used to fabricate the test specimens.....	118
Table 5.2: Tabulation of experimental data for flexure specimens with various relative densities and unit cell sizes. Values indicated are mean \pm 1 standard error.	124
Table 7.1: Randomization schedule for the sequence of surgeries.	225
Table 7.2: Comparison between commercial and custom endoprotheses.....	233

LIST OF FIGURES

Figure 2.1: Illustration showing a cortical allograft limb sparing surgery. The resected tumor is replaced with a suitable cortical allograft (left) and the construct is reduced with plating that typically involves pancarpal arthrodesis (right).....	11
Figure 2.2: Illustration of the ulnar transposition technique of limb sparing for distal radial osteosarcoma in dogs. The lesion is resected (left) along with the ulna which is rotated into the defect (center). The construct is reduced with plating that typically involves pancarpal arthrodesis (right).....	19
Figure 2.3: Illustration showing the use of external fixators to transport the bone segment through the segmental defect.	23
Figure 2.4: Photographs showing a commercially available metal endoprosthesis for limb sparing in dogs.	24
Figure 2.5: Custom limb sparing implant for the radius of a dog. CT scans reconstructed into 3D models are used for designing the implant (a) which was printed using selective laser melting (b). Post-operative radiograph showing the custom implant in place (c).	30
Figure 2.6: Chart showing the frequency and mode of reported mechanical failures of limb sparing constructs for the distal radius in dogs.	34
Figure 3.1: Schematic cross section illustrating the macroscopic components of a canine radius.....	41
Figure 3.2: Plot illustrating the relationship between the volume fraction of fiber and the predicted tensile modulus for various conditions of fiber alignment (using 20 micrometer diameter, 793 micrometer long fibers).....	47
Figure 3.3: Images showing the microstructure of the polyurethane cancellous bone analog (left) and cancellous bone sectioned from the distal epiphysis of a canine radius (right). Scale bar indicates 200 μ m.	48
Figure 3.4: Photograph of the tensile testing fixture and strain gauge for epoxy-fiberglass cortical bone analog samples	51
Figure 3.5: Plot showing the results of a regression analysis comparing the tensile modulus measured in the experiments and the tensile modulus predicted (Error bars represent 95% confidence intervals of the measured data).....	54

Figure 3.6: Images showing (A) a screenshot of CT data, (B) images of the cortical and cancellous bone 3-D models with the filling sprue (B-1), air vents (B-2) and 3-D geometric locating features (B-3,4); (C) finished plastic models of the cortical and cancellous models with mold registration features(C-1), patient-specific bone geometry (C-2) and built in mold parting line (C-3) ; (D) polyurethane rubber mold for cortical bone with built in mold clamping features (D-1) and patient specific mold cavity (D-2). 57

Figure 3.7: Photographs showing several steps of analog bone fabrication process; (A) molding of the polyurethane cancellous bone analog insert, (B) cancellous insert coated with ceramic, (C) placement of the ceramic coated cancellous bone analog insert within the cortical bone analog mold..... 59

Figure 3.8: Photograph showing the finished patient specific analog radii..... 60

Figure 3.9: Images showing the microstructure of the 0.30 fiber volume fraction bone analog material before processing (left) and after processing (right)..... 62

Figure 3.10: Histograms showing the in plane and out of plane fiber orientation for the composite analog radius..... 63

Figure 3.11: Images showing the microstructure of the tangential surface of the 0.30 fiber volume fraction bone analog material. Note the predominant axial (vertical) fiber alignment (scale bar indicates 200 μ m). 64

Figure 4.1: Photographs showing the setup for four point bending for both cadaveric radii (left) and analog radii from dog 4 (right)..... 70

Figure 4.2: Illustration of the custom torsion testing fixture (left), and a photograph showing the fixture mounted on the materials testing machine with a composite radius between the grips (right). 72

Figure 4.3: Illustration showing the relationship between the variables used to convert the linear loading of the materials testing machine into torque and angular displacement 73

Figure 4.4: Photograph showing the setup for axial loading of analog and cadaveric radii... 74

Figure 4.5: Photograph showing the set up for screw withdrawal testing..... 76

Figure 4.6: Photographs showing the set up for cyclic testing of the composite radii/bone plate construct. 77

Figure 4.7: Chart showing the stiffness of composite and cadaveric radii in 4 point bending tests. Error bars indicate one standard deviation from the mean. 78

Figure 4.8: Load deformation plots for one sample from each group of analog radii, as well as the cadaveric radius from which the analog bones were modeled. 79

Figure 4.9: Load deformation plot for destructive testing in four-point bending of an analog radius with 0.30 fiber loading, and the cadaveric radius from which the analog radii were modeled. 81

Figure 4.10: Chart showing the energy at failure (J) for the cadaveric and composite radii. Error bars indicate one standard deviation from the mean. 81

Figure 4.11: Load displacement plot for a pair of screw withdrawal tests, showing the failure load of both cadaveric and analog samples (circled).4.1.4 Screw withdrawal tests. 83

Figure 4.12: Chart showing the results of destructive 4 point bending tests. Error bars indicate one standard deviation from the mean. 83

Figure 4.13: Chart showing the internal and external torsional stiffness of composite and cadaveric radii. Error bars indicate one standard deviation from the mean..... 84

Figure 4.14: Chart showing the axial stiffness of composite and cadaveric radii. Error bars indicate one standard deviation from the mean. 86

Figure 4.15: Chart showing the coefficient of variation across all mechanical testing modes. 87

Figure 4.16: Plot showing the load vs. displacement for the plated analog radii at 3, 4, 5 and 6 million cycles. 88

Figure 4.17: Plot showing cranio-caudal measurements of the diaphysis of the cadaveric radii versus the stiffness in 4-point bending. Data with the same marker shape indicate contralateral limb pairs. 91

Figure 5.1: Plot summarizing the relationship between relative density and relative modulus of elasticity derived from EBM fabricated Ti6Al4V foam structures reported in the literature. 100

Figure 5.2: Plot summarizing the relationship between relative density and relative compressive strength derived from EBM fabricated Ti6Al4V foam structures reported in the literature. 101

Figure 5.3: Plot summarizing the relationship between strut diameter and compressive modulus of elasticity from EBM fabricated Ti6Al4V foam structures reported in the literature. 101

Figure 5.4: Plot summarizing the relationship between strut diameter and relative compressive strength derived from EBM fabricated Ti6Al4V foam structures reported in the literature. 102

Figure 5.5: Plot summarizing the relationship between pore size and compressive modulus of elasticity derived from EBM fabricated Ti6Al4V foam structures reported in the literature. 102

Figure 5.6: Plot summarizing the relationship between pore size and compressive modulus of elasticity derived from EBM fabricated Ti6Al4V foam structures reported in the literature. 103

Figure 5.7: Plot summarizing the relationship between strut diameter and relative density derived from EBM fabricated Ti6Al4V foam structures reported in the literature. 103

Figure 5.8: Plot summarizing the relationship between pore size and relative density derived from EBM fabricated Ti6Al4V foam structures reported in the literature. 104

Figure 5.9: Illustration of rhombic dodecahedron unit cell geometries with relative densities of 0.2 (left), 0.3 (center) and 0.4 (right). 107

Figure 5.10: Illustrated photograph of the Arcam A2 build chamber (left) and electron beam column (right). 110

Figure 5.11: Plot illustrating the relative contribution of each processing step within a layer. 111

Figure 5.12: Photograph showing the test specimens partially removed from the sintered Ti6Al4V powder. 113

Figure 5.13: Photograph illustrating the technique for visual confirmation of powder removal (3mm unit cell, 30% nominal relative density). 114

Figure 5.14: Photograph showing one sample of each of the nine specimen types. Note that unit cell size and relative densities shown are nominal. 114

Figure 5.15: Photograph showing the four point flexure test setup for one of the samples (Nominal 6mm and 20% relative density). 117

Figure 5.16: Mean measured strut dimension of EBM-fabricated mesh structures, error bars indicate 95% confidence intervals, dashed columns specify target dimension measured from CAD models. The dotted line represents the approximate EBM melt pool width. 119

Figure 5.17: Photo micrographs showing representative struts of each of the nine specimen types tested. Scale bar indicates 2000 μ m. 120

Figure 5.18: Representative load-displacement curves for each of the nine specimen types. 122

Figure 5.19: Graph showing the modulus of elasticity for different nominal relative densities and nominal unit cell sizes. Error bars indicate 95% confidence interval. 122

Figure 5.20: Graph showing the ultimate strength for different nominal relative densities and nominal unit cell sizes. Error bars indicate 95% confidence interval. 123

Figure 5.21: Plot of relative flexural modulus versus relative density. 126

Figure 5.22: Plot of relative strength versus relative density. 126

Figure 6.1: Schematic showing the placement and contouring of the proximal portion of the standard cranial limb sparing plate. 140

Figure 6.2: Finite element results showing plate deflection at two locations for both cranial and medial contoured designs. 141

Figure 6.3: Illustration showing the ovoid cross section of the graft segment. Open boundaries of lattice unit cell structures are identified (left). 143

Figure 6.4: Photograph showing EBM fabricated, Ti6Al4V test specimens with varying relative density and ovoid cross section. 144

Figure 6.5: Screen capture illustrating 5 plate configurations (0.4 relative density mesh shown); biplanar with 12 holes (A), biplanar with 6 holes (B), cranial-conformal (C), cranial-contoured (D), and medial (E). 145

Figure 6.6: Screen capture illustrating the random assignment of samples to builds 1-3 and, subsequently, to positions 1-25. 147

Figure 6.7: Photograph showing the EBM produced test implants from build 1. 148

Figure 6.8: Solidworks model of the drilling and cutting guide. The orientation and position of drill axes are shown as cylinders. 149

Figure 6.9: Photographs showing; the cutting and drilling guide with composite analog radius (A), the clamped and located radius (B), placement of the drilling guides on the cranial and medial planes (C) and drilling of cranial holes (D). 150

Figure 6.10: Photograph showing the cut, drilled and tapped proximal radii corresponding to each implant configuration. 151

Figure 6.11: Photographs showing the CNC laser cutting of the Fujifilm prescale film..... 153

Figure 6.12: Photograph of the Fujifilm prescale calibration test setup (A), a test cylinder using an EBM fabricated surface rather than a polished surface (B) and a 3D surface contour plot of the EBM surface roughness..... 154

Figure 6.13: Graph showing calibration curves for the Fujifilm prescale LW pressure sensitive film produced with both polished and as fabricated EBM surfaces. Zones A-D represent the manufacturers calibration curves as a function of relative humidity (room temperature, D=0-45% relative humidity, C=45-60%, B=60-80%, A=80-100%)..... 155

Figure 6.14: Photograph showing the components of the prescale assembly including the calibrated torque driver (A), the aligned prescale film with distal screw installed (B), the construct with six screws applied to a torque of 2Nm (C), the disassembled construct and stained precale file (D)..... 156

Figure 6.15: Illustration of Fujifilm prescale analysis steps. Raw data (A) were converted to black and white by thresholding (B), the convex hull area and perimeter were calculated (C), particle number, area and perimeter were calculated (D)..... 158

Figure 6.16: Example of composite image averaging ($n=15$) for a contoured plate..... 159

Figure 6.17: Photograph showing an assembled test implant (Cranial-conformal, 0.2 relative density mesh) with strain gauges installed in proximal and distal plate locations. 161

Figure 6.18: Photograph of the Strainsmart 7000 setup (cantilever test shown). 162

Figure 6.19: Photograph showing the cantilever testing fixture installed in the ATS 1600C (Cranial conformal plate with 0.4 relative density mesh)..... 164

Figure 6.20: Assembled torsional testing fixture (top) and disassembled (bottom). The moment (lever) arm accommodates both internal and external torsion..... 165

Figure 6.21: Photograph of the torsion testing fixture installed on the ATS testing machine (12 screw, biplanar configuration with 0.2 relative density mesh shown). 166

Figure 6.22: Axial testing fixture, the proximal split housing is capped by a hemisphere to permit minor rotations during compression testing, the distal end is fixed into a pocket milled into the base plate. The bottom of the pocket is angled 1.6 degrees to the horizontal to align the axial centroid of the construct with the loading axis. 167

Figure 6.23: Plot showing the measured stiffness (in four point flexure) of analog radii produced with each of three batches of resin.....	169
Figure 6.24: Retrospective Shewhart control chart for individuals for the four point flexure stiffness of analog radii as a function of manufacturing sequence.	169
Figure 6.25: Load displacement plots for non-destructive testing in four point flexure . Test bars consisted of ovoid cross sections with rhombic dodecahedron unit cell structures of various relative densities.....	170
Figure 6.26: Plot of relative modulus of elasticity as a function of relative density for the ovoid cross section bars, these results are compared with the same for the rectangular bars tested in chapter 5.	171
Figure 6.27: Composite image averages for each of the cranial plate configurations tested, biplanar (left), cranial-contoured (center) and cranial conformal (right).	172
Figure 6.28: Histogram showing the number of pixels of each grayscale value for the composite average images (0 = black, 255 = white).....	172
Figure 6.29: 3D surface plots representing the contact area and intensity for the composite average of each plate design.	173
Figure 6.30: ANOVA results for the effect of plate type on the percentage of contact area.	174
Figure 6.31: ANOVA results for the effect of plate type on the convex hull area.	175
Figure 6.32: ANOVA results for the effect of plate type on the percent solidity of the prescale stains.	175
Figure 6.33: ANOVA results for the effect of plate type on the number of particles counted in the prescale stains.	176
Figure 6.34: Plot showing the effect of plate type on the average size of particles in the Fujifilm prescale stains.	177
Figure 6.35: Plot showing the pair correlation function for each of the three plate types, a greater likelihood of encountering a neighboring particle is apparent for contoured plates as compared to conformal plates suggesting a greater dispersion of contact for the conformal plates.	178

Figure 6.36: Chart showing the effect of the relative density of the segmental repair on the Cantilever stiffness for each plate configuration. Error bars indicate ± 1 standard deviation. 180

Figure 6.37: Recorded average maximum principal and shear strains for the proximal and distal locations during cantilever testing at a 55 N load as a function of implant relative density. 181

Figure 6.38: Recorded average maximum principal and shear strains for the proximal and distal locations during cantilever testing at a 100 N load as a function of implant relative density. 182

Figure 6.39: Recorded average maximum principal and shear strains for the proximal and distal locations during cantilever testing at a 55 N load as a function of implant plate configuration. 182

Figure 6.40: Recorded average maximum principal and shear strains for the proximal and distal locations during cantilever testing at a 100 N load as a function of implant plate configuration. 183

Figure 6.41: Polar plot showing the average magnitude and direction of the maximum principal strain (relative to the gauge center) during cantilever testing for each implant configuration. Log strain (μ strain) is represented on the vertical axis while the orientation angle (degrees) is represented on the circumference. 184

Figure 6.42: Chart showing the effect of the relative density of the segmental repair on the axial stiffness for each plate configuration. Error bars indicate ± 1 standard deviation. 186

Figure 6.43: Plot of axial stiffness as a function of percent contact area. 186

Figure 6.44: Recorded average maximum principal and shear strains for the proximal and distal locations during axial testing at a 150 N load as a function of implant relative density. 187

Figure 6.45: Recorded average maximum principal and shear strains for the proximal and distal locations during axial testing at a 350 N load as a function of implant relative density. 188

Figure 6.46: Recorded average maximum principal and shear strains for the proximal and distal locations during axial testing at a 150 N load as a function of implant configuration. 189

Figure 6.47: Recorded average maximum principal and shear strains for the proximal and distal locations during axial testing at a 350 N load as a function of implant configuration. 190

Figure 6.48: Polar plot showing the average magnitude and direction of the maximum principal strain (relative to the gauge center) during axial testing for each implant configuration. Log strain (μ strain) is represented on the vertical axis while the orientation angle (degrees) is represented on the circumference. 191

Figure 6.49: Chart showing the effect of the relative density of the segmental repair on the torsional stiffness for each plate configuration. Error bars indicate ± 1 standard deviation. 193

Figure 6.50: Recorded average maximum principal and shear strains for the proximal and distal locations during torsional testing at a 1750 Nmm moment as a function of implant relative density. 194

Figure 6.51: Recorded average maximum principal and shear strains for the proximal and distal locations during torsional testing at a 3100 Nmm moment as a function of implant relative density. 194

Figure 6.52: Recorded average maximum principal and shear strains for the proximal and distal locations during torsional testing at a 1750 Nmm moment as a function of implant configuration. 195

Figure 6.53: Recorded average maximum principal and shear strains for the proximal and distal locations during torsional testing at a 3100 Nmm moment as a function of implant configuration. 195

Figure 6.54: Polar plot showing the average magnitude and direction of the maximum principal strain (relative to the gauge center) during torsional testing for each implant configuration. Log strain (μ strain) is represented on the vertical axis while the orientation angle (degrees) is represented on the circumference. 196

Figure 7.1: Illustration showing the bony anatomy of the canine forelimb. 204

Figure 7.2: Photograph of the custom built fixture holding paired limbs with 12° carpal extension during CT scanning (left) and image of a 3D reconstruction of a scanned forelimb pair (right). 209

Figure 7.3: Illustration showing the process steps for the custom limb sparing endoprosthesis design. 211

Figure 7.4: Screen capture showing the use of curvature analysis to simplify the carpal joints for plate design. 213

Figure 7.5: Screen capture illustrating the use of curvature analysis for defining custom plate geometry.	214
Figure 7.6: Screen capture showing the layout of the EBM build platform.	216
Figure 7.7: Photograph showing the five custom endoprostheses after EBM processing and powder removal.	217
Figure 7.8: Photograph showing the five custom endoprostheses after finishing.	218
Figure 7.9: Photograph showing a side-by-side comparison of the two endoprosthesis configurations evaluated in this study. The EBM fabricated custom endoprosthesis (top) and the commercial endoprosthesis (bottom).	219
Figure 7.10: Photograph showing the use of the test fixture to align the limbs during potting.	221
Figure 7.11: Photograph showing the dorsolateral incision and the surgical approach.	222
Figure 7.12: Photograph showing additively manufactured guides for strain gauge placement.	223
Figure 7.13: Photograph showing the placement of the uniaxial strain gauge on the dorsolateral surface proximal to the osteotomy site.	224
Figure 7.14: Photograph showing the placement of the proximal portion of a custom endoprosthesis.	227
Figure 7.15: Photographs showing the placement of commercial (top) and custom (bottom) endoprostheses immediately after surgical placement.	228
Figure 7.16: Photograph of the biomechanical testing of a forelimb prior to the surgical placement of an endoprosthesis.	230
Figure 7.17: Photographs showing the biomechanical testing of forelimbs after placement of commercial (left) and custom (right) endoprostheses.	232
Figure 7.18: Graph showing the average stiffness of limbs before surgery and after placement of endoprostheses.	234
Figure 7.19: Graph showing the average elastic potential energy stored at a load of 150 N for limbs before surgery and after placement of endoprostheses.	235

Figure 7.20: Graph showing the strain at a load of 150 N for limbs before surgery and after placement of endoprostheses. 236

Figure 7.21: Plot showing ANOVA results comparing the duration of the surgeries for the two implant configurations evaluated. 238

1.0 INTRODUCTION

In companion animals, such as dogs, the decision to amputate a limb has traditionally been one of last resort. However, in the case highly metastatic cancers of the bone, amputation is often the standard of care. Although primary bone cancers are relatively rare, accounting for approximately 5% of all cancer found in canines, 98% are malignant (LaRue et al. 1989). Osteosarcoma is the most common primary bone tumor in dogs. The high growth metaphyseal regions of the appendicular skeleton are the most commonly afflicted. The most common site is the distal aspect of the radius (Liptak, Dernell, Straw & Rizzo, 2004). Osteosarcoma is highly aggressive and rapidly forms micro-metastases, the principle cause of death for roughly 80% of patients. The standard of treatment for canine osteosarcoma consists complete surgical amputation of the affected limb for primary tumor control, and adjuvant chemotherapy for metastasis control.

An emerging alternative to amputation is limb sparing surgery, a procedure by which the diseased portion of the bone is resected followed by endoprosthetic reconstruction. However, in clinical settings, the use of endoprosthetic reconstruction has been associated with high rates of failure and complications including; aseptic loosening, joint or prosthetic instability, infection, implant failure, and fatigue fracture (Liptak, Ehrhart, Santoni, Wheeler, 2006). A key factor in the failure of these constructs may be attributable to the difference in stiffness between the bone and the metallic implant, while lack of bone fixation results in

increased loads being transmitted through the bone plate and screws through cyclic loading. This can lead to bone resorption at the endoprosthesis-bone interface, screw/plate fracture or fatigue, and ultimately, the failure of the prosthetic device. However, *in vitro*, and *in vivo* biomechanical performance data are sparse, and the factors influencing implant design, fixation, and performance are poorly understood.

This work seeks to address the shortcomings of current limb sparing endoprosthesis design by taking advantage of relatively new additive manufacturing technologies to develop a novel, custom implant for limb sparing surgery. Additive manufacturing is a process by which components are fabricated by selectively curing, consolidating, or depositing materials in successive layers. These technologies, which include electron beam melting (EBM) and selective laser sintering (SLS), are now capable of manufacturing extremely complex, patient specific, geometries using a variety of biocompatible metals directly from three-dimensional computer models. By eliminating the need for product specific manufacturing tooling, additive manufacturing facilitates precise control of mechanical properties, surface topography, and geometry of implants without incurring the high costs associated with tooling and setup. Patient specific implants designed from computer models can be designed using medical imaging data (e.g. computed tomography, magnetic resonance imaging, etc.) allowing orthopedic procedures to be carried out with little or no modification to the underlying bone structure thereby improving the bone-implant interface (Harrysson &

Neyfeh, 2007). Implants can also be optimized for both bone fixation, and transfer of mechanical loads through the implant (Harrysson, Cansizoglu, & Marcellin-Little, 2008).

The objectives of this research will be two fold. The first is to design and fabricate a patient specific limb sparing implant using medical imaging and electron beam melting technology. The novel endoprosthesis needs to address stress shielding and construct failure at the bone implant interface. Experimental analysis of several plate/endoprosthesis configurations is required to improve the characteristics of the implant. The large sample size requirements of such a study precludes the use of cadaver bones. To overcome this limitation, new experimental techniques have been developed that involve analog representations of patient specific bones. A secondary objective will be to develop the experimental techniques necessary to compare the biomechanical characteristics of commercially available limb sparing endoprosthesis to custom, EBM endoprosthesis in an *in vitro* experiment.

This dissertation is divided into 8 chapters, The first section reviews the state of canine limb sparing at the distal radial site with a focus on highlighting the reported modes of clinical failure. The next section examines additive manufacturing as it relates to the design and development of patient specific implants. Despite the advantages of additive manufacturing, there is still a great deal of difficulty associated with the mechanical testing and evaluation of patient specific implants. A large portion of this work, in chapters 3 and 4,

has therefore been dedicated to the development and validation of a patient specific analog of the canine radius to serve as an experimental platform for evaluating multiple configurations of custom implants. In order to further develop this concept, the fifth chapter investigates the flexural mechanical properties of non-stochastic metal foams for low stiffness implants and the sixth chapter presents an experimental evaluation of multiple plating and stiffness configurations for the proximal portion of limb sparing implants. Metrics such as construct stiffness, strain and contact at the bone implant interface are evaluated. An *in vitro* biomechanical comparison of patient specific limb sparing endoprosthetics (manufactured using electron beam melting technology) to commercially obtained limb sparing endoprosthetics is reported in the seventh chapter.

2.0 LITERATURE REVIEW: THE CURRENT STATE OF CANINE LIMB SPARING TECHNOLOGY FOR THE DISTAL RADIUS

Limb-sparing for the palliative treatment of canine osteosarcoma has been proposed as a viable alternative to amputation for primary tumor control. Preservation of limb function has been achieved through surgical removal of the primary tumor and replacement of the bony defect with either a cortical allograft, metal endoprosthesis, transposition of an autograft, or through transport osteogenesis. Limb sparing in dogs often involves arthrodesis of the joint. Dogs with tumors of the distal radius, tibia, or ulna are preferable candidates because dogs can retain excellent limb function after arthrodesis (Straw & Withrow 1996). Arthrodesis of the scapulohumeral joint is poorly tolerated (Kuntz et al., 1998).

However, limb-sparing surgery has been linked to high complication rates, ranging from 15 to 55% in some cases. Complications include implant mechanical failure, infection, fracture, allograft resorption and local tumor recurrence (Straw & Withrow, 1996). Compared to other veterinary orthopedic procedures these rates are remarkably high (Wesse, 2008). The literature is skewed toward investigations of oncologic outcomes and less towards the biomechanical performance and failure modes of limb sparing procedures. Elucidating the means and mechanisms of failure is a critical part of increasing the clinical applicability of limb sparing procedures. Furthermore, no recent work is known to have consolidated the few biomechanical performance data that are reported. To this end, this

review focuses on the current state of limb sparing techniques, evaluations of biomechanical performance, and failure mechanisms of limb sparing constructs.

2.1 Introduction to Canine Osteosarcoma

Perhaps the greatest sources of variability obfuscating multi-study analyses of canine limb sparing can be traced to the rarity of the disease and the diversity of treatments. Canine osteosarcoma (OSA) is a highly aggressive mesenchymal bone tumor. Approximately 75% of cases originate in the appendicular skeleton in regions most commonly associated with high growth rates, such as the metaphyses of the femur, humerus, radius and tibia (Dernell, Ehrhart, Straw, & Vail, 2007). An early study involving 394 dogs showed that 20.4% of OSA cases occurred in the femur, 19.5% occurred in the humerus, 19.3% occurred in the tibia, 19.2% occurred in the radius, and 4.4% occurred in the ulna (Lui, Dorfman, Hurvitz, & Patnaik 1977). In a more recent retrospective study on 12 dogs, the distal radius and the proximal humerus were the most commonly affected sites at 34.9%, and 18.4%, respectively (Liptak et al., 2004). Dogs weighing greater than 80 pounds have 185 times the risk of developing the disease compared to dogs weighing less than 20 pounds, predisposing large and giant breed dogs such as the Rottweiler, Saint Bernard, and Great Dane (Withrow, Powers, Straw & Wilkins, 1991). Early work indicated a bimodal age distribution for onset with 10% of the cases being under 2 years old, and the average age being approximately 7-8 years (Brodey & Riser 1969). A slight predilection towards males over females has been shown (Brodey & Abt, 1976; Lui et al. 1977). However, these results may be skewed by

newer evidence showing that neutered males are twice as likely as intact males to develop OSA (Liptak, Dernell, Ehrhart & Withrow, 2004).

OSA typically causes localized destruction of the bone which may result in both osteoblastic and osteolytic regions (Hillers, Dernell, Lafferty, Withrow, & Lana, 2005). Radiological characteristics include propagation through the periosteum, lysis of the cortical bone, and sub-periosteal bleeding. The most common symptoms upon presentation are lameness or swelling at the primary tumor site (Dernell et al., 2007). OSA rapidly metastasizes, progressing through the blood to other organs and bones. At the time of diagnosis greater than 90% of dogs already have metastases of some form. Secondary tumors are most commonly detected in the lungs (Liptak, et al., 2004). Prognosis for dogs with OSA is generally poor; without curative treatment, the anticipated median survival time is about one to three months (Coomer et al. 2009; Gayathri & Kirpensteijn, 2010). Despite the aggressive nature of these sarcoma, Dernell et al. found that OSA rarely crosses a joint surface, for example, from the radius to the ulna (2007).

Treatments for canine OSA are widely varied. Palliative options include analgesics (Lester & Gaynor, 2000), radiation (Liptak, Dernell, Ehrhart, Withrow, & Sequin, 2004), or amputation of the affected limb (Liptak, Dernell, Ehrhart, Withrow, 2004). Chemotherapy is one of several curative strategies which may also include amputation or radiation therapy.

The existing data do not show analgesics as having any influence on survival time. Median survival time for dogs treated solely with analgesics is approximately 1-3 months. Radiation therapy has been demonstrated as a curative treatment for control of the primary sarcoma, as reported by Liptak et al. (2004), as well as a palliative treatment (Mayer & Grier, 2006). Chemotherapy (e.g. cisplatin, doxorubicin, and carboplatin) is used in curative intent treatments, often adjuvant to surgical removal of the primary tumor. As documented in Liptak et al. (2004), removal of the primary tumor alone has a minimal influence on the survival time of dogs with osteosarcoma. Likewise, chemotherapeutic agents used without elimination of the primary tumor have not been shown to significantly improve survival time. Berg et al. (1992) found that survival was significantly longer for dogs that were treated with cisplatin after amputation when compared to dogs that were treated with amputation alone.

Amputation is highly effective as a treatment strategy for OSA. Recurrence of the primary tumor is reported in only 1% of such cases (Straw & Withrow 1996). In addition to removing the primary tumor site, limb amputation has been demonstrated to be an effective method of controlling pain (Liptak et al., 2004). Most dogs are able to ambulate well after amputation (Dernell, Ehrhart, Straw & Vail, 2007). Clinical data shows that the median time to adaptation to amputation is 4 weeks, but in many cases dogs can walk unassisted after 12-24 hours (Liptak et al., 2004).

2.2 Limb Sparing Techniques for the Distal Radius

Canine limb sparing has not been shown to improve survival time, therefore, the potential benefits of better mobility and quality of life must be carefully weighed against the inherent risks, complexity and often long recovery periods associated with these procedures. Limb sparing can however result in local control of the disease while simultaneously maintaining limb functionality with minimal pain. In many of the examples reviewed in this paper, adjuvant and neoadjuvant treatments for metastatic disease (chemotherapy, radiation, etc.) are administered in parallel with limb sparing. The effects of various treatments on the biomechanical performance of limb sparing constructs is not well understood.

2.2.1 Allografts

Limb sparing using cortical allografts is the most commonly reported method in the literature. The procedure involves surgical resection of the tumor lesion which is then replaced with the allograft, typically frozen bone grafts from cadavers available from commercial bone banking facilities. Dernell, Ehrhart, Straw and Vail, describe the procedure in detail (2007). The radius is cut 3-5 cm proximal to the margins of the tumor, as determined from radiologic assessment, and disarticulated close to the carpal bones. Computed tomography has been reported to be the most accurate imaging modality for determining the length of osteosarcoma tumors (Davis, et al. 2002). It is rare that the tumor should invade the ulna, but it is often removed as a precaution. Still, a recent

biomechanical study in cadaveric forelimbs tested cortical allograft and metal endoprosthesis to failure at a loading rate of 300N/s with and without ulna preservation and found no significant difference in the constructs, or in the mode of failure. These results suggest that preservation of the ulna does not significantly improve the stiffness of the constructs (Liptak, Ehrhart, Santoni, & Wheeler, 2006).

Figure 2.1 shows an illustration of cortical allograft limb sparing surgery for the distal radius. The frozen allograft is thawed in saline solution, cartilage and tissue in the medullary canal are removed, and the graft is cut and shaped to fit the segmental defect. The allograft is then reduced with a bone plate and screws, usually with a dynamic compression plate or specially designed limb sparing plate. Five or more cortical bone screws are typically reported for the proximal radius (Liptak et al. 2006; Pooya et al. 2004). In the case of distal-radial osteosarcoma, the bone plate is usually affixed to the third metacarpal bone distal to the allograft requiring pancarpal arthrodesis; distally, it covers at least 50-70% of the carpal bone. The plates are often manually bent to approximately conform to the contour of the host bone, and the angle of the arthrodesis ranges from about 7° to 12°. Liptak, Ehrhart, Santoni, and Wheeler, report stabilizing the cortical allograft with 2 cortical bone screws, 1 distal and 1 proximal (2006).

Attenuation of blood supply is also a concern; vasculature is typically poor in the distal radius and is preserved to the extent possible. Withrow and Straw have linked the lack of blood perfusion after limb sparing to infections and construct failure (1996). Dogs are usually able to use the limb well after approximately ten days, but four to six weeks are typically required for soft tissue healing (Dernell, Ehrhart, Straw and Vail 2007). Limited soft tissue coverage and poor vascularization, particularly in areas such as the distal aspect of the radius, intuitively suggests that matching the geometry of the original bone may play a role in the success of an allograft implant.

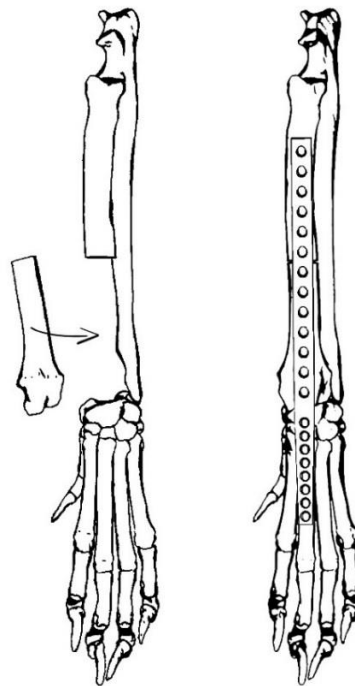


Figure 2.1: Illustration showing a cortical allograft limb sparing surgery. The resected tumor is replaced with a suitable cortical allograft (left) and the construct is reduced with plating that typically involves pancarpal arthrodesis (right).

Incorporation of the cortical allograft into the host through osteoconduction requires long time periods (Johnson et al., 1992). The median survival time for dogs with OSA is usually less than 1 year so a significant level of incorporation is unlikely to be observed in practice. For limb sparing of the distal radius in dogs, the cortical allograft functions as a spacer. Mechanical tests on allograft bones implanted in humans *in vivo* have shown a loss of strength over time due the presence of micro-cracks and a decrease in bone mineral density (Wheeler & Enneking, 2005). In addition the preparation, sterilization and storage of allografts takes time, and is relatively expensive (Liptak, Dernell, Ehrhart & Withrow, 2004). Extreme care must be taken when harvesting the allografts from cadaveric specimens to avoid contamination.

Very high complication rates have been associated with cortical allograft limb sparing. One study of 18 dogs with appendicular allografts reported local tumor recurrence in 5 dogs (28%), local infections in 7 dogs (39%), and implant failure in 2 dogs (11%) as a result of plate fracture. In one of the cases, plate failure occurred after 26 days (distal radial);subsequent amputation was selected. The authors do not report on the type of plates or the type and number of screws used (Morello et al. 2001). Liptak et al. reported an infection rate of 60% in dogs that received cortical allografts for distal radial limb sparing, and a construct failure rate of 40%. The median time to failure in this study was 237 days, and predominantly involved screw loosening or screw breakage in the metacarpal or radiocarpal bones (2006). In a retrospective study of 16 dogs with diaphyseal limb sparing

implants, screws pulling from the cortical allograft was the cause of failure of 4 of the implants (Liptak et al. 2004). A slight reduction in screw loosening from the allograft was detected in a retrospective study (n=60) by packing the medullary cavity with polymethylmethacrylate bone cement at the time of surgery (Kirpensteijn et al., 1998). However, there was no improvement in the failure rates associated with the screws in the proximal radius or metacarpals. A composite allograft/polymer material was used to fill the segmental defect in one reported case that also utilized both cranial and medial plating (Renwick & Scurrall, 2013).

An infection rate of 68% was reported in a study involving 47 dogs with osteosarcoma of the distal radius that had undergone limb sparing surgery with cortical allograft implants (Lascelles et al., 2005). An interesting finding from this study shows that dogs that contract post operative infections were less likely to die (hazard ratio = 0.446). The reasons for this are not entirely known, however increased immune activity resulting from infection may exhibit antineoplastic properties. LaRue et al. (1989) reported an infection rate of 31% in a study of 21 dogs with cortical allograft limb sparing constructs that received either adjuvant chemotherapy or a multimodal treatment combining chemotherapy and fractionated radiotherapy. In one dog the cortical allograft had been almost completely resorbed.

Thrall et al. (1990) administered relatively large doses of radiation, 36-52 Gy, prior to cortical allograft limb sparing in 17 dogs. Construct failure occurred in 9 dogs associated with host bone necrosis and was directly related to radiation dose. Kuntz et al. (1998), in a study involving cortical allograft limb sparing of the proximal humerus in 17 dogs, also reported high construct failure rates. Plate loosening occurred in 12%, allograft fracture occurred in 5.9%, and biomechanical failures occurred in 58%. Amputations were ultimately required in 41% of these cases. Although widely used, cortical allografts for limb sparing in dogs have been associated with numerous pitfalls. The major disadvantages of cortical allograft limb sparing are the high rate of infection/complication and biomechanical failure.

2.2.2 Autografts

Limb sparing using autografts addresses some of the significant problems associated with cortical allografts such as the scarcity and expense of bone banking facilities, as well as, the relatively poor anatomic fit that is achieved. In theory, the likelihood of infection is greatly reduced because the bone is autogenous and therefore not foreign to the immune system. The major disadvantage of using autografts is the risk of local tumor occurrence, and the risk of mechanical failure of the construct which may be exacerbated by inherently compromised graft tissue. A major challenge is the eradication of the OSA with minimal damage to the surrounding tissues while simultaneously preserving osteoinduction and the efficacy of the graft.

Pasteurization of autografts has been reported in several studies. Basic research has shown that bone morphogenic protein (harvested from rabbits) that was heated at various temperatures and time periods retained osteoinductive properties after implantation into the muscle tissues of mice. Heating at 70°C for 10-15 minutes resulted in the maximum preservation of osteoinduction (Nakanishi, Sato, Sato, & Takahashi, 1992). A later study found that autoclaving at 60°C for 30 minutes was sufficient. However, bending and torsion tests in rat femurs subjected to this treatment showed significant degradation of mechanical strength (Manabe, 1993). Buracco, Morello, Martano, & Vasconi reported the use of a pasteurized autograft as used for distal radial limb sparing in a 9 year old maremma shepard (2002). Pasteurization (65°C, 40 minutes) in sterile saline solution (0.9% NaCl) was performed to kill the tumoral cells. The pasteurized bone segment was then repositioned and stabilized with a bone plate and screws with adjuvant cisplatin. Implant loosening was noted at 23.5 months, and the plate was removed because the autograft appeared to be fused. The pancarpal arthrodesis fractured at 48 months, however limb function was fair and pain free.

Morello et al. extended this study to include an additional 12 dogs using the same protocol (2003). Limb function in 12 of the dogs was rated as good, and fair in 1. When compared to 18 dogs having undergone cortical allograft limb sparing, Morello et al., found improved survival (probably due to different chemotherapy protocols) and found no difference in the rate of infection between the two groups (2001). Complications arising from the pasteurized autograft technique include local recurrence (15%), allograft infection (31%),

and implant failure (23%). Implant failure was associated with screw loosening or breakage in all cases. Radiographs were taken at various time points for each case so it is not possible to precisely determine the duration until implant failure. One dog presented with multiple screws loose at 350 days, while two others had 2 loose screws at 76 days and 316 day. The location of the failures was not reported. Limb function was rated as good in 12 dogs and fair in 1.

Irradiation of the autograft has been reported as a method to destroy primary tumor cells. This typically involves wide resection and removal/isolation of the bone tumor followed by a relatively large radiation dose (50 Gy -300 Gy), removal of the adjacent soft tissues, and replacement of the irradiated bone. Approximately 50 Gy has been shown to be tumoricidal (Davidson et al., 2005). Boston, Duerr, Bacon, and LaRue attempted this in a study of five dogs with distal radial osteosarcoma. The resected autograft was exposed to 70Gy and replaced. However, plating of the graft in this study did not involve arthrodesis of the radiocarpal joint. Implant failures occurred in one dog (screw loosening) and fracture of the irradiated autograft occurred in 3 dogs (2007). Liptak et al. reported, in a retrospective study, on 13 dogs that underwent limb sparing surgery using extracorporeal intraoperative radiation therapy (IORT) (2004). Both *in vivo* and *ex vivo* IORT was used for the treatment. For the *ex vivo* cases (n=11), the tumors were osteotomized with 2 cm margins and placed in a plastic (zip-loc) bag filled with 0.9% sterile saline solution for transportation to a radiation suite where a single 70 Gy dose of 6MV photons were delivered to the segment. For the *in*

vivo cases (n=2), Kirschner wires were inserted into the segment, which were suspended from the ceiling hook of the radiation suite where a 70 Gy dose of 6MV photons was delivered. The irradiated segments were replaced and stabilized with dynamic compression plates, interlocking pin, intramedullary pin, or a combination of these. Limb function was graded as excellent in four dogs, good in six, and poor in three (based on level of weight bearing /mobility). The rate of infection was not improved with IORT. Surgical complications included implant failure in five dogs, infection in three, and nerve paralysis in one. Failure occurred as a result of screw, plate, and interlocking nail (ILN) breakage in dogs with humeral OSA. In three dogs with distal tibial metaphyseal osteosarcoma, bending of the distal ILN screw and screw pullout occurred. It was speculated that these failures were preceded by pathologic fracture and collapse of irradiated metaphyseal bone. Pathologic fracture of irradiated bone occurred in 7 dogs. Only one of the subjects in the study involved the distal radius and no complications were reported for this case. Bone degradation resulting from irradiation may render autografts susceptible to fracture, delayed healing and non union (LaRue, Wrigley, & Powers, 1987). In a study conducted in rabbits the bending modulus of bone exposed to 20 Gy radiation decreased significantly during the first 24 weeks, but then partially recovered at 52 weeks (Sugimoto, Takahashi, Toguchida, & Kotoura, 1991).

2.2.3 Ulnar transposition

The use of autogenous grafts has also been investigated using adjacent bones such as the ulna (adjacent to the radius), or the fibula (adjacent to the tibia). This technique facilitates vascular preservation of the graft which may improve union and hypertrophy.

Transplantation of the ulna as either a vascularized bone graft or an avascular graft to the tibia has been demonstrated in six dogs. Rapid graft incorporation and hypertrophy were seen in all of the vascularized grafts, while extensive resorption was seen in the avascular grafts (Szentimrey, Fowler, Johnston, & Wilkinson, 1995). A study by Seguin et al. investigated a surgical rollover technique of the vascularized distal ulna into a distal radial defect (2003). Ulnar osteotomy was performed on the thoracic limbs of 11 canine cadavers to allow the styloid process and 40% of the distal aspect of the radius to be removed *en bloc*. The graft was rolled over into the radial defect and a 3.5 mm broad dynamic compression plate of the length from the proximal aspect of the radius to the distal aspect of the fourth metacarpal bone was placed on the cranial aspect of the radius to secure the graft. The plates were pre-bent to provide 10° of extension at the antebrachiocarpal level. Vascularization was confirmed with radiographic examination. The ulnar transposition technique was also clinically performed on 3 dogs with distal radial osteosarcoma. Figure 2.2 shows an illustration of the ulnar transposition technique.

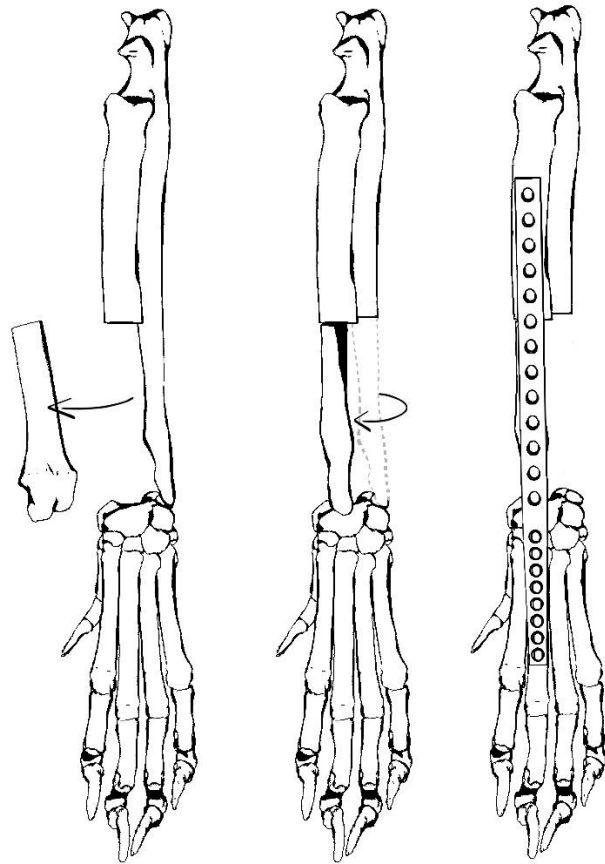


Figure 2.2: Illustration of the ulnar transposition technique of limb sparing for distal radial osteosarcoma in dogs. The lesion is resected (left) along with the ulna which is rotated into the defect (center). The construct is reduced with plating that typically involves pancarpal arthrodesis (right).

Results from the clinical portion of this study suggest that ulnar transposition can be an acceptable limb-sparing technique for tumors of the distal aspect of the radius. After 49 days post implantation, the limb function of Dog 1 was evaluated as good to excellent (75% to full weight bearing). Dog 2 was evaluated after 10 days with excellent limb function and remained excellent for re-evaluation after 241 days. Dog 3 also had excellent limb function at 127 days (Seguin et al., 2003). A biomechanical disadvantage may be the much smaller

cross sectional area, and therefore lower stiffness of the ulna as compared to the radius. Pooya et al. compared the ulnar rollover technique to a cortical radial graft limb sparing procedure in a mechanical test designed to evaluate the biomechanical properties of limbs that had been reconstructed with the two methods (2004). Six pairs of forelimbs from cadaveric dogs (from the Seguin, 2003 study) were used, one of each pair was reconstructed using the ulnar transposition technique, and the contralateral limb was reconstructed with a cortical allograft (the medullary cavity of the allograft segment was filled with polymethylmethacrylate). The plate was pre-bent to provide 10° of extension, and the same number and placement of screws was used in each pair. Limbs were tested for axial loading in a mechanical testing system with an elbow flexion angle between 125° and 130°. The foot was secured with liquid methylmethacrylate to prevent slippage during the loading tests. Axial compression was applied at a rate of 300 N/s until failure of the limbs. The radial cortical graft limbs had significantly greater stiffness (68%), yield load (62%), maximum load (60%), maximum energy (30%) and post-yield energy (28%) than the ulnar transposition graft limbs. This study could not, however, assess the improvements in the load bearing capabilities that result from vascularization and hypertrophy of the transposed ulna. Pooya et al. also analyzed the plate coverage of the metacarpal and reported that limbs with less than 80% plate coverage of the metacarpal were significantly more likely to fail (2004). Complication rates for vascularized ulnar bone grafts have been shown to be similar to other limb sparing techniques for the distal radial site. In a recent retrospective study on 8 dogs, screw loosening and implant failure occurred in 50% of the cohort, and

infection occurred in 62.5% (Hodge, Degner, Walshaw, & Teunissen, 2011). Construct failure brought on by screw loosening was also reported in a great dane case (75kg) six months post op. In this case the ulnar graft was secured with two 15 hole, 4.5mm broad dynamic compression plates applied cranially and cranio-laterally on the proximal end and to the 3rd and 4th metacarpals (Gasch, River, & Bardet, 2013).

2.2.4 Bone transport osteogenesis

Bone transport osteogenesis (BTO); a form of distraction osteogenesis, a process by which new bone tissue is generated between two segments of bone that are slowly pulled apart. This is typically used as a method to fill large gaps in bone after trauma or, more recently, in limb sparing surgery (Denga, Ehrhart, & Ferretti, 2000). An external ring fixator construct is used to achieve distraction while also transferring the mechanical loads through the fixator supports. In BTO limb sparing, the tumor lesion is resected and a small section of healthy bone adjacent to the defect is cut and suspended with tensioned wires close to its original position. The segment is slowly moved distally across the defect over time by adjusting the external fixator rings. In the pathway of the segment new bone is generated. Continual yet gradual distraction that does not interfere with the blood supply is critical to the process. The resulting regenerate bone remodels into lamellar bone at rate that typically exceeds that of normal fracture healing (Ehrhart 2005). When the segment reaches the opposing side of the defect compression is initiated in order to promote densification and union at the docking site (Denga, Ehrhart, & Ferretti, 2000). Ehrhart reported the results of

using this technique on 9 dogs with appendicular osteosarcoma (2005). The mean size of the defect was 9.5 cm. A 2 cm transport segment was cut from the distal end of the proximal portion of the defect. The distraction process began 3-7 days after surgery because of the neoadjuvant chemotherapy treatments that were administered, and took place at a rate of about 1 mm/day. Adjustments to the fixator were necessary four times per day (e.g. 0.25 mm per adjustment). The average time until docking reported was 123 days, ranging from 66 days to 150 days. The average time between surgery and fixator removal was 205 days with a range from 90 to 350 days. Limb salvage was rated as good in 7 dogs, one of which had complications associated with a previous allograft limb sparing surgery. Complications included 2 local tumor recurrences that resulted in limb amputation, and non-union in one dog that required an internal plate. The time and effort required for this procedure is the most prominent disadvantage. An Illustration of a typical BTO construct is shown in Figure 2.3. Double bone transport osteogenesis has been reported in at least one case study involving a tibial limb spare (Rovesti, Bascucci, Schmidt, & Marcellin-Little, 2002). In this procedure, two adjacent segments were transported 0.25 mm for the proximal segment and 0.5 mm for the distal segment every 8 hours. Radiographic evaluations 4 weeks post operation showed evidence of bone regeneration. The frame was removed after 162 days and the limb was immobilized with a plaster cast until tarsal arthrodesis was complete. At day 201, the canine underwent tibiotarsal arthrodesis. The canine died of metastatic disease 239 days after initial surgery. A transverse ulnar bone transport osteogenesis technique for distal radial limb sparing was developed using 10 cadaver dogs in an effort to accelerate bone formation and

minimize owner involvement (Jehn et al., 2007). The technique involves making longitudinal and transverse osteotomies of the distal ulna (while preserving the vascularization) and then transporting this segment transversely (relative to the longitudinal axis of the bone) through the defect using linear reeling motors. The process was implemented in one *in vivo* case in which 50% of the radius was excised. The distraction of the ulnar segment was completed after day 23. By day 45 the regenerate bone had radiographically evident dense cortices, and on day 94 the construct was removed.

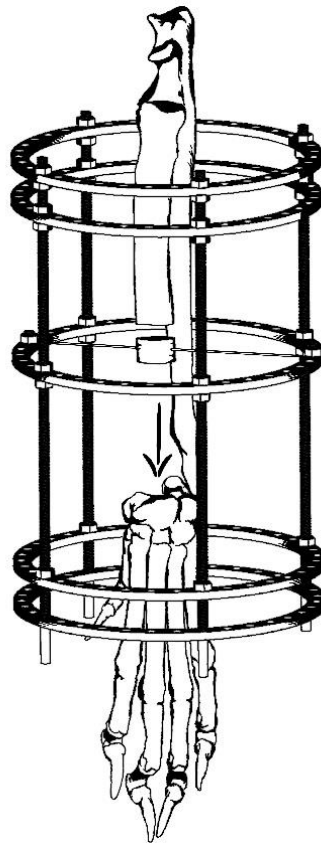


Figure 2.3: Illustration showing the use of external fixators to transport the bone segment through the segmental defect.

2.2.5 Metallic endoprosthesis

Limb sparing with modular endoprostheses has several advantages; treatment does not depend on special equipment, bone banking facilities, or external beam radiation machines. Metallic endoprostheses and plates designed for distal radial limb sparing in dogs are now commercially available. These are similar in appearance to limb sparing constructs using cortical allograft, only a metallic spacer bridges the segmental defect. The surgical technique for placing this type of limb sparing implant is similar to the technique used for the cortical allograft implants, and is described in great detail elsewhere (Dernell, Ehrhart, Straw, and Vail, 2007). These endoprostheses are made from solid 316 stainless steel therefore no incorporation, osseointegration, or vascularization occurs. Although compression between the bone and the spacer is surgically imposed, mechanical loads are likely transferred primarily through the plate and the bone screws. Figure 2.4 shows an example of the commercially available endoprostheses for canine limb sparing surgery (Veterinary Orthopedic Implants, Burlington, VT).

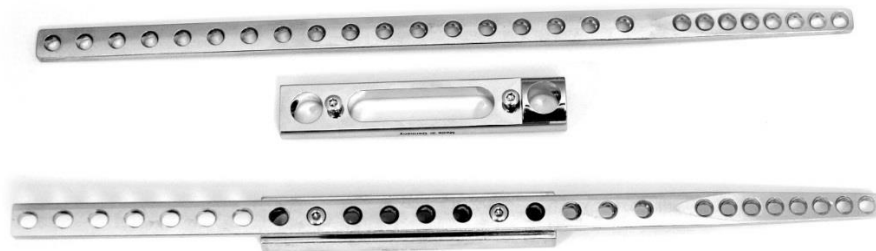


Figure 2.4: Photographs showing a commercially available metal endoprosthesis for limb sparing in dogs.

Known limitations to endoprostheses, however, include aseptic loosening, infection, joint or prosthetic instability, fatigue fracture, and wear or dissociation of modular components. Differences in the modulus of elasticity between the endoprosthesis and cortical bone can result in stress concentration at the endoprosthesis-bone interface and abnormal load transfer to the surrounding bone. These factors may lead to bone resorption at the endoprosthesis-bone/ bone-screw interface. A prospective clinical study conducted to compare the surgical outcome of dogs with osteosarcoma of the distal radius randomly treated with limb sparing surgery, using either cortical allograft (n=10) or metal endoprosthesis (n=10), found no statistical difference in the rate of infection or the occurrence of failures (Liptak, Dernell, Ehrhart, & Lafferty, 2006). Infection was seen in 11 of the 20 dogs included in this study. The infection rate for the cortical allograft group was 60% with a median time to infection of 80 days. For the endoprosthesis group, the infection rate was 50% with a median time to infection of 61 days.

Limb sparing in both groups was performed from a craniocaudal approach to the radius. In the groups that received cortical allograft limb sparing, the radius was osteotomized 3cm proximal to the tumor. These margins were larger in the endoprosthetic group because the 122 mm length of the metal spacer dictated the size of the section removed. The percentage of the radius replaced was significantly different in the two groups, the median for the endoprosthesis group was 60.9%, while for the cortical allograft group the median was 48.6%. The proximal surface of the radiocarpal bone was also osteotomized to

provide a flat surface to place the cortical allograft or endoprosthesis. Antibiotic impregnated PMMA was placed in the medullary cavity of the cortical allograft. The endoprosthetic constructs had no antibiotic cement. The radial defect was then filled by either one of the two implant configurations. The bone plates were either applied straight or pre-bent to between 10 and 15 degrees at the carpal joint based on the preference of the surgeon. A minimum of five cortical screws (3.5mm or 4.5mm) were placed in proximal to the defect, and five cortical screws (2.7mm or 3.5mm) were used in the radial carpal, and third metacarpal bones, and a minimum of 50 % of the length of the third metacarpal was covered by the plate.

Construct failure occurred in 8 dogs, 4 from the cortical allograft group and 4 from the endoprosthesis group. In the cortical allograft group, the median time to failure was 309 days. Three failures were associated with screw loosening or breakage in the metacarpal bone, and one was associated with screw breakage in both the radiocarpal bone as well as the cortical allograft. In the endoprosthesis group, the median time to failure was 180 days. All four of the constructs in this group failed due to screw loosening or screw breakage in the proximal portion of the radius. One dog was also diagnosed with a fracture of the metacarpal at the distal screw hole. No patient specific data regarding weight, age, or percent of limb resected was reported.

The clinical comparison between cortical allograft constructs and endoprostheses was paralleled with a laboratory biomechanical comparison conducted on 12 paired cadaver limbs from dogs weighing more than 30 kg (Liptak, Ehrhart, Santoni, & Wheeler, 2006). Half of the limbs were randomly assigned to have the ulna resected as well. Results of the biomechanical tests conducted with an elbow flexion angle of about 125° and a loading rate of 300 N/s showed that limbs reconstructed with the endoprosthesis had 47% greater yield load, 64% greater yield energy, and 41% greater ultimate load than limbs reconstructed with cortical bone grafts when the ulna was preserved. With the ulna resected, the endoprosthesis had 85% greater yield load, 113% greater yield energy, and 61% greater ultimate load than limbs reconstructed with cortical bone grafts. The constructs were attached to the limb using four 3.5 mm cortical bone screws in the proximal radius, two 3.5 cortical bone screws (in the cortical bone graft) or specialized machine screws (in the endoprosthesis), and seven 3.5 cortical bone screws in the radial carpal bone and third metacarpal bone.

The failure modes observed in this study included metacarpal fracture, metacarpal plate pullout, graft failure, plate bending/fracture, fracture of the radius, and plate pullout from the proximal radius. With the exception of the one metacarpal fracture, none of these failure modes were observed in the clinical study. Although the ultimate and yield loads reported in this study are relevant to understanding the limits of the constructs, they are not realistic in a clinical setting. There was no significant difference in the stiffness reported for the cortical allograft (195 ± 48 N/mm) and for the endoprosthetic reconstructions (245 ± 33

N/mm). However, the relatively high variability suggests that more samples would be required to investigate this further. A recent case report showed radiographic evidence of bone resorption around screws in the proximal radius of a 48 kg Rottweiler prior to endoprosthesis failure (Venzin, Grundmann, & Montavon, 2012) in which a locking plate version of the endoprosthesis was used (Veterinary Orthopedics Implants). The use of both locking plate and standard plating of the endoprosthesis was later reported in 3 dogs. None of the plates were pre-bent at the distal arthrodesis site (Venzin, Grundmann, & Montavon, 2012). Loosening of 2 proximal screws was radiographically identified in the first case (standard plate) after 2 weeks. By 8 months loosening of screws in the proximal radius and metacarpal led to failure of the implant. This case used a 122 mm endoprosthesis spacer, seven 3.5 mm bicortical screws proximally and 2.7 mm bicortical screws in the third metacarpal. The second case used a 98 mm endoprosthesis spacer.

At least one case report has attempted to address the high stiffness of modular endoprostheses by replacing the spacer with tantalum foam which was affixed to the host bone with a dynamic compression plate (MacDonald & Schiller, 2010). However no data were presented on the mechanical performance of this implant. Other studies have reported that the structure of porous implants reduces the mechanical properties of titanium, making them closer to natural bone, with a higher compressive strength than bone and an appropriate elastic modulus. An implant with a lower elastic modulus results in stresses and strains that

are close to intact bone, and may be better able to reduce stress shielding that would otherwise be present (Li, Li et al. 2006; Zou, Zhang et al. 2007).

Recently the use of additive manufacturing, or 3D printing has been reported for the printing of low modulus metal implants for the reduction of stress shielding (Harrysson et al., 2008). Additive manufacturing technologies such as electron beam melting and laser melting fabricate components from biocompatible metals in a layerwise fashion. This affords a unique opportunity of manufacturing without the use of complex tooling or fixtures. Three-dimensional geometry data obtained with medical imaging systems such as computed tomography or magnetic resonance imaging facilitates the design of custom implants and constructs that conform to a given individual's anatomy (Harrysson, Cormier, Marcellin-Little, & Jajal, 2003). These custom implants are directly fabricated by additive manufacturing processes, and may incorporate features to optimize healing and long term success by precisely controlling mechanical properties, material properties, surface topography, and implant structure. Custom implants can be made to conform to the individual patient's anatomy, therefore, orthopedic procedures can be carried out with little or no modification to the underlying bone structure thereby optimizing the bone-implant interface (Harrysson, Hosni, & Neyfeh, 2007). The same process facilitates the generation of engineered lattice structures with controlled porosity and geometry which can be optimized for both bone fixation, and transfer of mechanical loads through the implant and into the healthy bone tissue, thus minimizing stress shielding and bone resorption. With additive

manufacturing porous structures can be fabricated together with solid portions of an implant as a single component. This process has also been used in reported cases of custom limb sparing endoprosthesis (Peck & Marcellin-Little, 2013). Figure 2.5 shows a patient specific limb sparing implant that incorporates conformal cranial and medial plating integrated with a geometrically accurate metal graft (mirrored from the contralateral limb). The distal plating is also incorporated into the implant with fixation at the radio-carpal bone as well as the third and fourth metacarpals. Despite the promising appeal of additive manufacturing for limb sparing, very little work has been published on the subject.

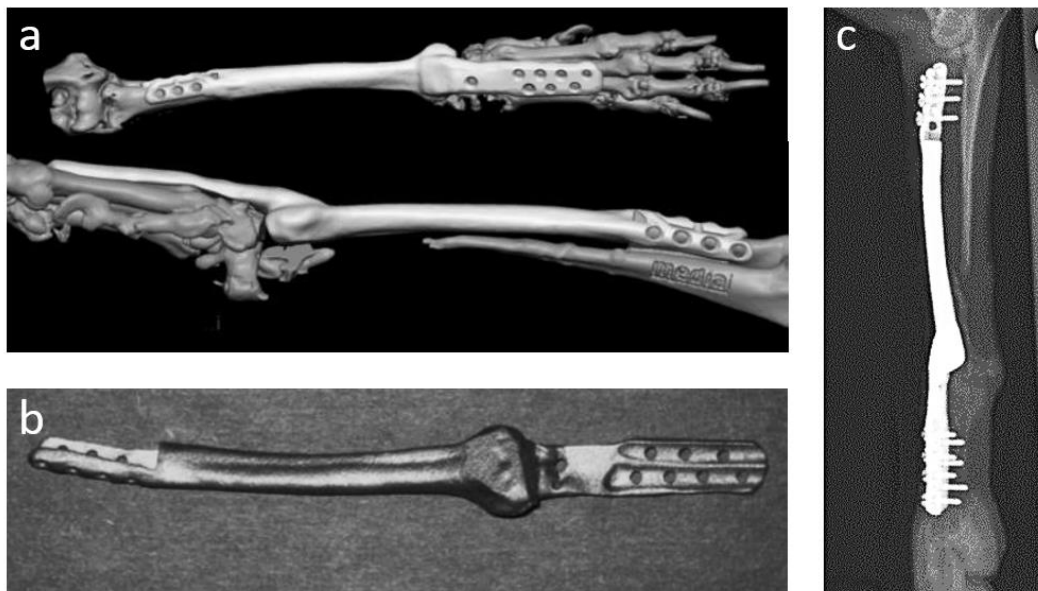


Figure 2.5: Custom limb sparing implant for the radius of a dog. CT scans reconstructed into 3D models are used for designing the implant (a) which was printed using selective laser melting (b). Post-operative radiograph showing the custom implant in place (c).

2.3 Discussion

Part of the challenge in gathering conclusive evidence on the failure mode and frequency for distal radial limb sparing lies in the relative scarcity of the disease, and part of the challenge lies in the lack of reporting on those factors which are well known to influence the performance of biomechanical implants. Of the literature reviewed a total of 263 cases of limb sparing were reported for the distal radial site (excluding bone transport osteogenesis). Most reports were based on cortical allograft limb sparing (n=220), followed by metal endoprosthesis (n=15), pasteurized autografts (n=14), ulnar transposition (n=12), irradiated autografts (n=1) and trans-tumoral plating (n=1). The type of limb sparing plate used was only reported in 105 cases (39.9%) and included 3.5mm (n=45) and 4.5mm (n=3) broad dynamic compression plates (DCP), 3.5mm narrow compression plates (n=16), 4.5mm narrow compression plates (n=15) and custom limb sparing plates (n=26). The length of the segmental defect was reported in 78 (29.7%) cases and its length as a percentage of the radius length in 22 (8.4%) of the cases. The type and number of proximal screws used was reported in 26 (9.9%) and 37 (14.1%) of cases respectively. The type and number of distally placed screws was reported in 36 (13.7%) and 26 (9.9%) cases respectively, and the type and number of screws affixing the plate to the segmental defect was reported in 24 (9.1%) and 100 (38.0%) of cases. Of the cases that reported the number of screws (37) the mean number of screws was 5.73 (range 3 to 9) for the proximal portion of the plate and 6.56 (range 3 to 10) for the distal portion of the plate. There are few reports that have investigated the

influence of the number of screw engagements. A diminishing advantage of additional screws was reported for placement of more than four 2.7 mm cortex screws in cantilever bending of a bovine rib (Haug, 1993).

From the literature on internal fracture fixation, the diameter of screws used should not exceed 40% of the bone diameter (Johnson, Houlton & Vannini, 2005) therefore limb sparing in large breed dogs typically means using screws between 2.7 mm and 4.5 mm. For metacarpal bones bone screws, Piermattei & Flo recommend that screw diameters should not exceed 25-30% of the bone diameter (1997). For non-locking plates the primary means of force transfer between the implant and the bone is through friction. Compression of the plate against the bone is induced by the screw. If the compression between the screw and the plate decays, rigidity is lost, and movement, non-union and failure of fixation may be the outcome. (Shatzker, Horne, & Sumner-Smith, 1975). Screw torque was not reported in any of the studies reviewed.

Pancarpal arthrodesis has been described in nearly all of the limb sparing procedures discussed. A retrospective study of metacarpal fractures in 54 dogs with dorsally applied pancarpal arthrodesis recommended that at least 50% of the metacarpal be covered by the plate (Whitelock, Dyce, & Houlton, 1999). Pooya et al. recommended that at least 80% of the metacarpal should be covered by the plate based on the results of their biomechanical study comparing ulnar transposition to cortical allografts (2004). However, plate coverage of the metacarpal was reported in 21 (8.0%) of the cases reviewed. Plates should be placed on the tension side of the bone whenever possible in order to minimize the motion between plated bone segments (Johnson, Houlton & Vannini, 2005). However, in the case of pancarpal arthrodesis, the plating is most often done on the compression surface of the metacarpal bone (Piermattei & Flo 1997). Plates are often pre-bent to provide a 10-12° hyperextension of the carpus (Parker, Brown, & Wind, 1981). The degree of plate pre-bending was reported in 37 (18%) of the distal radial limb sparing cases and ranged from 0 to 15 degrees of extension. Of the 263 cases of distal radial limb sparing reported in the literature the mode(s) of failure have been reported in 115. However, the true failure rates may be higher because several papers did not report any data regarding construct failure/complications. The frequency and mode of reported failures is shown in Figure 2.6.

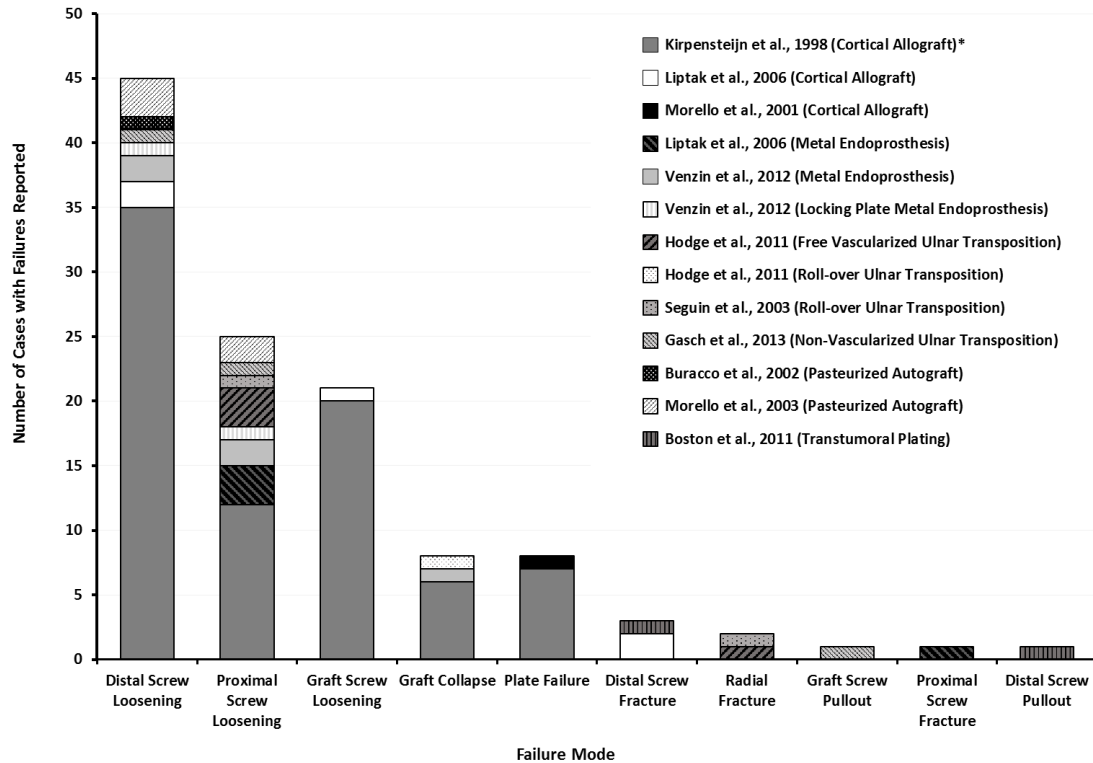


Figure 2.6: Chart showing the frequency and mode of reported mechanical failures of limb sparing constructs for the distal radius in dogs.

Loosening of the distal screws and the proximal screws constitutes 39.1% and 21.7% of the reported failures respectively. Loosening of the screws in the graft accounts for 18.3% of the failures. 7% of the failures can be attributed to graft collapse and 7% to plate failure. Graft collapse and plate failure are loosely defined in the literature as (1) a fracture of the graft (2) a large displacement of the graft/plate or (3) looseness of the graft/plate, so these failure modes may be closely correlated to prior screw loosening. The remaining failure modes reported are distal screw fracture (2.6%), fracture of the radius (1.7%), graft screw pullout (0.9%), proximal screw fracture (0.9%), and distal screw pullout (0.9%). It should be

noted that many of these data (52.1%) are from a single source (Kirpensteijn et al., 1998). While these data do not support any statistically significant conclusions, inferences may be drawn that may illuminate some of the potential short comings of these limb sparing methods. What is immediately evident from Figure 2.6 is that the failures are dominated by screw loosening; what is not entirely clear is whether the screw loosening led to implant failure or underlying degradation of the bone substrate led to the loosening of the screws. Such inferences must also be tempered with the tremendous variability associated with species, surgical technique, graft type/source, patient health, medical treatments (chemotherapeutic, antibacterial, analgesic, etc.) and level of owner involvement. Further controlled prospective clinical studies and biomechanical testing will be required to identify failure mechanisms and optimize limb sparing construct design. Endoprosthetic implants for limb sparing offer the promise of greatly reducing the variability and uncertainty associated with limb sparing. However, only 15 individual cases have been reported that involve limb sparing with metal endoprosthesis (Liptak et al., 2006; MacDonald & Schiller 2010; Venzin et al., 2012). Metal endoprosthesis eliminate the need for bone banking facilities, and may reduce the risk of infection and rejection associated with cortical allografts but the data are inconclusive as of yet. Currently, endoprostheses are only available in standard sizes which may not be optimal for individual patients and the endoprosthetic reconstructions are also geometrically intrusive and do not resemble the geometry of the original anatomy. For the distal radial location, soft tissue is limited and conformity to the existing anatomy is an important consideration. In addition, the high stiffness of the stainless steel endoprosthesis

may cause stress concentrations that result in stress shielding and bone resorption at the bone implant interface. In the clinical study by Liptak et al. (2006), 4 out of 10 limbs reconstructed with the stainless steel endoprosthesis failed due to screw loosening or screw breakage at the proximal end of the implant (on the radius), while four out of 10 of the implants with the cortical allograft failed due to screw loosening or breakage distally, on the third metacarpal bone. While not statistically significant, these data may suggest that the stiffness of the construct may also play a role in the distribution of stresses in screws during loading.

2.4 Conclusions

This review has consolidated those data in the literature pertinent to the high failure rates, failure modes and mechanisms typically seen in canine distal-radial limb sparing. These data includes number of screws, screw types, screw placements, plate pre-bending, etc. which have been included in this document to the extent that they are reported in the literature. Many of the studies were retrospective in nature and factors such as breed, disease condition, age etc. are not often controlled or censored. Variations within the treatment of cohorts for metastatic disease (adjuvant chemotherapy, chemotheroputic compounds, radiation doses etc.) may have an influence on the biomechanical outcomes, but this has not been well studied. Cost and time constraints have often resulted in sample sizes that are too small to make adequate statistical comparisons between studies, and often within studies (with several techniques only one case was reported making any reasonable comparison

between studies impossible). In these cases statistical type II errors have a high probability. In the few cases where *in vitro* laboratory testing on the mechanical aspects of constructs was conducted, the loading profiles and peak loads used were not clinically relevant. Therefore, the experimental results do not necessarily approximate clinical results. This report also highlights the necessity for improved biomechanical testing for the optimization of limb sparing implants coupled with enhanced censorship and reporting of failure modes in both prospective and retrospective clinical studies.

3.0 DEVELOPMENT OF A PATIENT-SPECIFIC BONE ANALOG FOR THE BIOMECHANICAL EVALUATION OF CUSTOM IMPLANTS

Recent interest in the use of direct metal additive manufacturing for the fabrication of patient specific implants has presented new challenges for the design of biomechanical testing protocols. In vitro biomechanical testing has traditionally used cadaveric bones as a testing substrate. Cadaveric bones closely approximate the size, shape, and properties encountered in vivo and are available as matched pairs (Markel, 1994). Although the mechanical characteristics between matched pairs of cadaveric bone are approximately symmetric, the use of cadaveric bone as a substrate typically limits testing protocols to pairwise comparisons of a single independent parameter between the two experimental groups. The high variability in mechanical properties of cadaveric bone between separate individuals then necessitates the use of large sample sizes to detect small differences between different implants or surgical methods (Sumner, Turner, & Galante, 1988). This problem is greatly exacerbated when it may be desirable to compare multiple configurations of a custom implant designs. The use of cadaveric specimens is further complicated by high cost, scarcity, biodegradation and the potential transmission of infectious diseases, (Dunlop et al., 2008, Szivek & Gealer, 1991).

Various materials have been investigated for use as a substitute for cadaveric bone for biomechanical testing. Hammel et al. used polyvinylchloride (PVC) tubing as a model for testing the fatigue properties of plating systems used for fracture fixation (2006).

Polyurethane foam was used as a model for cancellous bone by Murphy et al. to study the pull out properties of self-tapping bone screws (2001). Ricalde et al. used red oak blocks for the mechanical testing of several maxillofacial plating systems (2008). The use of these materials as substrates for biomechanical testing can reduce variability in testing (and therefore the required sample size) but such models lack realistic bone geometry. More recently, bone models that replicate the shape of representative human long bones have become commercially available (Sawbones™, Pacific Research Laboratories, inc. Vashon, WA), which utilize discontinuous fiber reinforced resin molded around a foam core (Heiner, 2008). These models have demonstrated some mechanical properties that model natural human bones and at the same time exhibit comparatively low interspecimen variability (Cristolofini & Viceconti, 2000; Heiner, 2008; Zdero et al., 2009).

However, scientific data regarding the formulation and manufacture of these fiber-reinforced composites are absent from the literature. Bone analog geometries are not currently available for many applications, particularly for veterinary orthopedics. Furthermore, commercially available analogs do not adequately address the importance of matching substrate geometry with patient specific implants for biomechanical testing, nor do they allow the researcher to adjust the material properties based on individual requirements.

The objective of the present study is to address this significant gap in the literature and to provide an improved experimental platform for the mechanical testing of custom implants in the form of a patient-specific bone analog that not only reduces experimental variability and the required sample size, but also addresses the importance of substrate geometry at the bone/implant interface. To be suitable for evaluating custom implants and devices, a patient-specific bone analog should exhibit similar mechanical properties to real bone and accurately represent the patient-specific bone geometry. This chapter discusses the development and testing of materials that represent the intensive material properties of cortical and cancellous bone within a relevant range; the development of rapid tooling derived from the CT data from a canine radius; and the fabrication of patient specific bone analog models.

3.1 Selection of bone Analog Materials

In order to develop the materials for the bone analog models it is important to consider the basic function and composition of bone. Bone provides basic structural support for the body. Microscopically bone can be thought of as a composite material made up of type I collagen (a fibrous protein), carbonated hydroxyapatite (a mineral phase), and water (Weiner and Wagner, 1998). These components are either organized into groups of osteons that form the bulk of the dense outer shell of the bone called cortical bone, or into the less dense lamellae that form cancellous bone. Cortical bone is anisotropic, exhibiting different properties when loaded parallel and perpendicular to the fiber arrangements. Figure 3.1

illustrates, on a much larger scale, how the long bones of the appendicular skeleton consist of a long, hollow central shaft, called the diaphysis, with wider portions at each end termed the metaphysis and epiphysis. The primary component of the diaphyseal portion of the bone is cortical bone, while the metaphysis and epiphyses contain a higher portion of cancellous bone surrounded by a thin cortical shell. The development of these analog models will focus on representing these large scale characteristics of bones. The materials that may be considered for the fabrication of bone analog models are required to; exhibit intensive mechanical properties that are similar to cortical and cancellous bone, be readily available and inexpensive, be relatively simple to prepare and process and, vary composition to match the properties of patient-specific data when necessary.

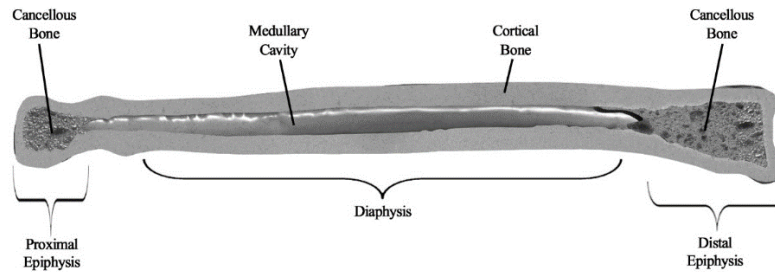


Figure 3.1: Schematic cross section illustrating the macroscopic components of a canine radius

The reported values for the modulus of elasticity of cortical bone from a variety of species vary significantly from about 7 GPa to 34 GPa as reported by An and Draughn. The tensile elastic modulus of cancellous bone varies depending upon the location in the body, the presence of disease, age, etc. The tensile modulus of elasticity of cancellous bone ranged

from 69 MPa to 349 MPa (1999). The relatively high spread is, in part, due to the natural variability of the material, the species examined, the type of bone tested, as well as the variability in testing methods from one study to another. A fiber-reinforced resin was selected as an initial analog for cortical bone. Fiber-reinforced resin is easily mixed and injection molded, it is readily available, and its properties may be easily altered by adjusting the fiber loading, fiber dimensions and fiber/matrix.

Several theoretical methods have been applied to the study of the mechanical properties of reinforced materials. This investigation is primarily concerned with predictions of the modulus of elasticity and tensile strength. Hill assumed continuous, aligned fibers embedded in a matrix (1963). The Halpin-Tsai equations provide a simplified form of Hill's work by directly embedding the tensile and shear moduli into the equations (Halpin & Kardos, 1976, 1978). In an investigation into the strength of paper, Cox proposed a shear-lag stress transfer model for the predictions involving discontinuous and randomly oriented fibers (1952). The relative insensitivity of these models to the fiber length provides a relatively simple approach to predict the tensile modulus of elasticity for discontinuous fiber composites that can be reduced to a modified rule of mixtures, represented in Equation 3.1. This model has previously was used for predicting the modulus of elasticity of fiber reinforced stereolithography resins (Zak, Park, and Benhabib, 2000).

Equation 3.1:

$$E_{ca} = \chi_1 \chi_2 \phi_f E_f + \phi_m E_m$$

E_{ca} , E_f , and E_m are the tensile elastic moduli of the composite, the fiber and the matrix respectively (loaded axially and parallel to the fibers), ϕ_f and ϕ_m are the fiber volume fraction and the matrix volume fraction, and χ_1 represents the fiber orientation efficiency factor, which has been shown to be equal to 1 for axially aligned discontinuous fibers and 1/5 for randomly oriented fibers (Cox, 1952, Gibson 2007). The variable χ_2 represents the fiber length correction factor. The rule of mixtures can also be applied to determine a reasonable lower bound for the composite modulus by considering the case of transversely aligned fibers (in which both the fiber and the matrix are under the same isostress condition) as given in Equation 3.2.

Equation 3.2:

$$E_{ct} = \frac{E_m E_f}{E_f \phi_m + E_m \phi_f}$$

The composite shear modulus (G_c) and composite Poissons ratio (ν_c) can be determined in a similar way, considering both isostress and isostrain loading. To estimate the fiber orientation factor, χ_1 , a composite laminate model is used (Sanadi & Piggott, 1985). The modulus of elasticity of a single fiber loaded at an angle θ , is calculated from the translated stress and strain tensors and is given in Equation 3.3

Equation 3.3:

$$E_{c,\theta} = \left[\frac{\cos^4\theta}{E_{ca}} + \left(\frac{1}{G_c} - \frac{2\nu_c}{E_{ca}} \right) \sin^2\theta \cos^2\theta + \frac{\sin^4\theta}{E_{ct}} \right]^{-1}$$

The thickness of each lamina, t , represents the proportion of fibers within a given range θ_i . Therefore, as shown in equation 3.4, χ_1 represents the ratio of the summation of the modulus of elasticity of the individual lamina, $E_{\theta,i}$ to the axially aligned modulus of elasticity, E_{ca} . As fibers become more aligned with the loading direction χ_1 approaches 1.

Equation 3.4:

$$\chi_1 = \frac{\sum_{i=1}^n E_{\theta,i} t_i}{E_{ca} \sum_{i=1}^n t_i}$$

As demonstrated by Gibson (2007), the fiber orientation factor has a much greater impact on the mechanical properties of the composite than does the fiber length. Therefore, axially aligned discontinuous fibers represent an upper bound for the modulus of elasticity of the composite, while transversely aligned fibers (where both the fiber and the matrix are under the same isostress condition) provides a lower bound.

The fiber length factor, χ_2 is based on the shear-lag method of stress transfer analysis and is primarily concerned with the transfer for stress from the fiber to the matrix and vice versa (Cox, 1952; Nairn, 1997). The cox model assumes a fiber embedded in matrix that is perfectly straight and loaded only in shear along the fiber at the fiber/matix interface, not the ends and presents a shear-lag parameter (β) shown in Equation 3.5 (assuming the fiber is a cylinder). As the length of the fiber increases χ_2 approaches 1.

Equation 3.5:

$$\beta = \sqrt{1 - \frac{2G_m}{E_f \ln\left(\frac{\pi}{4\phi_f}\right)}}; \quad G_m = \frac{E_m}{2(1 + \nu_m)}$$

Where G_m is the shear modulus of the matrix, and ν_m is the Poisson ratio of the matrix. The stress at a point in the fiber σ_f as derived by the cox model is;

Equation 3.6:

$$\sigma_f = \frac{P}{A} = E_f \varepsilon \left[1 - \frac{\cosh\beta \left(\frac{l}{2} - x\right)}{\cosh\left(\frac{\beta l}{2}\right)} \right]$$

Where l is the fiber length, ε is the strain in the matrix, and A is the cross sectional area of the fiber.

The average fiber stress is therefore;

Equation 3.7:

$$\bar{\sigma}_f = \frac{E_f \varepsilon \int_0^{\frac{l}{2}} \left[1 - \frac{\cosh \beta \left(\frac{l}{2} - x \right)}{\cosh \left(\frac{\beta l}{2} \right)} \right] dx}{\frac{l}{2}} = E_f \varepsilon \left[1 - \frac{\tanh \left(\beta \frac{l}{2} \right)}{\beta \frac{l}{2}} \right] = \chi_2$$

For the cortical bone analog, two matrix materials were used. One material was epoxy resin and hardener (Fiberglast Corporation, Series 2000 and 2060 respectively) mixed in a 100:23 ratio (by weight). The second was DSM Somos Watershed XC 1112 ultraviolet curing resin (DSM Somos, Elgin, IL). The average published modulus of elasticity (from the manufacturer of the cured resin was 3.091 GPa. The fibers were measured using a digital optical microscope (Hirox KH-7700). The mean length was 793 μm and the mean diameter was 20 μm . The modulus of elasticity of the glass fibers, as reported by the manufacturer was 89 GPa. The values for the materials were incorporated into the model in Equations 3.1-3.7 to predict the range of attainable material properties. Figure 33.2 shows a plot illustrating this relationship. The tensile modulus was predicted by varying the fiber volume fraction for various conditions of fiber alignment.

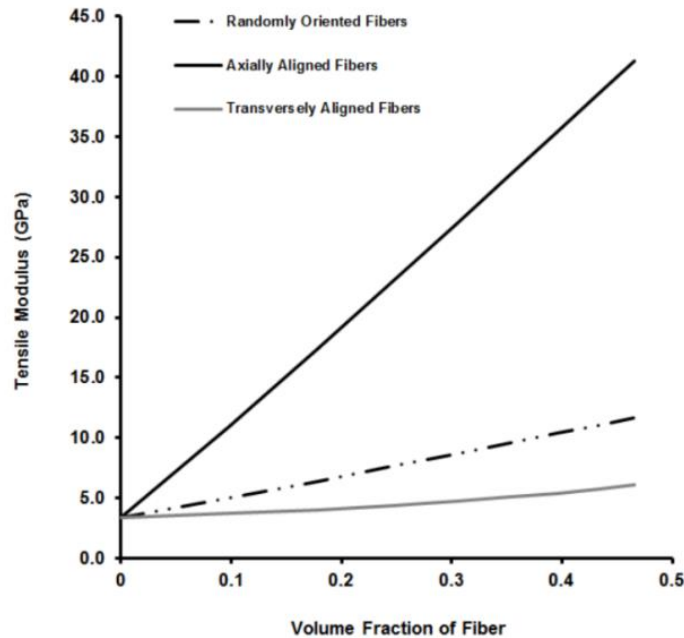


Figure 3.2: Plot illustrating the relationship between the volume fraction of fiber and the predicted tensile modulus for various conditions of fiber alignment (using 20 μm diameter, 793 μm long fibers).

Cancellous bone is commonly found in the epiphysis of long bones. The structure of cancellous bone is very similar to that of open celled foam, and unlike the cortical bone analog, there is widespread documentation in the literature regarding material formulations for cancellous bone analog materials. Typically, rigid polyurethane foam materials are used as a model for cancellous bone. ASTM F1839 provides the specifications for preparing polyurethane samples for use in testing orthopedic devices. This material is easily mixed and poured/injected into molds, cures quickly, and exhibits material properties with much less variability compared to cancellous bone specimens obtained from cadavers (Szivek, Thompson & Benjamin, 1995). By varying the ratio of isocyanate to resin in the mixture, it

was demonstrated that the mechanical properties of polyurethane foams could be adjusted to match the mechanical properties of a wide range of cancellous bone materials. In addition the internal structure of polyurethane bone bears a similarity to cancellous bone. Figure 3.3 shows images of the microstructure of polyurethane foam used in this test, and cancellous bone sectioned from the distal epiphysis of a canine radius.

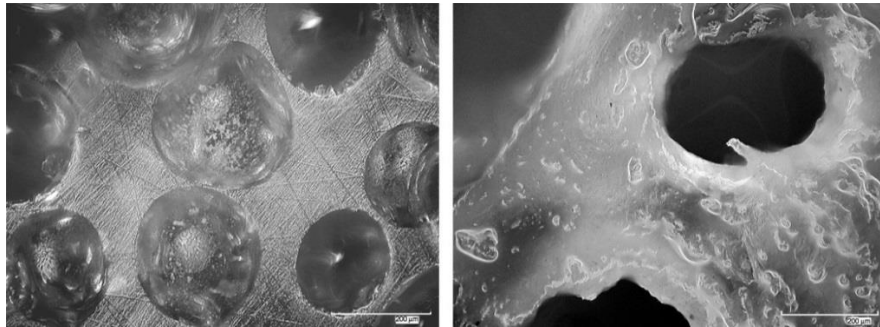


Figure 3.3: Images showing the microstructure of the polyurethane cancellous bone analog (left) and cancellous bone sectioned from the distal epiphysis of a canine radius (right). Scale bar indicates 200 μ m.

3.2 Methods of Testing of Bone Analog Materials

Tensile specimens of the cancellous and cortical bone materials were prepared in accordance with the ASTM standard D638-08. Fifty-six tensile specimens were prepared with four different fiber loading conditions; 0%, 18%, 30%, and 39% by volume, and two types of matrix material; epoxy resin and SLA resin. The fiber loading fractions were selected based on the model in Equations 3.1-3.7 which indicated a good match with canine cortical bone. In addition, these fractions also facilitated a simplified resin/fiber mixing

protocol (1:2, 1:1, and 2:3 resin to fiber by weight). A silicone rubber mold (Smooth-on Moldmax 30TM) was used to fabricate the samples to the required dimensions. The tensile specimens measured 150mm in length with a 50.8 mm gauge length. The width and thickness of the specimens was nominally 12.70 mm and 6.35 mm respectively. For the epoxy samples, resin and hardener were mixed with glass fibers inside of a custom built vacuum/mixing chamber for 10 minutes to remove gasses from the mixture and then poured into the silicone rubber mold. The 10 minute mixing time was determined *a priori*. The filled mold was placed in a pressure chamber at 480 kPa for a period of one hour, until the epoxy cured. The samples were then post cured in a convection oven at 75°C for one hour. For the SLA resin samples, the mold was placed into an ultraviolet chamber (PCA250 3D Systems) and cured for 12 hours, after which the samples were flipped and then cured for another 12 hours. The exposure level was not known and the exposure was based on a visual and tactile assessment of polymerization. In addition, seven samples of the same geometry were fabricated with the same resin (0% fiber) but using the stereolithography process (SLA 250, 3D Systems Rock Hill, SC). The SLA resin samples with 39% fiber volume fraction did not cure properly as a result of the fibers settling in the mold during the long cure time, and were therefore excluded from further comparisons (this phenomenon was not observed in the other samples). The samples were milled to final dimensions using a CNC milling machine (HAAS VF3).

Tensile testing on the polyurethane cancellous bone analog material was carried out in accordance with ASTM D638-08 and the dimensions were the same as has been previously described. Polyurethane foam (16lb/ft³, U.S. Composites, West Palm Beach, FL) was used to prepare the cancellous tensile specimens, it was mixed in a ratio of 1:1 (by volume) and poured into the same silicone rubber mold that was used to fabricate the cortical bone tensile specimens. The polyurethane cured for 1 hour at 21°C. Moisture in the air may affect the properties of the foam during curing, therefore the relative humidity was recorded at 42%. Tensile testing was carried out at a loading rate of 1.27 mm/min.

Tensile testing was carried out on each of the formulations using an ATS 1620C testing machine with square, serrated grips (Applied Test Systems, Butler, Pa.). An extensometer with a gauge length of 50.8 mm (Epsilon Technologies Corp, Jackson, WY) was affixed to the narrow section of the samples, and testing was carried out at a loading rate of 1.27 mm/min. A 22,241 N capacity load cell was used to record loading data. Figure 3.4 shows a photograph of the tensile test setup.

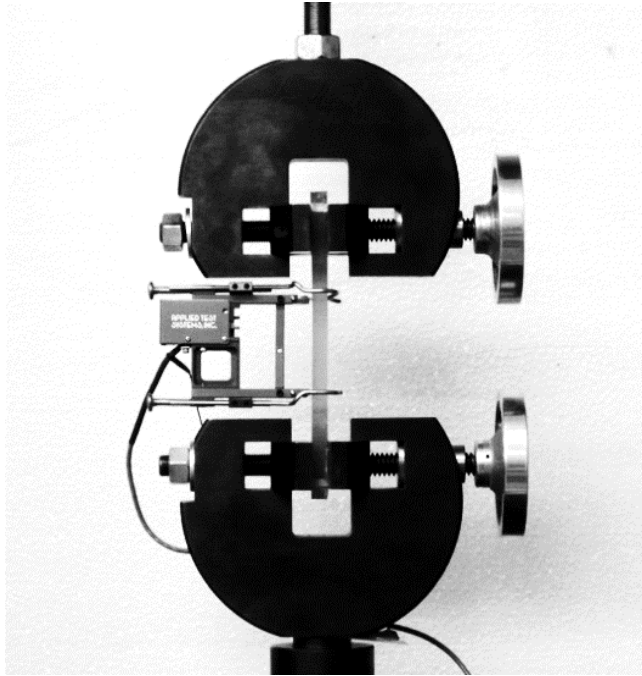


Figure 3.4: Photograph of the tensile testing fixture and strain guage for epoxy-fiberglass cortical bone analog samples

3.3 Results of Bone Analog Material Testing

The modulus of elasticity of each sample was calculated from a linear regression of the elastic portion of the stress-strain curve. Each sample was selected in random order (determined *a priori* using statistical software, jmp 8.0) and loaded non-destructively for a total of four repetitions, and the average of the last three was recorded. The results were tested for normality using the Shapiro-Wilk test. The mean and standard deviation of the modulus of elasticity was calculated for each group. A 2-parameter general linear regression model (shown in Equation 3.7) was used to compare the means between the groups. Means

between the samples cured under UV light and using the SLA 250 were compared between groups using 2-tailed Student's t-tests with pooled variance and significance was set at 95% ($\alpha = 0.05$). The results are summarized in Table 3.1.

Equation 3.7:

$$Y_{ijk} = \mu + \alpha_i + \beta_j + (\alpha\beta)_{ij} + \varepsilon \quad \varepsilon \sim \mathcal{N}(0, \sigma^2)$$

Where α represents the fiber loading fraction, β represents the matrix material and the error terms, ε are independent and normally distributed.

Table 3.1: Results of tensile testing of cortical bone and cancellous bone analog materials. Means with identical subscripts do not differ statistically.

Mixture (Volume Fraction)	Mean Modulus of Elasticity (GPa)	Standard Deviation	95% CI
0.0 Fiber, 1.0 Epoxy	3.091 _a	0.271	2.840-3.342
0.18 Fiber, 0.82 Epoxy	5.954 _b	0.410	5.574-6.333
0.30 Fiber, 0.70 Epoxy	7.890 _c	0.854	7.100-8.681
0.39 Fiber, 0.61 Epoxy	10.607 _d	1.331	9.376-11.838
Polyurethane Foam	0.305 _e	0.030	0.230-.380
0.0 Fiber (SLA fabricated)	2.752 _a	0.054	2.617-2.886
0.0 Fiber, 1.0 XC 1112	2.594 _a	0.089	2.372-2.816
0.18 Fiber, 0.82 XC 1112	2.752 _b	0.270	3.174-4.516
0.30 Fiber, 0.70 XC 1112	3.845 _c	0.128	5.797-6.435

Fiber content had a statistically significant effect ($F < 0.001$) on modulus of elasticity for epoxy-based and SLA-based resins. The high viscosity in the samples with 39% fiber volume caused difficulties when mixing, degassing and filling the mold that may have led to some of the higher standard deviations. The matrix material also had a statistically significant effect ($F < 0.001$) on modulus of elasticity. The epoxy matrix had a higher modulus of elasticity compared to the samples with the SLA resin matrix ($p < 0.001$). There

was no significant difference between the 0% fiber tensile specimens made using the SLA additive manufacturing process and the 0% fiber/SLA resin tensile samples cured in the mold ($p = 0.059$). The average tensile modulus of elasticity for the polyurethane foam samples was 305MPa with standard deviation of 30.06 Mpa.

In general, the measured tensile modulus fell within the lower end of canine cadaveric bone elastic modulus properties. However, the alignment of fibers for the tensile specimens was random, while the axial alignment of fibers associated with the injection molding of the analog radius is expected to increase the modulus to a more clinically relevant value. A regression analysis comparing the measured tensile modulus of elasticity from the experiments to the tensile modulus predicted by Equations 3.1-3.7 showed that for the epoxy matrix and the SLA resin matrix the model parameters explained 98% and 93% of the variability respectively (Figure 3.5) and the residuals plots showed evidence of randomness. A χ^2 test was used to evaluate the model goodness of fit to the measured data. For both the epoxy and the SLA resin the test failed to reject the null hypothesis ($\chi^2=2.38$, $df=3$ and $\chi^2=3.34$, $df=2$) respectively.

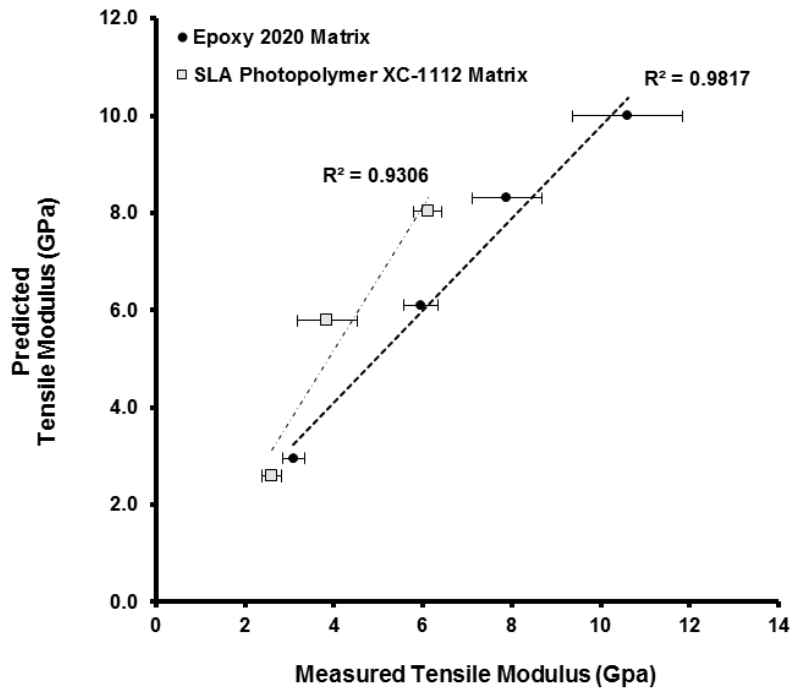


Figure 3.5: Plot showing the results of a regression analysis comparing the tensile modulus measured in the experiments and the tensile modulus predicted (Error bars represent 95% confidence intervals of the measured data).

3.4 Methods for the Design and Manufacture of Patient Specific Analogs

In the previous section materials have been investigated that mimic tensile properties of cortical and cancellous bone, as well as the ability to vary those properties based on the predictive model (Equations 3.1-3.7). This section describes the development of patient specific rapid tooling derived from CT data. The rapid tooling demonstrated here is used as a means to mold a polyurethane cancellous insert which is subsequently over molded with the cortical bone analog material. When combined in a patient specific geometry, the extensive

mechanical properties of the whole bone of a given patient can be modeled and validated experimentally. For this study, the canine radius was chosen to demonstrate the process.

Nine adult dogs weighing more than 30 kg were collected after euthanasia. The dogs were euthanatized at a local animal shelter for reasons unrelated to this study. Age, breed, gender, and method of euthanasia were recorded (See Appendix 1). The thoracic limbs were disarticulated at the glenohumeral joint, wrapped in saline solution (0.9% NaCl) moistened gauze, sealed in a plastic bag, and frozen at -20 °C. The limbs were later thawed at room temperature and computed tomography imaging was performed using a helical CT (Siemens SOMATOM Sensation 16-slice configuration, Siemens Medical Solutions, Malvern, PA) with 512 x 512 resolution and 0° gantry tilt. The CT images were retro-reconstructed into 1.0 mm slices with a pixel size of 0.727 mm. Mimics software (Materialise, Leuven, Belgium) was used to isolate and reconstruct the three-dimensional geometry of each specimen (the cancellous portion has been extended to include the medullary canal for ease of manufacture). The boundary between the cancellous and cortical bones was set by thresholding below 286 Hounsfield units. These geometries were then exported in standard tessellated format. Materialise Magics software was used in order to design the mold and mold parting lines, add geometric features for mold filling, clamping, venting, as well as features that facilitate the three dimensional alignment of the cancellous bone analog insert within the cortical bone mold. The parting line was determined using the built-in tooling module in Magics. An 8.0 mm boundary was added around the parting line for stability. The

positive plug for the mold was fabricated in photopolymer using an additive manufacturing technology (Objet Alaris 30, Rehovot, Israel). The models were coated with mold release agent (Ease-release 200, Smooth-on Inc., Easton, PA). Room temperature vulcanizing rubber (Reoflex 60, Smooth-on Inc.) was mixed in a 1:1 ratio (by weight) and degassed in a vacuum chamber, then poured around the mold plug and allowed to cure overnight. The rubber used for the molds was of a relatively high durometer (60 Shore A) in order to minimize mold deformation during injection molding, yet still provide some flexibility to facilitate the demolding of parts with slight undercuts. The second half of the mold was poured the following day. Figure 3 shows several images from the process. As specified by the manufacturer, the molds were post cured for 4 hours at 75°C. Of the nine cadaveric specimens for which CT data was acquired, one of the cadaveric samples, a 39.8 kg female Rottweiler, was chosen at random and was used to fabricate molds and analogs for validation.

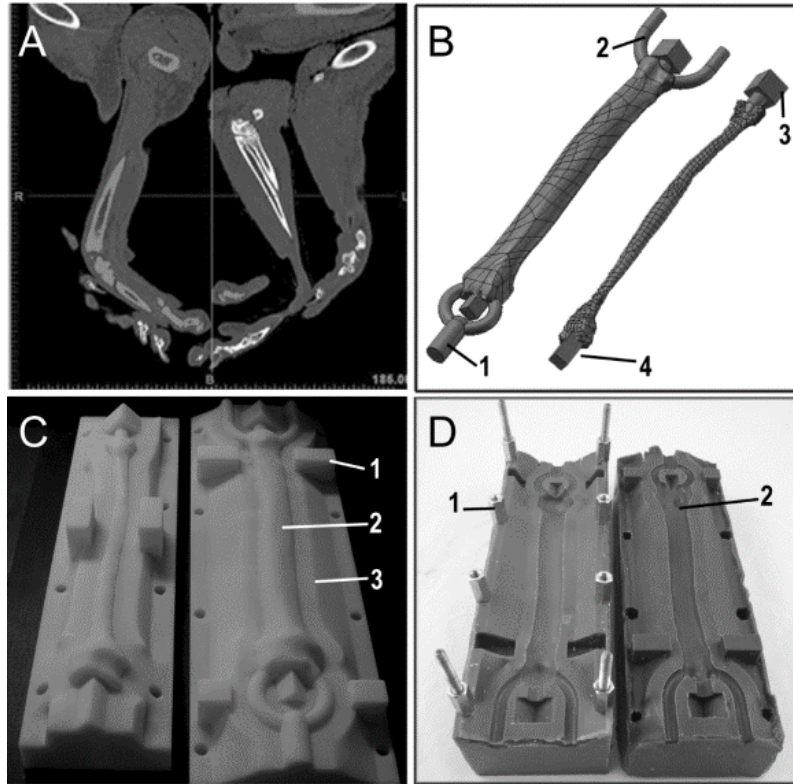


Figure 3.6: Images showing (A) a screenshot of CT data, (B) images of the cortical and cancellous bone 3-D models with the filling sprue (B-1), air vents (B-2) and 3-D geometric locating features (B-3,4); (C) finished plastic models of the cortical and cancellous models with mold registration features(C-1), patient-specific bone geometry (C-2) and built in mold parting line (C-3) ; (D) polyurethane rubber mold for cortical bone with built in mold clamping features (D-1) and patient specific mold cavity (D-2).

To fabricate the cancellous bone inserts, the mold halves were coated with mold release agent and then closed using built in clamping features. Ten milliliters of the two part FOAM-1604 polyurethane were combined and mixed for 30 seconds, and then poured into the cancellous insert mold. A 3.0 mm diameter brass rod was placed along the axis of the cancellous bone mold. This rod provided structural support during the injection molding and was easily removed leaving the medullary canal hollow. Initial testing showed that the rod

significantly decreased the deformation of the cancellous insert without affecting the ultimate properties of the bone. 3.0 mm approximately corresponded to the diameter of the hollow portion of the diaphysis (as was evident on the CT scans). The mold was capped, and the polyurethane mixture was allowed to cure for 25 minutes at 21 °C and 42% relative humidity. After curing, the models were removed from the mold and rinsed with acetone solution to remove the mold release agent. To prevent the open pockets on the surface of the foam models from creating bubbles in the final product, the surface was coated with a thin layer of epoxy resin (Loctite 5 min epoxy, Henkel, Düsseldorf, Germany). In addition, the surface of the cancellous bone insert was coated with high temperature ceramic coating (VHT Ceramic Coating, Sherwin-Williams) that prevented the formation of bubbles from the high heat generated in the curing process. The coating was allowed to dry for one hour. Mold release agent was then used to coat the surfaces of the cortical bone mold. The cancellous insert was precisely located within the cortical bone mold, using the built-in geometric locating features. Epoxy resin and short glass fibers in the ratios described earlier (a total of 200 g) were mixed under vacuum using a custom-built mixer within a vacuum chamber for 10 minutes. While still under vacuum, the epoxy-fiberglass mixture was drawn into a 60.0 cm³ syringe. The mold and syringe were then loaded into a custom-built injection molding machine that introduced the resin into the mold with a pressure of 70.0 kPa. Figure 3. shows photographs of the process. Immediately after mold filling (verified visually by the presence of the epoxy-fiberglass mixture extruding from the mold air vents), the mold was placed inside of a custom-built pressure vessel at 480 kPa for one hour until the epoxy cured. This reduced the

volume of any bubbles that formed either as a result of the epoxy curing process, or from the interaction between the epoxy and the polyurethane cancellous bone analog insert. The samples were then post cured in a convection oven at 75°C for one hour before being removed from the mold. Figure 3.8 shows the finished radii.

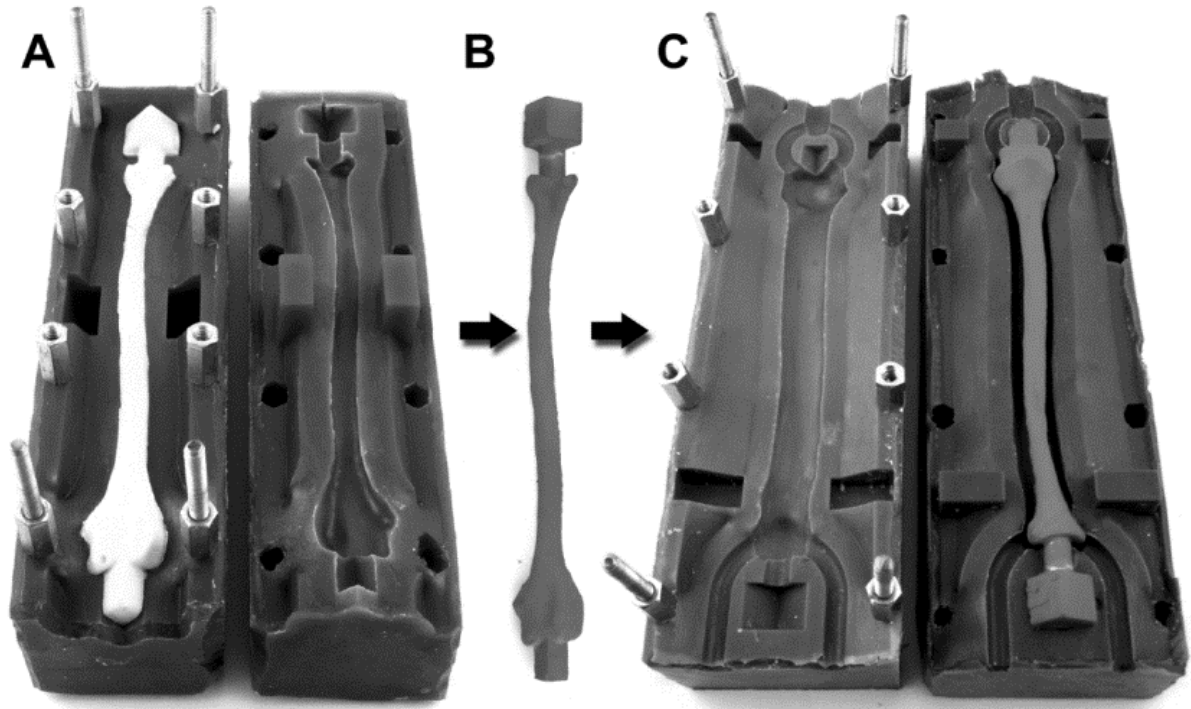


Figure 3.7: Photographs showing several steps of analog bone fabrication process; (A) molding of the polyurethane cancellous bone analog insert, (B) cancellous insert coated with ceramic, (C) placement of the ceramic coated cancellous bone analog insert within the cortical bone analog mold.

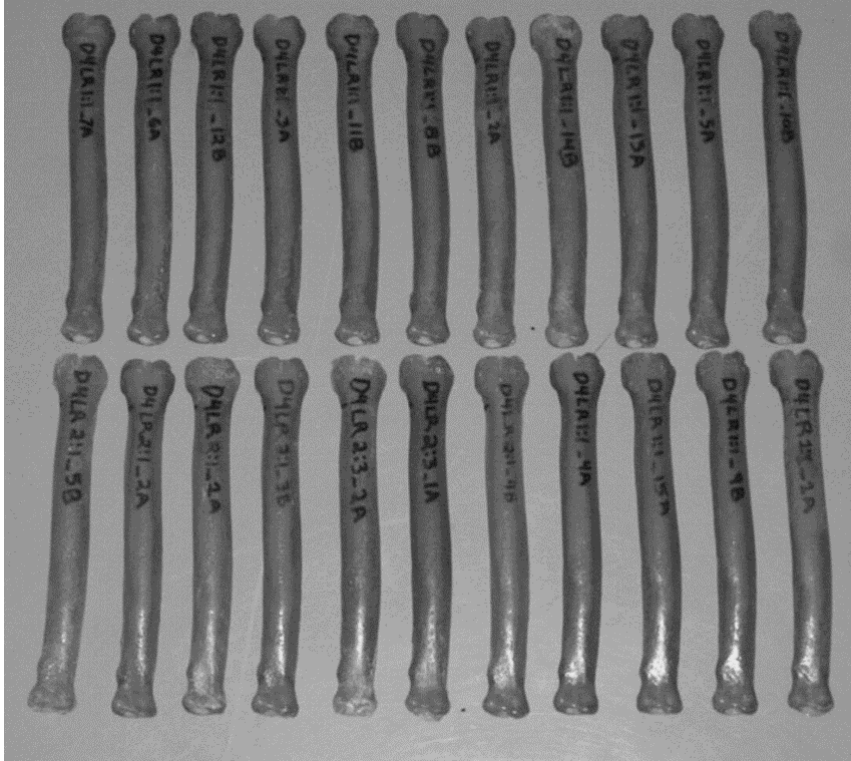


Figure 3.8: Photograph showing the finished patient specific analog radii.

One of the key parameters for the prediction of the modulus of elasticity of the short fiber composite bone analog is the orientation of the fibers within the composite. A number of methods have been described for measuring the fiber orientation distribution, most of the techniques that are practical involve sectioning the composite, polishing the surface of a sample, and examining the microstructure. When sectioned, the cylindrical fibers that are at an angle to the section plane appear as ovals. The minor diameter of the oval is equal to the diameter of the fiber. Assuming the fibers are relatively short and rigid, the in-plane and out of plane orientations can be calculated by the magnitude and orientation of the major diameter (Blanc et al., 2006; McGrath & Willie, 1995).

However, using this method is somewhat ambiguous because the in plane orientation could be one of two values (i.e θ or $\theta+\pi$). Clarke, Archenhold, and Davidson (1995) overcome this by taking two images at different planes a known distance apart. Unfortunately, this is difficult in that it requires sectioning and polishing twice, and relocating/recognizing pairs of ovals that belong together. Kawamura et al. utilize scanning acoustic microscopy to detect interference fringes that result from echoes reflected from the fiber, the fringes appear in the direction that the fiber is facing giving an unambiguous result. In this study the ambiguity is not of critical importance to the predictive model because only uniaxial loading (in tension) was applied. To evaluate the fiber orientation within the composite bone analogs, bone samples were fabricated in which the epoxy matrix was dyed dark blue (Smooth-on Inc.). Eight cross sections were cut from the bone analog models which were progressively ground (120-2000 grit paper) using standard methods (ASTM E2015-04). The microstructure of the composite was then digitally photographed at a 350x magnification as shown in Figure 3.13.9. Six micrographs were analyzed from each section. LabviewTM software was used to threshold and filter noisy data points and objects touching/overlapping with the borders of the field of view. Labview's built-in ellipse fitting algorithm was used to calculate the orientation, the center, the major axis (a) and the minor axis (b) for each fiber cross-section. From this a two-parameter fiber orientation distribution $\psi = [\Phi, \theta]$ was measured; where θ is the in-plane fiber orientation and, Φ is the out-of-plane fiber orientation ($\cos^{-1} b/a$). Figure 3.10 shows a histogram of the two parameter fiber orientation distribution.

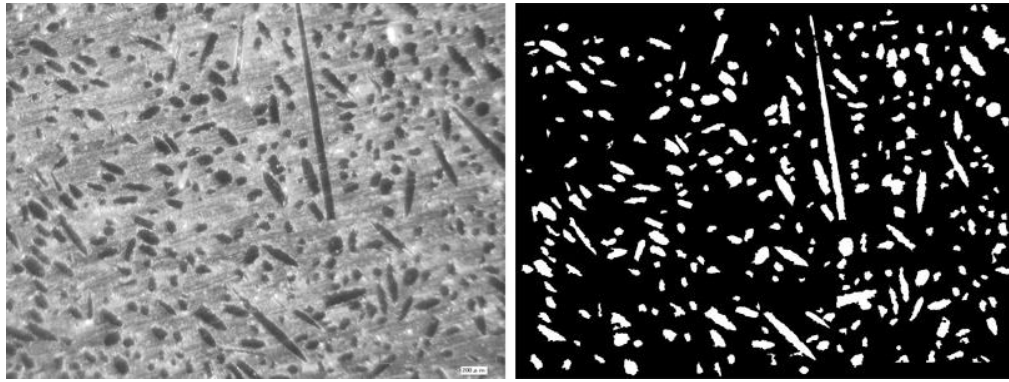
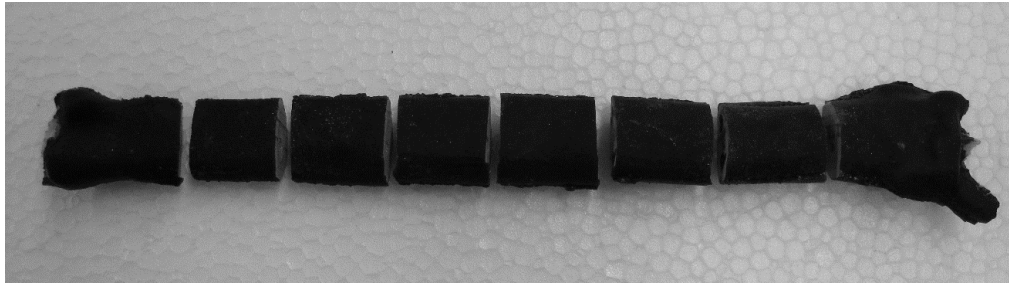


Figure 3.1: Images showing the microstructure of the 0.30 fiber volume fraction bone analog material before processing (left) and after processing (right).

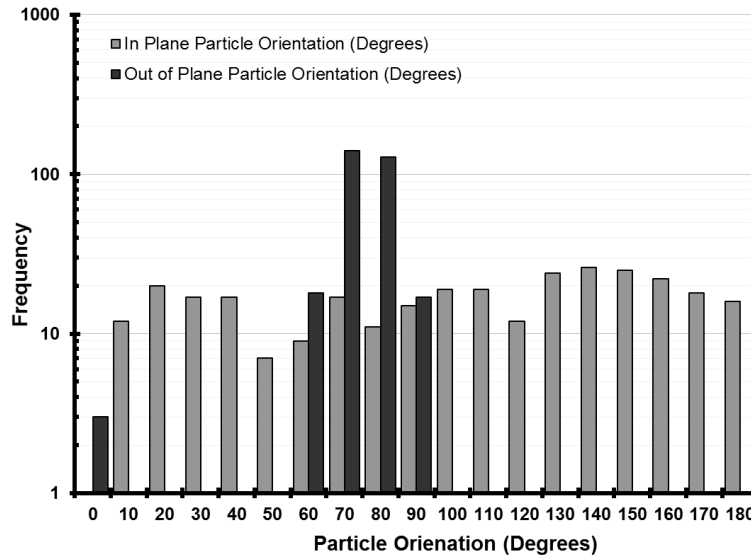


Figure 3.10: Histograms showing the in plane and out of plane fiber orientation for the composite analog radius.

The in plane particle orientation was compared to a uniform distribution using a χ^2 test. The analysis suggests that the fibers are randomly oriented in plane ($\chi^2 < 0.0001$), but are relatively aligned with the longitudinal axis of the bone (out-of-plane). Despite the ambiguity of the in-plane orientation, a close estimate of fiber orientation was obtained. However, to confirm that the out of plane measurements were not parallel, sections were polished tangential to the cranial surface on each sample, and processed with the same image processing program. Figure 3.11 shows the raw image of a tangential surface taken at a 350x magnification, the vertical direction in the image corresponds to the longitudinal axis of the bone.

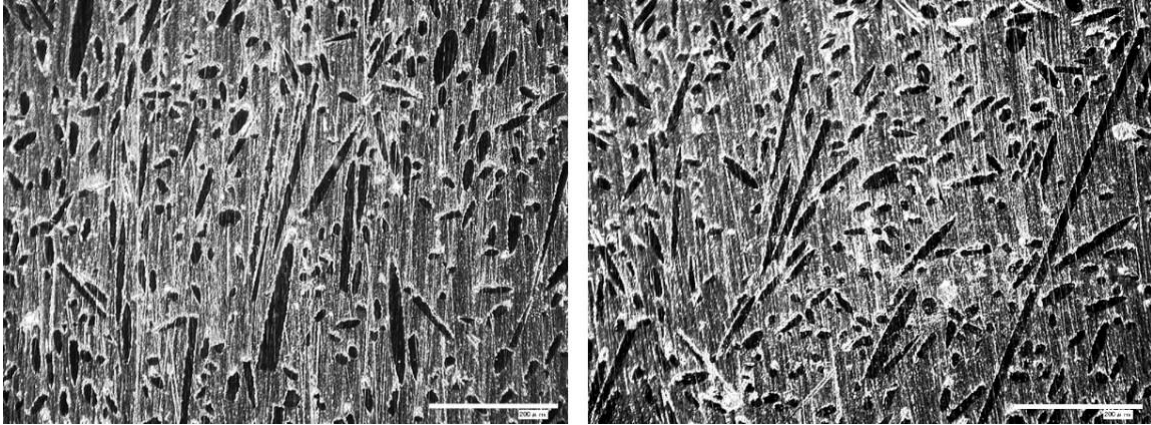


Figure 3.11: Images showing the microstructure of the tangential surface of the 0.30 fiber volume fraction bone analog material. Note the predominant axial (vertical) fiber alignment (scale bar indicates 200 μm).

3.5 Discussion

The cortical bone and cancellous bone analog materials described herein have been shown to exhibit a tensile modulus of elasticity, a key intensive material property, within the expected range of cadaveric specimens. This is advantageous on several levels, particularly because it allows the reduction in the required sample size while also providing the ability to evaluate multiple implant parameters simultaneously. Computed tomography combined with traditional, plastic-based, additive manufacturing facilitates the fabrication of rapid tooling for patient-specific bone geometries which will support the mechanical testing and evaluation of custom implants and devices.

Only two materials were combined in these models to represent cancellous and cortical regions of the bone, this creates a distinct boundary at the interface between the two materials. In reality, the transition between cancellous and cortical bone is much more gradual suggesting the need for investigating functionally graded materials to better represent this transition. In addition, the molding of the cortical bone tensile specimens may not be entirely representative of the same material molded into the form of the radius because of differences in fiber orientation. While the tensile data match the predictive model for randomly oriented fibers, the sections of analog radii examined showed a preferential fiber alignment along the longitudinal axis of the bone.

In this study, materials were combined using injection molding however, future advances in additive manufacturing technologies may address the need for direct fabrication of analog bones for biomechanical testing. As a precursor to this future work, several of the tensile specimens fabricated utilized a relatively common stereolithography resin. While the results were comparable to the epoxy resin, settling of the fibers in the stereolithography resin suggests that resin/fiber combinations should be carefully considered. However, this work also offers the potential for the direct fabrication of composite bone analogs dependent upon development of the appropriate supporting technologies.

4.0 VALIDATION OF ANALOG RADII

Biomechanical testing of novel orthopedic implants is often performed *in vitro* using cadaveric bones which typically available as matched pairs. Cadaveric bones typically allow a close approximation of *in vivo* situations. However, lack of availability, high cost, high inter-specimen variability, and biological degradation present barriers to their effective use for testing implants (Dunlap 2008). High variability necessitates large sample sizes in order to detect small differences between implants, surgical methods, constructs etc. For example, the variability in axial strain of human femurs, was shown to approach or exceed the mean in a group of 10 intact cadaveric femurs (Crowninshield 1980). Variability in canine bone mineral content was between 40-60% of the mean in long bones from thirty-six dogs (Lorinson 2008), and large variability between specimens was present in canine biomechanical studies of limb sparing constructs (Pooya 2004, Liptak 2006). The coefficient of variation of the modulus of elasticity and yield strength for cortical bone from canine femurs was 16.6% and 18.4% respectively. The same study found significant differences in the modulus of elasticity of cortical bone samples taken from the cranial surface of canine femurs as compared to samples taken from the medial, lateral or caudal surfaces (Autefage et al., 2012). In order to reduce this variability and minimize the sample size requirements for biomechanical testing, surrogate materials have been used to simulate the properties of both cancellous and cortical bone. The previous section has reviewed these and, has described efforts aimed at developing and testing the materials and methods for producing patient

specific, canine radii analogs. The purpose of this research is to evaluate and validate the extensive mechanical properties of these analog radii. Validation of several extensive mechanical properties of the composite analog radii was carried out through comparison to the same in cadaveric radii of similar size; including the radius from which the molds were patterned. Three fiber loading conditions were tested to determine which best matched the properties of the original. It was hypothesized that the composite radii would have mechanical properties comparable to cadaveric canine radii with lower variability among specimens and, that increasing the quantity of glass fibers in the epoxy resin would increase the axial, bending, and torsional stiffness of the composite bones. The energy to failure is hypothesized to be lower for the composite radii based on the brittle failure mechanism of cortical analog tensile specimens observed in the previous study. The sample size of 7 composite analog radii for the validation study was determined *a priori* based on power analyses of sample variability from epoxy-fiberglass-bone meal replicas reported in a previous study (Marcellin-Little, Harrysson, & Cansizoglu, 2008).

4.1 Analog Radii Testing Methods

Forelimbs of adult dogs weighing more than 30.0 kg were collected after euthanasia. The dogs were euthanatized at a local animal shelter for reasons unrelated to this study. Age, breed, gender, and method of euthanasia were recorded. The thoracic limbs were disarticulated at the glenohumeral joint, wrapped in saline solution (0.9% NaCl) moistened gauze, sealed in a plastic bag, and frozen at -20° C. The limbs were thawed at room

temperature and the radii were removed. Bones were excluded if osteoarthritis of the elbow or carpus, angular deformities, or signs of prior fracture were visible. Three groups of analog radii were fabricated with fiberglass to epoxy ratios of 0.18, 0.30, and 0.39 by volume. Two separate molds were used to reduce the time required to produce the analog bones. The mold used was recorded and used in the analysis. Twenty-one composite analog radii, and five cadaveric radii were tested non-destructively in random order in four-point cranial bending, axial loading, and internal and external torsion using a materials testing machine (Allied Test Systems, Butler PA). Testing parameters were selected based on destructive tests of first generation radii used in preliminary experiments. The replicas and bones were loaded four times for all non-destructive bending, axial, and torsional tests. The first loading event in each mode was considered as a pre-conditioning load and was not used in the analyses. Load-displacement curves of the second, third, and fourth loading events were recorded. Destructive testing was carried out in four-point bending after all non-destructive tests were completed. Destructive testing in screw withdrawal was done on small segments of the proximal portion of each sample.

Stiffness was calculated from the linear portion of the load displacement plots. Axial, torsional, and flexural stiffness were compared using statistical software (JMP, 8.0). The second, third and fourth loading events for each test were compared within groups using paired t-tests (after confirmation of normal distribution using the Shapiro-Wilk test for normality). This was done to determine whether the non-destructive testing was indeed non-

destructive. No conditioning effects over loading cycles were detected during external torsion, axial compression, or four-point bending. The three recorded data sets for each test were then averaged and the mean of these three was used during further analyses. Significance was set at $P < 0.05$. Mean internal and external torsional stiffnesses were compared by use of a 1-way ANOVA. The mean bending stiffnesses, mean axial stiffnesses, and mean torsional stiffnesses of analog radii made from the 2 molds were compared by use of a 1-way ANOVA.

The mean 4-point bending yields and ultimate loads to failure for all groups were analyzed by use of a 1-way ANOVA. Differences between groups were compared by use of Tukey-Kramer honestly significant difference tests. The mean ultimate loads leading to screw pullout were analyzed by use of a 1-way ANOVA. Differences between groups were compared by use of Tukey-Kramer honestly significant difference tests.

4.1.1 Four point bending

Four point bending tests were conducted on the cranial surfaces of the radii to loads of up to 500 N with a crosshead speed of 1.5 mm/min for each group of analog radii, and cadaveric radii. This loading rate has been used in previous studies (Jain, Podworny, & Hearn, 1998). The major span was 139.7 mm and the minor span was 50.8 mm. Four point bending results in a constant moment between the inner supports.

Figure 4.1 shows the four point bending set up for both the cadaveric and analog radii. The specimens were oriented with the cranial surface convex to the inner supports to facilitate positioning in the testing apparatus (i.e. in four point bending the cranial surface is subjected to compressive strains while the caudal surface is subjected to tensile strain). Several *in vivo* strain gauge studies have reported conflicting results; strains on the cranial surface of the canine radius measured during gait cycles were reported as tensile (Carter et al., 1980; Coleman et al., 2002) or compressive (Burr et al., 1989). Compressive strains were reported on the caudal surface as well (Rubin & Lanyon, 1982).

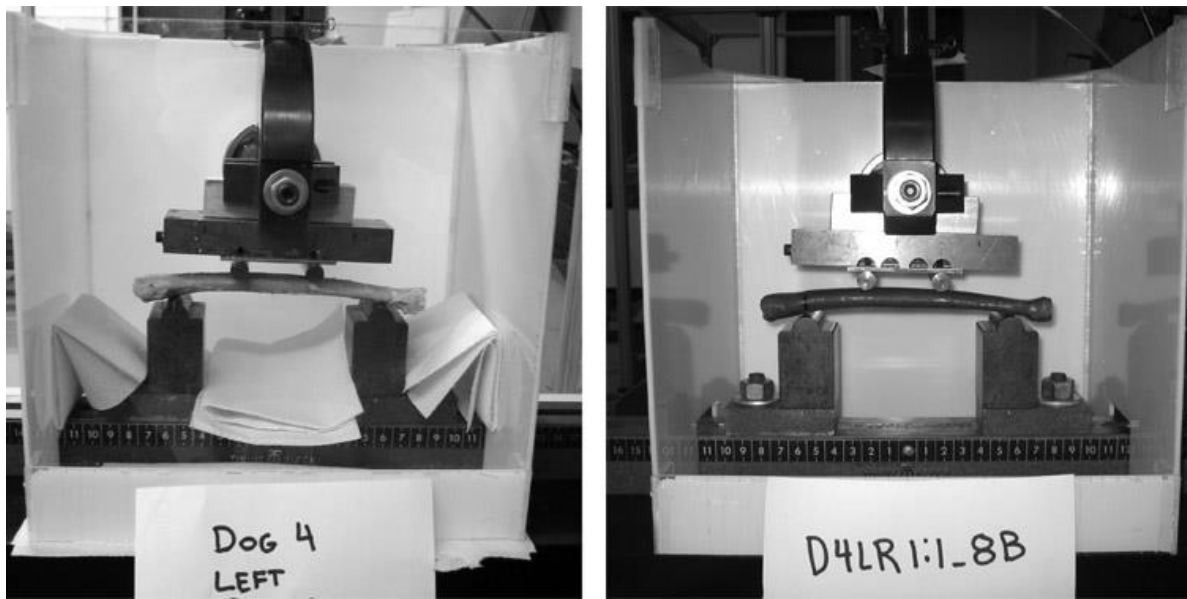


Figure 4.1: Photographs showing the setup for four point bending for both cadaveric radii (left) and analog radii from dog 4 (right).

4.1.2 Torsion tests

The proximal and distal 2.12 cm of the radii were potted in epoxy cylinders, measuring 4.92 cm in diameter and 2.54 cm long, by using a silicone rubber mold. The cylinders were used to affix the samples to the testing fixture. The torsional stiffness of the analog radii and the cadaveric radii was measured by placing an angular displacement of up to 10° at a rate of 6.5 °/min. in both internal and external rotation (i.e. clockwise and counterclockwise). Shear stresses calculated from the *in vivo* strain gauge studies of Carter et al., indicated that during the gate cycle, the proximal radius was subject to external torsion (1980). Torsional stiffness was calculated from a linear regression of the elastic portion of the load-angular deflection curve. A custom testing fixture was machined from 25.4mm thick, ground steel plate for rigidity and bolted to the materials testing machine. A loading fixture consisting of a plate with a steel cylinder (perpendicular to the loading direction) was affixed to the crosshead with serrated clamps. This was used to transfer the load to a lever arm that would then apply torque to the bone/analog sample. A radial bearing conforming to class ABEC 5 was used on the freely rotating portion of the fixture. An ABEC 5 roller thrust bearing, preloaded with two Belleville springs stacked in parallel to prevent racking of the radial bearing. Figure 4.2 shows an illustration of the torsion testing fixture, as well as a photograph of the fixture on the materials testing machine. The recorded load was converted into torque by the relationship shown in Equation 4.1:

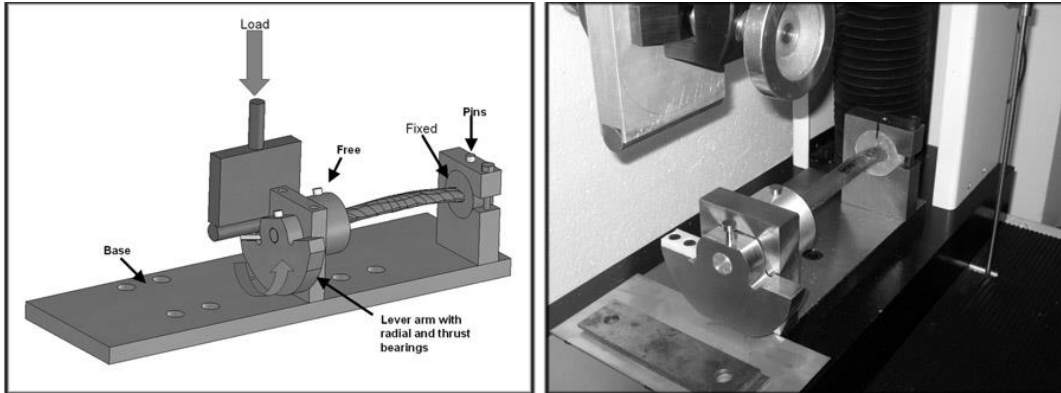


Figure 4.2: Illustration of the custom torsion testing fixture (left), and a photograph showing the fixture mounted on the materials testing machine with a composite radius between the grips (right).

Equation 4.1:

$$T = \frac{Px}{\cos^2(\omega)}$$

The crosshead displacement was converted into angular displacement by the relationship in Equation 4.2. These values are illustrated in Figure 4.3.

Equation 4.2:

$$\omega = \tan^{-1} \frac{y}{x}$$

Where:

- P = load recorded by the load cell
- ω = angular displacement of the sample
- θ_1 = instantaneous angle of rotation
- θ_2 = instantaneous angle between the crosshead and the normal force, F_n applied to the lever arm.
- x = linear distance between the center of rotation and the axis of loading
- y = displacement of the crosshead
- m = moment arm
- F_n = normal component of the load, P

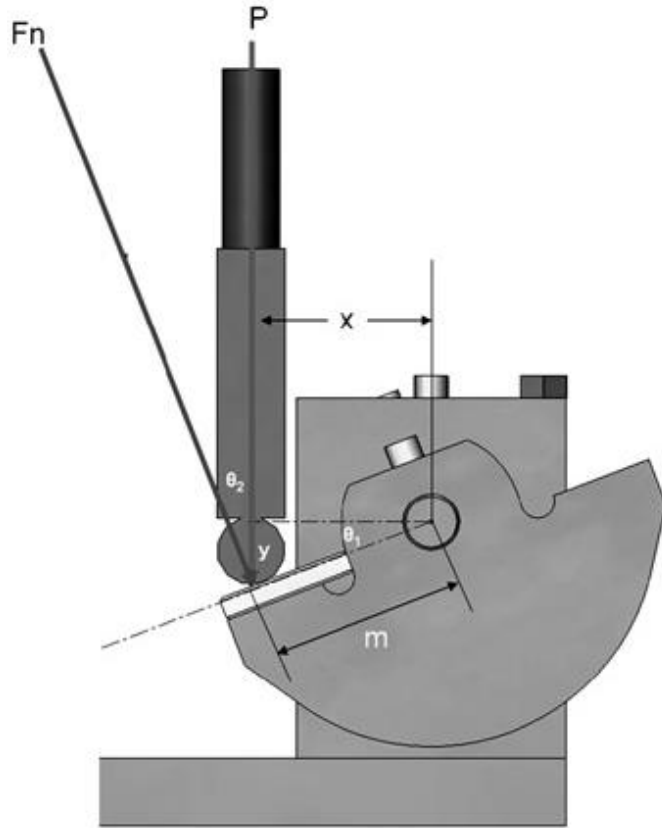


Figure 4.3: Illustration showing the relationship between the variables used to convert the linear loading of the materials testing machine into torque and angular displacement

The compliance of the testing fixture was evaluated by applying torsional load to a 50.4 mm diameter aluminum rod, which was confirmed to be linear and at least two orders of magnitude higher than the stiffness values reported in this study. The fixture was calibrated by testing known materials (abs plastic, and aluminum), with a known cross section (25.4 mm diameter) and calculating the modulus of elasticity. This was cross checked with published values for the materials.

4.1.3 Axial compression

Steel adapters were machined on a CNC Lathe (HAAS L1) to connect the potted ends of the bones to the materials testing machine base and crosshead for the axial loading tests. The bones were loaded to 4000 N with a crosshead speed of 1.5 mm/min. Figure 4.4 shows a photograph of the axial loading setup.



Figure 4.4: Photograph showing the setup for axial loading of analog and cadaveric radii.

4.1.4 Screw withdrawal tests

Comparing the screw withdrawal characteristics between the analog radii and the cadaveric radii is an important consideration, particularly for plated connections. Screw withdrawal was performed on a portion of the proximal radius that was not damaged during any destructive mechanical testing. 3.5 mm stainless steel cortex screws (Synthes Ltd, Paoli, Pa.) were inserted in a cranio-caudal direction in the proximal portion of the radial shaft. A jig was used for consistent screw placement using a 2.5 mm drill bit and a 3.5 mm tap. Mechanical testing was performed using the guidelines in the American Society for Testing and Materials standard for axial pullout load of medical bone screws (ASTM F543-07). This standard is intended to evaluate different screw designs/configurations in a standard material, however in this test the material was the variable, and the same screw design was used across all samples. A tensile load was applied to the screw head at 1.5 mm/min until screw pullout or failure. The ultimate axial pullout load (maximum load of the load displacement curve) was recorded. Figure 4.4.5 shows a photograph of the screw withdrawal setup.

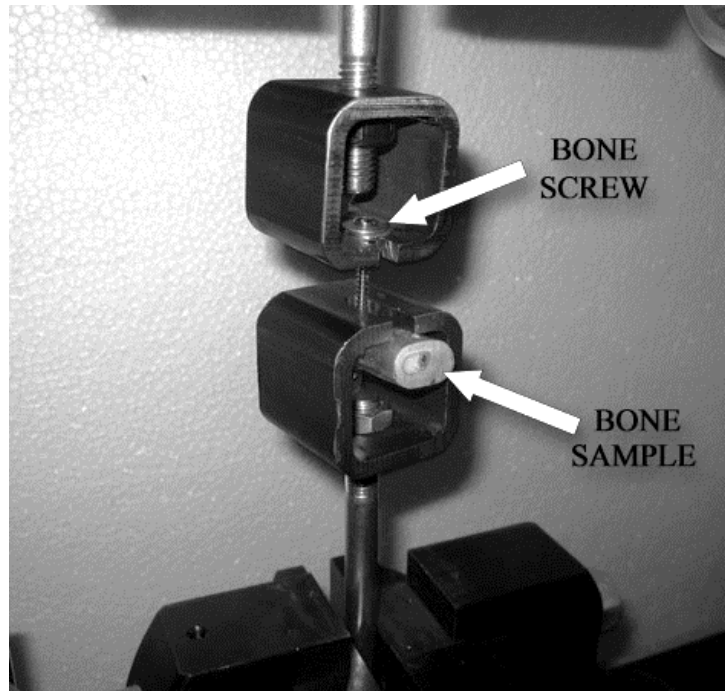


Figure 4.5: Photograph showing the set up for screw withdrawal testing.

4.1.5 Cyclic loading of a plated connection

Preliminary data was collected to assess the suitability of the analog radii for evaluating the term performance of plated connections. A bone plate conforming to the dimensions of the dedicated limb sparing plate (veterinary orthopedics) was machined from a bar of cold-rolled 316L stainless steel. The distal portion of the five hole plate transitions to a block designed to integrate with the testing machine grips. Four holes were pre-drilled and tapped into the cranial surface of the analog radius. The plate was affixed to the cranial surface of the proximal portion of the analog radius with four 3.5mm cortical bone screws tightened to a torque of 2.0 N-mm. The construct was connected to the fatigue testing

machine (Test Resources 910 Series, Shakopee, MN) with custom fixtures, shown in Figure 4.6. Loading was applied in a tension-tension profile from 66.7 N - 667.2 N for 6 million loading cycles at 10 Hz. The loading was chosen to simulate the *in vivo* loading of the radius at a trot (Riggs, DeCamp, & Soutas-Little, 1993). Uniaxial strain gauges, aligned with the bone/plate longitudinal axis were applied to the cranial surface of the bone and the plate as well as on the caudal surface. All strain gauges were glued to the surfaces with cyanoacrylate and were located between the 2nd and 3rd most distal screw locations. The angular position of the screw heads was marked to identify screw loosening.



Figure 4.6: Photographs showing the set up for cyclic testing of the composite radii/bone plate construct.

4.2 Analog Radii Testing Results

The mean four-point bending stiffness was higher for analog radii with 0.39 fiber loading than 0.30 fiber loading ($P < 0.001$), 0.18 fiber loading ($P < 0.001$), and cadaveric radii ($P < 0.001$). The analog radii with 0.30 fiber loading showed a higher stiffness than the 0.18 fiber loading ($P = 0.002$). The mean bending stiffness of cadaveric radii did not differ statistically from analog radii with 0.18 fiber loading ($P = 0.531$) or 0.30 fiber loading ($P = 0.263$). Figure 4.7 shows the results of the non-destructive four point bending tests.

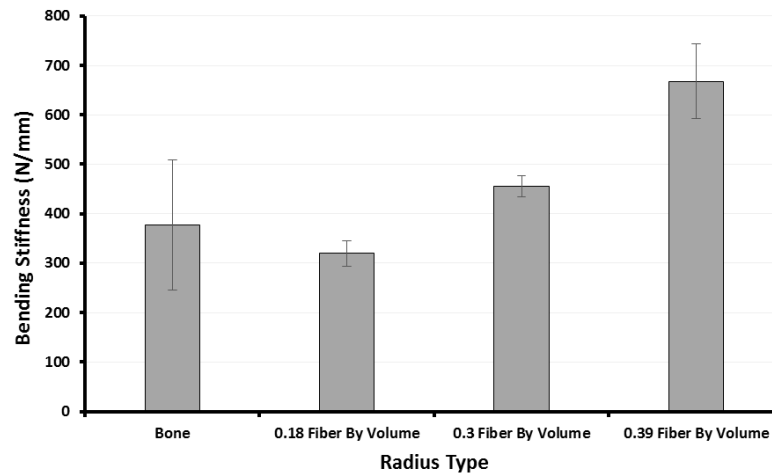


Figure 4.7: Chart showing the stiffness of composite and cadaveric radii in 4 point bending tests. Error bars indicate one standard deviation from the mean.

There was no difference detected in the mean bending stiffness for analog radii made from the two different molds with 0.30 fiber loading ($P = 0.248$), or the analog radii with 0.18 ($P = 0.628$) fiber loading. Due to the high viscosity and, presumably, minute differences

in the molds, there was significant difficulty in producing analog radii with 0.39 fiber loading in one of the molds. Therefore only one mold (A) was used. Figure 4.8 shows the load deformation plots for one sample from each fiber loading group, as well as the cadaveric radius from which the analog bones were modeled. The mean yield and ultimate loads of cadaveric radii in four-point bending were 959 ± 347 N and 1482 ± 539 N, respectively. The mean yield load in four-point bending did not differ statistically between groups of analog radii or between analog radii and cadaveric radii ($F = 0.611$). The mean ultimate load in four-point bending did not differ statistically between groups of analog radii or between analog radii and cadaveric radii ($F = .084$). The analog bones failed through transverse or short oblique mid-diaphyseal fractures.

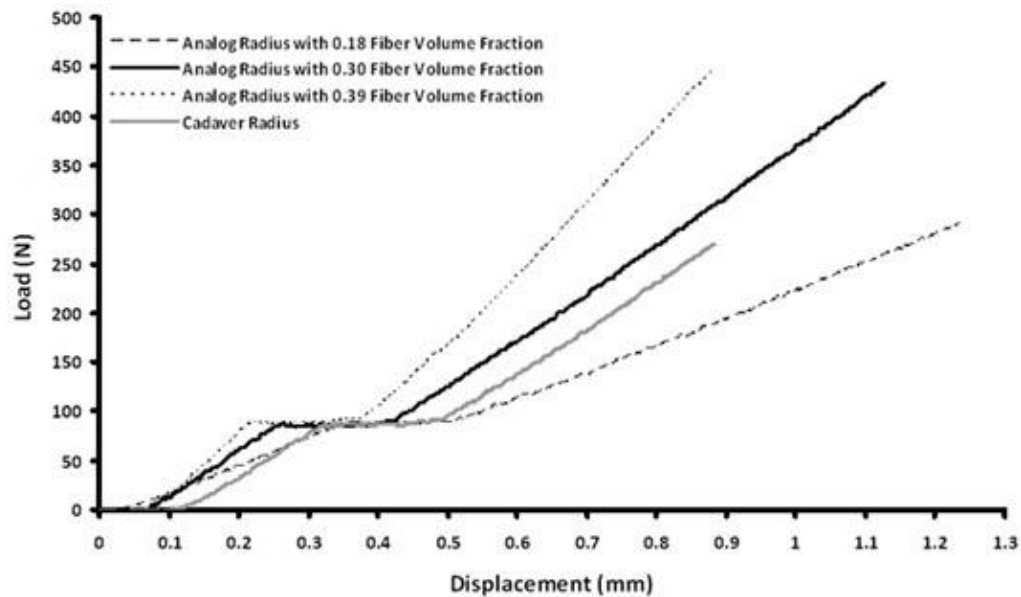


Figure 4.8: Load – deformation plots for one sample from each group of analog radii, as well as the cadaveric radius from which the analog bones were modeled.

By comparison, the cadaveric bones exhibited non-linear, elastic deformation. In two cases, the test was stopped when the metaphyses contacted the upper supports. Although there was no significant difference in the yield load and the ultimate load, the energy at failure for the cadaver bones as compared to the analog bones was significantly higher. The energy at failure was calculated as the total area under the load-deformation curve. The mean energy at failure for the cadaveric specimens was 9.20 ± 5.14 J while for the specimens with 0.30 fiber loading, the energy at failure was 2.16 ± 0.70 J. These data are shown in Figure 4. The cadaveric radii absorbed significantly more energy at failure than did the composite radii ($P < 0.001$). There was no detectible difference between the 0.39 and 0.30 fiber loading ($P = 0.923$), the 0.39 and the 0.18 fiber loading ($P = 0.7513$), or the 0.30 and 0.18 fiber loading ($P = 0.950$). Figure 4.4.9 shows a load-deformation plot for the destructive testing in four-point bending of an analog radius with 0.30 fiber volume fraction, and the cadaveric radius from which the analog bones were modeled (Dog 4). Figure 4.10 shows the energy at failure for the groups tested.

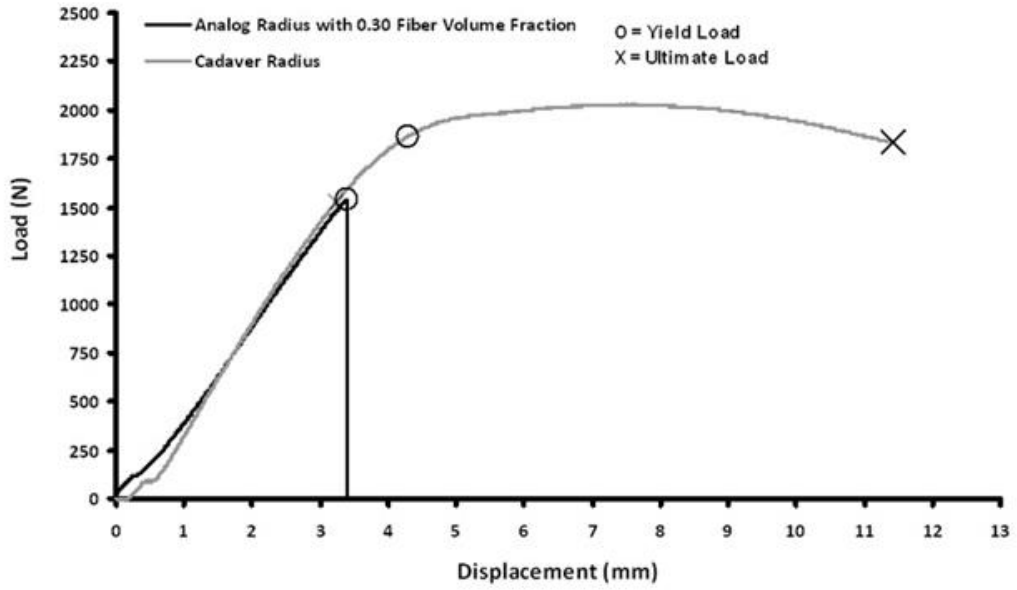


Figure 4.9: Load deformation plot for destructive testing in four-point bending of an analog radius with 0.30 fiber loading, and the cadaveric radius from which the analog radii were modeled.

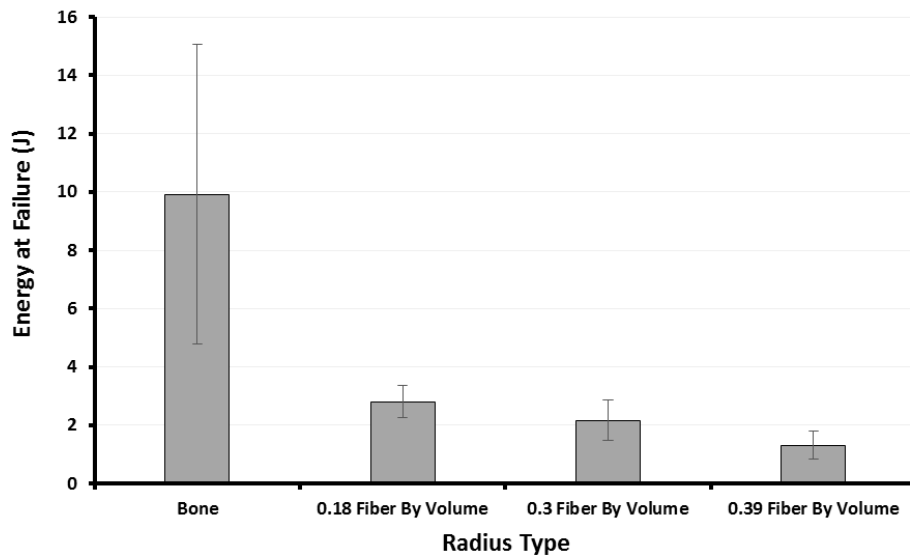


Figure 4.10: Chart showing the energy at failure (J) for the cadaveric and composite radii. Error bars indicate one standard deviation from the mean.

The mean ultimate loads leading to screw pullout were compared between groups using two-tailed Student's t-tests. The mean load leading to screw pullout was higher for analog radii with 0.39 fiber loading fraction than for analog radii with 0.18 fiber loading fraction ($p = 0.048$) and cadaveric radii ($p = 0.010$). The mean tensile load leading to screw pullout did not differ between analog radii with 0.39 and 0.30 fiber loading fraction ($P = 0.200$), between analog radii with 0.30 and 0.18 fiber loading fraction ($P = 0.125$), between analog radii with 0.30 fiber loading fraction and cadaveric radii ($p = 0.271$), and between analog radii with 0.18 fiber loading fraction cadaveric radii ($p = 0.256$). Figure 4.11 shows the load displacement plot for screw withdrawal for an analog radius section (0.30 fiber volume fraction) and a cadaveric radius section. The peak load is identified on the plot. Figure 4.12 shows the results of the destructive four point bending test and the screw withdrawal tests.

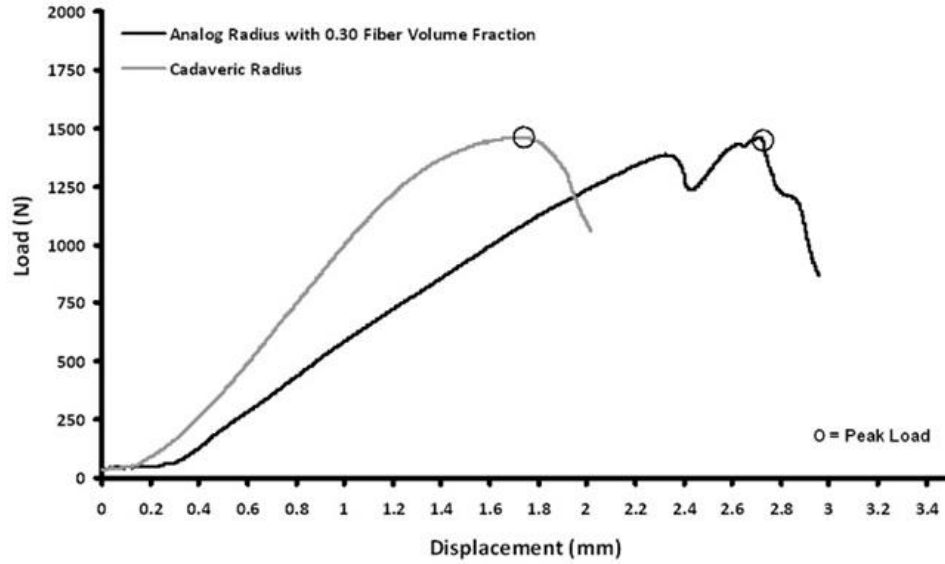


Figure 4.11: Load displacement plot for a pair of screw withdrawal tests, showing the failure load of both cadaveric and analog samples (circled).

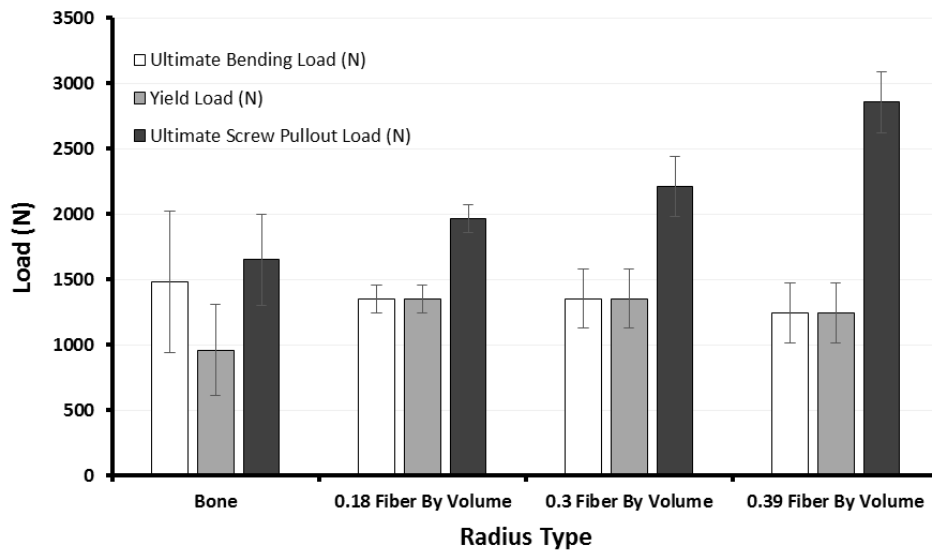


Figure 4.12: Chart showing the results of destructive 4 point bending tests. Error bars indicate one standard deviation from the mean.

Torsional testing results are shown in Figure 4.113. Two analog radii (0.39 fiber loading) failed in external torsion unintentionally and were censored from further analysis. The mean internal torsional stiffness of analog radii with 0.39 fiber loading fraction was higher than analog radii with 0.30 fiber loading fraction ($P < 0.001$), analog radii with 0.18 fiber loading fraction ($P < 0.001$), and cadaveric radii ($P < 0.001$). Analog radii with 0.30 fiber loading fraction were stiffer than Analog radii with 0.18 fiber loading fraction ($P = 0.004$) and cadaveric radii ($P < 0.001$). Analog radii with 0.18 fiber loading fraction were stiffer than cadaveric radii ($P = 0.018$).

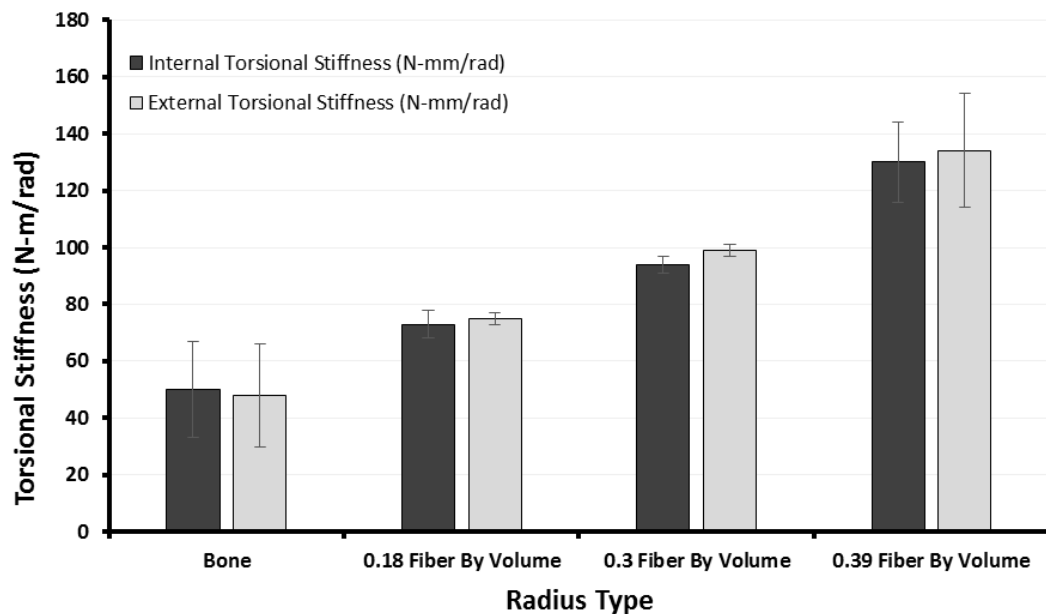


Figure 4.1: Chart showing the internal and external torsional stiffness of composite and cadaveric radii. Error bars indicate one standard deviation from the mean.

The mean external torsional stiffness of analog radii with 0.39 fiber loading fraction was higher than analog radii with 0.30 fiber loading fraction ($P < 0.001$), analog radii with 0.18 fiber loading fraction ($P < 0.001$), and cadaveric radii ($P < 0.001$). Analog radii with 0.30 fiber loading fraction were stiffer than analog radii with 0.18 fiber loading fraction ($P = 0.006$) and cadaveric radii ($P < 0.001$). Analog radii with 0.18 fiber loading fraction replicas were stiffer than cadaveric radii ($P = 0.020$). No difference was detected in internal torsional stiffness ($P = 0.735$ and 0.798), external torsional stiffness ($P = 0.908$ and 0.160).

The mean axial stiffness was higher for analog radii with 0.39 fiber loading fraction than for analog radii with 0.30 fiber loading fraction ($P = 0.008$), analog radii with 0.18 fiber loading fraction ($P < 0.001$), and cadaveric radii ($P < 0.001$). The analog radii with 0.30 fiber loading fraction were stiffer than analog radii with 0.18 fiber loading fraction ($P < 0.001$) and cadaveric radii ($P < 0.001$). The mean axial stiffness of analog radii with 0.18 fiber loading fraction and cadaveric radii did not differ statistically ($P = 0.053$). The analog radii with 0.30 fiber loading fraction made using the first mold had a higher mean axial stiffness than those made using the second mold (3534 N/mm vs. 3180 N/mm, $P = 0.044$). There was no difference detected between molds for the mean axial stiffness of analog radii with 0.18 fiber loading fraction ($P = 0.879$). Figure 4.14 shows a chart of the mean axial stiffness of composite and cadaveric radii. Figure 4.15 shows a chart of the coefficient of variation across all tests and radii types. The variability of the composite analogs were equivalent (for screw pullout) or lower (for all other testing regimens) than the variability of cadaveric radii.

Interspecimen variability (coefficients of variation) was 2 to 19 times larger among cadaveric radii than among analog radii.

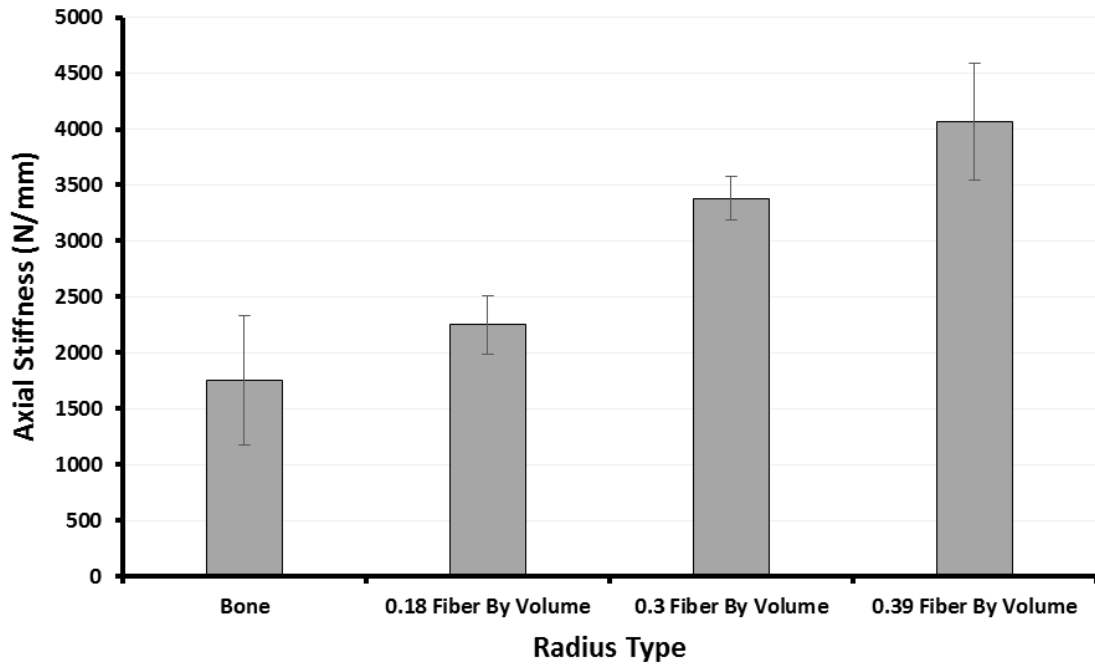


Figure 4.14: Chart showing the axial stiffness of composite and cadaveric radii. Error bars indicate one standard deviation from the mean.

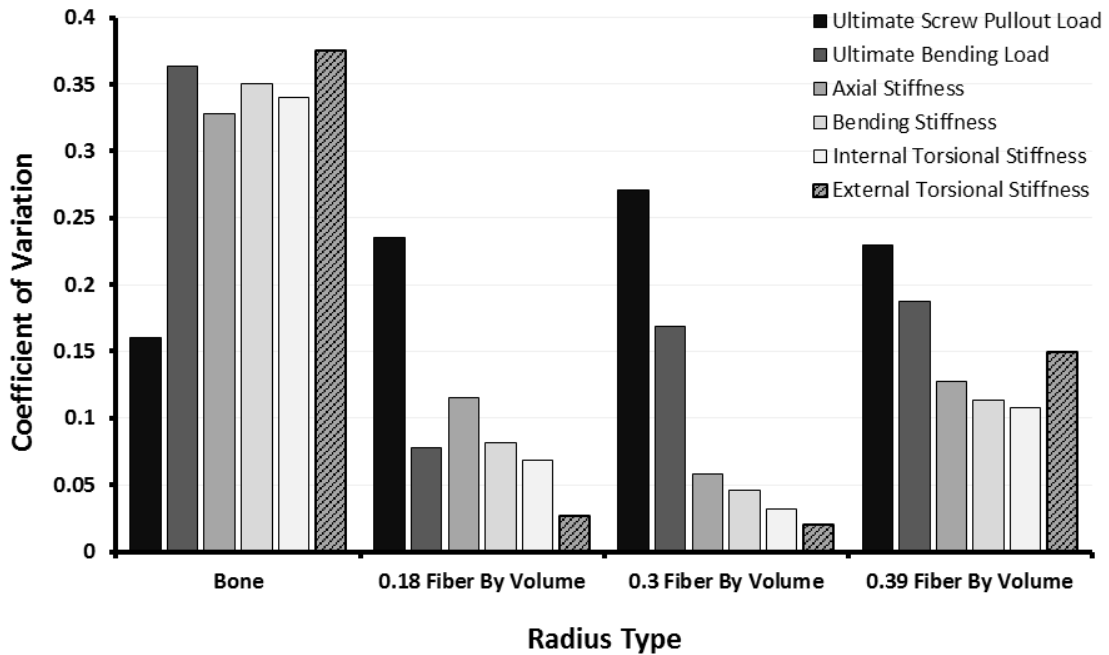


Figure 4.15: Chart showing the coefficient of variation across all mechanical testing modes.

No change in displacement was detected over 6 Million cycles for the plated analog radii when loaded between 66.7 N and 667.2 N as seen in Figure 4.16. Data were sampled at the maximum and the minimum of the stroke to reduce the size of the data file. These results suggest that the analog radii would serve as a suitable platform for the cyclic testing of bone/plate/screw constructs. The number of strides (cycles) for dogs during recovery has been estimated at 4,500 per hour for walking, and 9,000 per hour for trotting (Liptak et al. 2006b). A 1,000,000 cycle test would therefore model 222 days of walking, slightly less than the expected survival time of canines with distal radial limb sparing. These cyclic tests modeled clinically relevant loads however, work done by Zand, Goldstein and Matthews

(1983) resulted in a load-number of cycles curve suggesting that fatigue testing of plate/bone/screw constructs could be accelerated by increasing the load without loss of accuracy.

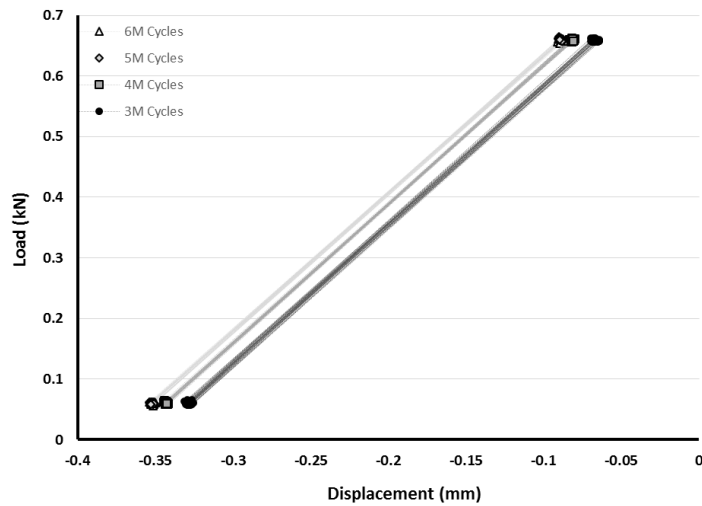


Figure 4.16: Plot showing the load vs. displacement for the plated analog radii at 3, 4, 5 and 6 million cycles.

4.3 Discussion on the Validation of Composite Analog Radii

This study evaluated the mechanical properties of canine composite radii in comparison to canine cadaveric radii. The influence of fiberglass loading on stiffness, bending, torsion, and screw pullout strength was analyzed. The properties of analog composite bones can be varied easily by changing fiber loading. The hypotheses that composite radii could be tailored to match the mechanical properties of canine radii while

decreasing the variability of their mechanical properties was accepted for most testing modes.

The bones made with 0.30 fiber volume fraction most closely matched both the intensive and extensive mechanical properties of the original radius bone. Across all fiber loadings, the analog radii exhibited a higher torsional stiffness than the cadaveric radii. This phenomenon was also seen in a study involving human femora and tibiae (Heiner, 2008) The lower torsional stiffness of bone, compared with that of the replicas, may result from the fact that the high degree of anisotropy typically seen in cadaveric bone. While no attempt was made to optimize or control fiber orientation in this study, other studies have demonstrated that fiber orientation is a function of aspect ratio, viscosity, injection pressure and nozzle shape (Crowson, Folkes, & Bright, 1980; Kunji, 2006). Future work could focus on investigating these parameters for optimizing fiber orientation. In addition, the higher viscosity of the 0.39 fiberglass fraction mixture could not be easily mixed or injected into the molds with the available equipment. This suggests that there may be challenges associated with producing models stiffer than the ones tested in this study. Alternatively, stiffness could also be increased by using a lower fraction of higher modulus fiber such as Kevlar or Carbon fiber. Only two materials were combined in these models to represent cancellous and cortical regions of the bone, this creates a distinct boundary at the interface between the two materials. In reality, the transition between cancellous and cortical bone is much more

gradual suggesting the need for using functionally graded materials to better represent this transition.

Furthermore, the testing herein has been quasi-static. These analog models have not been shown to address the complex microscopic or viscoelastic behavior of bone in the present study. A key assumption of the present technique is that the simplifications and compromises in materials and biological detail in favor of manufacturability have not undermined the original objective. The data from the mechanical testing suggest that this assumption is justified. It is important to note that the materials used here are only intended to replicate a simplified model of the bone suitable for mechanical testing of custom implants. These analogs only mimic the material properties of bone on a macro scale and, then, only within a relatively narrow range (the linearly elastic region of the bone analog). Nevertheless, the data also show that the holding power of the 3.5 mm cortical bone screws was equal to or greater than cadaveric bone for all fiber loading conditions. The screw withdrawal test results are a good indication that the analog models will be suitable for testing implants. The data also do not indicate a difference in the ultimate load and the yield load between the composite radii and the cadaveric radii. However, the brittle failure mode of the analog radii observed in this study (coupled with the significantly higher energy at failure for the cadaver bones) suggests that the analog radii should only be used for non-destructive tests. For instance, the analog bones tested here could be used to assess the stability of

specific surgical procedures, for example when designing low-modulus implants whose mechanical properties should match the host bone.

Further work will be required to fully validate this technique. In this study, one radius was chosen, at random, from the cohort to provide the digital geometry for the composite radii. The stiffness, or resistance to loading that was measured is an extensive property highly dependent upon geometry (e.g. a doubling of cross section in the direction of loading results in an 8 fold increase in stiffness). The relatively large variation that is evident in the stiffness of cadaveric bones can, in part, be explained by the differences in geometry, as shown in Figure 4.17. Future work should focus on replicating these data, comparing each new composite bone with its biological equivalent thus minimizing the variation between the two groups.

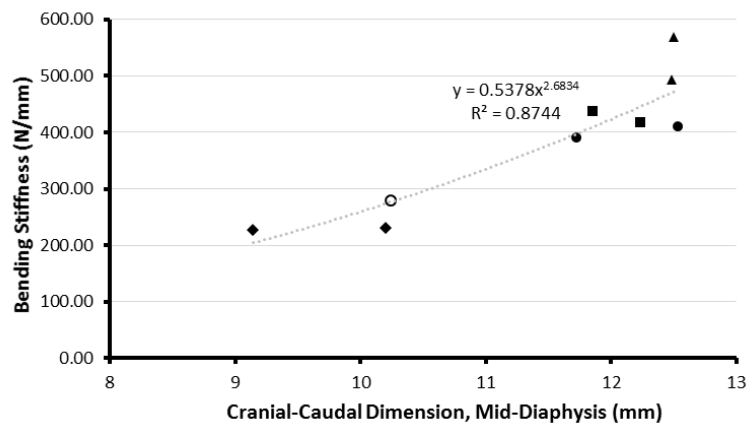


Figure 4.17: Plot showing cranio-caudal measurements of the diaphysis of the cadaveric radii versus the stiffness in 4-point bending. Data with the same marker shape indicate contralateral limb pairs.

The consistency of in the properties of composite radii is a substantial advantage during biomechanical testing in that small differences between orthopedic devices are more detectable. A smaller sample size would be required to detect differences between groups of orthopedic constructs if replicas were used instead of cadaveric bones. For example, if a group of bones had a 50% coefficient of variation, 199 bones would be required to detect a 20% difference between 2 groups of constructs with a power of 0.8. However, if a group of analog radii had a 5% coefficient of variation, only 5 would be necessary to detect the same difference with the same power. The use of analog models rather than cadaveric bone in biomechanical testing also offers the advantage of simultaneous comparisons of more than 2 experimental groups of constructs because paired comparisons are no longer necessary.

Although various materials and commercial products appear suitable for simulating specific bone properties, their lack of patient-specific bone geometry complicates the evaluation of custom implants. The primary arguments supporting the use of custom implants are typically associated with the ability to match patient specific geometries which may significantly decrease surgical margins, improve blood proliferation and improve implant stability (i.e. conformal fracture fixation plates). The importance of an isomorphic substrate at the implant interface is therefore essential for any meaningful testing protocol. To date these characteristics of custom, additively manufactured, implants have not been widely tested in the literature. The development of patient-specific bone models establishes a

means of mechanical testing and evaluation for custom, patient specific implants that are fabricated using EBM and LM technologies.

5.0 EVALUATION OF Ti6Al4V CELLULAR STRUCTURES FABRICATED WITH EBM

Limb sparing is a surgical procedure that includes the removal of a bone tumor and adjacent tissues followed by the placement of a bone graft or metal implant that is secured in place by a bone plate. When the tumor is close to a joint, limb sparing may include a total joint replacement or fusion of the joint. Limb sparing is done in dogs, most often to remove tumors of the radius, in the forearm. In some instances, more than 50% of the radius is removed. The procedure has a high failure rate: large cortical allografts are predisposed to fracture, non-union, lack of osseointegration, allograft resorption, and persistent infections (Liptak et al., 2006). Metal endoprostheses have been used, however, these also carry high risk of failure. The large difference in stiffness between bone and metallic implants creates a stress riser that contributes to failure of fixation. New manufacturing technologies may bridge the mechanical gap between allograft and metal endoprostheses and address current limb sparing limitations.

A growing area of research involves the use of low stiffness metallic foams for biomedical applications. Such foams have been fabricated through the sintering of biocompatible metal powders, the injection of gases into molten metal, and the deposition of metal vapors onto organic scaffolds. These manufacturing technologies produce both open and closed-cell stochastic foams. Characteristically, the size of cells is not uniform throughout the material. These foams are found readily in nature and inherent in the structure

of materials like bone or wood. Processes for manufacturing stochastic metal foams have been reviewed (Gibson, 2000). More recently, interest in the fabrication of non-stochastic metal foams with predictable, predetermined or repeatable geometries has grown substantially. The mathematics of such structures have been previously described but, until recently, experimentation has been hindered by the lack of a suitable manufacturing processes.

Powder bed metal additive manufacturing technologies such as Electron Beam Melting (EB) or Laser Melting (LM) have demonstrated the capability to fabricate such structures in a wide variety of materials. These processes selectively melt fine metal powders in successive layers with a focused energy beam and the resulting components typically exhibit properties consistent with the bulk material. The biocompatibility of titanium, and its alloys, make them ideal for low stiffness/porous biomedical structures. Various commercial systems cover powder size fractions from 1 to 300 μm . Since the profile of each cross section is generated from 3-D computer models, additive manufacturing facilitates small batch sizes (as low as one) by the eliminating part specific tooling/machine requirements. Naturally, this level of geometric flexibility is also enticing for biomedical applications because these mesostructures can be optimized for either bone fixation (Haslauer et al., 2010), or the transfer of mechanical loads, minimizing stress shielding and bone resorption (Harrysson et al., 2008). Porous structures may also be combined and fabricated together with solid portions of an implant. The EBM process is particularly well suited for the fabrication of

implants like limb sparing endoprostheses. EBM-manufactured implants require minimal supporting structures to build and have acceptable material properties minimizing the need for post processing steps such as heat treatment or machining.

Mechanical evaluations of EBM-manufactured metal foams in the literature have traditionally relied on observation of compressive properties (Cansizoglu et al., 2008, Heintz et al., 2008). These data have been successfully applied to the classic, generalized, model for the mechanical behavior of cellular materials proposed by Gibson and Ashby (1982). However, this approach has not been widely used to evaluate the flexural properties of high aspect ratio structures used in the repair of large segmental defects, and therefore fails to illuminate potential modes of failure. Moreover, much of the work has focused on optimizing unit cell geometries for tissue scaffolds rather than low stiffness grafts. This study examines the relationship between relative density and pore size for non-stochastic Ti6Al4V mesh structures fabricated with the EBM process.

5.1 Background

A key advantage of additive manufacturing over other approaches of metallic foam production is the ability to engineer, or otherwise explicitly design foam properties via an idealized computer model. In addition to being computationally expensive, process limitations such as powder size, layer thickness, and thermal distortions, have hindered the practical applicability of such models. Investigations in the literature have relied on the same approximations of the bulk properties that have traditionally been utilized for stochastic foams. The property of an open cellular foam structure, as described by Gibson and Ashby (1982), is proportional to the relative density (ρ/ρ_0) to the power of n , multiplied by a constant, c , as follows:

Equation 5.1

$$\frac{x}{x_0} = C \left(\frac{\rho}{\rho_0} \right)^n$$

The constant c is a function of the cell geometry and the property investigated. For Young's modulus (E) of open cell foams, c tends to approach 1.0, but can range from 0.1 to 4.0, and n typically varies from 1.8 to 2.2 (Ashby, 2000). Ashby also assumes that the flexural modulus and the compressive modulus are approximately equal ($E_f = E_c$). For strength (σ), c is approximately 0.3, and n is approximately 1.5. Investigations by multiple groups have characterized the properties of EBM fabricated Ti6Al4V open cell, non-stochastic mesh

structures. While the methodologies, unit cell geometries, and applications rarely overlap, several studies showed good agreement with the general Gibson & Ashby model.

The compressive and flexural properties of hexagonal mesh structures with relative densities ranging from 5.3 to 11.2% were reported by Cansizoglu et al. (2008). The calculated modulus of elasticity of the samples ranged from 25.7 MPa (5.3% relative density) to 211.3 MPa (11.2% relative density). The calculated flexural modulus ranged from 61.26 MPa (3.2% relative density) to 336.84 MPa (7.1% relative density). Since mesh struts were designed smaller than the electron beam melt pool diameter, the relative density was not controlled but instead varied as a function of pore size.

A repeating rhombic dodecahedron unit cell was used to populate a hip stem geometry resulting in a low stiffness implant reported to have reduced stress shielding in finite element modeling of the bone implant interface (Harrysson et al., 2008). These data were corroborated by experimentation, which showed a relative load displacement ratio of 2.38 compared to solid hip stems. The calculated strength of the structures, from experiments, increased with increasing relative density in approximate agreement with the Gibson-Ashby model ($c = 0.341$). For three-point bending specimens the highest modulus achieved was 12.7 GPa for a 3 mm unit cell with a 39.5% relative density. Heintl et al. (2008) describe two geometries: a diamond tetrahedron structure and a hatched structure fabricated by rotating the scanning direction of the electron beam by 90° every eighth layer.

The pore sizes ranged from 0.45 mm for the hatched structure to 1.23 mm for the diamond structure and the compressive modulus ranged from 0.9 to 12.9 GPa. A similar honeycomb structure exhibited a compressive modulus of 2.5 GPa for a porosity of 66.3% (Li, Wang, Zhang and Li, 2010). Parthasarathy, Starly and Raman (2010 and 2011) examined the compressive properties of four sets of EBM fabricated cubic structures. The strut sizes for three of the sets were nominally 800 μm , while the struts for the fourth were 450 μm . For porosities ranging from 50.75 to 70.32%, the compressive stiffness ranged from 0.57 to 2.92 GPa. A strength reduction from 163 to 7.28 MPa corresponding the reduction in measured strut size was reported. In several cases, the reported observed failure mode in compression was through shear (Cansizoglu et al., 2008, Parthasarathy, Starly and Raman, 2011).

Murr et al. (2010) demonstrated the use of resonant frequency and damping analysis (RFDA) to determine that the elastic modulus of several different mesh geometries, ranging from 0.48 to 6.78 GPa with respective relative densities ranging from 12 to 43%, showed a good fit to the Gibson-Ashby model (n ranging from 2.2 to 2.4). The RFDA technique was also used to investigate the effect of process settings on the elastic properties of diamond tetrahedron mesh structures (Heinl, Körner, and Singer, 2008). A trabecular foam model was generated from μCT data with both hollow and solid struts (Murr et al., 2010). The modulus and strength of the trabecular foam were compared to a rhombic dodecahedron structure. While both followed the same power law for modulus, the non-stochastic structure had higher specific strength and different failure characteristics as compared to the trabecular

structure (Cheng et al., 2012). Yang et al. (2012), proposed a direct analytical approach to determine the mechanical properties of a negative Poisson's ratio reentrant structure. Experimental results from these studies suggest that, while relative density is a good predictor of modulus and strength, increasingly negative Poisson's ratios showed a stronger influence over these properties, possibly due to improved resistance to shear. Wieding, Jonitz, and Bader (2012) evaluated three different types of mesh structures with cuboid and diagonal struts. Figure 5.1 summarizes the results of several of the studies discussed and shows the effect of the relative density on the relative modulus. Figure 5.2 compiles the available data on compressive strength.

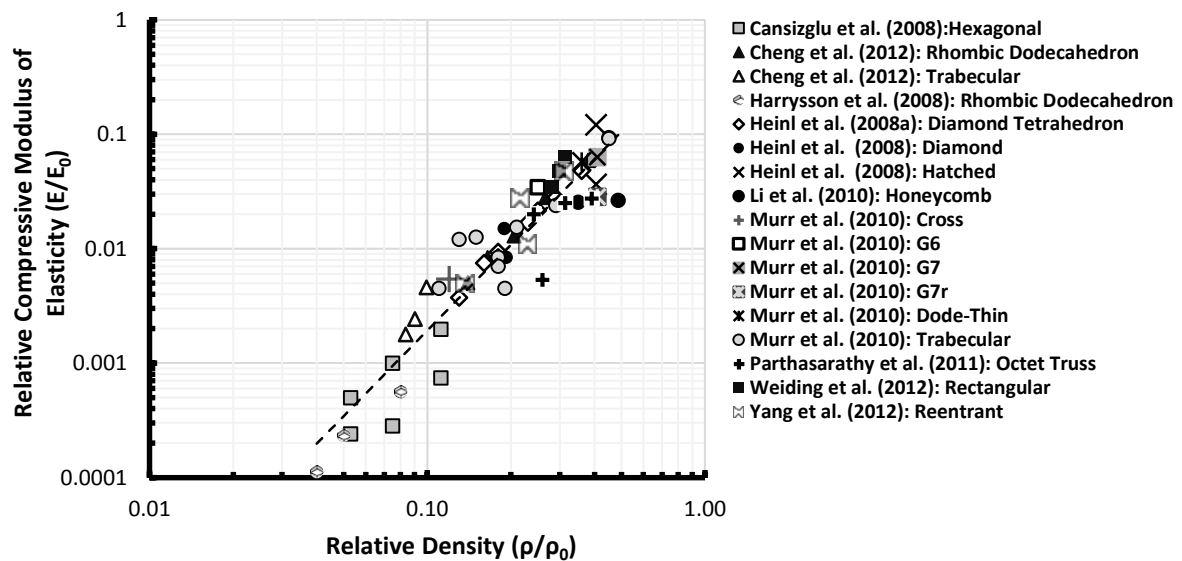


Figure 5.1: Plot summarizing the relationship between relative density and relative modulus of elasticity derived from EBM fabricated Ti6Al4V foam structures reported in the literature.

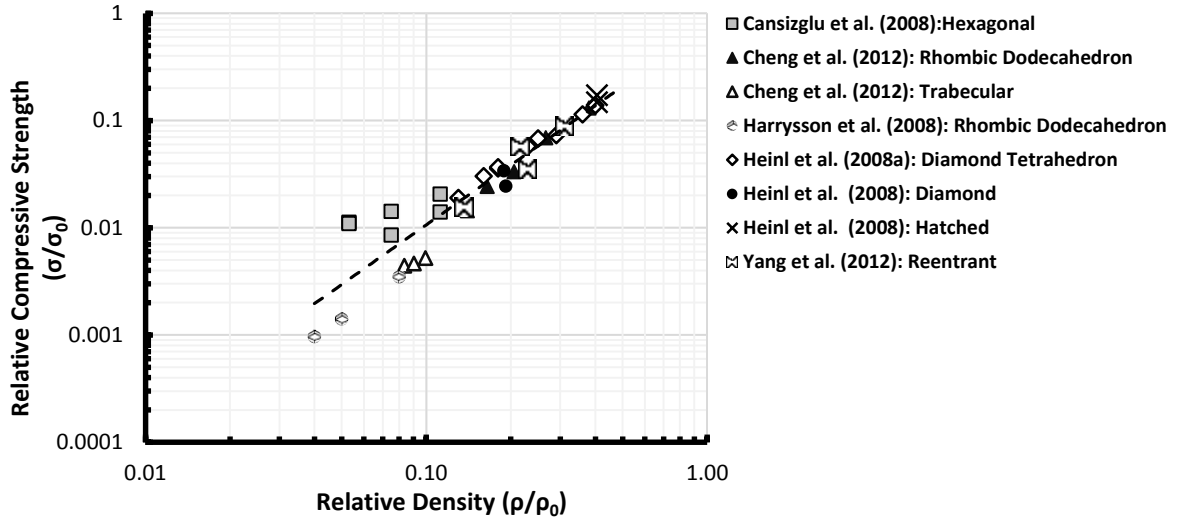


Figure 5.2: Plot summarizing the relationship between relative density and relative compressive strength derived from EBM fabricated Ti6Al4V foam structures reported in the literature.

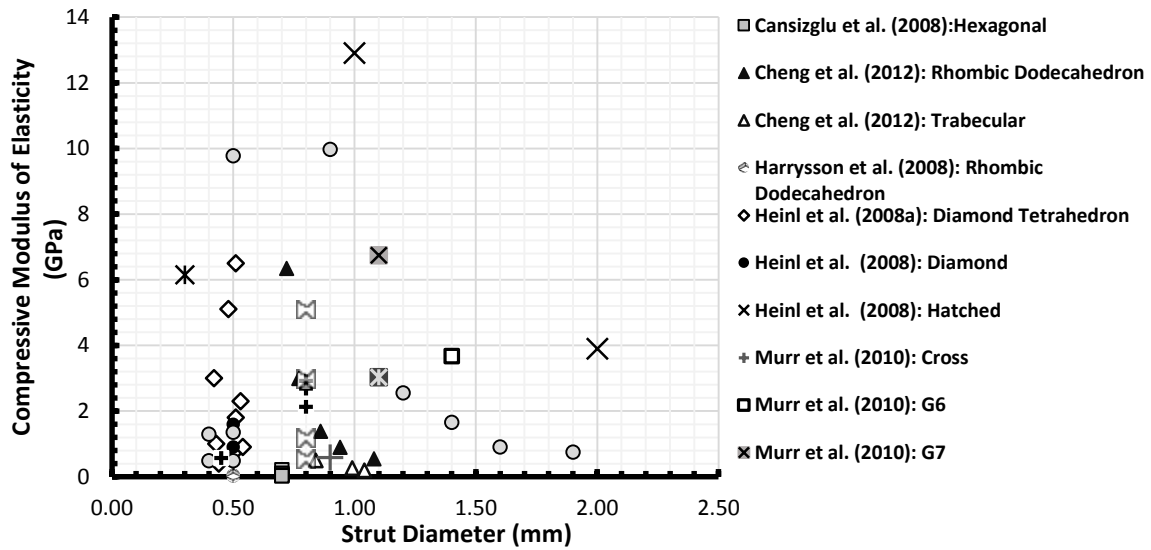


Figure 5.3: Plot summarizing the relationship between strut diameter and compressive modulus of elasticity from EBM fabricated Ti6Al4V foam structures reported in the literature.

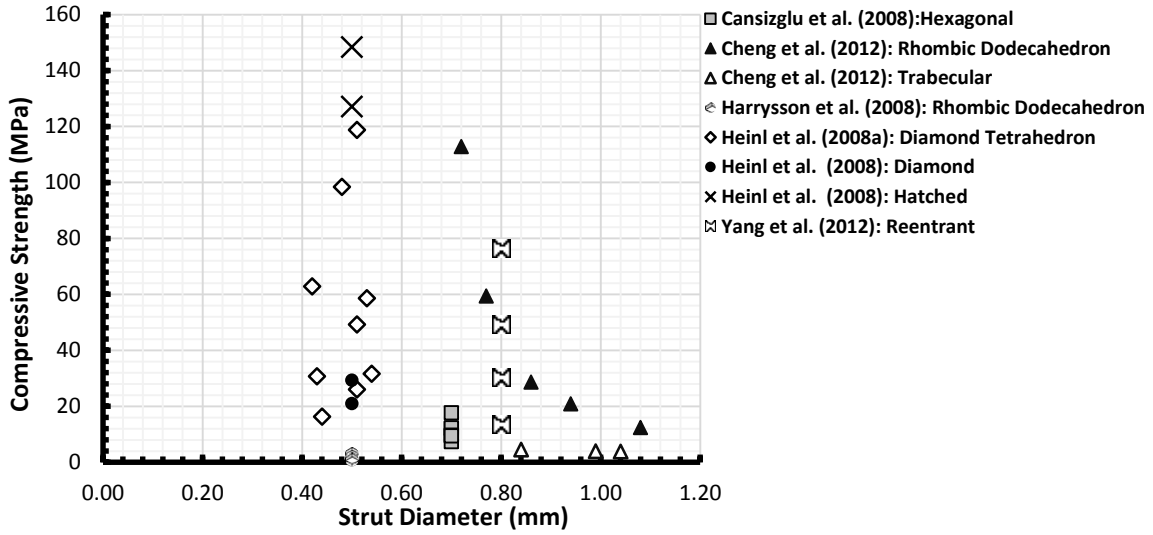


Figure 5.4: Plot summarizing the relationship between strut diameter and relative compressive strength derived from EBM fabricated Ti6Al4V foam structures reported in the literature.

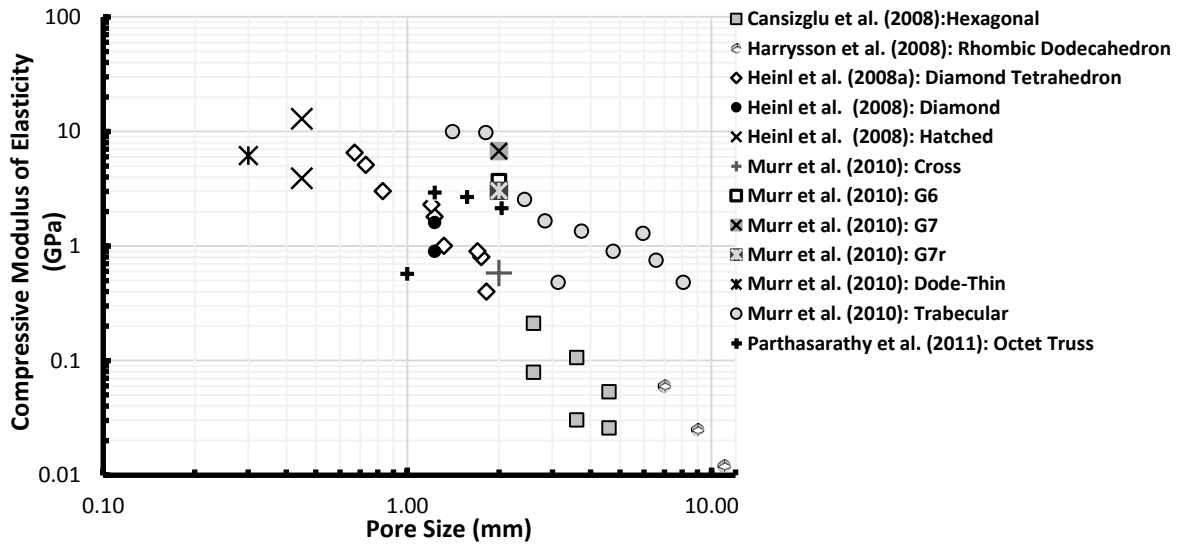


Figure 5.5: Plot summarizing the relationship between pore size and compressive modulus of elasticity derived from EBM fabricated Ti6Al4V foam structures reported in the literature.

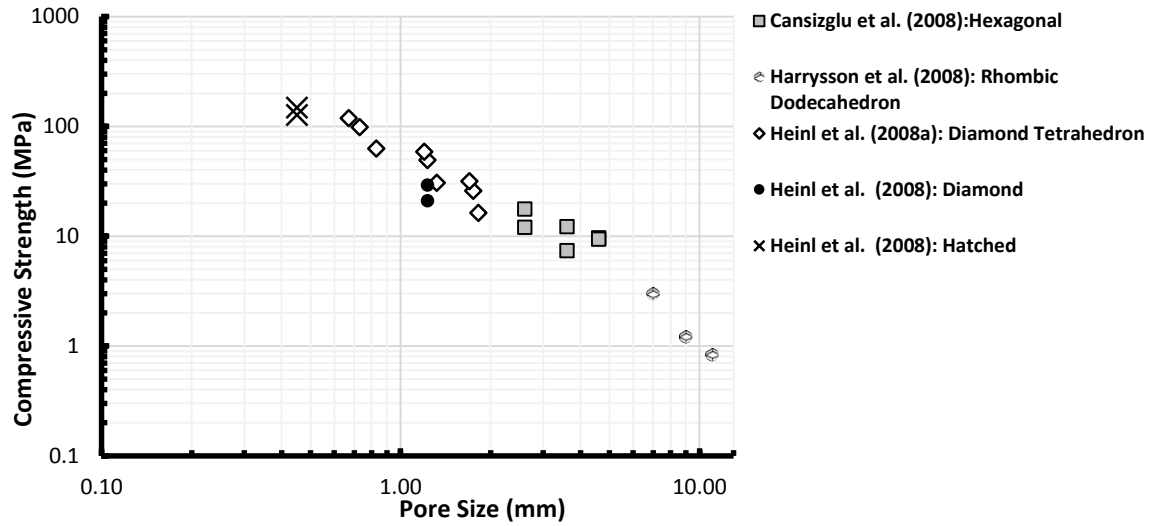


Figure 5.6: Plot summarizing the relationship between pore size and compressive modulus of elasticity derived from EBM fabricated Ti6Al4V foam structures reported in the literature.

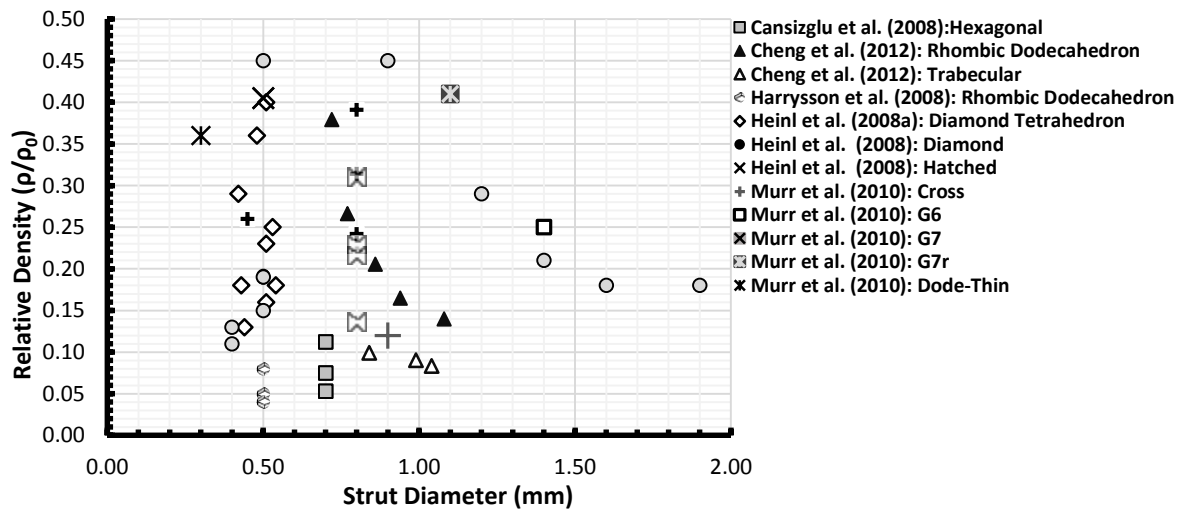


Figure 5.7: Plot summarizing the relationship between strut diameter and relative density derived from EBM fabricated Ti6Al4V foam structures reported in the literature.

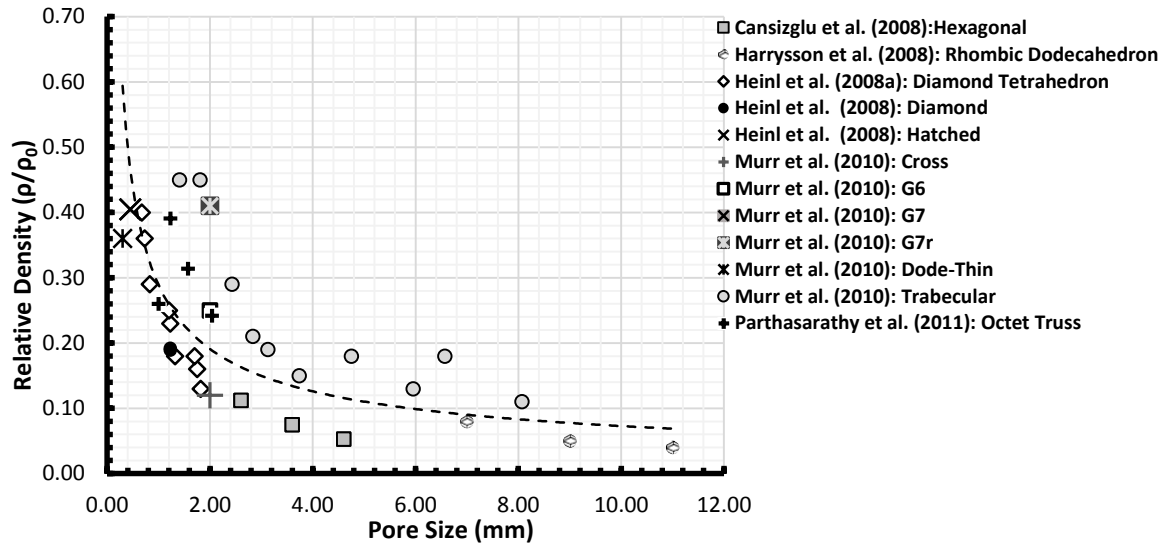


Figure 5.8: Plot summarizing the relationship between pore size and relative density derived from EBM fabricated Ti6Al4V foam structures reported in the literature.

Despite differences in fabrication, cell geometry, and testing methods, data in Figure 5.1 indicate that the Gibson-Ashby relationship can be used to predict strength and modulus of elasticity. An effect of strut size was noted in one study (Parthasarathy et al. 2011) and a weak correlation between pore size and relative density ($R^2 = 0.568$) was detected across all data. This may be because relative density was not a controlled parameter in the studies reviewed but, rather, the result of scaling or beam/melt pool effect. A parameterized mixed effects model was developed to further investigate the influence of these effects using statistical software (JMP v.11, SAS, Cary, NC). Model effects included pore size, strut size, relative density, and a correlation effect between pore size and relative density. The remaining correlation effects were excluded because initial models indicated that these effects were not apparent in the data. In several studies, whether pore sizes and strut sizes

were from idealized CAD models or from measurements, was not reported. For the purposes of this analysis, these two conditions were considered equivalent, although for strut diameters measuring $< 350\mu\text{m}$, the validity of this assumption is questionable. Distributions for modulus and strength were slightly skewed, however, normality was acceptable for analysis at $\alpha = 0.05$. Results for modulus ($R^2 = 0.74$) indicate a significant effect of relative density ($p < 0.001$) while no effects of strut size or pore size were detected ($p = 0.625$ and $p = 0.877$ respectively).

These two effects are illustrated in Figures 5.3 and 5.5. A very weak correlation between pore size and relative density may be present, but was not statistically significant ($p=0.188$), illustrated in Figure 5.8. The overall fit of the model to the strength data was much better than for the modulus ($R^2=0.98$). Relative density also had a significant effect on compressive strength ($p=0.017$). Strength was also influenced by strut size ($p=0.003$) illustrated in Figure 5.4, and a moderate interaction between relative density and pore size was detected ($p=0.043$). As shown in figure 5.6, the effect of pore size independent of relative density was not statistically significant ($p=0.176$). While this analysis has accounted for missing data, the robustness of model may be weakened by underreporting of key parameters in the literature. For example, only 5 articles directly reported both pore size and compressive strength.

This review uncovered several key areas of research absent from the available literature, including the evaluations of porous Ti6Al4V structures in which relative density, strut size and pore size are controlled. Also, the literature is skewed toward small strut sizes; the dimensions reported are often below the threshold of machine capability. The resulting specimens are therefore unreliable vehicles for model validation. Studies reporting on the flexural behavior of EBM fabricated foam structures are relatively sparse, and finally, the low relative densities often reported result in modulus values insufficient for matching the properties of cortical bone, particularly when considering the repair of large segmental defects in appendicular bones.

5.2 Methods

5.2.1 Sample design and preparation

Parametric rhombic dodecahedron unit cell geometries were designed using CAD software (Solidworks 2013, Dassault Systèmes, Waltham, Massachusetts). Struts were designed with circular cross sections. Nine unit cell geometries were designed with 3 unit cells sizes and 3 relative densities. Bounding cube geometries of 3mm, 6mm and 9mm and relative densities of 0.2, 0.3, and 0.4 were chosen. Figure 5.9 shows an illustration of three unit cell geometries.

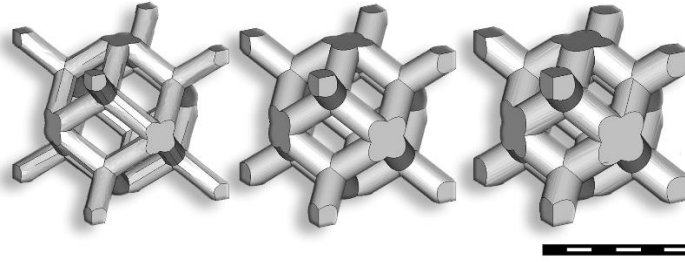


Figure 5.9: Illustration of rhombic dodecahedron unit cell geometries with relative densities of 0.2 (left), 0.3 (center) and 0.4 (right). Scale bar indicates 6 mm.

The unit cell models were converted to standard tessellation format (STL) with a minimum facet deviation of 0.01mm. Modeling the struts with circular cross sections requires significantly more computational power as compared to modeling struts with square cross sections (~4506 triangles vs. ~650 for square struts). However, this was an important consideration for comparing the idealized CAD geometries with the dimensions of the experimental specimens.

Using an STL processing software (Magics, Materialise, Plymouth, MI), prismatic bars for flexure samples measuring 9 x 18 x 150 mm were generated and populated with arrays of each of the nine unit cells using a Boolean intersect operation. Five replications of each design ($n = 45$) were oriented vertically in the ZYX direction, as described in ASTM F2921. Sample sizes were determined from power analysis of preliminary trials. The samples were arranged on a 150 mm square build platform spaced 3 mm apart. The samples were then merged into a single STL file and exported to the Arcam build assembler software

(Arcam, Mölndal, Sweden). The software sliced the 3D STL into two dimensional, 50 μm -thick cross sections that drove the machine control system.

5.2.2 Powder measurement and characterization

The samples were fabricated from Ti6Al4V gas atomized powder (Arcam) with a specified size distribution from 45 μm -105 μm . Prior to processing the chemical makeup of the powder was measured using inductively coupled plasma analysis (ICP), Hydrogen and Oxygen content were measured with combustion analysis (LECO-ASTM E1019).

5.2.3 Sample fabrication using electron beam melting

An Arcam model A2 was used to fabricate the samples for these experiments. All processing parameters used were commercially available from Arcam for Ti6Al4V (Arcam Build Control Software V3.2, SP2) Figure 5.10 illustrates the principle components of the system. The electron gun column (right) houses a ~4 kW thermionic tungsten filament under a vacuum of about 6×10^{-6} mbar. The filament is heated to above 2000 °C by a current of approximately 10A which causes electrons to be emitted; then a potential difference of 60kV between a cathode and an anode causes the electrons to accelerate. Astigmatism correction, focus, and deflection coils form the electrons into a narrow high energy beam that is guided across the powder surface. The energy density within the electron beam can be as high as 106 kW/cm². The transfer of energy from the electron beam to the electrons in the outer shells of the material generates the heat required for melting. The system vacuum level

is maintained by a controlled vacuum system that introduces small quantities of helium into the build area. A secondary benefit is that the helium is ionized by the beam which helps to reduce charge build up in the powder.

The vacuum chamber (left), which maintains an internal pressure of 2×10^{-3} mbar, contains the build tank and powder dispatching system. The build tank is lowered a distance of $50 \mu\text{m}$ per layer by a lead screw outside the chamber. The powder is contained within the hoppers and is spread across the build surface by the rake mechanism. The amount of powder dispatched is measured by sensors under the build platform. A stainless steel (304 series) start plate measuring 150 mm x 150 mm x 10 mm rests a 40mm thick bed of loose titanium powder. A thermocouple under the start plate monitors the temperature throughout the build. A copper wire also connects the bottom of the start plate to the build chamber providing a path to ground. The start plate is visually leveled to the rake mechanism by systematically spreading powder with the rake and raising the table until the start plate is clean. The start plate is then lowered 0.6 mm to accommodate thermal expansion of the plate.

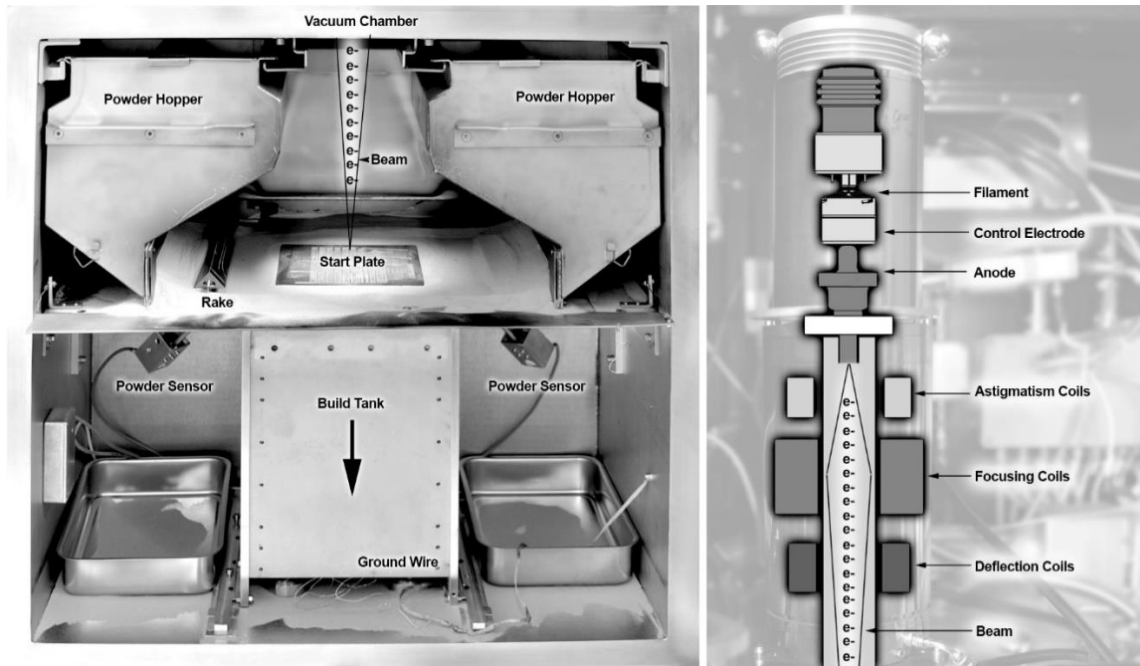


Figure 5.10: Illustrated photograph of the Arcam A2 build chamber (left) and electron beam column (right).

Initially the beam scans the surface of the start plate at very high power and high speed (~ 33 mA and ~ 15 m/s) raising the temperature of the plate to 300 °C. The current is reduced to ~ 4 mA to maintain this temperature for 30 minutes. This outgassing step allows the system to evacuate impurities such as water vapor from the machine surfaces thus reducing contamination of the powder. After the outgassing step, the current is again increased to rapidly heat the start plate to a temperature of 760 °C (as measured by the thermocouple). A final step briefly maintains this temperature to sinter the powder underneath the start plate.

The processing of each layer typically requires 2-4 separate steps which are assigned by the user following general pattern illustrated in Figure 5.11. Each step is called a “theme” that contains all of the process parameters required (beam speed, beam power, focus offset etc.).

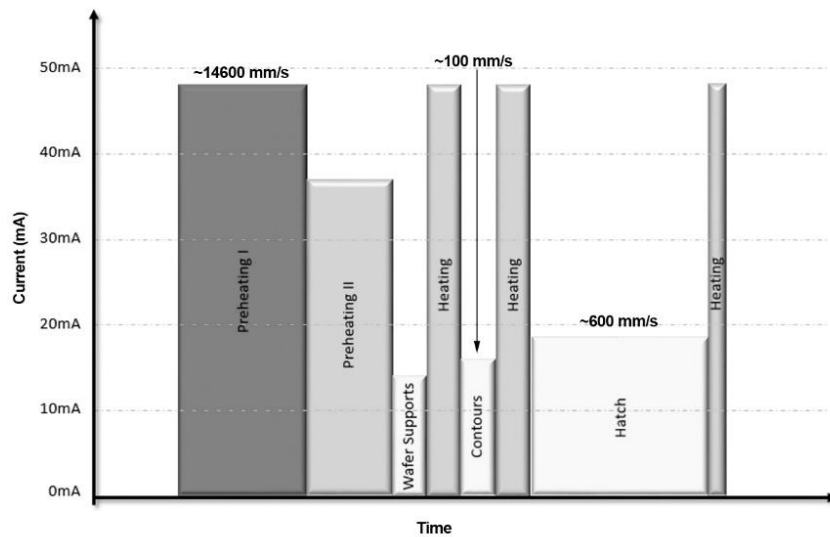


Figure 5.11: Plot illustrating the relative contribution of each processing step within a layer.

The first step is preheating which raises the temperature of the powder causing it to lightly sinter together. This mechanical bond facilitates the next step, melting. Melting is divided into two sub-steps, contours and hatching. The contours step uses a relatively low current and speed (~7 mA, 100 mm/s) to trace the outline of each layer using a proprietary control step called “multi-beam”. This utilizes the high scan rate capabilities to jump between multiple locations on the contour approximating multiple beams which are able to

simultaneously maintain multiple melt pools (~60). This approach improved surface finish (over single spot contouring) while maintaining productivity. The second component of the melt theme is the “hatch” step. Here, the beam current and speed are increased (~15 mA, 600 mm/s) and the beam is rastered to melt the area between the contours. The hatch direction is rotated 90° every layer, and the spacing between the hatch lines is offset by 0.05mm each layer. A specialized melt theme is used for metal foam structures (called “network”). Other themes are used to produce breakaway support structures (requires for downfacing part surfaces at an angle <30° to the build surface). The rhombic dodecahedron structures described here did not require support structures. It is also important to note that the parameters are not held constant throughout a build, but instead vary (within limits) based on the output of an internal, and proprietary, thermal model designed to maintain a constant heat input per layer, and a constant surface temperature of about 650°C (accounting for variations in cross sectional area and heat loss through conduction/radiation). The extra heating steps shown in Figure 5.11 may or may not be added. Two themes were used for the fabrication of the rhombic dodecahedron mesh structures in this study, the preheat theme and the melt theme.

After build completion (about 26 hours) the build chamber is flooded with helium to accelerate cooling (still below atmospheric pressure). The samples were allowed to cool to room temperature (27°C), as indicated by the thermocouple, before removal from the machine. Upon removal, the samples were encased in lightly sintered titanium powder

which was removed by abrasive blasting using additional Ti6Al4V powder as media (Arcam Powder Recovery System). Figure 5.12 shows a photograph of the partially completed powder removal process.

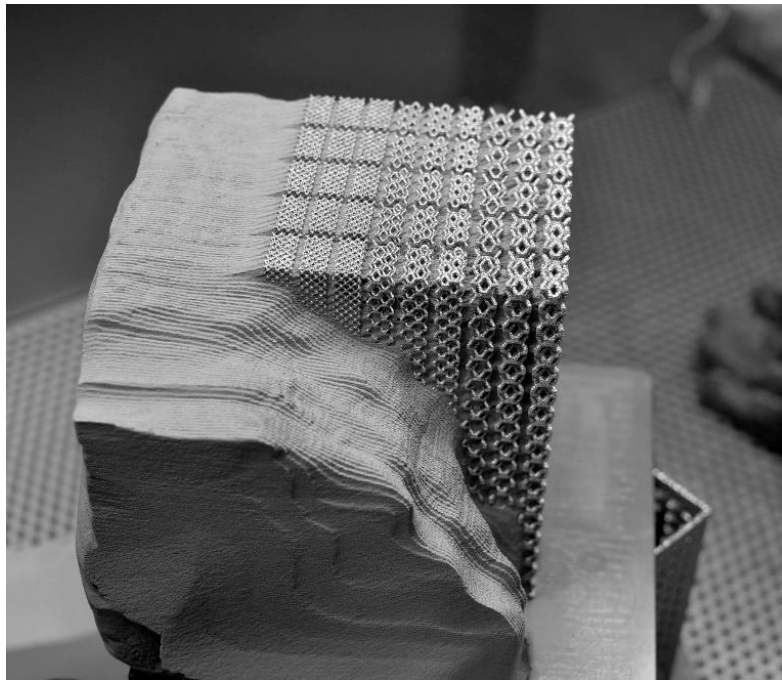


Figure 5.12: Photograph showing the test specimens partially removed from the sintered Ti6Al4V powder.

No description of validating the powder removal process was found reported in the literature. Here, powder removal was validated by visual inspection with the aid of a white back light (Figure 5.13). Figure 5.14 shows a photograph of one of each of the finished specimens.

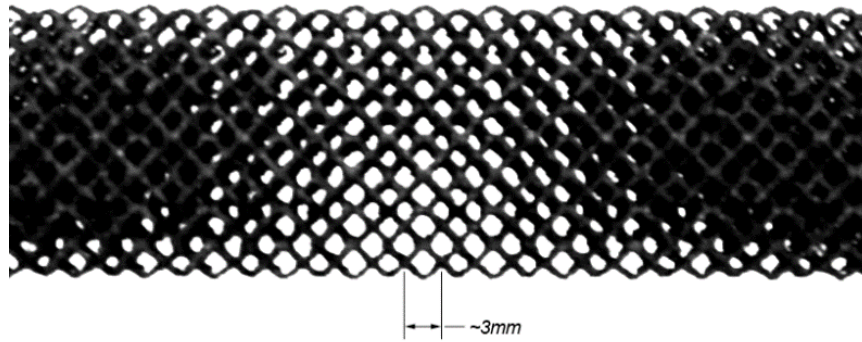


Figure 5.13: Photograph illustrating the technique for visual confirmation of powder removal (3mm unit cell, 30% nominal relative density).

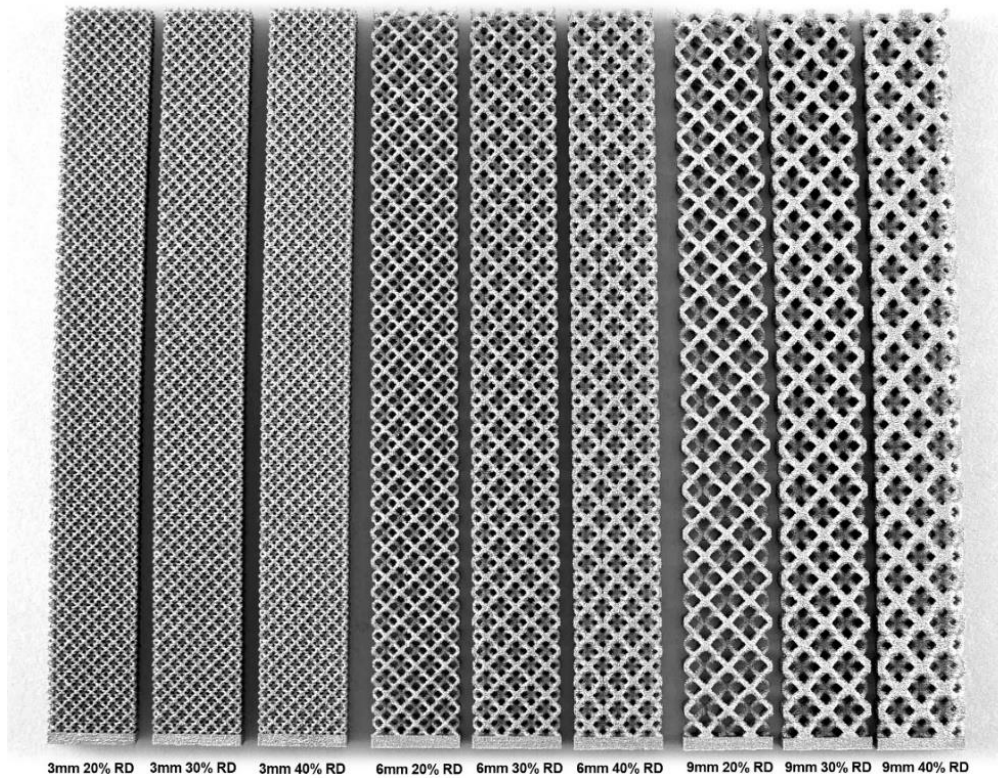


Figure 5.14: Photograph showing one sample of each of the nine specimen types. Note that unit cell size and relative densities shown are nominal.

5.2.3 Sample measurement and characterization

The bounding volume of each of the samples was measured with digital calipers accurate to 0.01mm. Marin et al. (2010) used several methods to measure the bounding volume of EBM fabricated mesh structures including the Archimedes method, calipers and a latex shell filled with water. Among these they found 2% variation in measurements. After visual confirmation of powder removal, the mass of each sample was recorded to the nearest 0.001 g using a draftshield protected electronic balance (Ohaus Adventurer, Parsippany, NJ). The density of each sample was calculated from these mass and volume measurements. Struts were measured at 70x magnification using a digital optical microscope (Hirox KH-7700, Tokyo, Japan). Twelve strut measurements were collected from the left, center and right regions of each sample. The modulus and ultimate strength for solid EBM fabricated Ti6Al4V was determined from preliminary tensile tests to be 113 GPa and 860 MPa, respectively.

5.2.4 Mechanical testing

Four point flexure testing was carried out on each of the 45 samples using an ATS 1620C universal testing machine (Figure 6). The diameter of the supports was 12.7 mm, the major span was 127 mm, the minor span was 50.8 mm, and the loading rate was 2.54 mm/min. A fixed point stop on one end and the back of each sample provided consistent sample placement. The loading supports were allowed to pivot about the center to

compensate for any misalignment. A 22.2 kN capacity load cell was used to record loading data at a rate of 100 Hz. Using crosshead displacement as a measure of deflection, modulus of elasticity was calculated from the slope of the load-deflection curve using the relationship shown in Equation 5.2. Ultimate strength was calculated from the maximum moment at the peak load using the bounding dimensions of the sample to calculate moment of inertia. Statistical software (JMP v.11), was used for data analysis and curve fitting.

Equation 5.2

$$E_f = \left(\frac{P}{\delta}\right) \frac{a^2(3L - 4a)}{12I}$$

Where P is the load recorded by the load cell and δ is the crosshead displacement; a is the distance between the centers of the outer supports and the loading supports and L is the distance between the two outer supports. I is the area moment of inertia of the bounding rectangular cross section. After testing a small section was cut from the unloaded portion of each sample. These were potted (TR-1 mounting powder, MarkV, East Granby, CT), wet ground progressively from 120 grit to 2000 grit and polished with 0.3 μm alumina powder (Mark V 3B/4B series grinding and polishing station station). Microhardness measurements were recorded using a Knoop indenter with a 500 g load (MHT Series 200, LECO Corporation, St. Joseph, MI).



Figure 5.15: Photograph showing the four point flexure test setup for one of the samples (Nominal 6mm and 20% relative density).

A Shapiro-Wilk test was performed on all measurements to analyze the fit of each data set, consisting of $n = 60$ measurements, to a normal distribution. For each case, the test failed to reject the null-hypothesis that the data were normally distributed. One-way ANOVA was used to analyze the differences between the groups by target relative density and target unit cell size and means were compared with 2-tailed Student's t -tests ($\alpha = 0.05$). A 2-parameter mixed effects model was used to evaluate the influence of both relative density and strut size on the measured mechanical properties and model the results. A correlation effect was included in the model between strut size and relative density.

5.3 Results

5.3.1 Powder Analysis

The results of the chemical analysis are shown below in Table 5.1. These data indicate that the powder was within specifications for Ti6Al4V for additive manufacturing (ASTM F2924). The manufacturer, Arcam, requires that Oxygen and Nitrogen are 0.19% and 0.05% by weight respectively.

Table 5.1: Elemental analysis of Ti6Al4V powder used to fabricate the test specimens.

Element	Weight %	Element	Weight %
Al	6.24	Cr	<0.01
V	3.98	Ni	<0.01
Fe	0.15	Sn	<0.01
Si	0.03	Co	<0.01
Mn	<0.01	Nb	<0.01
Mo	<0.01	Zr	<0.01
Cu	<0.01	O	0.05
N	0.03		

5.3.2 Strut measurement results

Figure 5.16 compiles the average strut measurements for each of the experimental groups. Figure 5.17 shows representative photomicrographs of struts from each sample set.

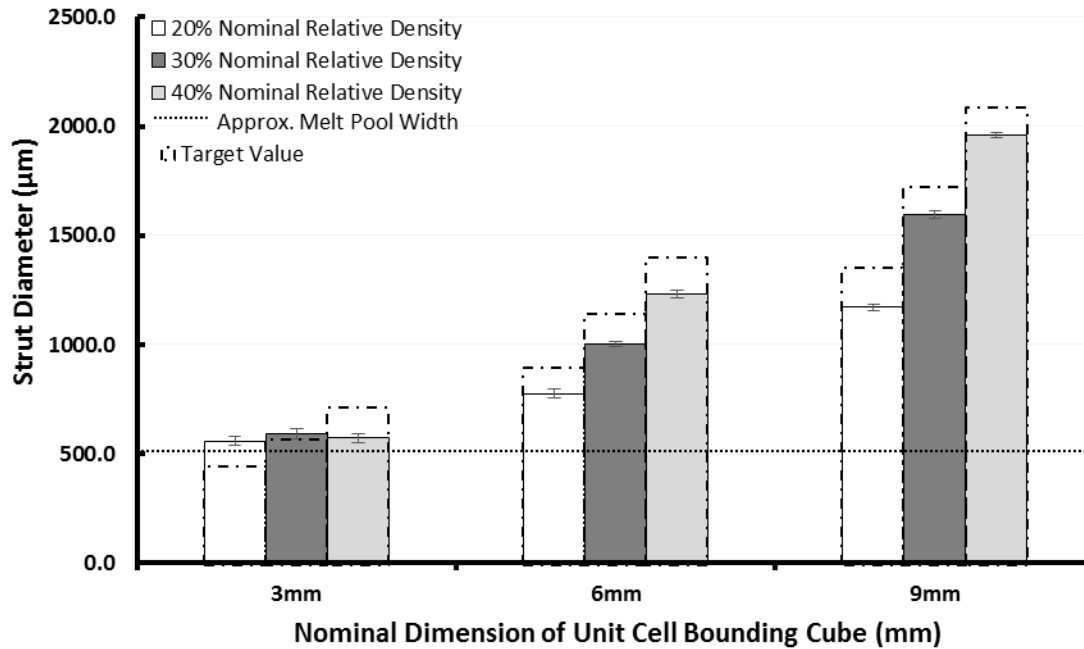


Figure 5.16: Mean measured strut dimension of EBM-fabricated mesh structures, error bars indicate 95% confidence intervals, dashed columns specify target dimension measured from CAD models. The dotted line represents the approximate EBM melt pool width.

Strut measurements between 6 and 9 mm groups differed significantly ($p < 0.001$, Figure 8) and a strong linear correlation between measured relative density and strut size was detected ($R^2 = 0.983$ and 0.989 , respectively). For the 3 mm unit cell group, differences in measured strut size across the three nominal relative densities were not detected ($F = 0.3161$). Also, strut size and measured relative density for the 3 mm group had a low correlation ($R^2 = 0.069$).

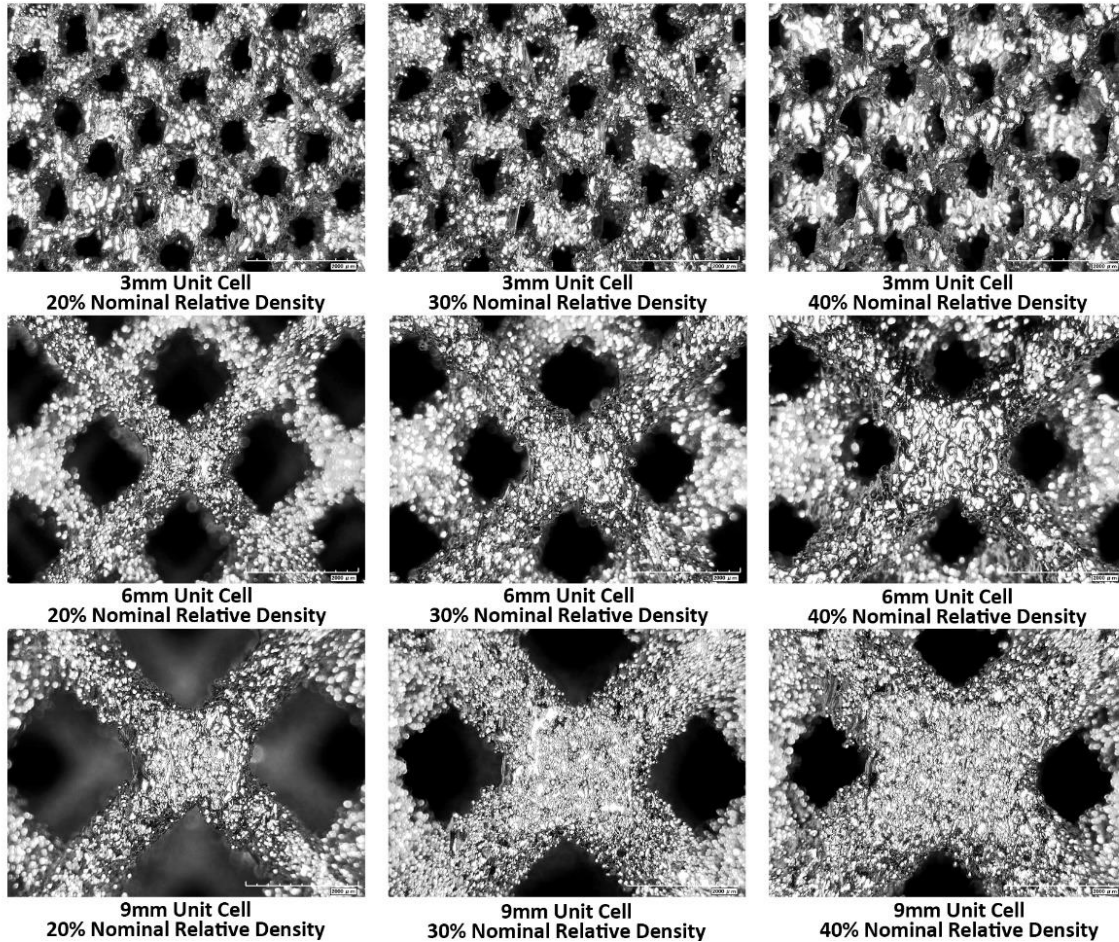


Figure 5.17: Photo micrographs showing representative struts of each of the nine specimen types tested. Scale bar indicates 2000µm.

For small diameter struts, measured diameters were larger than target diameters and, for larger diameter struts, measured diameters were smaller than target diameters. The standard deviations of strut measurements were similar across the sample groups, however the variance of the relative difference between actual and measured strut diameters was significantly higher for the 3 mm unit cell group ($F = 0.019$). The 6 and 9 mm unit cell

groups did not differ statistically. The approximate EBM melt pool width is also indicated on Figure 5.16.

5.3.3 Mechanical Testing

Mechanical test data were analyzed with one way ANOVA to determine the differences between the groups (by nominal relative density and nominal unit cell size) after confirmation of normality with a Shapiro-Wilk test. For each case, the test failed to reject the null-hypothesis that the data were normally distributed. The mean, standard deviation and 95% confidence interval were also calculated from these data. Means between the experimental groups were compared with 2-tailed Student's t-tests ($\alpha = 0.05$). Correlations between strut size and flexural modulus, and between strut size and ultimate strength were not statistically significant ($R^2 = 0.159$ and 0.229 , respectively). Correlations between ultimate strength and strut size, and between flexural modulus and strut size were statistically significant for the 40% target relative density group ($R^2 = 0.937$), but not for the 20% and 30% target relative density groups. Figure 5.18 shows representative load-deformation curves for each of the nine samples. Figure 5.19 shows the results for flexural modulus and Figure 5.20 shows the results for the ultimate strength of the samples. In each sample, failure was observed to initiate on the tension side of the sample between the inner supports and was relatively brittle such that $\sigma_{\text{ultimate}} \sim \sigma_{\text{yield}}$. No plastic deformation of the material under the loading supports was observed. Data were categorized by the target relative densities and the target unit cell size (i.e. the idealized dimensions).

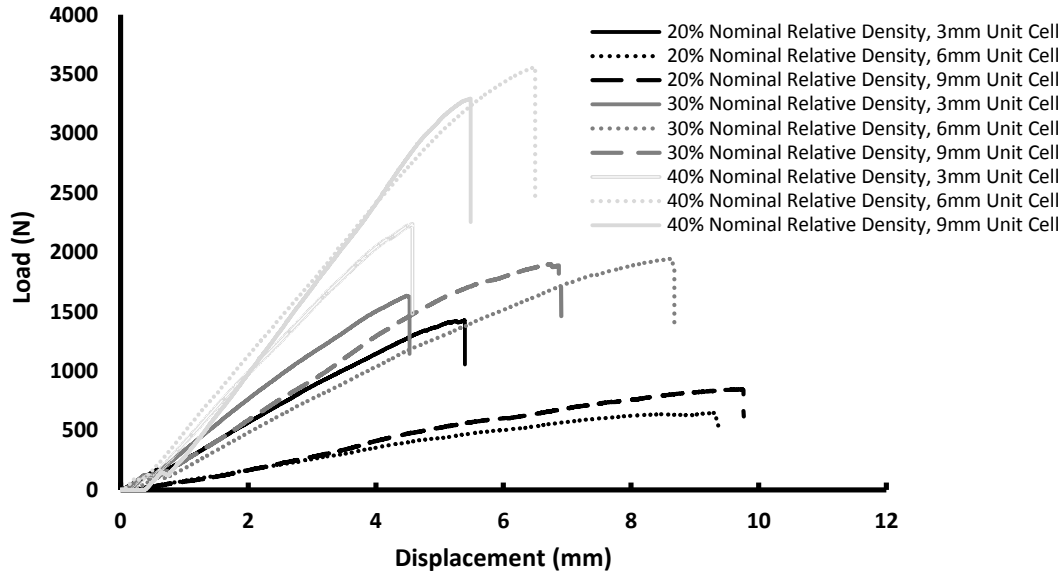


Figure 5.18: Representative load-displacement curves for each of the nine specimen types.

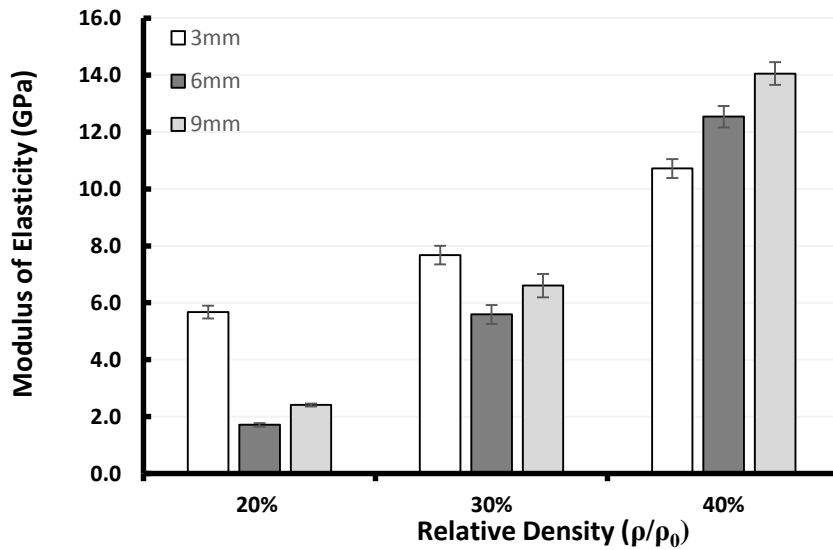


Figure 5.1: Graph showing the modulus of elasticity for different nominal relative densities and nominal unit cell sizes. Error bars indicate 95% confidence interval.

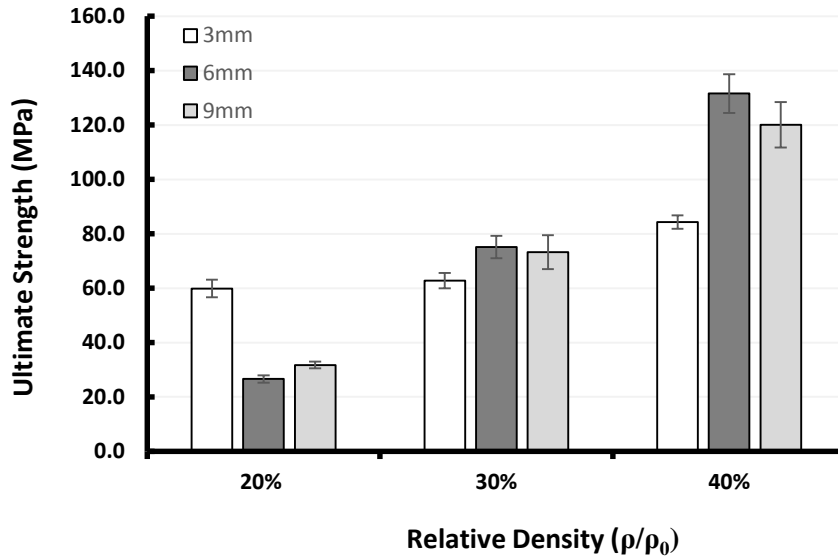


Figure 5.2: Graph showing the ultimate strength for different nominal relative densities and nominal unit cell sizes. Error bars indicate 95% confidence interval.

Significant differences in flexural modulus and ultimate strength were detected among the three different unit cell sizes ($F < 0.001$). Within the 20% target relative density group, 3 mm unit cell samples had a higher flexural modulus and strength than 6 mm or 9 mm unit cells ($p < 0.001$). The difference in flexural modulus and ultimate strength between the 6 and 9 mm samples was less pronounced ($p = 0.003$). Within the 30% target relative density group, significant differences in flexural modulus ($F < 0.001$) and strength were detected ($F = 0.002$). The 3 mm unit cell group exhibited lower ultimate strength than the 6 and 9 mm groups ($p = 0.001$ and $p = 0.004$), but there was no difference between the 6 and 9 mm groups ($p = 0.5289$). Significant differences in both strength and flexural modulus were evident across all unit cell sizes in the 40% target relative density group ($F < 0.001$). The

variability in the relative differences between the measured relative density and the CAD model relative density was much higher for the 20% target relative density group (SD = 0.016) as compared to the 30% and 40% target relative density groups (SD = 0.009 and 0.003, respectively). These data are presented in Table 5.2.

Table 5.2: Tabulation of experimental data for flexure specimens with various relative densities and unit cell sizes. Values indicated are mean \pm 1 standard error.

Unit Cell Size (mm)*	Relative Density*	Measured Relative Density	CAD file Strut Diameter (μm)	Measured Strut Diameter (μm)	Flexural Modulus of Elasticity (GPa)	Flexural Ultimate Strength (MPa)
3	0.2	0.246 \pm 0.004	454	559 \pm 25	5.67 \pm 0.22	59.87 \pm 3.26
3	0.3	0.267 \pm 0.005	575	590 \pm 36	7.67 \pm 0.33	62.79 \pm 2.86
3	0.4	0.277 \pm 0.007	722	573 \pm 30	10.72 \pm 0.33	84.28 \pm 2.50
6	0.2	0.114 \pm 0.002	905	777 \pm 35	1.71 \pm 0.06	26.59 \pm 1.32
6	0.3	0.184 \pm 0.003	1153	1003 \pm 15	5.59 \pm 0.33	75.16 \pm 4.11
6	0.4	0.263 \pm 0.002	1408	1229 \pm 25	12.54 \pm 0.38	131.60 \pm 7.11
9	0.2	0.120 \pm 0.001	1361	1172 \pm 26	2.41 \pm 0.05	31.75 \pm 1.24
9	0.3	0.204 \pm 0.001	1732	1595 \pm 38	6.60 \pm 0.41	73.26 \pm 6.22
9	0.4	0.291 \pm 0.003	2096	1959 \pm 23	14.05 \pm 0.40	120.08 \pm 8.31

*indicates a nominal/categorical value

To evaluate the influence of both relative density and strut size on the measured mechanical properties, A 2-parameter mixed effects model (shown in Equation 3.7) was used to model the results.

Equation 5.4:

$$Y_{ijk} = \mu + \alpha_i + \beta_j + (\alpha\beta)_{ij} + \varepsilon \varepsilon \sim \mathcal{N}(0, \sigma^2)$$

Where α represents the relative density, β represents the strut diameter (μm) and the error terms, ε are independent and normally distributed, since ANOVA indicated a possible correlation between strut size and relative density, a correlation effect was included in the model. The mixed effect model results explained 90% of the variability for predicting the flexural modulus of elasticity and 78% for the ultimate strength. The strut diameter and correlation were not significant in either model ($t = 0.579$ and 0.090 , respectively for modulus and $t = 0.808$ and 0.471 for strength). The effect of relative density was significant for the modulus ($t = 0.001$) and strength ($t = 0.026$) predictions.

Figure 5.21 shows a plot of the relative density and the relative flexural modulus. The flexural modulus data were fitted to the Ashby-Gibson relation, C_1 was determined to be 1.082 and n was 1.9026. For the model of ultimate strength shown in Figure 5.22, the value best fit for C_1 was 0.6001 and n was 1.3106. Mean Knoop hardness ranged from 364 HK for the largest strut size (9 mm, 40% relative density target group) to 370 HK for the smallest strut size (3 mm, 20% relative density target group).

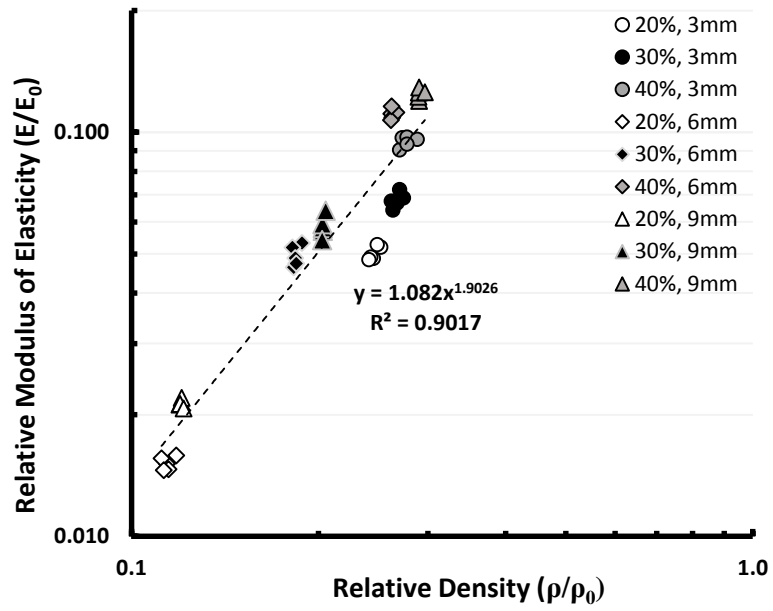


Figure 5.21: Plot of relative flexural modulus versus relative density.

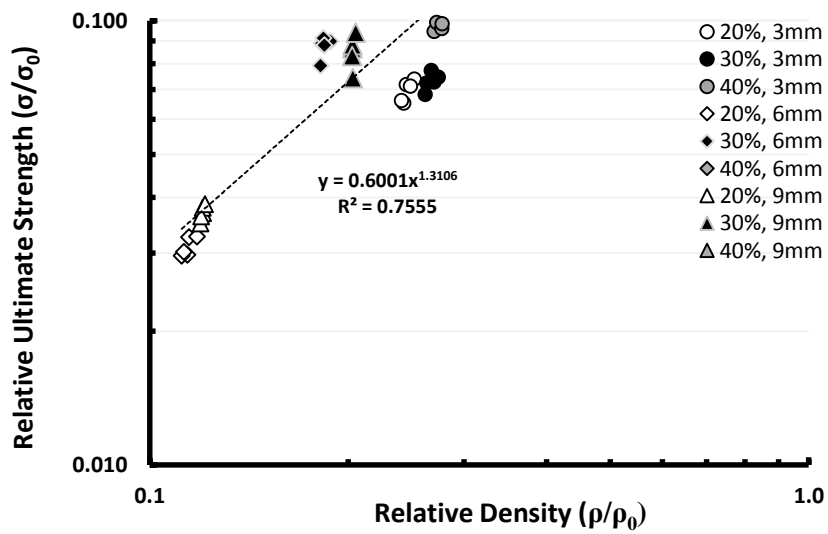


Figure 5.22: Plot of relative strength versus relative density.

5.4 Discussion

In this study, the variability in the relative difference between the modeled and measured struts was much higher for samples with small beam thickness, indicating that the robustness of the Gibson – Ashby model as a predictive tool for designing non-stochastic lattice structures is limited in part by the resolution of the additive machine. For the EBM machine configuration and process parameters used in this study, the minimum attainable strut size is a function of melt parameters including, strut angle, and powder size, and these data suggest a lower limit of between 0.3 and 0.5 mm.

The reported modulus values for cortical bone vary broadly from approximately 7 to 34 GPa, and the reported the tensile elastic modulus of cancellous bone ranges from approximately 69 to 349 MPa (An and Draughn, 2010). The modulus of bone varies depending on location subject age, pathology, etc. Given this wide target range, the challenge lies not in fabricating mesostructures with properties similar to bone, but rather in approximating patient specific bone properties. To date no model reported for EBM produced Ti6Al4V has demonstrated this necessary level of accuracy. The results presented here show significant variation between the CAD model and the final geometry, particularly for the smaller strut sizes. In this study, the coefficient of variation in measured modulus of elasticity was 54% among the samples with a target relative density of 20%, and 11.7% for the samples with 40% target relative density.

Previous literature often relied on compression testing to determine the intensive properties of similar EBM fabricated mesostructures. Ashby (2000) assumed that the compressive modulus and flexural modulus are interchangeable. However, because of the complex loading conditions present in flexure, particularly those of shear and tension, this study has focused on direct measurement of the flexural properties. Further studies will be required to determine if a compressive testing can be used as an accurate predictor of flexural properties for these structures. In addition, other studies have noted that the rapid solidification of the melt pool results in increased hardness in mesh structures fabricated with EBM (Murr et al., 2010). Cormier et al. (2004) previously demonstrated that thin walled Ti6Al4V components fabricated with EB exhibit a refined microstructure as compared to thick components. In this study, no difference was detected in the Vickers hardness of the sectioned and polished struts indicating that this factor should not influence the relationship between relative density and strength as strut size is varied.

Much of the literature has focused on using EBM for the optimization of tissue ingrowth into scaffolds; the non-stochastic unit cell geometries frequently reported in the literature have pore sizes measuring < 1 mm (often 300 to 800 μm) and strut sizes measuring < 0.5 mm (Haslauer et al., 2010; Weiding, Jonitz and Bader, 2012; Heintz et al., 2007; Ponader et al., 2010; Thomsen et al., 2009). The scale of these geometries often exceeds machine resolution resulting in both spatial and mechanical discrepancies between idealized CAD geometries and physical parts. This has complicated attempts to conduct predictive

modeling. Conflicting objectives have arisen between optimizing the mesh geometries and relative densities for bone ingrowth and for approximating the patient specific mechanical properties of appendicular bone.

For the repair of large segmental defects, such as in limb sparing, where relatively high axial and bending loads are anticipated, larger strut sizes may be necessary. One potential solution may rely on functional grading of cell geometries, providing osseointegration on some outer surfaces while utilizing larger struts or cells for mechanical optimization. This concept was briefly explored by Murr et al. (2010). In addition, the effect of strut angle relative to the build plane on mechanical properties was investigated by Cansizoglu et al. [6]. Small diameter struts ($< 700 \mu\text{m}$) with an angle to the build plane of less than 20° showed catastrophic reductions in mechanical properties. For instance, the strut angle relative to the build plane of the hatch unit cell of Heindel et al. was 0° (2008). In part, this reduction in strength was thought to be a result of the relatively large (with respect to the strut diameter) layer resolution of powder bed additive manufacturing. At the time of the Cansizoglu report, EBM layer thicknesses were typically $100 \mu\text{m}$, but more recently layer thicknesses of $50 \mu\text{m}$ or less are routinely produced. In the study by Wieding, Jonitz and Bader (2012), a twofold increase in modulus was noted for samples with diagonal struts over the hatch structures. The authors do not speculate on the source of the discrepancy, however, the low angle of the struts relative to the build plane could have significantly degraded the properties. A rhombic dodecahedron was chosen for this study partly because it is

particularly well suited for manufacturing using a wide variety additive processes, including EBM. This is because the structure can be oriented such that every strut is oriented at an angle of $\sim 35.3^\circ$ thus minimizing this aspect of variability. In addition, rhombic dodecahedra are orthotropic (Babaee et al., 2012). Each face of the unit cell is a rhombus with angles of $\sim 70.5^\circ$ and $\sim 109.5^\circ$. Each edge of a rhombus is shared by three neighboring unit cells. In lieu of analytical or computational approaches, the Gibson-Ashby model serves as a reasonably good approximation of the flexural properties of the rhombic dodecahedron structures tested here. At the design stage, however, great care must be taken to adjust CAD model geometries to achieve the desired relative densities. This could be done by either increasing the strut diameters in the CAD file or by altering the process parameters as demonstrated by Heinel, Körner, and Singer (2008). For EBM fabrication, this is particularly critical for strut diameters of 500 μm or less. Previous work has shown that the size of the unit cell does not impact the relative density (Ashby, 2000) so this constraint could potentially be relaxed without significantly influencing the functional characteristics of the mesh.

The removal of powder from the samples is another important consideration for testing additively produced metal foams. While this important step could clearly influence mechanical test results, especially the compressive properties, cleaning methods were not reported in any of the studies reviewed. In this study we have followed the protocol recommended by the manufacturer, Arcam, using the powder recovery system. This system requires line of sight and sufficient kinetic energy for the ballistic particles to reach and

dislodge the sintered powder within the metal foam. For small pore sizes ($< 400 \mu\text{m}$), relatively thick samples ($> 2\text{mm}$), or trabecular/quasi-stochastic structures, powder removal with this method is extremely challenging. In this study, cleaning the powder from the meshes was particularly challenging for samples with 3 mm unit cells and 40% target relative density, taking approximately 15 minutes per sample at 8 Bar blasting pressure. Notably, this unit cell geometry is roughly 5 times larger than the hatch structure produced by Heinel et al. (2008), Weiding, Jonitz and Bader (2012) and Haslauer et al. (2010) and roughly three times larger than the pore sizes reported by Parthasarathy et al. (2010).

Previous studies have reported an influence of strut diameter on the mechanical properties, in particular strength (Parthasarathy et al., 2010). Indeed, when evaluated as independent parameters, the effect of strut size on strength and modulus is evident. However, the statistical analysis presented in this study, which included this as a correlation effect, does not support the same conclusion. As demonstrated by Gibson and Ashby (1982) in the derivation of relative density, it is closely correlated with strut dimensions, being: $\rho/\rho_0 \propto t/l$. Where t is the strut thickness and l is the length. The results in this study indicate that the large variability in the strut diameters (when cells and struts are small) may be the contributing factor. Very few studies have considered the fatigue properties of EBM fabricated mesh structures, a notable exception is Hrabe et al. (2011). For applications where fatigue performance is critical, beam diameters should be carefully chosen to be well within

machine capability. For limb sparing applications, future studies will need to focus on evaluating the fatigue characteristics of high aspect ratio mesh structures.

This study evaluated the flexural properties of a sample populated with a single design of unit cell of various sizes and built in a single orientation. While it has been demonstrated that size effects do not typically play a significant role in the determination of the model constants (Ashby, 2000) when the cell size is small relative to the sample size, no attempt was made in this study to vary the size of the specimen to control for the number of cells per sample. In some of the designs, particularly the 9 mm target unit cell size, the cell size would be considered very large, to the point where edge effects and boundary conditions would be expected to influence the results, although this limitation does not seem to be reflected in the data.

The vertical ZYX build orientation was chosen for this study since most additive processes have relatively small cross section build platforms, therefore it was speculated that most segmental defect repairs (with high aspect ratios) will need to be fabricated in this orientation. Similarly, the sample dimensions used in this study were chosen to closely simulate the dimensions of a typical graft for canine limb sparing while at the same time respecting the required maximum ratio of beam length to height required to generate pure bending deflection. The Bernoulli-Euler beam theory requires a ratio > 10 . Here, the ratio of beam length to beam height ratio was 16.7. In addition, the dimensions were constrained by

the requirement of being divisible by the unit cell dimension to minimize edge effects and to prevent asymmetry in the sample design. The physical constraints on specimen size and orientation described should be carefully factored into implant design.

The fabrication of low stiffness structures using EBM shows significant promise. The flexure test results shown here suggest that implants could be fabricated that are mechanically suitable for graft repairs of large segmental defects. Ti6Al4V and other biocompatible alloys fabricated using EBM are fully dense with properties closely matching the values found in cast and wrought materials with similar composition (Murr et al., 2009). High beam scanning speeds enable the process to maintain high temperatures greatly reducing thermally induced stresses. Further, the vacuum environment prevents oxidation and greatly reduces the contamination risk. Unlike other metal foam production processes, direct metal additive manufacturing enables a comparably high degree of control over cell geometry and mechanical properties. However, the results of this study reinforce the notion that for the small pore sizes required for bone ingrowth, the limitations of EBM process capability result in variability that undermines the predictive capabilities of the Gibson-Ashby model. For larger unit cell sizes, close to 9 mm, edge effects may become more significant. Optimal graft design geometry must therefore lie between these extremes.

6.0 EXPERIMENTAL EVALUATION OF KEY IMPLANT FEATURES OF THE PROXIMAL ENDOPROTHESIS FACILITATED BY ADDITIVE MANUFACTURING

Canine limb sparing has been associated with a high failure rate. Fatigue failure of screws may be related to stress concentration resulting from the large difference in stiffness between the endoprosthesis and the bone. Additive manufacturing technologies such as electron beam melting or laser melting may facilitate improvements in endoprosthesis design. Decreasing the stiffness of the implant may decrease the stress concentration at the bone-implant interface.

6.1 Background

Additive manufacturing facilitates precise control of implant mechanical properties, surface topography, and geometry; without incurring the high costs associated with production tooling and setup (Horn & Harrysson, 2012). Patient specific implants designed via 3D medical imaging data sets (i.e. computed tomography, magnetic resonance imaging, etc.) may provide a better anatomic fit and allow orthopedic procedures to be carried out with little or no modification to the underlying bone structure thereby improving the bone-implant interface (Harrysson & Neyfeh, 2007). Additively manufactured bone plates that match the surface contours of the bone do not require pre-bending and can significantly improve accuracy while reducing surgery times (Marcellin-Little, Harrysson & Cansizoglu, 2008). Intervertebral disc implants; fabricated with a laser melting process, with conformal

bearing surfaces showed increased contact area (45% vs. 10%) and stiffness (9.09 kN/mm vs. 3.83 kN/mm) compared to those with flat bearing surfaces (de Beer et. al, 2012). Many reports have highlighted case studies, commercial demonstrations or simulations of conformal implants (Koptug, et al., 2013, Zhou et al., 2010, Ciocca et al., 2012, Bagaria et al. 2011), yet controlled biomechanical evaluations are absent from the literature, particularly when plating appendicular bones. Further, the long term outcomes of such procedures have not yet been reported. Before the biologic question of clinical outcomes can be raised, the question of whether or not conformal plating results in a clinically relevant difference in contact area and contact pressure must first be addressed.

Screw location and orientation can also be optimized from CT data to avoid osteoporotic regions, or facilitate multi planar stabilization (Dobbe, et. al, 2013). A study by Kohles et al. (1994) showed improved stiffness using double plate (orthogonally oriented) constructions over single plate constructions. The layer-wise deposition/consolidation of biocompatible metals enables the fabrication of shapes and geometries that would otherwise be impossible to manufacture, such as engineered lattice mesostructures which can be optimized for the specific requirements of the implant such as strength, bone ingrowth, and the reduction/elimination of stress shielding (Harrysson et. al, 2008; Cansizoglu et al., 2008). The use of additively manufactured lattice structures for the repair of segmental defects has been investigated by Razi et al. (2012). Finite element modeling of compressive loading in cylindrical structures populated with various unit cell geometries to demonstrate that porosity

and geometry could be optimized to produce strains sufficient to stimulate bone healing while maintaining the mechanical integrity of the implant. Limb sparing presents a unique set of clinical challenges, in many cases the segmental defect measures 40-60% of the host bone length (Liptak et al. 2006). Clinical data suggests that implant configuration and stiffness may play a role in long term biomechanical outcomes. Without tooling and traditional manufacturing design constraints, implants can also be fabricated as monolithic structures that incorporate both solid and porous structures (Murr et. al, 2010). However, despite a growing body of literature, the purported benefits of patient-specific implants produced with direct metal additive manufacturing have not been widely investigated. This study seeks to quantify the effects of plate contact area, plate orientation and implant stiffness on the measured mechanical properties of constructs, in the context of canine radial limb sparing endoprostheses. For limb sparing at the distal radial site in canines, an alternative that has not yet been investigated is a monolithic endoprostheses that incorporates a low stiffness implant with conformal and multidirectional plate fixation.

A full factorial experiment of variants representing the proximal portion of limb sparing implants was designed to elucidate the effects of plate contact area, plate orientation and implant stiffness, on implant mechanical characteristics. Implants were designed with either; (1) a conformal or contoured (bent) plate design, (2) cranial, medial or bi-planar/orthogonal plate orientations and, (3) solid or a non-stochastic porous graft mesostructure. Implants were fabricated in high-strength titanium alloy, Ti6Al4V, using the

EBM (Arcam, Mölndal, Sweden) process of direct metal additive manufacturing. The implants were then affixed to composite analogs of a patient specific radius designed in a previous study (Horn et. al, 2014; Little et al., 2012) and subjected to non-destructive biomechanical testing in three modes; axial, cantilever and torsional.

6.2 Materials and Methods

6.2.1 Fabrication of new analog radii

The analog radii fabricated for this study were derived from scans of a 16 month old male dog, mined from the North Carolina State University College of Veterinary Medicine medical imaging database (eFilm Workstation V3.3). From these data the left radius was segmented and reconstructed into voxelized models of the cortical and cancellous bone following the methodology described in Chapter 3. These models were converted to standard tessellation format (.stl) using Materialise Mimics (Version 17.0). The fabrication analog radii followed the procedure discussed previously (Horn et al., 2014). The cortical bone simulant was mixed with a fiberglass to epoxy ratio of 0.30 by volume. Two molds were used to fabricate 80 replicas of the radius. Three batches of resin matrix material (Fiberglast Corporation, Series 2000 Epoxy and 2020 Hardener) were mixed in a 100:23 ratio (by weight). Sprue and mold features were removed from the cured bone analogs by sawing and

the resulting surfaces finished by hand sanding (220 grit wet/dry sandpaper). The mold ID, epoxy batch ID, and mass of each sample were recorded. Mass was measured using a draftshield protected scale (Ohaus Adventurer, Parsippany, NJ) and recorded to the nearest 0.001 g. Each analog radius was also subjected to non-destructive four-point flexure tests to a load of 500 N with a crosshead speed of 1.5 mm/min. The major span was 139.7 mm and the minor span was 50.8 mm. Three loading events for each sample were recorded and the stiffness was calculated from the slope of the load deformation curve of the last event.

6.2.2 Design of test implants and features

Test implants were designed to represent the proximal and segmental portions of the limb sparing endoprostheses. Five plate configurations were selected to evaluate the influence of plate location and contact. Three of these consisted of plates with a standard limb sparing plate (commercially available from VOI, Veterinary Orthopedic Implants, St. Augustine, FL) cross section including; a cranial plate, a medial plate, and a cranial plate combined with a medial plate. A fourth group was a conformal cranial plate, this plate was designed to precisely match the surface contours of the bone subject to the area moment of inertia at any point along the longitudinal axis being equivalent to the standard plate at the same position. Each plate was designed with six holes for fixation. In order to account for the necessary increase in the number of screws associated with biplanar plating, an additional cranial-medial configuration was designed with a total of six holes (three per plate).

To evaluate the effect of the stiffness of the segmental defect repair, three configurations were selected; 0.2, 0.4 and 1.0 relative density. The 0.2 and 0.4 nominal relative density sections were populated with unit cells consisting of 6 mm open cell rhombic dodecahedra validated in Chapter 5 (Horn et al. 2014).

The virtual model of the canine radius was converted from .stl format to a NURBS surface model using the Solidworks mesh plugin (Solidworks 2013, Dassault Systèmes, Waltham, MA) with a maximum allowable deviation of 0.1 mm. The central longitudinal axis of the radius was identified from the centroid of two section planes 25 mm from the distal and proximal epiphyses. Orthogonal planes generated from this axis were used to locate the test implant/plate geometry. The CAD model was osteotomized 98.0 mm proximal to the styloid process (48% of the bone length) and orthogonal to the central axis to create the mating surface for the proximal end of the bone graft/spacer. Where possible, and appropriate, dimensions from the commercially available (VOI) limb sparing endoprostheses were used as a guideline for design. The cross section of the cranial plate was designed from measurements of the commercial plate (3.84 mm thick, 11.94 mm wide, ventral radius 28.56 mm). The placement and alignment of the plate on the cranial surface of the bone was determined with the assistance of veterinary surgeons (Marcellin-Little and Lascelles). Bone plates are typically contoured manually to best match the surface of the bone (Schatzker, 2005). The repeatability of manual contouring has not been investigated in the literature, therefore contouring was implemented in the CAD environment. The extrusion path for the

contour profile was divided into 6 axially constrained parametric segments, spaced 11.99 mm apart, with nodes located at the midpoint between two screw holes such that the segments are free to rotate cranially and caudally about these points. The plate was not contoured medially or laterally. Cranial screw holes for 3.5 mm cortical bone screws with spherical countersinks (per the dimensions described in ASTM F543) were placed in the center of each segment and normal to the plate surface. Figure 6.1 illustrates the cranial plate placement and contouring.

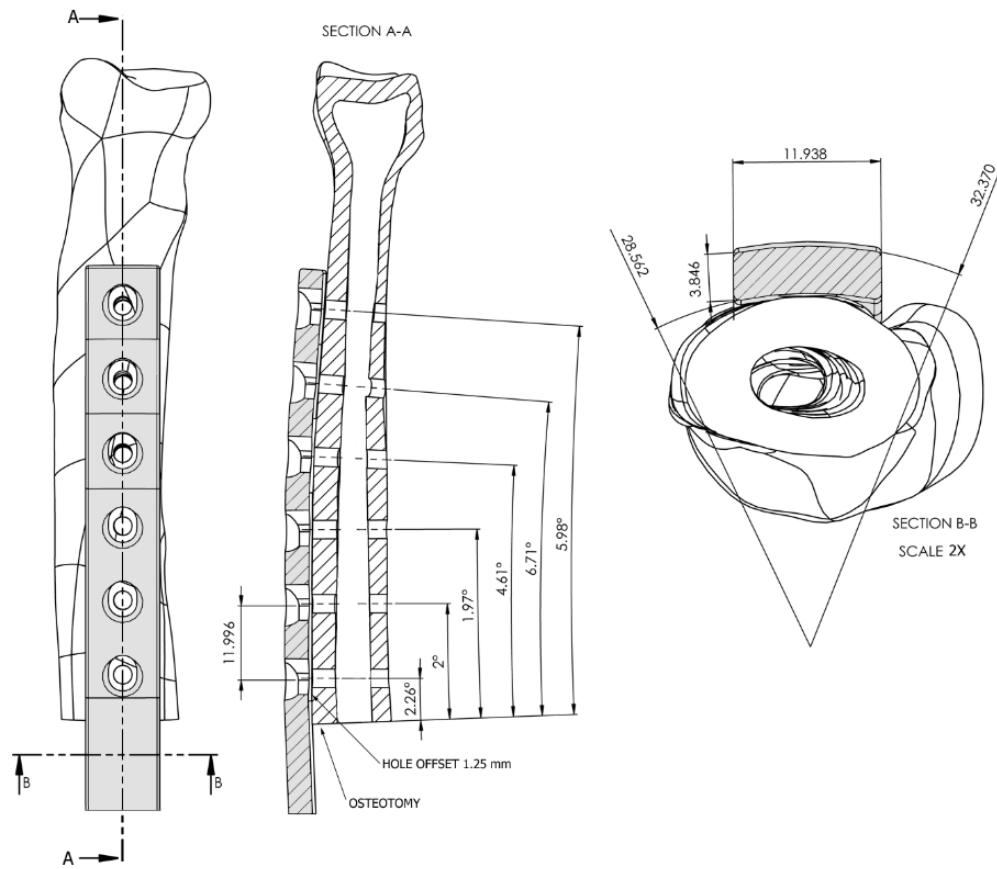


Figure 6.1: Schematic showing the placement and contouring of the proximal portion of the standard cranial limb sparing plate.

The same method was used to define the contouring of the medial plates. The medial plate was designed with second moment of inertia equivalent to that of the cranial limb sparing plate in the cranio-caudal cantilever bending mode (3.81 mm thick, 11.94 mm wide, lateral radius 28.58 mm). The medial plate screw holes, located in between the cranio-caudal holes, lie along the neutral axis with minimal contribution to plate stiffness. The deflection under load of the medial plate design was confirmed to be equivalent to the cranial plate design with finite element modeling (Solidworks, 2013) in cantilever bending, rigidly fixed at the base (Figure 6.2). The conformal cranial plate was designed by projecting the bounding geometry of the standard plate onto the surface of the radius model, this 11.94 mm wide surface was then offset 3.81 mm. The screw hole locations and angles are identical to those of the contoured plate design.

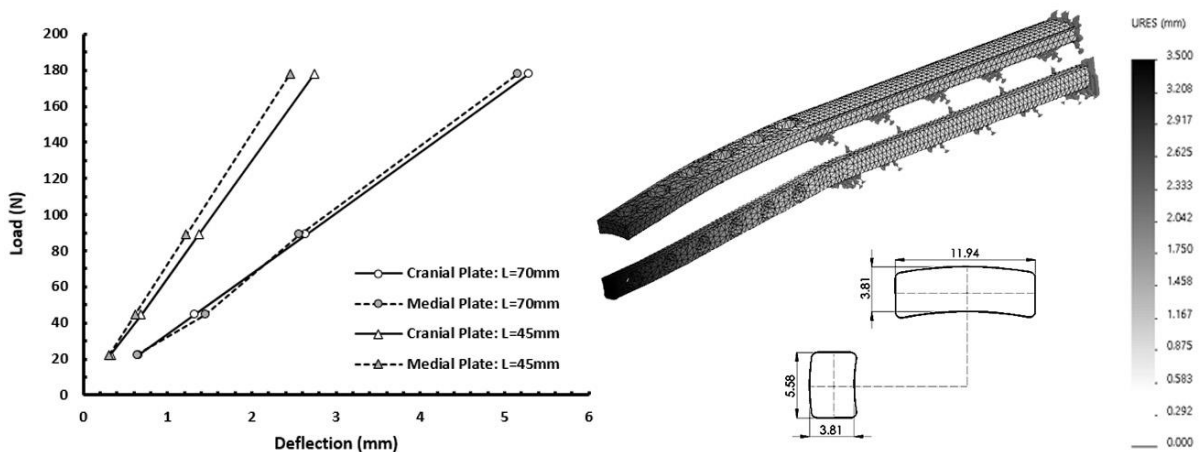


Figure 6.2: Finite element results showing plate deflection at two locations for both cranial and medial contoured designs.

The VOI limb sparing plate spans the segmental defect and is typically fixed to the graft with machine screws. Preliminary tests indicated that the stiffness of the plate dominated the stiffness of the entire construct particularly when a low stiffness graft material was investigated. In the current design, in order to decouple the effect of plate design/placement from the effect of graft stiffness, plates do not span the segmental defect, but are instead blended into the graft over an 18.0 mm distance. This facilitates plate contact with at least six unit cells on the underside of the plates.

The cross section of the graft segment was designed as an ovoid in order to encompass the bounding geometry of the original (VOI) defect repair block and both the cranial and medial plate cross sections. Figure 6.3 shows the dimensions of the cross section, and identifies open boundaries. The ovoid consists of a circle ($R = 9.755$ mm) tangent to an ellipse with the same minor radius and a major radius, a , (in the mediolateral, or “xx” orientation) of 12.253 mm. The moment of inertia, I_{xx} for craniocaudal bending, can be expressed as:

Equation 6.1:

$$I_{xx} = \int y^2 dA$$
$$I_{xx} = \frac{\pi}{4} (r^4 + r^3 a)$$

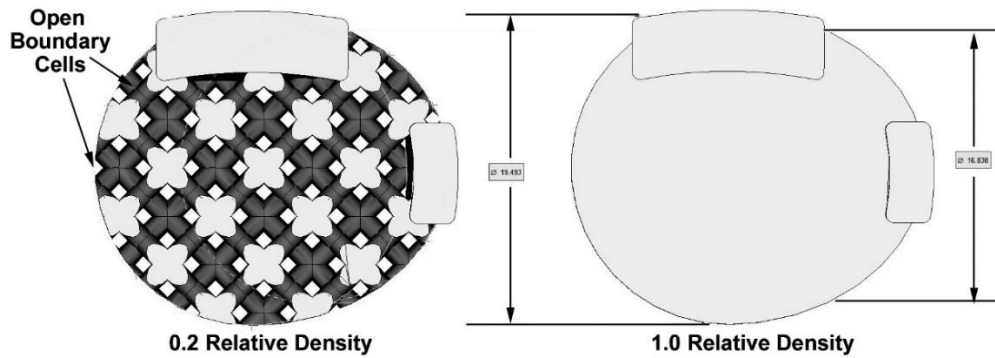


Figure 6.3: Illustration showing the ovoid cross section of the graft segment. Open boundaries of lattice unit cell structures are identified (left).

To validate the reduction in stiffness of the repair segment associated with reductions in relative density, and to ascertain the influence of free boundary cells, a preliminary experiment was conducted. Five graft segments, 165 mm in length, with the ovoid cross section were populated with rhombic dodecahedron unit cells with relative densities of 0.1, 0.2, 0.3, 0.4, and 1.0. The results of Chapter 5, reported by Horn et al. (2014), show the influence of relative density and strut size on the flexural properties of prismatic specimens populated with the same structure. These samples, shown in Figure 6.4, were arranged in an EBM build volume in the ZYX orientation and fabricated in Ti6Al4V alloy using the Arcam EBM process (using standard network parameter sets for SP2). Sintered powder was removed from the samples with abrasive blasting, and powder removal was confirmed with visual inspection. The specimens were loaded to failure in four-point flexure with a crosshead speed of 1.5 mm/min. Loading was applied in the cranial-caudal direction (across

the minor diameter). The major span was 139.7 mm and the minor span was 50.8 mm. From these data, the 0.2 and 0.4 relative density meshes were selected for incorporation into the test implant designs.

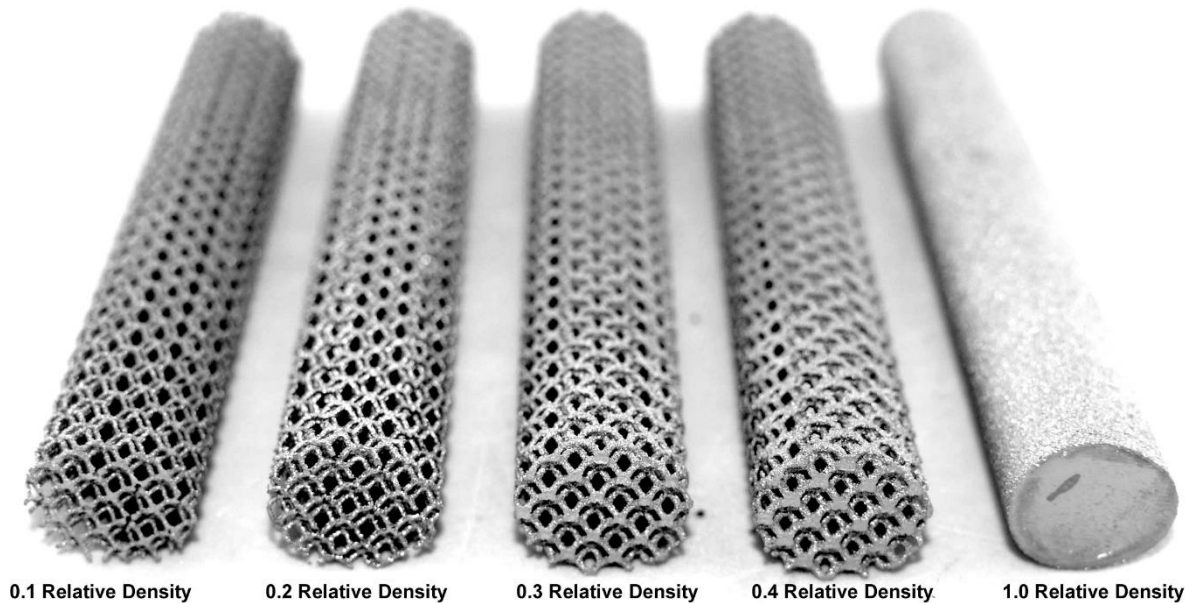


Figure 6.4: Photograph showing EBM fabricated, Ti6Al4V test specimens with varying relative density and ovoid cross section.

Based on the test results (shown in section 6.3.2), the 0.2, 0.4, and 1.0 relative density sections were selected for incorporation into the test implant geometries. These graft segments were combined with the five plate configurations. A dovetail boss was added to the distal end of the test implant to facilitate attachment to the test fixture. The solid models were converted to .stl format with a minimum feature size of 0.05 mm. The rhombic dodecahedra mesh structures were applied to the segmental portion of the model with

Boolean operations. Further, a unique identifier was engraved into the bottom of each sample, the nomenclature is as follows :

First Digit: Plate Orientation (B= Biplanar, C= Cranial, M= Medial)

Second Digit: Plate Contact Type (S=Standard Contoured, C=Conformal)

Third Digit: Number of Screws (6 or 12)

Fourth Digit: Mesh Type (A= Solid, B= 0.4 RD, C=0.2RD)

Fifth Digit: Replicate Number (1-5)

For instance, BS12B-3 is the 3rd replicate of a bi-planar, standard plate with 12 holes and a 0.4 relative density mesh. Figure 6.5 shows an illustration of the test implant designs.

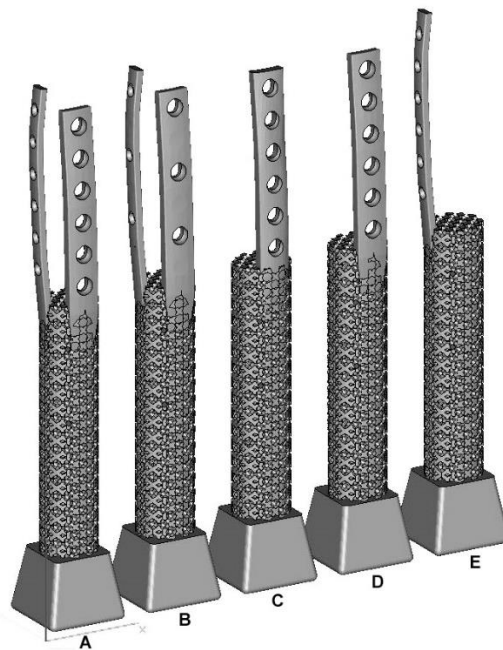


Figure 6.5: Screen capture illustrating 5 plate configurations (0.4 relative density mesh shown); biplanar with 12 holes (A), biplanar with 6 holes (B), cranial-conformal (C), cranial-contoured (D), and medial (E).

6.2.3 EBM fabrication of test implants

Three test builds were carried out in an Arcam A2 EBM machine to develop/verify the melting parameters and orientation for producing the test implants. Samples were fabricated with varying densities of supporting structures (necessary for downfacing surfaces). This was of particular concern in the screw holes. Measurements taken of the screw hole geometries showed no discernable reduction in accuracy as a result of (1) limiting and (2) removing the supporting structures. The 75 test implants were then fabricated from Ti6Al4V gas atomized powder (Arcam) with a specified size distribution from 45 to 105 μm . Prior to processing, the chemical makeup of the powder was analyzed using inductively coupled plasma analysis (ICP), hydrogen and oxygen content were measured with combustion (LECO Corporation, St. Joseph, MI-ASTM E1019). These results are shown in section 5.3.1 Powder Analysis. Three separate batches of implants were required since only 25 fit in each build platform (using a 190mm starting plate). To mitigate the risk of intra and inter-build variation, a random number generator (Microsoft Excel 2013) was used to assign each of the implants to a build (1-3). The same random number generator was then used to assign each of the implants to a position within the build (1-25), shown in Figure 6.6. Each build required 60 hours to complete with 12 additional hours of cool-down time.

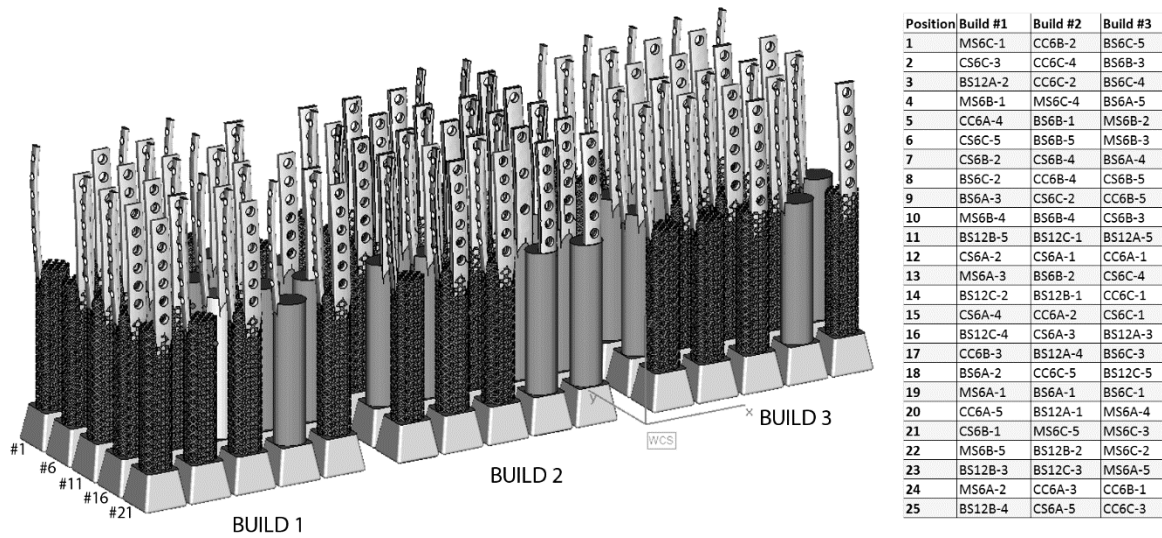


Figure 6.6: Screen capture illustrating the random assignment of samples to builds 1-3 and, subsequently, to positions 1-25.

Upon removal, the samples were encased in lightly sintered titanium powder that was removed by abrasive blasting using additional Ti6Al4V powder as media. Powder removal was observed by visual inspection with the aid of a white back light. Figure 6.7 shows the EBM fabricated test implants from build 1.



Figure 6.1: Photograph showing the EBM produced test implants from build 1.

6.2.4 Drilling, tapping and cutting of analog radii

To assist in the consistent cutting, drilling and tapping of the analog radii, a jig was designed from the solid models of the test implant, shown in Figure 6.8. Marcellin-Little et al. previously demonstrated the use of additively manufactured drilling and cutting guides using a thermoplastic extrusion process (Marcellin-Little, Harrysson, & Cansizoglu, 2008). The use of patient specific cutting and drilling guides for total knee replacement surgery was reviewed by Krishnan et al. (2012).

To position the drill guide bushings, the axis for each screw hole has been extended from the normal surface of the contoured plate design. The distal-most holes on the cranial and medial plates were intentionally offset 1.0 mm proximal to the true locations to assure compression between the analog bone and the test implant. A positive draft cavity of the ventral surface of the radii was created utilizing the styloid process as a locating datum. From these known references, a rigid frame was designed around the fixture that incorporated clamping features and two sets of pinned removable blocks for drilling and tapping bushings. For the location and angle of the osteotomy, a slot (from the CAD reference feature) was cut through the frame and lined with t-slotted stainless steel guides to support a reciprocating saw.

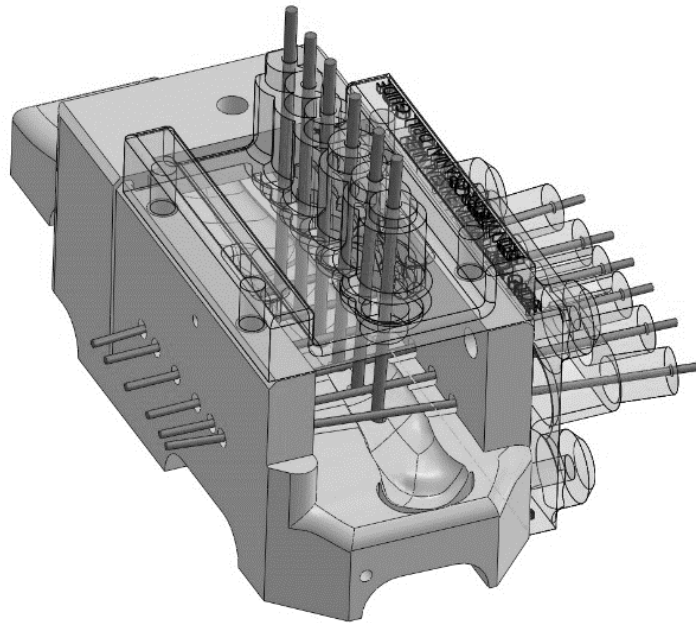


Figure 6.8: Solidworks model of the drilling and cutting guide. The orientation and position of drill axes are shown as cylinders.

The device was fabricated using an Objet Connex 350 (Stratasys, Eden Prairie, IN) . VeroWhite™ material, (acrylic monomer/oligomer) was used to produce the rigid portions of the device, while a 5 mm thick skin offset from the ventral surface of the analog radii was fabricated using an elastomeric material, Shore 60A Tango-Plus™ (urethane acrylate oligomer). The compliance of the elastomer accommodated the geometric variation in the radii associated with the manufacturing process while at the same time facilitating consistent location within the fixture. Analog radii, randomly assigned to each treatment (plate orientation, plate configuration and stiffness), were located in the fixture and clamped with a bolt (Figure 6.9). The bolt was angled 5° to create an interference with the proximal surface of the styloid process.

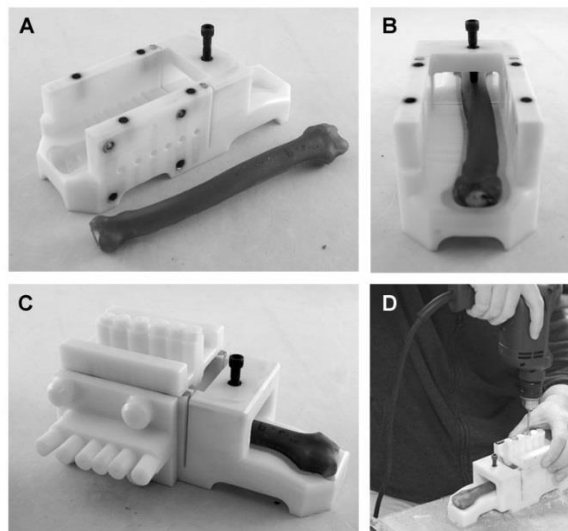


Figure 6.9: Photographs showing; the cutting and drilling guide with composite analog radius (A), the clamped and located radius (B), placement of the drilling guides on the cranial and medial planes (C) and drilling of cranial holes (D).

Cranial holes were drilled first, starting with the distal most hole using the cranial drill guide and a 2.5 mm bone drill at low speed (DePuy SynthesVet 310.25). The cranial drill guide was replaced by the cranial tap guide. Cranial holes were tapped with a 3.5 mm x 1.25 mm cortical bone screw tap (DePuy SynthesVet 311.32). For the medial and biplanar scenarios, the same process was repeated for the medial side using a 2.0 mm bone drill and a 2.7 mm x 1.0 mm cortical bone screw tap (DePuy SynthesVet 310.19 and 311.25 respectively). Using the metal cutting guide, the radius was osteotomized using a stainless steel hand saw (2.0 mm kerf, 0° set, 1.5 mm pitch). Figure 6.10 shows examples of each of the radii.

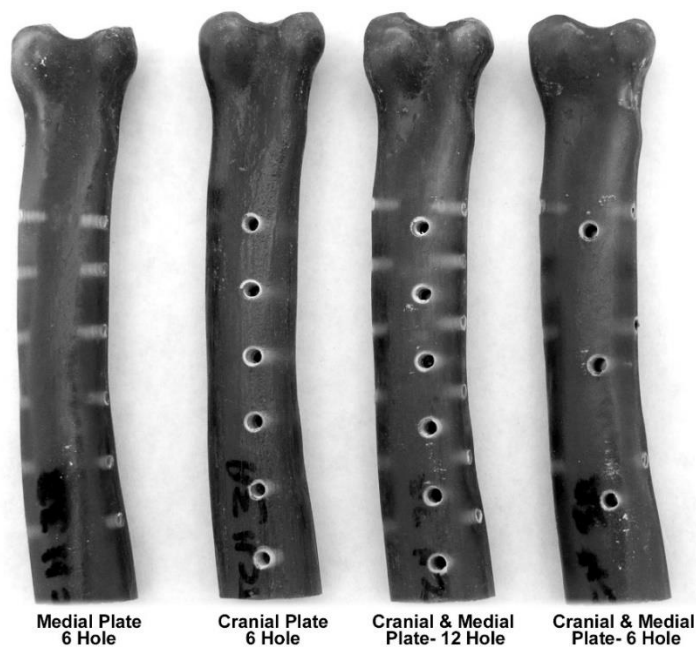


Figure 6.10: Photograph showing the cut, drilled and tapped proximal radii corresponding to each implant configuration.

6.2.5 Measurement of plate contact

Plate contact area and pressure was measured on implants with a cranial contoured plate, the cranial conformal plate, and the cranial portion of the biplanar plate designs, using pressure measurement film (Fujifilm prescale). Mono-sheet prescale film MS (10-50 MPa) and two-sheet LW (2.5-10 MPa) were cut to the exact width and length of the ventral surface of the bone plates. Hole diameters match the minor/root diameter of the 3.5 mm cortical bone screws. The film was cut with a CNC laser cutter (Universal Laser Systems vls4.60, Scottsdale, AZ) with a laser power of 24.5W, 1000 pulses per inch (39.37 pulses/mm), and a linear travel of 75 in/s (1905 mm/s) . A small tab for labeling and handling was included proximal to the measurement area. Figure 6.11 shows the laser cutting process and an example of the cut prescale film.

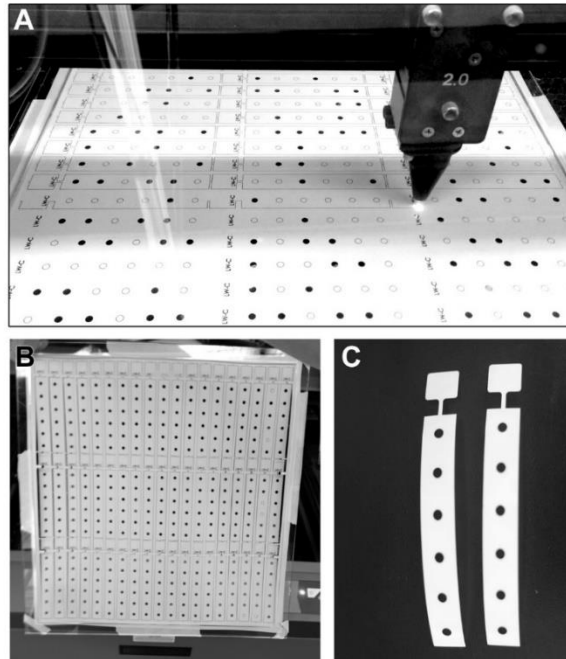


Figure 6.11: Photographs showing the CNC laser cutting of the Fujifilm prescale film being cut (A), a complete sheet, (B) and two plates (C).

The prescale film was calibrated using the methodology of Liggins et al. (1992). An aluminum cylinder (rather than steel) 50 mm in length was turned to a diameter of 25.4mm. One end was progressively flat ground and polished ($0.3 \mu\text{m Al}_2\text{O}_3$) and the other was recessed with a 120° countersink, 8 mm in diameter. The prescale film was loaded between the cylinder and a ground and polished platen. A 12.7 mm diameter ball bearing was placed between the loading cylinder and the load cell to align the axis of loading between the two components. Samples of the Fujifilm material $\sim 25 \text{ mm}^2$ were subjected to compressive loading at a rate of 0.01 mm/min on an ATS 1620C testing machine. A 22,241 N capacity load cell was used to record loading data at a rate of 95 Hz to peak loads between 1.0 and

12.0 MPa in 1.0 MPa increments. Figure 6.12 shows the experimental setup. The peak load was held for 60 seconds and then released. The samples were immediately optically scanned on a flatbed scanner at 2400 dpi and converted to 8 bit grayscale values. Each image was imported into ImageJ software (v1.47) to determine the average grayscale value that was correlated to the calculated pressures. This test was replicated with a similar cylinder machined from a block of Ti6Al4V material produced via EBM such that the vertical (z) surface remained intact (Figure 6.12B). The morphology of the vertical surface is representative of that of the EBM fabricated plates. Prior to testing, the EBM fabricated surface was measured optically at 70x magnification using a Hirox KH- 7700 optical microscope (Tokyo, Japan) as shown in Figure 6.12C.

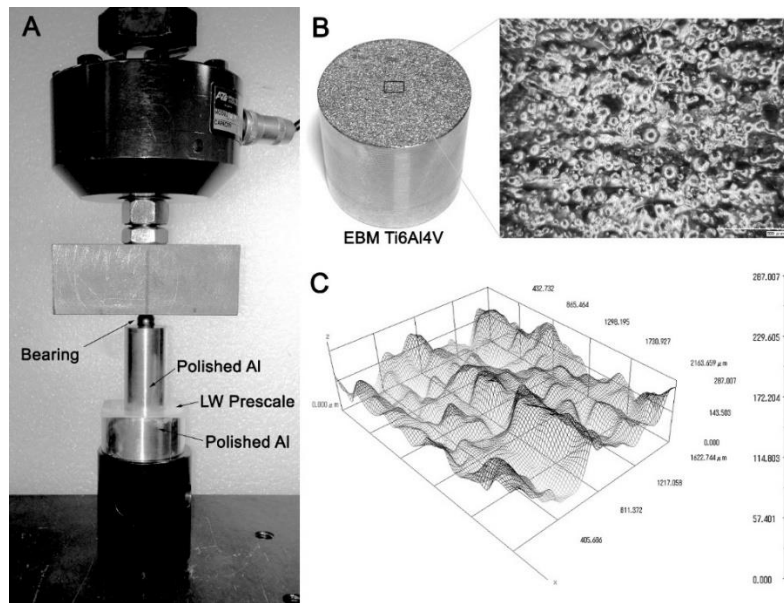


Figure 6.12: Photograph of the Fujifilm prescale calibration test setup (A), a test cylinder using an EBM fabricated surface rather than a polished surface (B) and a 3D surface contour plot of the EBM surface roughness (C).

From these data a calibration curve was fitted (shown in Figure 6.13). In addition, Figure 6.13 also shows the same curves generated from scanned color chips provided by the Prescale manufacturer. Zones A-D correspond to temperature and relative humidity windows.

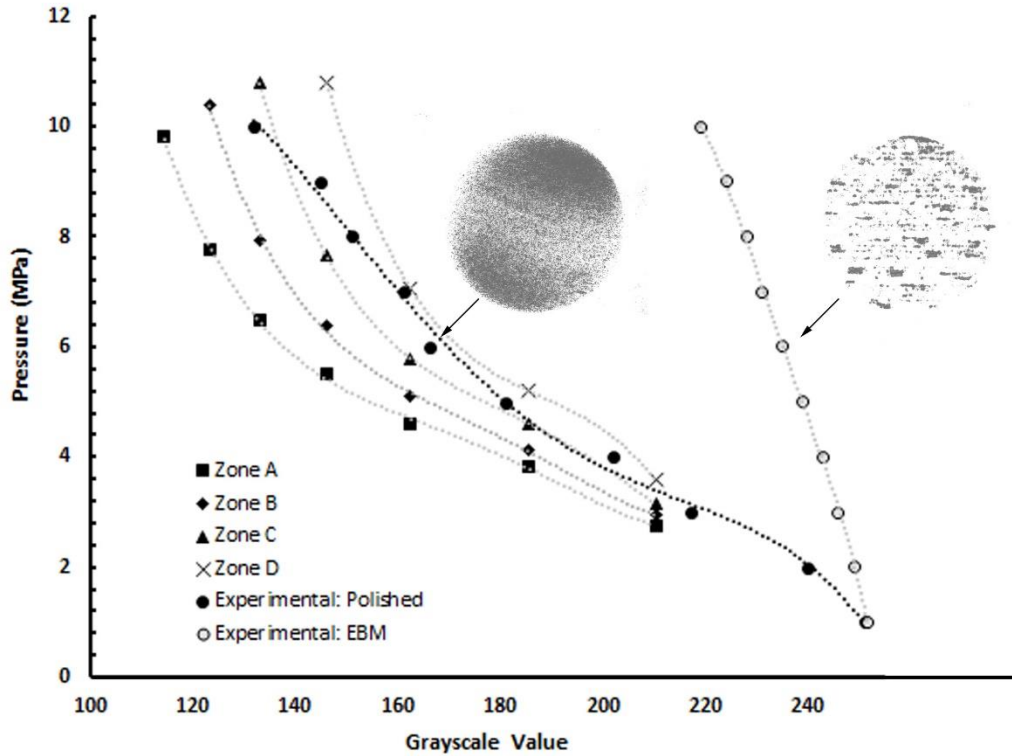


Figure 6.13: Graph showing calibration curves for the Fujifilm prescale LW pressure sensitive film produced with both polished and as fabricated EBM surfaces. Zones A-D represent the manufacturers calibration curves as a function of relative humidity (room temperature, D=0-45% relative humidity, C=45-60%, B=60-80%, A=80-100%).

The test implants were assembled to the analog radii with 3.5 mm titanium cortex screws obtained from the same lot (26 mm length, DePuy SynthesVet 404.026, lot ID 6514994). Samples were assembled in random order to minimize the risk of a sequential effect. The distal-most screw was inserted through the plate and prescale film and lightly threaded into the analog radii, as shown in Figure 6.14. Alignment with the remaining proximal holes and plate edges was visually checked as the screw was tightened to a torque of 1.2 Nm with a 2.5 mm hexagonal driver. The subsequent screws were inserted using the same technique, in sequence from the distal to proximal ends of the plate. Once all screws were placed, the torque was increased to 2.0 Nm in the same order. Torque was controlled by using a calibrated precision torque screwdriver, adjustable in 0.1 Nm increments from 1.2-3.0 Nm, accurate to within $\pm 6\%$ (EN ISO 6789, Wera, Germany). Thirty seconds after the last screw was tightened to the specified torque (timed with a stopwatch), the construct was disassembled in reverse order. The prescale film was carefully loaded into a custom transparency holder.

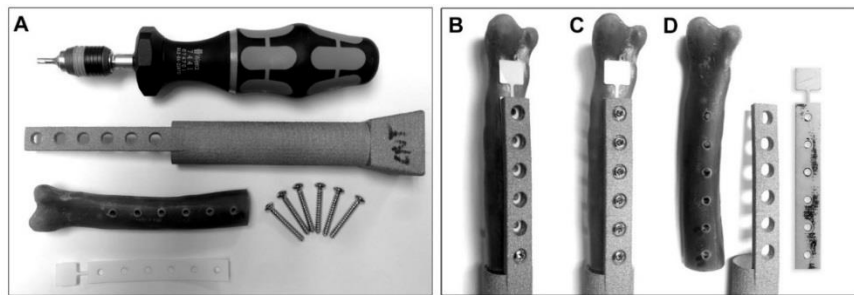


Figure 6.14: Photograph showing the components of the prescale assembly including the calibrated torque driver (A), the aligned prescale film with distal screw installed (B), the construct with six screws applied to a torque of 2Nm (C), the disassembled construct and stained prescale film (D).

The prescale films, in the transparency holder, were optically scanned at 2400 dpi and converted to grayscale at the completion of all tests (total duration < 2 hours). Individual film images were then cropped and saved to separate files. ImageJ (v 1.47, National Institutes of Health, USA) was used to quantify the prescale film results. Raw images, 555 px x 3432 px were converted to 8-bit grayscale. For particle analysis, a threshold was applied at a grayscale value of 110 resulting in a binary, black and white image. Boundary particles and edge effects were filtered using a 1 pixel erosion followed by a 1 pixel dilation. The built-in particle analysis function was used to count the particles and to measure the area, circularity, and perimeter of individual particles. These data were used in calculating other metrics such as total contact area, percent contact, and solidity (area/convex hull). Figure 6.15 illustrates the sequence of image analysis steps. The convex hull of the black pixels was calculated using the Hull and Circle algorithm (v2.0a) developed by Audrey Karperien and Thomas R. Roy (<http://imagej.nih.gov/ij/plugins/hull-circle.html>). The pair correlation function was used to derive a metric for particle dispersion. Results were analyzed with statistical software (JMP Pro v11.0). The distributions of measurements were compared to the normal distribution using the Shapiro-Wilk test. Plate contact measurements between the three plate configurations were compared with ANOVA with pooled variance. Means were compared with student's t-tests ($\alpha = 0.05$).

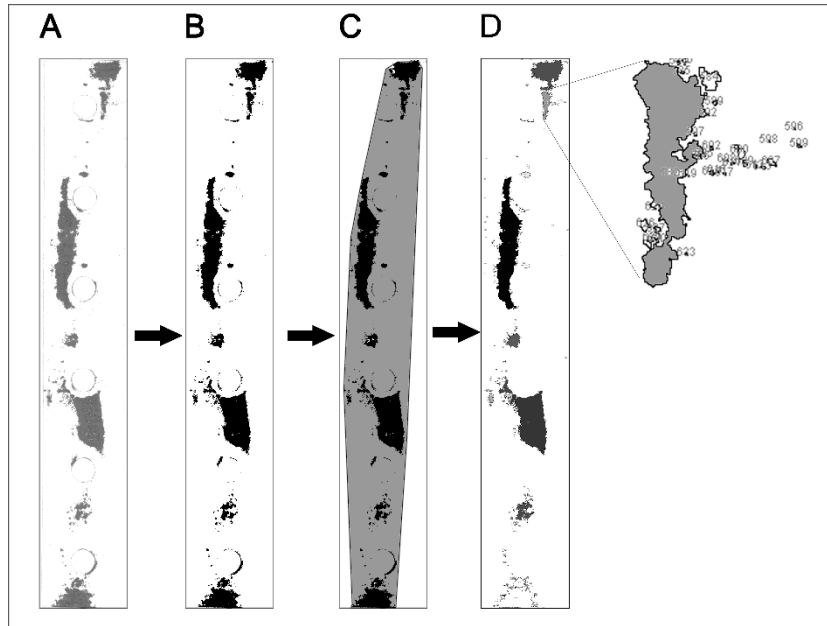


Figure 6.15: Illustration of Fujifilm prescale analysis steps. Raw data (A) were converted to black and white by thresholding (B), the convex hull area and perimeter were calculated (C), particle number, area and perimeter were calculated (D).

Average contact intensity mapping was calculated from a composite image generated from the arithmetic average of the ij^{th} pixel across all n measurements, as illustrated in Figure 6.16 for the biplanar-contoured plate case.

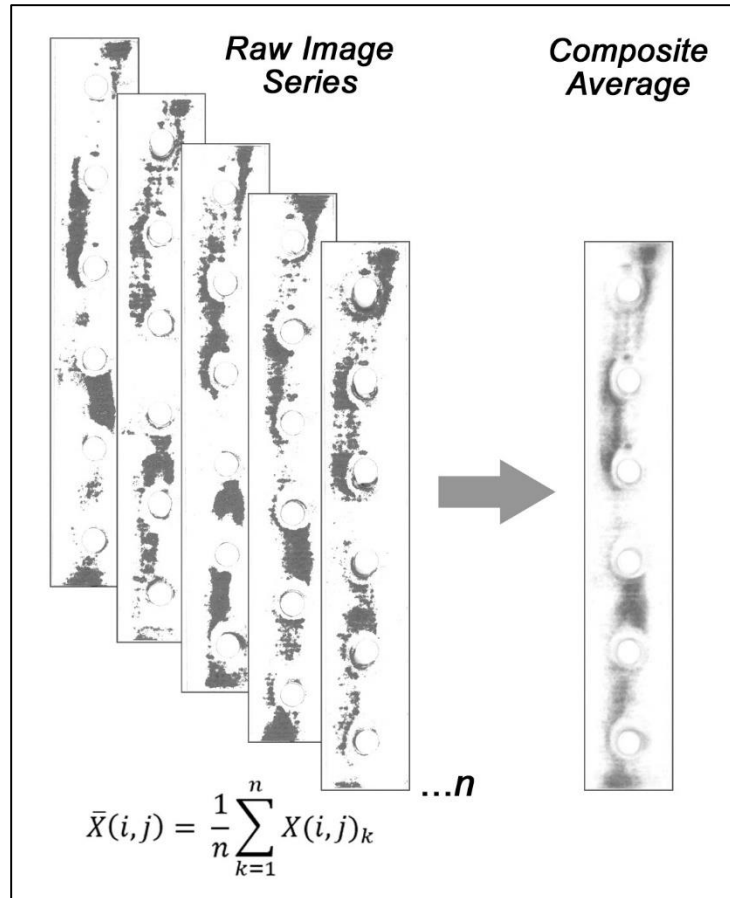


Figure 616: Example of composite image averaging ($n=15$) for a contoured plate

6.2.6 Application of strain gauges

The implants were reassembled using the same methodology described in section 6.2.5. Medial plates were fixed with 2.7 mm titanium cortex screws (26 mm length, DePuy SynthesVet 404.026, lot ID 6553843). Calibrated, preassembled, 350 Ω rosette strain gauges (Micro-Measurements, Raleigh NC) were applied to the cranial surface of the limb spring

test plates between the first and second holes (distal) and the fifth and sixth holes (proximal). Figure 6.17 shows a photograph of an assembled implant construct with applied strain gauges. The surface of the plate was manually ground and polished to remove the roughness of the as-EBM fabricated surface. The surface was then cleaned with ethanol followed by swabbing for 5 seconds with Micromeritics M-Prep Conditioner A (MCA-1, Phosphoric Acid) then 5 seconds of swabbing with Micromeritics M-Prep Neutralizer (MN5A-1, Ammonia/water). Cyanoacrylate adhesive was applied to both the plate and the underside of the strain gauge. Pressure was applied with a silicone rubber block for at least 15 minutes. After gluing, the gauges and leads were coated with RTV silicone for protection. A strain relief loop was loosely fixed to the proximal end of the segmental defect repair with a plastic tie. Each 3-wire cable was labeled according to channel number with a plastic marker, and terminated in an RJ45 connection. Strain gauges were only applied to three replications of each implant design excluding the medial and six-hole biplanar constructs.



Figure 6.17: Photograph showing an assembled test implant (Cranial-conformal, 0.2 relative density mesh) with strain gauges installed in proximal and distal plate locations.

6.2.7 Mechanical testing apparatus

Three loading scenarios were evaluated in this study, cantilever, torsion and axial compression. All mechanical testing was carried out using an ATS 1620C testing machine. ATS TestVue software (v4.22.00) recorded crosshead position and loading data from a 22,241 N capacity load cell (1210AF-5K-B). Custom testing fixtures, adapted from the analog radii validation study described in chapter 4 were fabricated in steel to accommodate these tests. Detail drawings are included in the appendices. Strain data were recorded by a Micro-Measurements system 7000 data acquisition system (Figure 6.18), with 8 channel DAQ card and StrainSmart software (Version 4.7.25.1161). Strain gage resistance (350 Ω),

gauge factor (2% @ 24°C) and temperature correction factors were provided by the manufacturer and input into the system. Strain data were collected in a half bridge configuration with a 5 V excitation at a sampling rate of (10 Hz). An additional 1122 N capacity strain based load sensor (SM-250, Interface, Scottsdale, AZ), mounted in series, output load data to the Micro-measurements system calibrated statically at 3 mV/V.

Constructs were randomly assigned to a testing sequence using the Microsoft Excel random number generator (for instance; torsion-cantilever-axial). Tests were organized round-robin to minimize the required number of setups.



Figure 6.18: Photograph of the Strainsmart 7000 setup (cantilever test shown).

6.2.7.1 Cantilever testing

Figure 6.19 shows a photograph of the cantilever testing apparatus. The connection for the distal portion of the implant/construct consists of a split steel housing measuring 76.20 mm x 31.75 mm x 101.60 mm). Four ground and hardened steel pins (6.35 mm diameter) align the top and bottom sections of the housing. A 6° square taper cavity matching the geometry of the test implant dovetail boss (22.97 mm x 22.97 mm, at the proximal end) bisects the split. The test implant is secured in the split housing with 3/8-16 bolts (9.5 mm). A 1/2-13 (12.7 mm) set screw through a 12 mm thick plate engages an interference connection from a plate on the housing. The position of the implant/analog bone construct is rotated about the medio-lateral plane (at the distal end of the device) 1.6 degrees from the horizontal to match the center of rotation of the construct, which is necessary to account for the curvature of the radius. On the proximal end, a split cylinder housing (measuring 50.8 mm in diameter and 25.4 mm in length) encases the epiphysis, secured with 1/4-28 (6.35 mm) bolts. The internal geometry of the housing was CNC machined to match the external geometry of the proximal epiphysis. The crosshead loading fixture consisting of a plate with a 19 mm diameter steel cylinder (perpendicular to the loading direction) was affixed to the crosshead with serrated clamp. The crosshead loading fixture contacted the test implant at a distance of 158.68 mm from the base of the distal housing fixture. Loading was applied at a crosshead speed of 1.5 mm/min for each group to a maximum load of 110 N for all constructs with

cranial plates. For the constructs consisting of only medial plating, a maximum load of 25 N was applied.

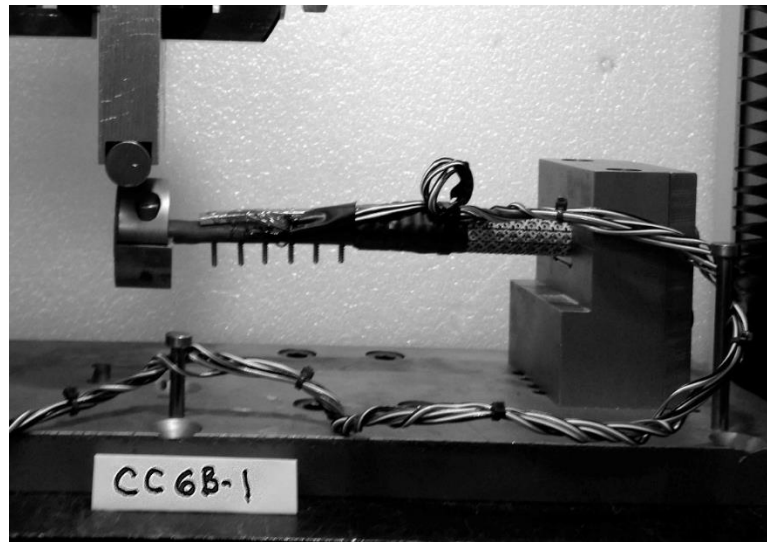


Figure 6.19: Photograph showing the cantilever testing fixture installed in the ATS 1600C (Cranial conformal plate with 0.4 relative density mesh).

6.2.7.2 Torsion testing

The torsional stiffness of the constructs was measured by placing an angular displacement of up to 10° at a rate of $6.5^\circ/\text{min}$. in external rotation. The functionality of the torsion testing fixture is described in detail in section 4.1.2. The stationary and driving supports of the fixture were redesigned to accommodate the limb sparing test implants. The distal split housing fixture used for cantilever tests was (repositioned) was also used for the torsional tests. The torque transmission drive on the proximal end of the implant consisted of a split housing matching the epiphysis geometry, as previously described, however in this case a shaft extended through a housed, and axially constrained, radial bearing conforming to

class ABEC 5. An ABEC 5 roller thrust bearing, preloaded with two Belleville springs stacked in parallel to prevent racking of the radial bearing. The distal-most end of the fixture consisted of a hexagonal drive that connected to the primary lever arm. A 3/8-16 (9.52 mm) bolt in the center of the drive shaft was used to compress the springs providing a preload of 25 N on the axial thrust bearing. Figure 6.20 shows photographs of the disassembled and assembled torsion fixture. Figure 6.21 shows the torsion test setup on the ATS testing machine.

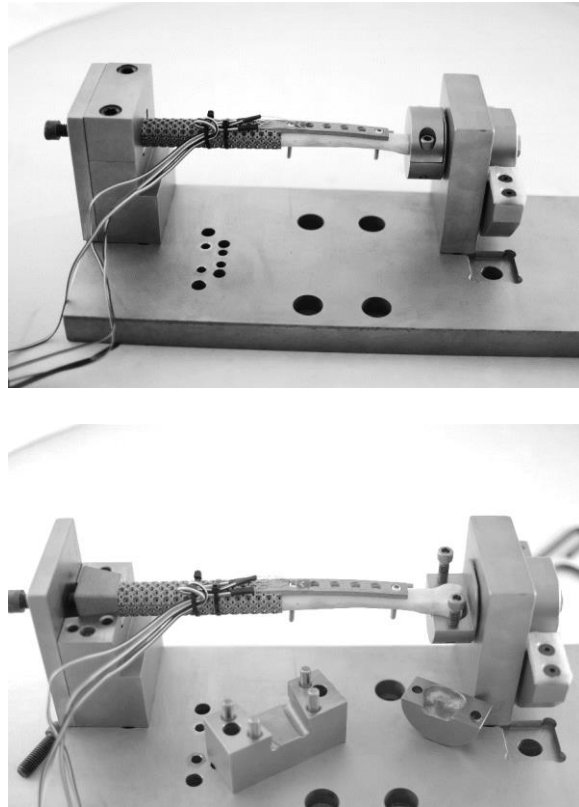


Figure 6.20: Assembled torsional testing fixture (top) and disassembled (bottom). The moment (lever) arm accommodates both internal and external torsion.

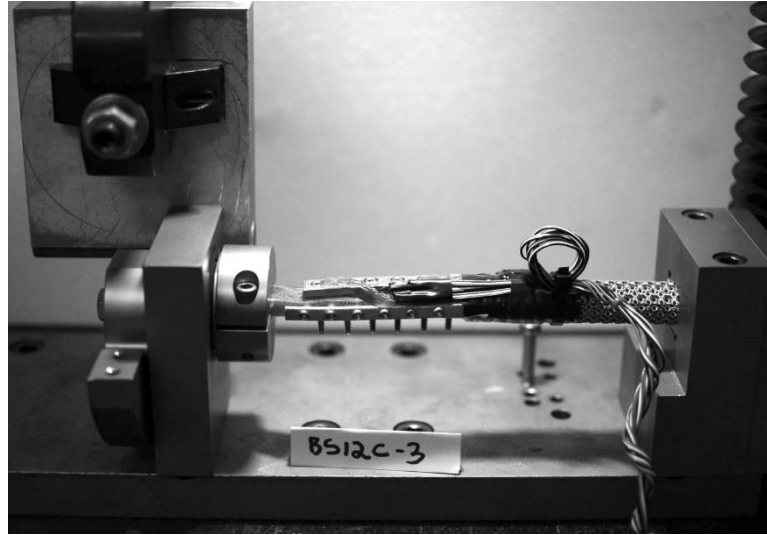


Figure 6.21: Photograph of the torsion testing fixture installed on the ATS testing machine (12 screw, biplanar configuration with 0.2 relative density mesh shown).

6.2.7.3 Axial testing

Axial loading to 450 N was applied to the limb sparing test implants with a crosshead speed of 1.5 mm/min. The distal dovetail feature was constrained in a 3.0 mm deep pocket the base of which is oriented at an angle of 1.6° to the horizontal in the cranial-caudal direction. The epiphyseal housing on the proximal end functioned as previously described. In this case the housing also included a hemispherical feature on the proximal end to facilitate additional degrees of freedom during loading. Figure 6.22 shows a photograph of the axial testing setup.



Figure 6.22: Axial testing fixture, the proximal split housing is capped by a hemisphere to permit minor rotations during compression testing, the distal end is fixed into a pocket milled into the base plate. The bottom of the pocket is angled 1.6 degrees to the horizontal to align the axial centroid of the construct with the loading axis.

6.3 Results

6.3.1 Analog radii

The stiffness of each sample was calculated from a linear regression of the elastic portion of the load-deformation curve. Each sample was selected in random and loaded non-destructively for a total of three repetitions, and the last was recorded. The mean and

standard deviation of the stiffness and mass was calculated for each group. The results distribution of results was determined to be normal using the Shapiro-Wilk test ($p=0.3046$), where $\mu=369.16$ N/mm and $\sigma=37.02$ N/mm. The distribution of sample mass was not normally distributed according to the Shapiro-Wilk test ($p < 0.0001$) where $\mu=0.0541$ kg and $\sigma=0.0028$ kg). There was no correlation between specimen stiffness and specimen mass ($R^2=0.035$). To evaluate the influence of both the mold identity and the epoxy batch identity a 3-parameter mixed effects model, (including a correlation parameter) was used to model the results. These results identified a significant difference in the stiffness of specimens made in batch 1 as compared to batches 2 and 3 ($p=0.0065$). The influence of the mold ID was not significant ($p=0.5390$). Means were compared between batch number groups using 2-tailed Student's t-tests with pooled variance and significance was set at 95%. Here, excluding the mold ID parameter, there were significant differences in the stiffness between each batch ($P < 0.0001$) as shown in Figure 6.23. No effect of manufacturing sequence was detected and, all specimens fabricated fell within Shewhart control limits for individuals for the first batch (Figure 6.24). The coefficient of variation for the stiffness of the analog radii, across all batches and molds, was 10.02%.

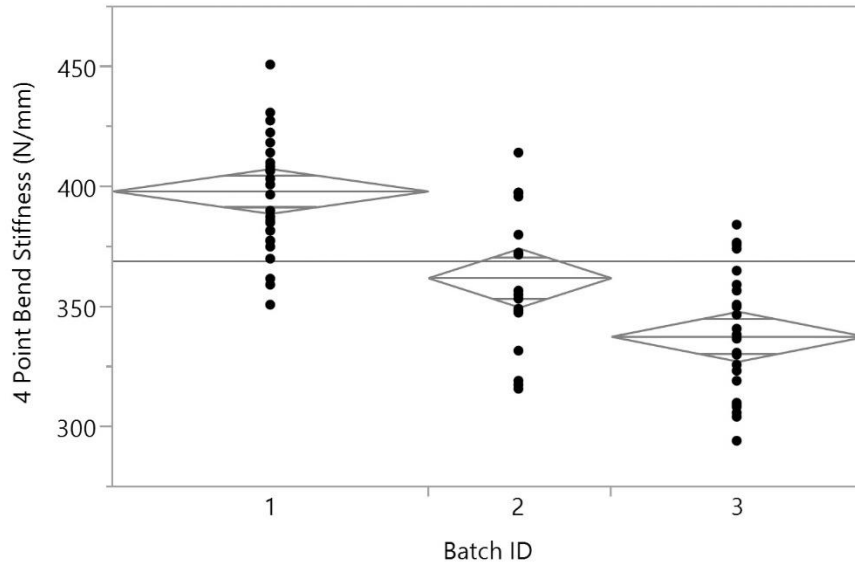


Figure 6.23: Plot showing the measured stiffness (in four point flexure) of analog radii produced with each of three batches of resin.

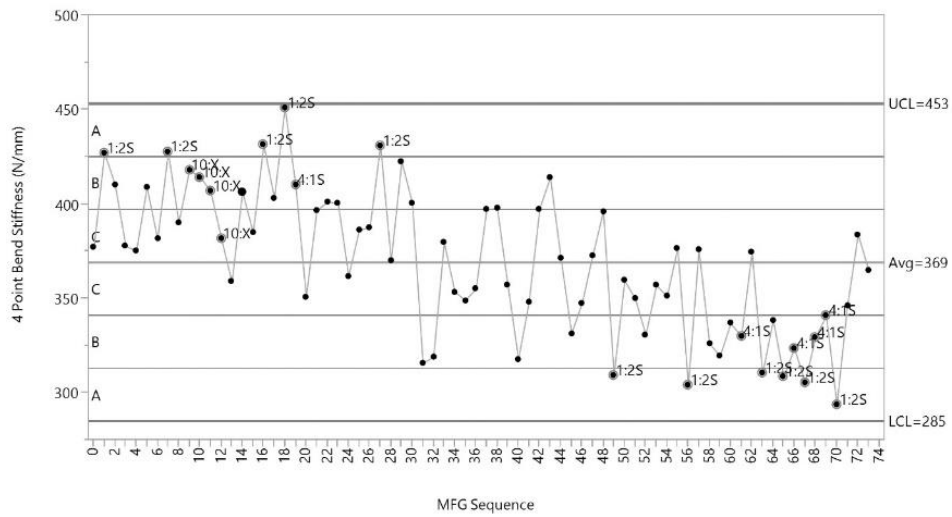


Figure 6.24: Retrospective Shewhart control chart for individuals for the four point flexure stiffness of analog radii as a function of manufacturing sequence.

6.3.2 Preliminary four point flexure of graft segments with ovoid cross section

The stiffness of the ovoid bars was calculated from the slope of the linear regression of the data load-displacement data. The flexural modulus of elasticity of the samples was calculated using Eq. 5.3, where the moment of inertia was determined from Eq. 6.1. The load deformation plots are shown in Figure 6.25. These data were plotted against earlier results from Chapter 5 and were determined to be consistent with those findings. While these data follow the power law of Gibson & Ashby, the presence of open cells on the periphery of the geometry may have contributed to the slightly lower moduli observed. Figure 6.26 shows the relative modulus of elasticity for these tests as it relates to relative density.

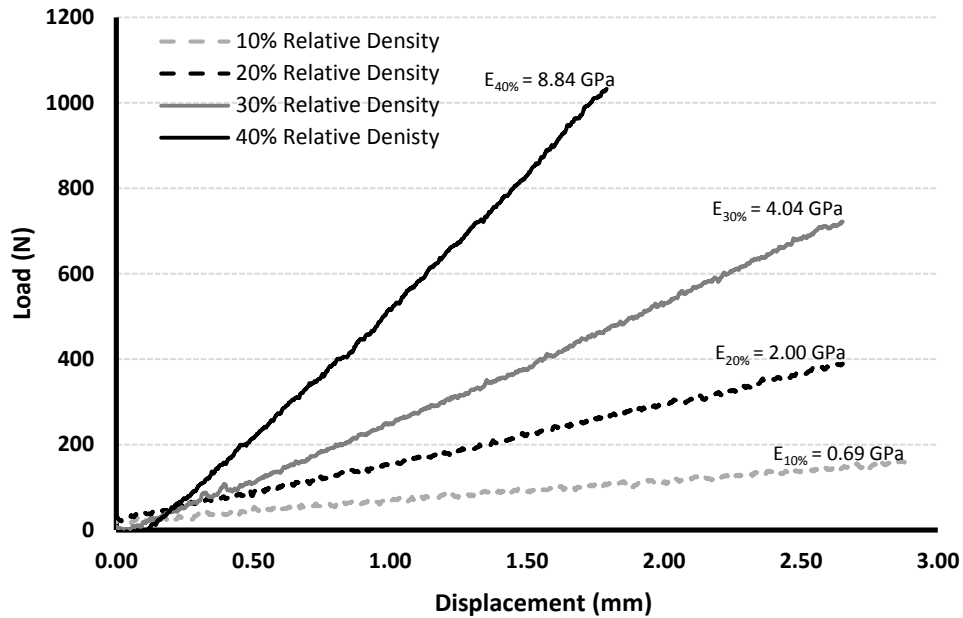


Figure 6.25: Load displacement plots for non-destructive testing in four point flexure. Test bars consisted of ovoid cross sections with rhombic dodecahedron unit cell structures of various relative densities.

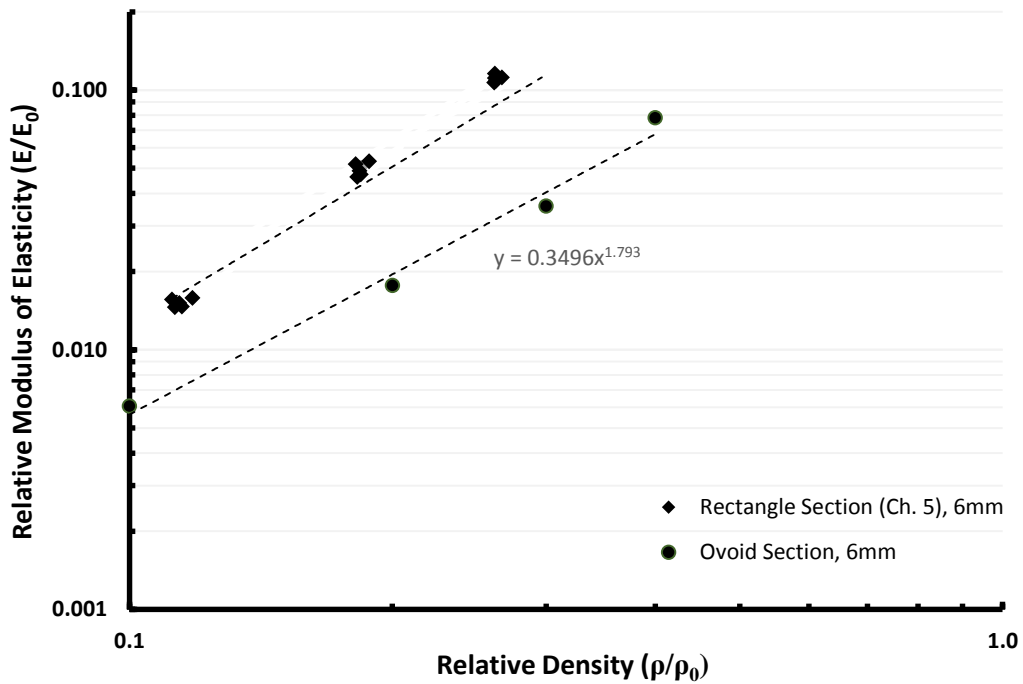


Figure 6.26: Plot of relative modulus of elasticity as a function of relative density for the ovoid cross section bars, these results are compared with the same for the rectangular bars tested in chapter 5.

6.3.3 Contact at the bone implant interface

Figure 6.27 shows the composite average ($n=15$) of the Fujifilm prescale impressions for each of the bone plate configurations tested. From these images, the limited contact of the contoured plates with the cranial surface of the radius is evident in the intensity of the impressions. The histogram in Figure 6.28, quantifies these data. The conformal plating resulted in greater contact area as compared to the contoured plates in both the cranial and biplanar configurations.

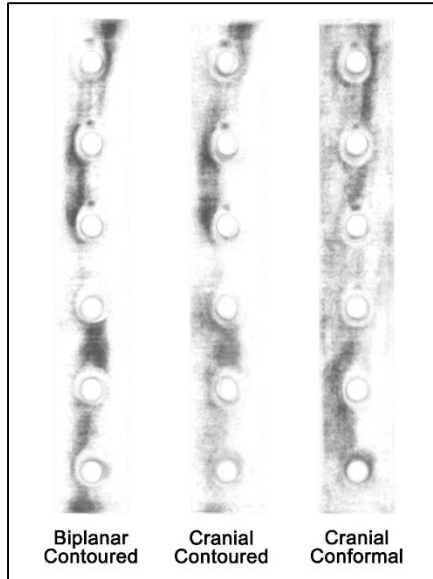


Figure 6.27: Composite image averages for each of the cranial plate configurations tested, biplanar (left), cranial-contoured (center) and cranial conformal (right).

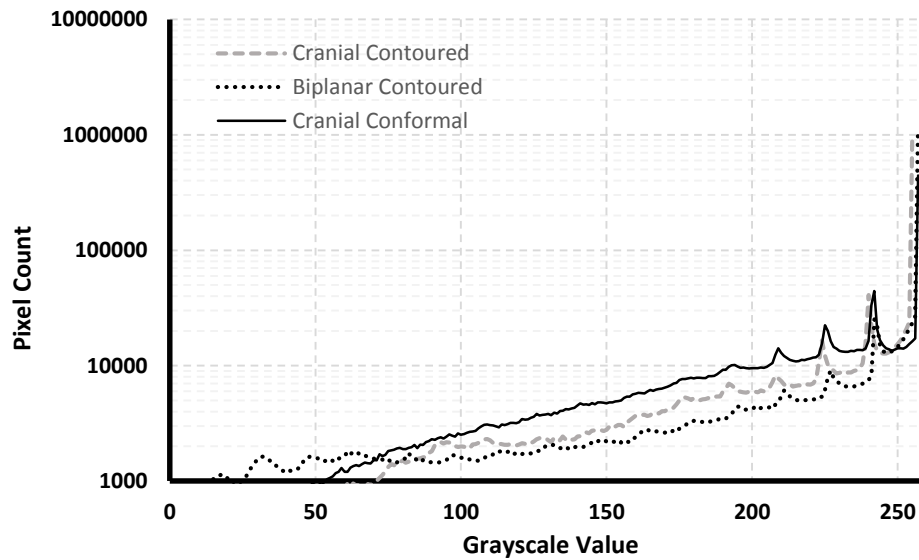


Figure 6.28: Histogram showing the number of pixels of each grayscale value for the composite average images (0 = black, 255 = white).

ImageJ was used to construct 3D surface plots (Figure 6.29) representing the magnitude of the contact area and pressure for each of the composite averages. The grayscale values on the scalebar do not necessarily correspond to the grayscale values of the pressure indicating film. Differences between the groups were quantified with ANOVA.

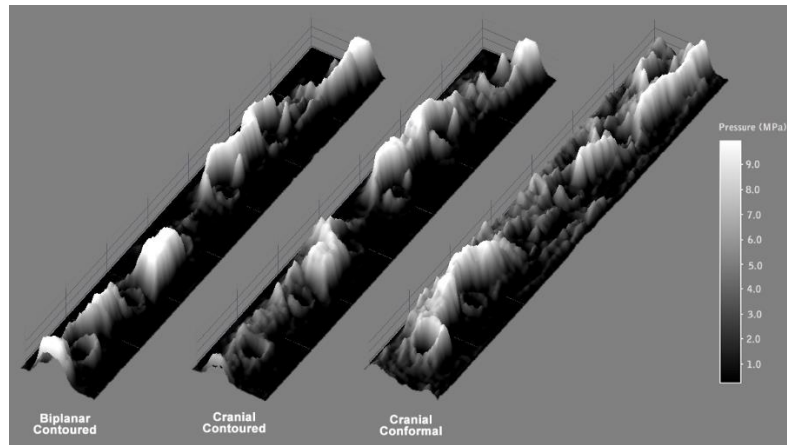


Figure 6.29: 3D surface plots representing the contact area and intensity for the composite average of each plate design.

The percentage of contact area (contact area / total area) measured across all samples in each group (biplanar contoured, cranial contoured and cranial conformal) was fit to a normal distribution, the Shapiro-Wilk test failed to reject the null hypothesis that the data were normally distributed ($W=0.0860, 0.2048, 0.4389$ respectively). ANOVA detected significant differences between the groups, as shown in Figure 6.30. Plate configuration explained 35.74% of the variability. The conformal plate had significantly higher relative contact as compared to the biplanar and cranial contoured plates ($p = 0.0001, 0.0002$

respectively). No difference was detected in the relative contact between the biplanar and cranial contoured plate groups ($p = 0.8609$).

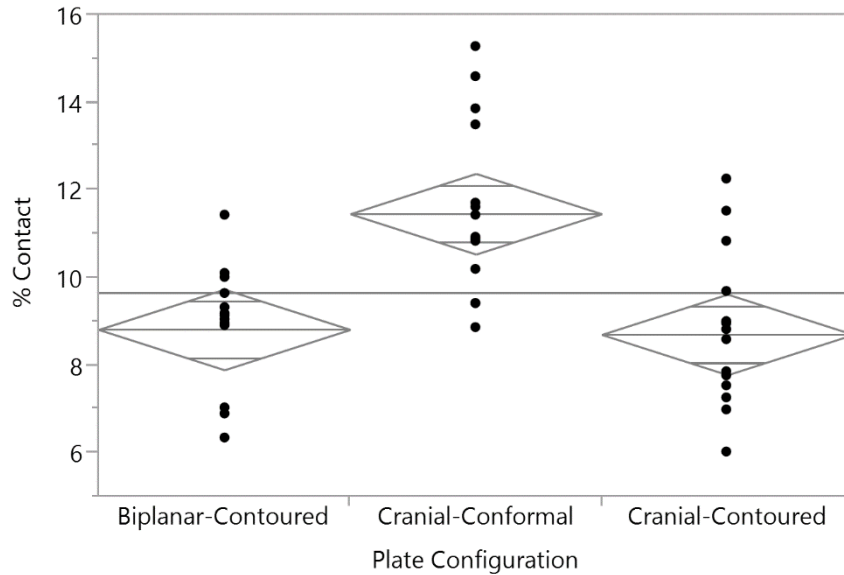


Figure 6.30: ANOVA results for the effect of plate type on the percentage of contact area.

The Shapiro-Wilk test failed to reject the null hypothesis that the convex hull data were normally distributed ($W=0.7405, 0.7362, 0.9728$ respectively). The area of the convex hull was significantly greater for the conformal plate, as shown in Figure 6.31 ($p < 0.0001$). No difference in convex hull area was detected between the two contoured plate types ($p = 0.8320$). Plate configuration represented 73.47% of the variability in the measurements.

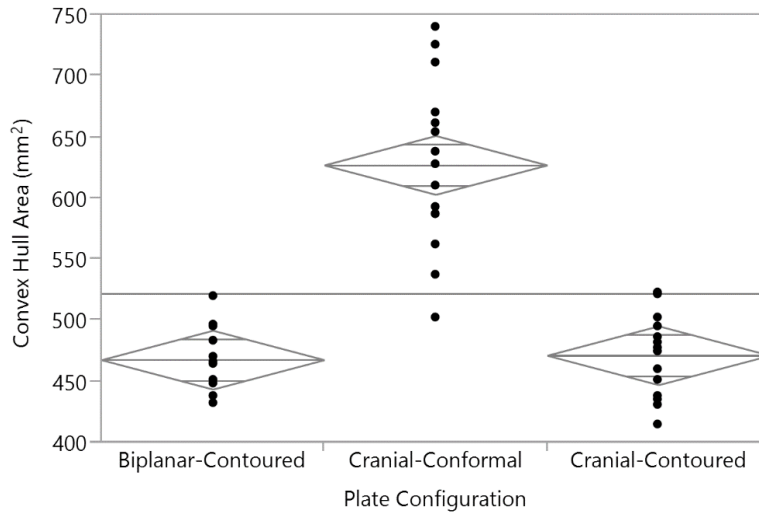


Figure 6.31: ANOVA results for the effect of plate type on the convex hull area.

Solidity is a measure of relative density defined as the proportion of the convex hull of the pixels occupied by active (black) pixels. No difference in percent solidity was detected ($F=0.9474$). Figure 6.32 shows these data.

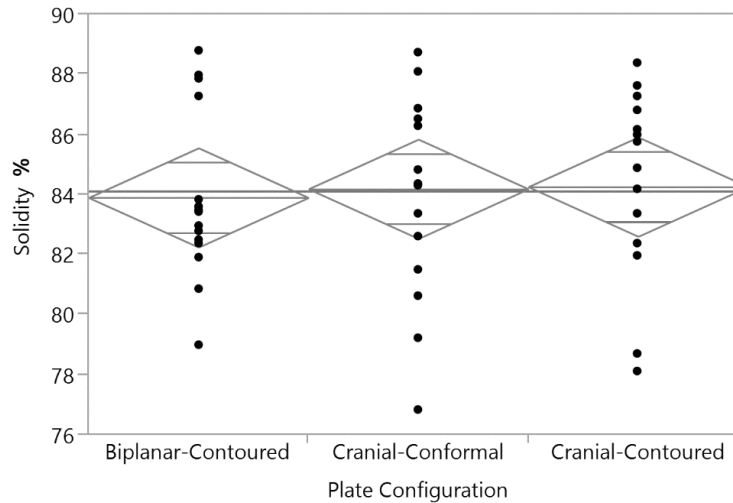


Figure 6.32: ANOVA results for the effect of plate type on the percent solidity of the prescale stains.

In addition to contact area and intensity, analysis also included measurements of particle/pixel dispersion between the plate configuration groups. This includes average particle size, number of particles and the pair correlation function. The results for the average number of particles are shown in Figure 6.33. The Shapiro-Wilk test failed to reject the null hypothesis that the average number of particles in the biplanar-contoured, cranial contoured and cranial conformal configurations were normally distributed ($W=0.2232, 0.7636, 0.4021$ respectively). However, Bartlett's test revealed significantly different variances between these groups ($F<0.0001$). For this reason the means were compared with Welch's test rather than ANOVA with pooled variance ($F<0.0001$). Plate configuration accounted for 53.11% of the variability. The cranial-conformal plate configuration resulted in a significantly higher average number of particles ($p < 0.0001$), while no difference was detected between the two contoured plate configurations ($p = 0.1228$).

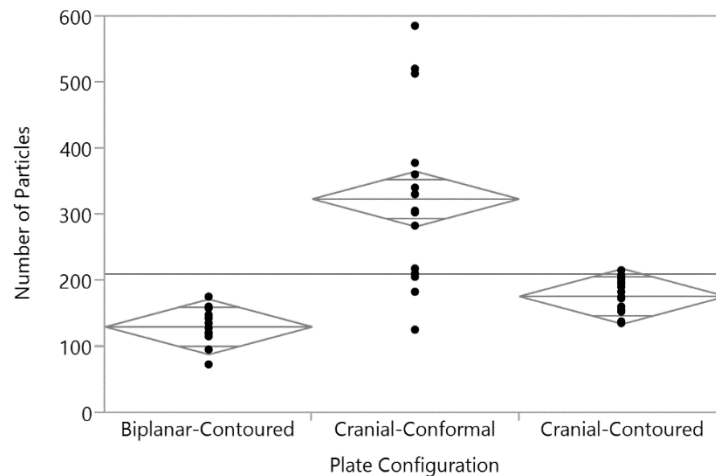


Figure 6.33: ANOVA results for the effect of plate type on the number of particles counted in the prescale stains.

Due to the presence of outliers on the cranial conformal and biplanar contoured configurations, the average size of particles (area in mm²) was not normally distributed according to the Shapiro-Wilk test ($W < 0.0001$). The test failed to reject the normality assumption for the cranial-contoured configuration ($W = 0.2515$). However, analysis of means methods and ANOVA yielded consistent results (Figure 6.34). The average particle size for the biplanar-contoured configuration was significantly higher than the cranial conformal ($p = 0.0076$) and cranial-contoured ($p = 0.0381$) configurations. The two cranial configurations did not differ significantly ($p = 0.5112$).

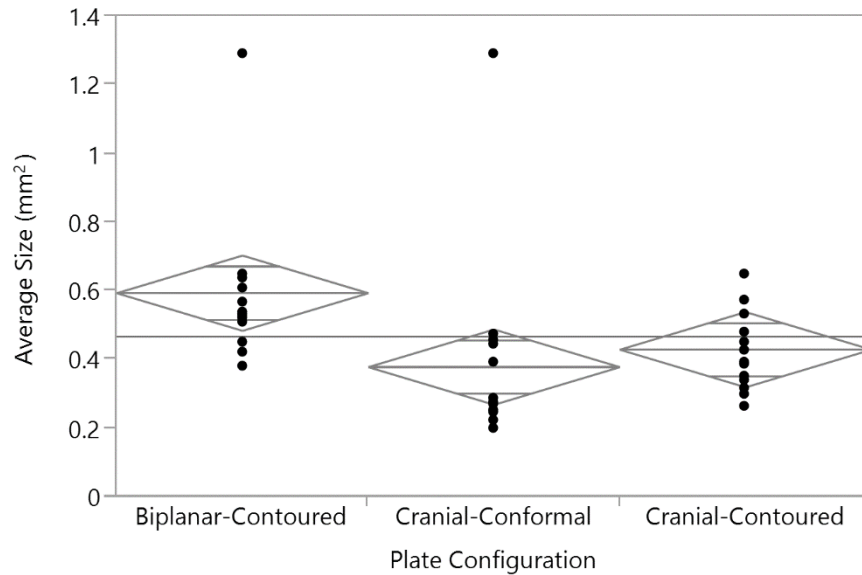


Figure 6.34. Plot showing the effect of plate type on the average size of particles in the Fujifilm prescale stains.

Analysis of the pair correlation function, shown in 6.35 shows a greater dispersion of particles associated with the cranial-conformal configuration as compared to the two contoured configurations.

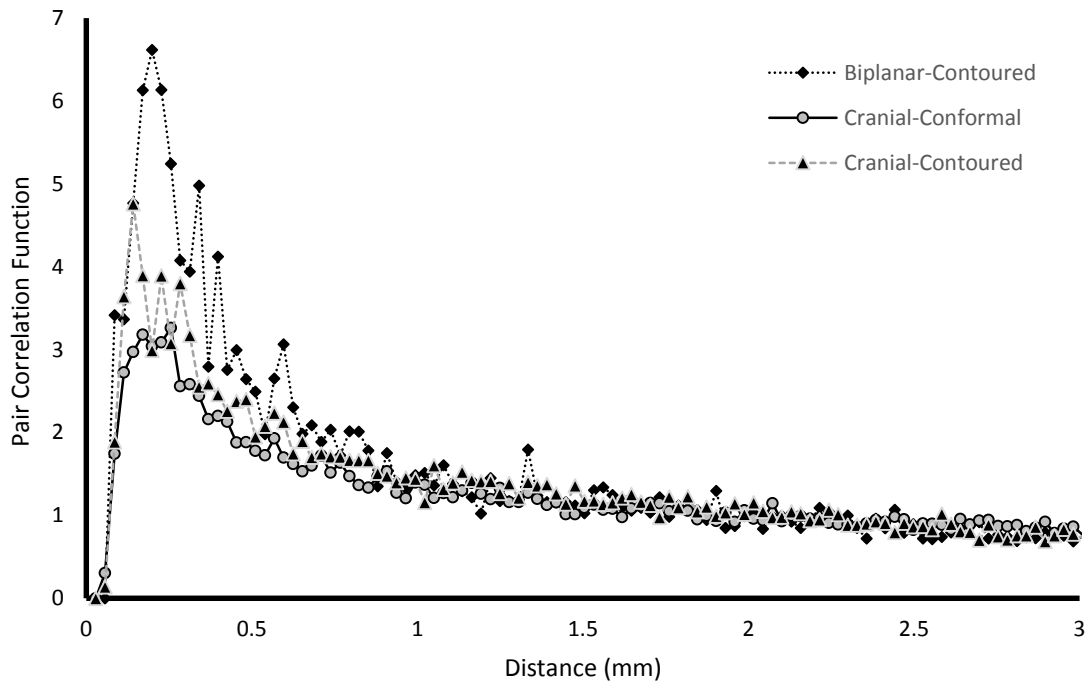


Figure 6.35: Plot showing the pair correlation function for each of the three plate types, a greater likelihood of encountering a neighboring particle is apparent for contoured plates as compared to conformal plates suggesting a greater dispersion of contact for the conformal plates.

6.3.4 Analysis of mechanical testing results.

For each of the three testing modes, the stiffness was determined from the slope of the linear portion of the load-displacement plots. In addition, data were also recorded from

strain gauges located distally and proximally on the cranial plates. Principal strains, shear strain and principal strain angle were measured at both locations at two intermediate loads.

Strain data were compared with a blocked ANOVA model. The Shapiro-Wilk test was used to evaluate the goodness of fit of each data set, by implant type, to the normal distribution. No correlation between the test metric and EBM build sequence, position within the build, host bone stiffness, or testing sequence were detected; these factors were therefore excluded from further analysis. One way ANOVA was used to investigate the influence of the number of screws for the two biplanar configurations. A parameterized linear regression model was developed to investigate the influence of diaphyseal stiffness, plate configuration, plate position, and number of screws on the mechanical characteristics measured.

6.3.4.1 Cantilever test results

Results are summarized in Figure 6.36. The number of screws for the biplanar (medial-cranial) plate configurations (6 or 12) did not significantly influence construct stiffness ($p = 0.6656$). Mesh relative density had a significant influence on the cantilever stiffness ($F < 0.0001$). The stiffness of the constructs with 1.0 relative density was significantly higher than both the 0.4 and 0.2 relative density constructs ($p < 0.0001$), the difference between the 0.4 and 0.2 relative density constructs was not significant ($p = 0.1278$). The data do not support a significant difference between the cantilever stiffness of cranial conformal plates and cranial contoured plates ($F = 0.7598$). For different plate

positions, (cranial, medial, biplanar), the Shapiro-Wilk test rejected the hypothesis that the cantilever stiffness data of the contoured plates were normally distributed ($W= 0.0005, 0.0034, 0.0007$), further these data exhibited unequal variance between the groups according to Bartlett’s test ($F < 0.0001$). Significant differences in the means were detected using analysis of means for unequal variances –Levene ($F = 0.0104$). Medial plate stiffness was significantly lower than cranial or biplanar stiffness, exceeding the ANOM lower control limits. The presence of the medial plate in the biplanar configuration did not increase the cantilever bending stiffness of constructs as compared to the constructs with only cranial plating.

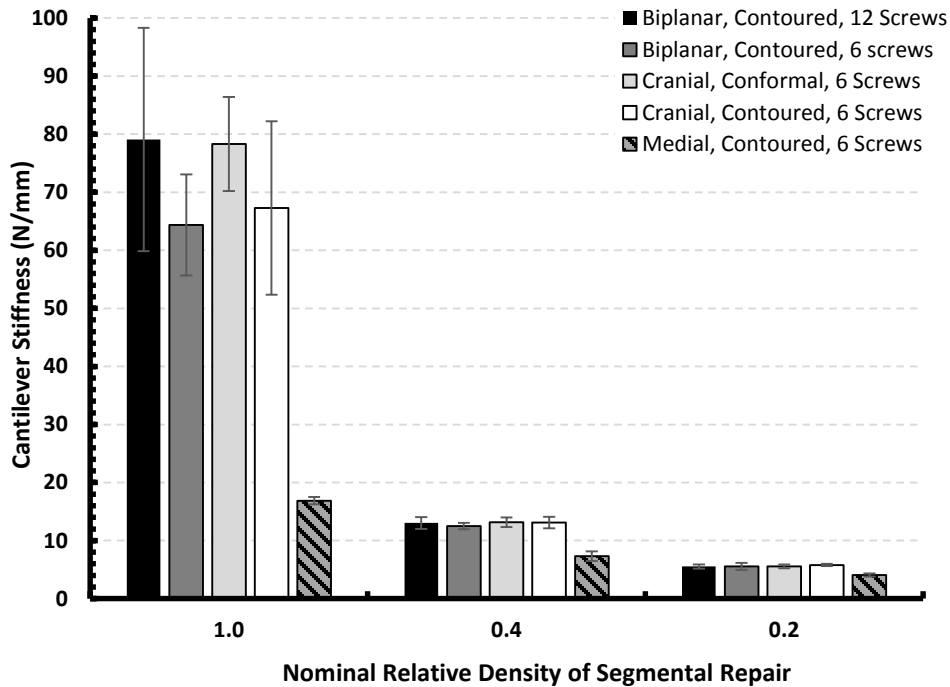


Figure 6.36: Chart showing the effect of the relative density of the segmental repair on the Cantilever stiffness for each plate configuration. Error bars indicate ± 1 standard deviation.

Cantilever strain results are shown in Figures 6.37-6.40. While variability in these data was relatively high, several significant measurements were detected. Constructs with 1.0 relative density graft segments showed a larger maximum principal strain at the proximal location than constructs of 0.4 or 0.2 relative density graft segments ($p = .0198$ and $.0298$, respectively). The angle of the maximum principal strain at the distal location for 1.0 relative density constructs was larger than 0.4 relative density constructs ($p=0.0183$). Figure 6.41 shows the principal strain angle and magnitude relative to the central axis of the construct. Constructs with a biplanar plate configuration showed lower maximum principal strains.

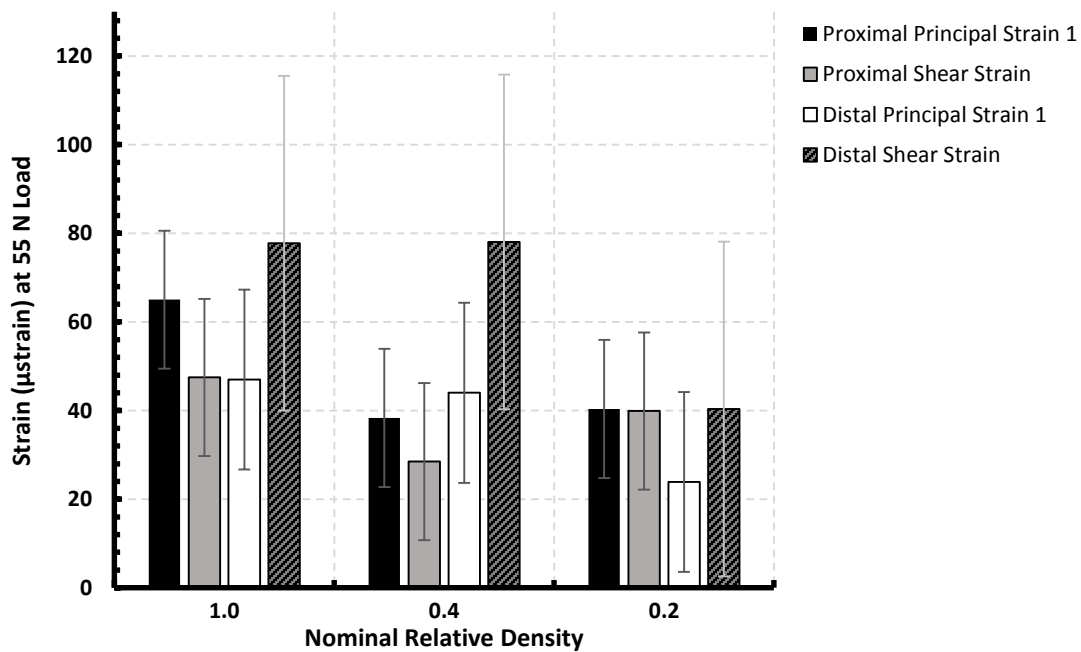


Figure 6.37: Recorded average maximum principal and shear strains for the proximal and distal locations during cantilever testing at a 55 N load as a function of implant relative density.

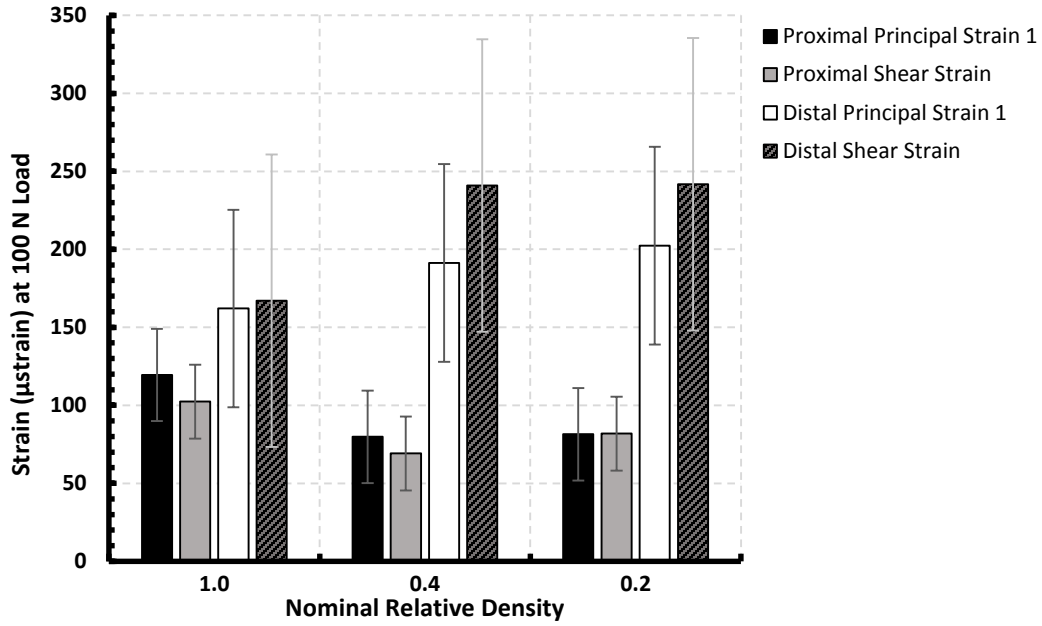


Figure 6.38: Recorded average maximum principal and shear strains for the proximal and distal locations during cantilever testing at a 100 N load as a function of implant relative density.

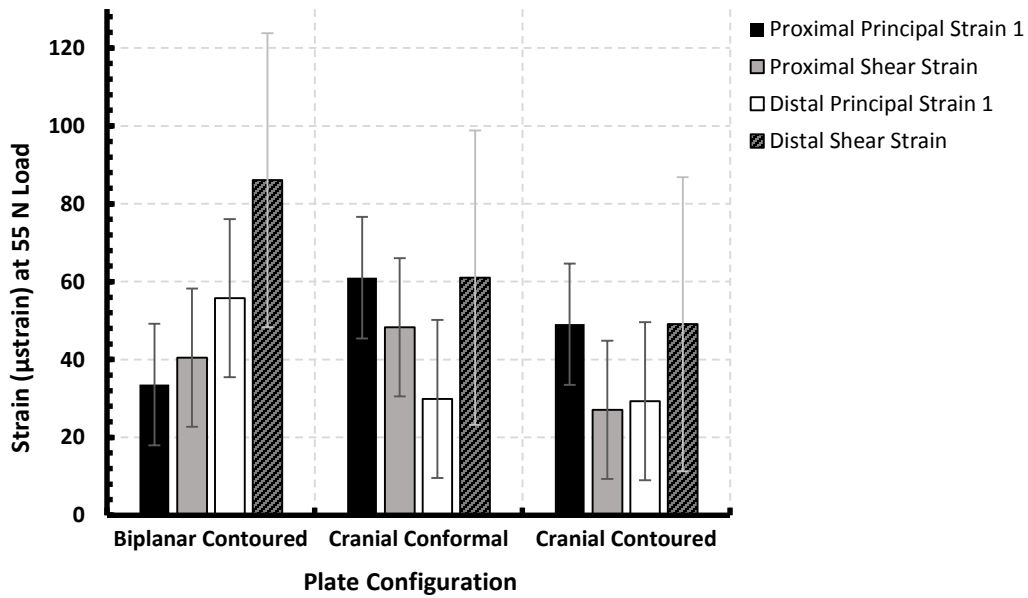


Figure 6.39: Recorded average maximum principal and shear strains for the proximal and distal locations during cantilever testing at a 55 N load as a function of implant plate configuration.

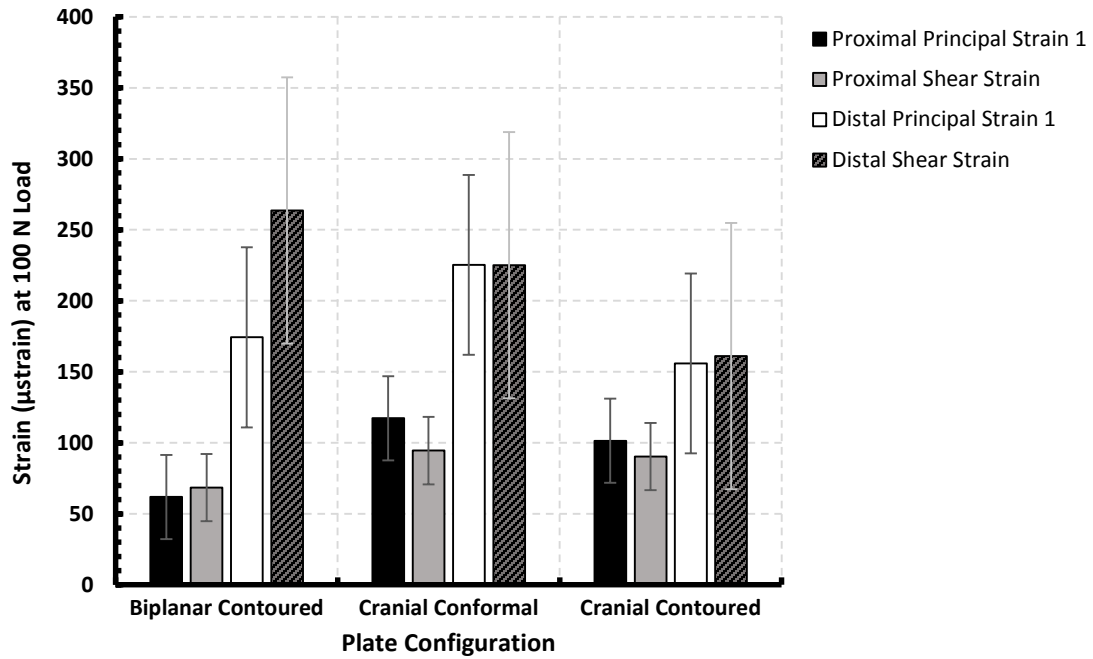


Figure 6.40: Recorded average maximum principal and shear strains for the proximal and distal locations during cantilever testing at a 100 N load as a function of implant plate configuration.

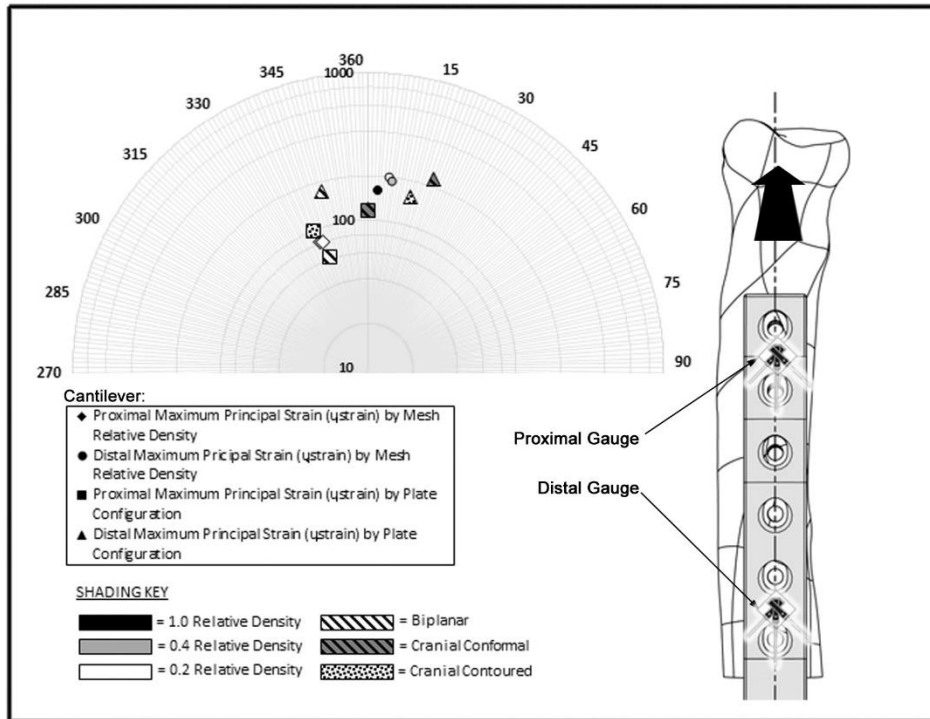


Figure 6.41: Polar plot showing the average magnitude and direction of the maximum principal strain (relative to the gauge center) during cantilever testing for each implant configuration. Log strain (μ strain) is represented on the vertical axis while the orientation angle (degrees) is represented on the circumference.

6.3.4.2 Axial test results

Results are summarized in Figure 6.42. Mesh relative density had a significant influence on the axial stiffness ($F < 0.0001$). The axial stiffness of the constructs with 1.0 relative density was significantly higher than both the 0.4 and 0.2 relative density constructs ($p < 0.0001$ and $p = 0.0048$ respectively), the difference between the 0.4 and 0.2 relative density constructs was also significant ($p = 0.0103$). Analyzed by construct configuration, ANOVA results show no significant difference in axial stiffness associated with relative density for the medially plated constructs ($F = 0.1076$). When blocked by mesh types, ANOVA results show biplanar (medial-cranial) plate configurations with 12 screws have higher axial stiffness than those with six screws ($F = 0.0088$). The effect was most pronounced for constructs with 0.2 relative density mesh structures ($F = 0.0057$).

The data do not support a significant difference between the axial stiffness of cranial conformal plates and cranial contoured plates ($F = 0.7598$). Figure 6.43 shows the relationship between plate/bone contact and axial stiffness. For different contoured plate positions, (cranial, medial, biplanar), Significant differences in the means were detected using ANOVA blocked by mesh relative density ($F = 0.0002$). Medial plate construct stiffness was significantly lower than biplanar or cranial plate stiffness ($p < 0.0001$ and $p = 0.0078$ respectively).

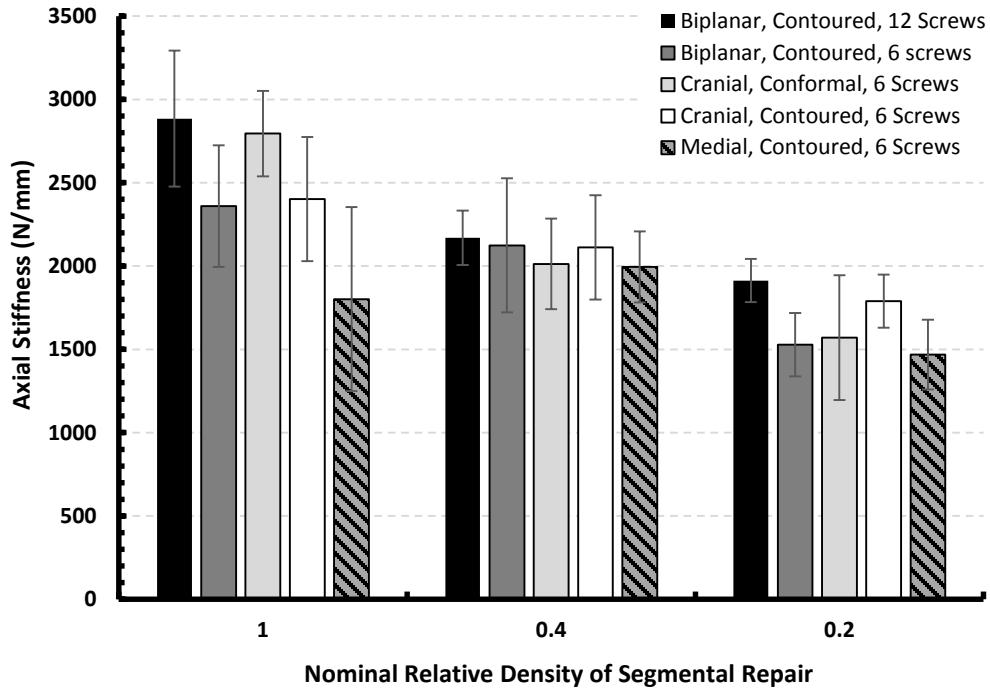


Figure 6.42: Chart showing the effect of the relative density of the segmental repair on the axial stiffness for each plate configuration. Error bars indicate ± 1 standard deviation.

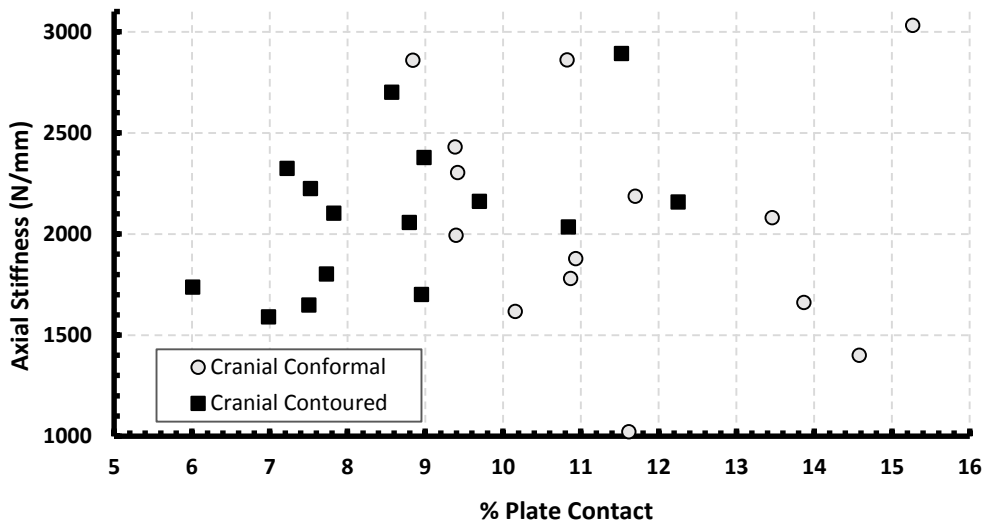


Figure 6.43: Plot of axial stiffness as a function of percent contact area.

Axial strain results are shown in Figures 6.44-6.47. Constructs with a relative density of 1.0 had a significantly higher maximum principal strain at the proximal location compared to constructs with 0.2 relative density meshes ($p = 0.0408$). The angle of the maximum principal strain was less for constructs with 0.2 and 0.4 relative density meshes when compared to those with 1.0 relative density ($p = 0.0103$ and 0.0083 , respectively). Figure 6.48 shows the maximum principal strain angle and magnitude relative to the central axis of the construct. Plate configuration had a significant effect on the angle of the maximum principal strain ($F = 0.0001$).

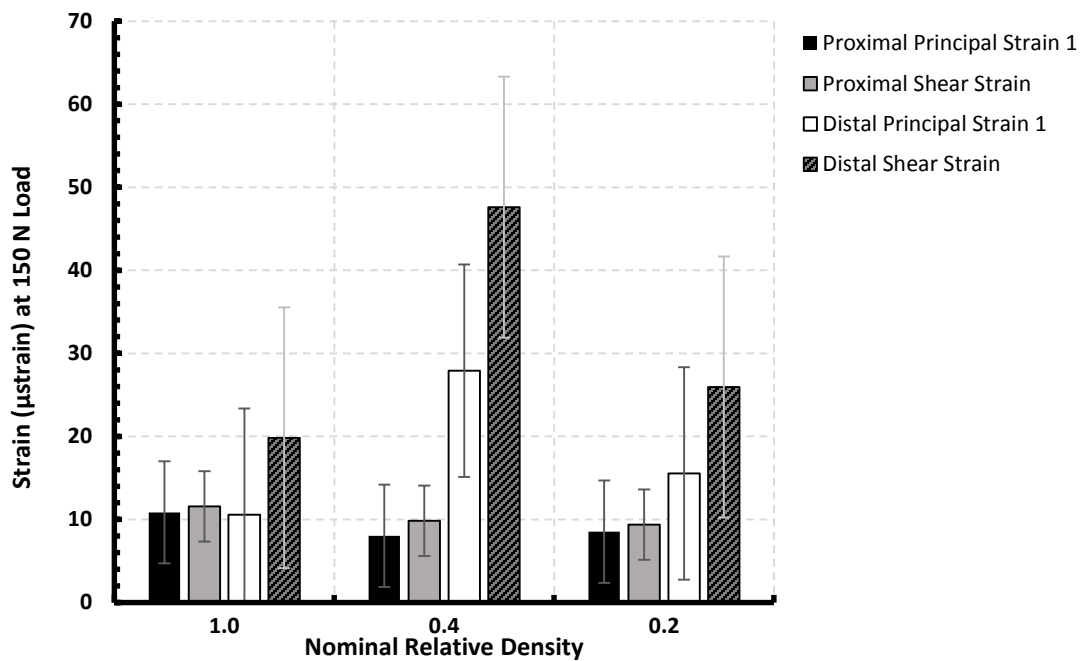


Figure 6.44: Recorded average maximum principal and shear strains for the proximal and distal locations during axial testing at a 150 N load as a function of implant relative density.

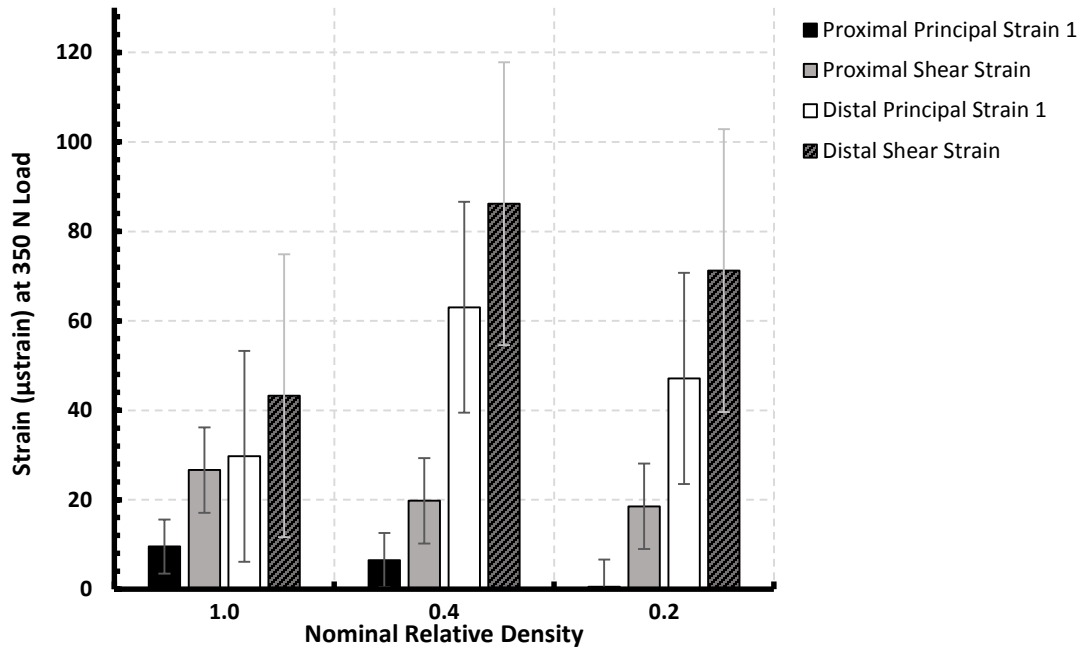


Figure 6.45: Recorded average maximum principal and shear strains for the proximal and distal locations during axial testing at a 350 N load as a function of implant relative density.

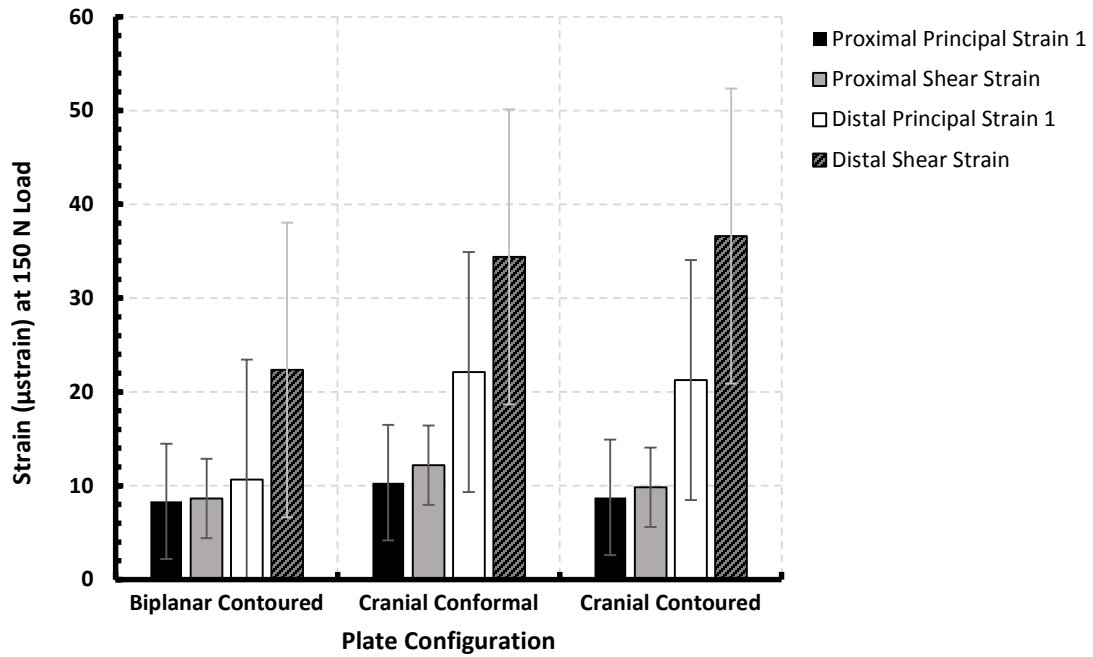


Figure 6.46: Recorded average maximum principal and shear strains for the proximal and distal locations during axial testing at a 150 N load as a function of implant configuration.

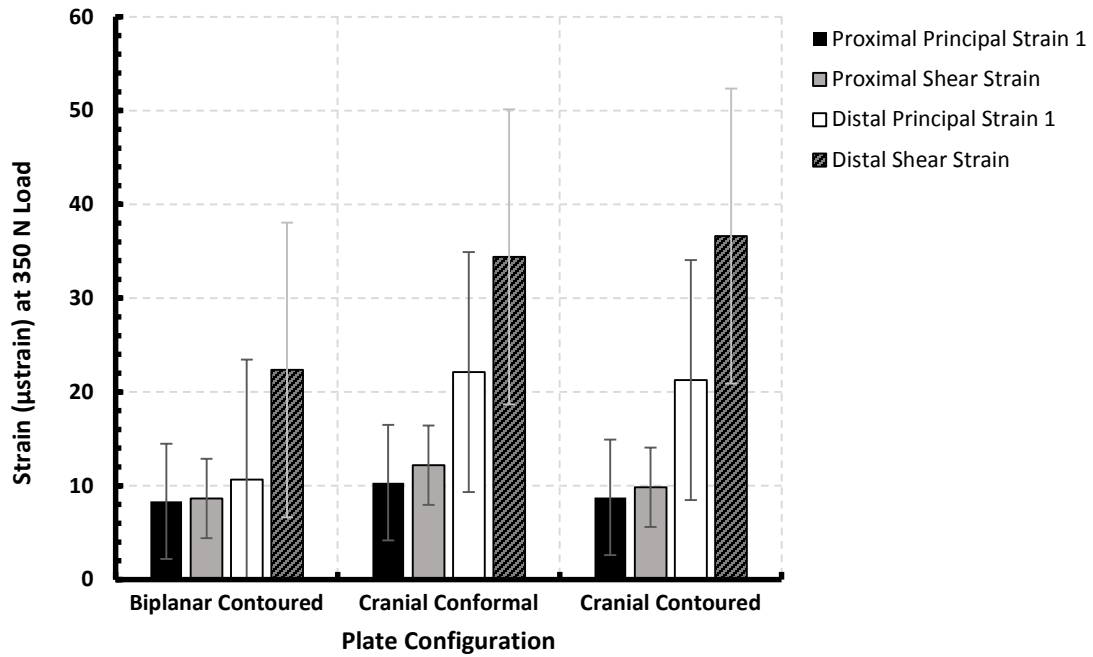


Figure 6.47: Recorded average maximum principal and shear strains for the proximal and distal locations during axial testing at a 350 N load as a function of implant configuration.

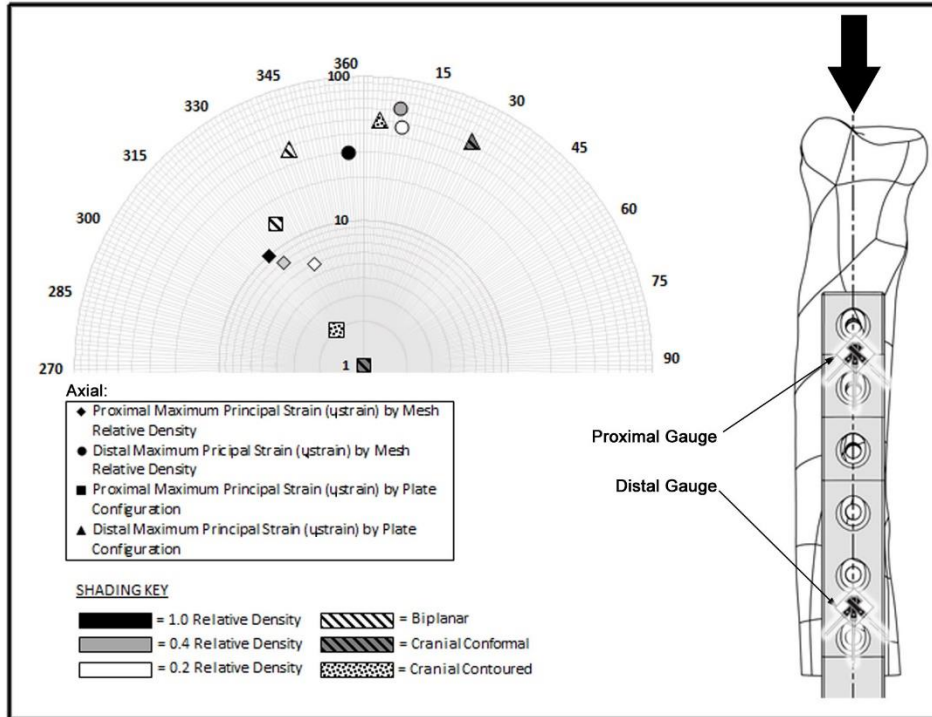


Figure 6.48: Polar plot showing the average magnitude and direction of the maximum principal strain (relative to the gauge center) during axial testing for each implant configuration. Log strain (μ strain) is represented on the vertical axis while the orientation angle (degrees) is represented on the circumference.

6.3.4.3 Torsional test results

Results are summarized in Figure 6.49. Mesh relative density had a significant influence on the torsional stiffness ($F < 0.0001$) in all cases ($p < 0.0002$). Analyzed by construct configuration, ANOVA results show no significant difference in torsional stiffness between 0.2 and 0.4 relative density meshes for the medially plated constructs ($F = 0.1076$). Blocked by mesh relative density, ANOVA shows that torsional stiffness was higher for biplanar plate configurations with 12 screws than those with six screws ($F = 0.0036$).

The data do not support a significant difference between the torsional stiffness of cranial conformal plates and cranial contoured plates ($F = 0.7246$). For different contoured plate positions, (cranial, medial, biplanar); significant differences in the means were detected using ANOVA blocked by mesh relative density ($F = 0.0001$). Medial plate construct torsional stiffness was significantly lower than biplanar or cranial plate stiffness ($p < 0.0001$). Cranial plate torsional stiffness was significantly lower than the biplanar configuration ($p = 0.0475$).

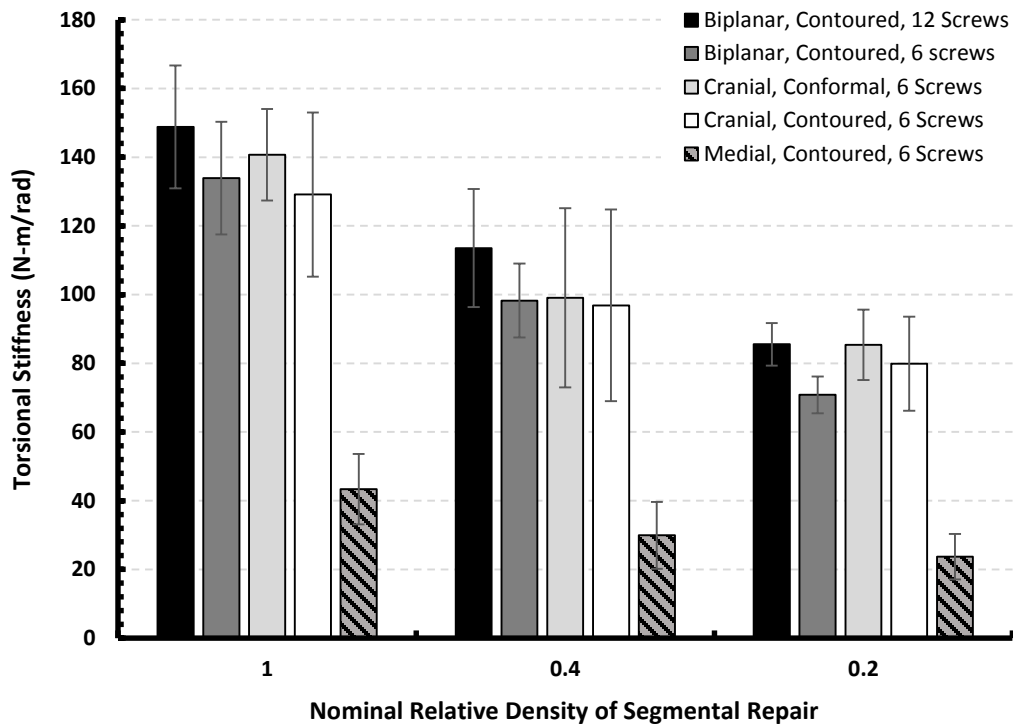


Figure 6.49: Chart showing the effect of the relative density of the segmental repair on the torsional stiffness for each plate configuration. Error bars indicate ± 1 standard deviation.

Strain results for the torsional tests are shown in Figures 6.50-6.53. Figure 6.54 shows the maximum principal strain angle and magnitude relative to the central axis of the construct. No significant differences among constructs with different relative density mesh structures or plate configurations were detected.

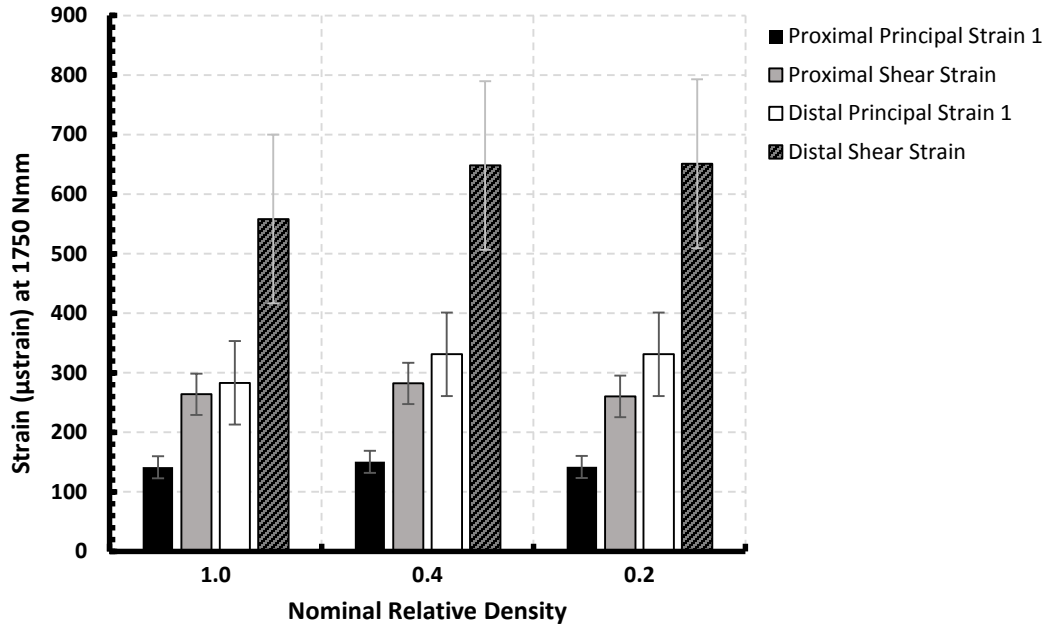


Figure 6.50: Recorded average maximum principal and shear strains for the proximal and distal locations during torsional testing at a 1750 Nmm moment as a function of implant relative density.

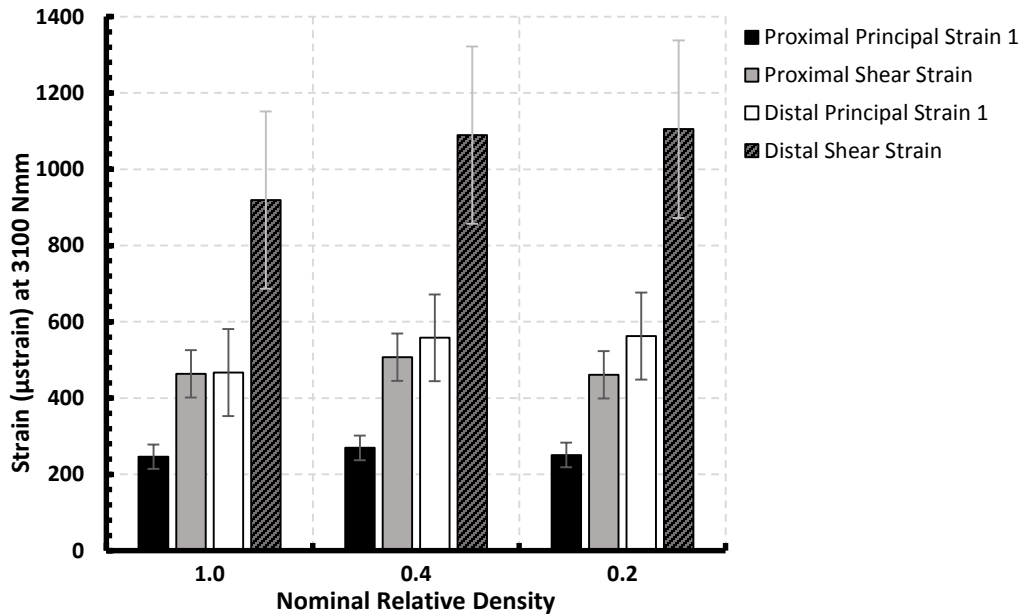


Figure 6.51: Recorded average maximum principal and shear strains for the proximal and distal locations during torsional testing at a 3100 Nmm moment as a function of implant relative density.

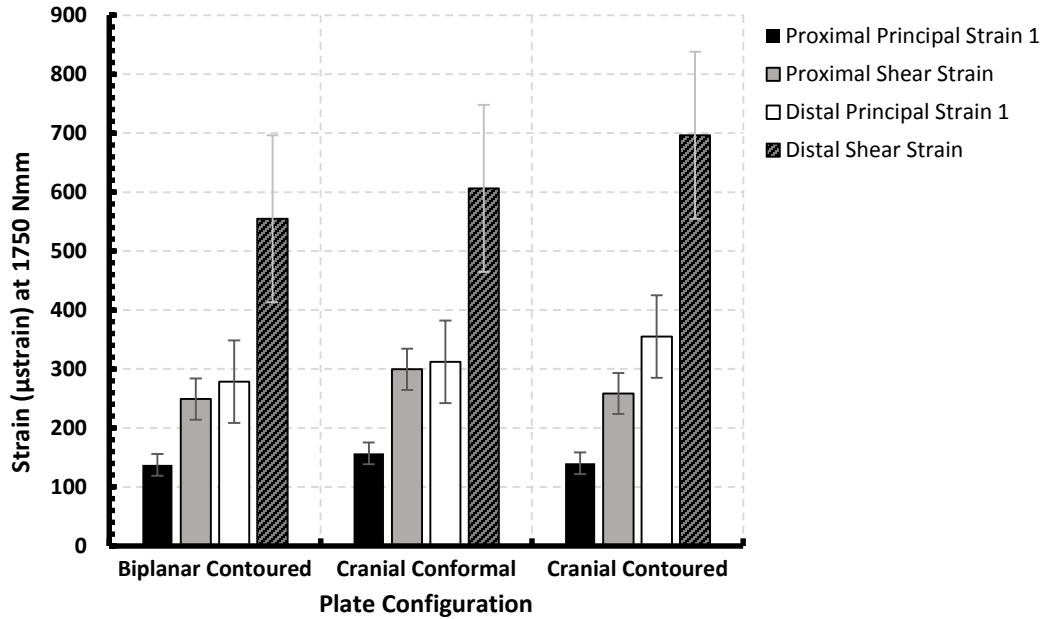


Figure 6.52: Recorded average maximum principal and shear strains for the proximal and distal locations during torsional testing at a 1750 N mm moment as a function of implant configuration.

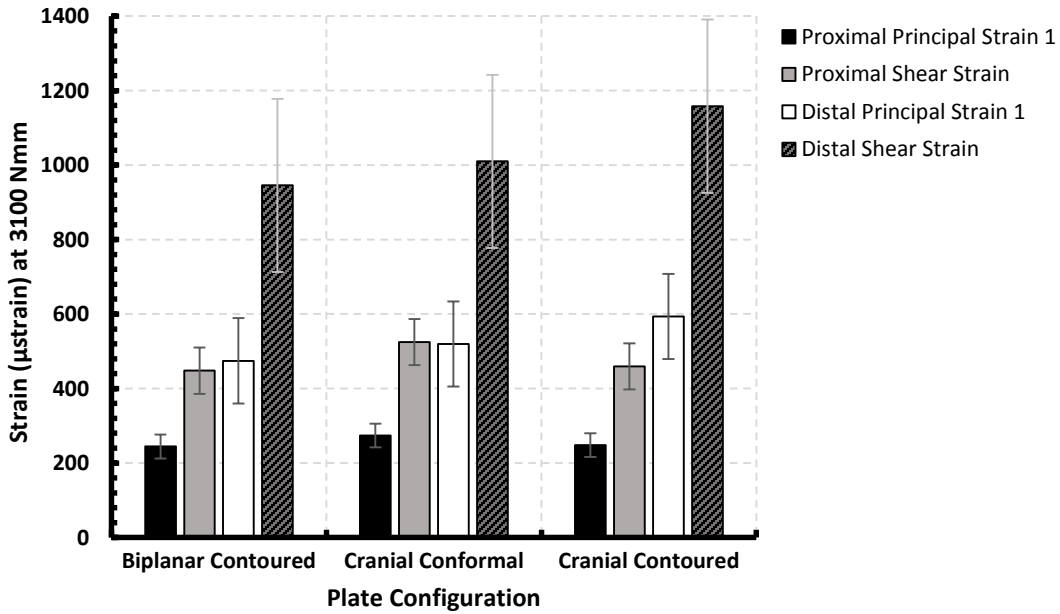


Figure 6.53: Recorded average maximum principal and shear strains for the proximal and distal locations during torsional testing at a 3100 N mm moment as a function of implant configuration.

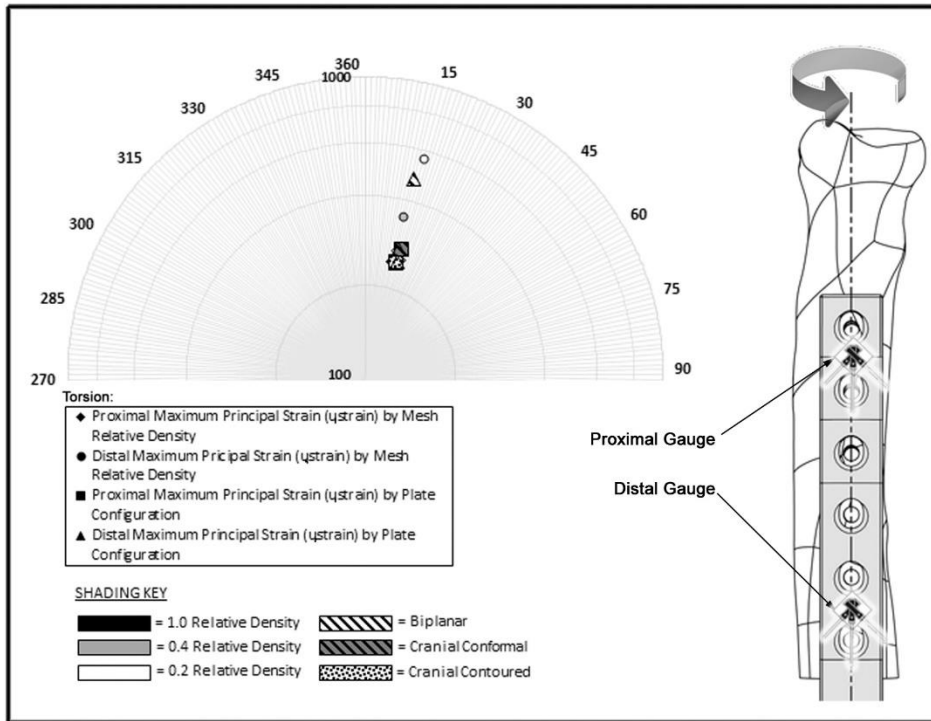


Figure 6.54: Polar plot showing the average magnitude and direction of the maximum principal strain (relative to the gauge center) during torsional testing for each implant configuration. Log strain (μ strain) is represented on the vertical axis while the orientation angle (degrees) is represented on the circumference.

6.4 Discussion

Parts fabricated using EBM typically have a surface roughness that is comparable to cast parts due to the sintering of particles adjacent to the melt pool. Materials fabricated using EBM can be fully dense and with properties closely matching the values found in cast and wrought materials with similar composition. The principal advantages of the EBM process are the relatively low input energy required, the good mechanical properties of the finished components, the ability to fabricate in a vacuum (which is important for highly reactive metals such as titanium), and the ability to manufacture relatively large metal components without high internal stresses. This report demonstrates the ability to utilize the EBM process to fabricate complex monolithic endoprostheses for canine limb sparing with geometric features not possible with traditional processes and quantifies the influence of these features through a series of controlled *ex-vivo* mechanical tests.

The ability to fabricate low stiffness non-stochastic structures in biocompatible materials such as titanium and titanium alloys represents a unique capability of direct metal additive manufacturing. While several studies discussed previously have highlighted this possibility, few have considered the use of such structures for the repair of large segmental defects in appendicular bone. Distal radial limb sparing in canines presents significant challenges because the margins of the resected tumor have been reported to be as high as 61% of the overall bone length (Liptak et al. 2006). This study demonstrates significant reductions in implant stiffness associated with decreases in the relative density of the EBM

mesh segment. Clinical reports, discussed in chapter 2, suggests that implant stiffness may play a role in the distribution of stresses at the bone implant interface; which in addition to influencing fatigue life of bone screws, also plays a role in remodeling of bone tissues. Early work by Bradley et al. observed an inverse relationship between the flexural rigidity of bone plates and the strength of bone taken from the opposite (non-plated) side of femurs after a healing period of 16 weeks (1979).

The stiffness of implants designed with medial plating only was significantly less than the other plate configurations. This effect was most noticeable in the torsional and the cantilever modes of testing. In addition, the influence of the number of screws in the biplanar configuration was significant in the axial and torsional bending modes when the graft segment stiffness was low (0.2 relative density). Liptak reported using an average of 5.5 screws for the proximal endoprosthesis plate (2006). The cross section of the medial plates was based on a theoretical moment of inertia in the cranio-caudal bending direction equivalent to the commercial (cranial) limb sparing plate. Renwick and Scurrill reported the use of a medially placed 2.7 mm compression plate in conjunction with a 3.5 mm cranially placed custom plate (no screws over lesion) in a case of cortical allograft limb sparing at the distal radial site (2008). However, no other precedent for a medial plate in canine limb sparing plate has been reported in the literature. The large differences evident in the data may be attributable to several contributing factors. Unlike the cranial plates, the surface area under the medial plate may not have provided sufficient contact with the graft segment to

assume a fixed or rigid connection. Further, in these tests it is impossible to dissociate the influence of the medial plate geometry from the difference in the diameter of screws used for fixation (2.7 mm for medial vs. 3.5 mm for cranial). The Arbeitsgemeinschaft für Osteosynthesefragen (AO) recommends that screw diameter not exceed 30% of the diameter of the host bone therefore the medial plate was designed for 2.7 mm cortical bone screws (Ruedi & Murphy, 2007). For dynamic compression plates, loads are transferred through friction at the bone implant interface, as opposed to bending of the screw shank (Cordey, Perren, & Steinemann, 2000). Wallace et al. found no statistically significant difference in the axial stiffness of cranially applied 5-hole 3.5 mm dynamic compression plate, a cranially applied 7-hole 3.5 mm T-plate, or a medially applied 7-hole 2.7 mm dynamic compression plate (1992).

Fujifilm prescale, a pressure sensitive film, was used to measure the interface contact area and pressure. Several types of film, corresponding to different pressure ranges, are available. The LW film (2.5 MPa to 10MPa) was used for the values reported in this study. Preliminary testing suggested that LLW film (< 2.5 MPa) became oversaturated and MW film (>10MPa) was not sensitive enough for these tests. It is therefore important to note that the contact area values reported here are associated with a particular pressure sensitivity. Several studies have utilized the prescale film to compare different plate designs such as limited contact plates (Xiong et al. 2010). Reductions in contact area associated with two limited contact plate designs were measured using prescale on human cadaveric specimens of

the right humerus, ulna and radius (Field, Edmonds-Wilson and Stanley, 2004). For stainless steel 4.5 mm and 3.5 mm dynamic compression and titanium limited contact-dynamic compression plates, the radius of curvature of the substrate (in this case acrylic rod rather than bone) was a significant predictor of interface contact area and average (Field, Hearn, and Caldwell, 1998). To date, the current literature on the subject has not addressed the question of whether additively manufactured conformal bone plates exhibit clinically relevant increases in contact area, reductions in contact pressure. Nor have they addressed the biological question of the clinical effects of an increase in contact area. Early studies have associated localized ischaemia associated with bone plate contact (Jacobs, Rahn & Perren, 1981). The conformal plates in this study showed significantly greater contact area compared to contoured plates. The surface roughness of the EBM fabricated plates resulted in non-homogeneous stains with (meso-scale) localized oversaturation. To address this, measurements of contact pressure were derived from composite averages ($n=15$) of the stains associated with each of the plate configurations. While these results suggest that interface contact pressure can be reduced by incorporating conformal plating, they also point out that minute variations in geometry (that may exceed additive machine tolerances) can result in localized pressure hot spots. Several measures of dispersion such as the convex hull, percent solidity and the pixel pair correlation function have been included in this study to further support these contact pressure results. Contact area (conformal or contoured) did not have a significant effect on the stiffness of the constructs in any of the testing modes. In this study, plates were carefully designed to isolate the effect of surface contact. The moments of

inertia, plate geometry, material, number of screws and screw torque were constant. This study does not address the potential for additive manufacturing to facilitate more complex plate designs and the associated possible improvements in stability.

Strain was recorded at two locations (distal and proximal) on the cranial surface of the limb sparing plates. In many cases, the relatively high variability, present in these data, does not support strong conclusions. This variability may be due, in part, to the small sample size ($n=3$) for each implant configuration, as well as, imperfections on the surface of the EBM fabricated plates that resulted. Nevertheless, these measurements illustrate trends that are promising and may warrant further investigation. In the cantilever and axial tests, maximum principal strains were lower for low stiffness implants (0.2 relative density) and biplanar plated implants resulted in lower strains than cranially plated implants. Difficulties associated with the placement and consistency of strain gauge measurements, particularly for biological specimens may necessitate improved methods of strain measurement.

7.0 IN VITRO EVALUATION OF NOVEL, PATIENT SPECIFIC LIMB SPARING ENDOPROSTHESES FABRICATED WITH ELECTRON BEAM MELTING

Direct metal additive manufacturing facilitates unprecedented freedom of implant design and manufacture. Three dimensional computer models of skeletal and soft tissue features derived from computed-tomography or magnetic resonance imaging systems provide a foundation for such designs. From these models a patient-specific implant may be designed, within a CAD (computer aided design) system, which exactly fits a given individual's skeletal anatomy. Control of mechanical/material properties, surface topography, and implant structure is also afforded. Yet, as previous sections have highlighted, many of these purported benefits have not been investigated or quantified. The aim of the previous chapters has been to isolate and elucidate the influence of key design parameters on the performance of implants. Using the results of the previous study, in Chapter 6, as a guide; the purpose of this study is to develop a patient specific implant for limb sparing by evaluating the biomechanical properties of cadaveric canine radii and carpi reconstructed with either a commercially available, 316 stainless steel limb sparing endoprosthesis (See section 2.2.5) or patient specific limb sparing implants directly manufactured using electron beam melting technology (EBM). It is hypothesized that when subjected to axial biomechanical testing, limbs reconstructed with the EBM manufactured titanium endoprosthesis will exhibit lower stiffness than the commercially available alternative and a strain distribution similar to untreated limbs.

7.1 Background

7.1.1 Relevant anatomy of the canine forelimb

Recent data suggest that the distal radius of canines is the most common site affected by osteosarcoma 34.9% (Liptak et al., 2004). While limb sparing impacts the entire thoracic limb, only the antebrachial, carpal and metacarpal regions are typically involved in limb sparing procedures. Limb sparing often involves pancarpal arthrodesis, and therefore a dorsal surgical approach. The bony anatomy of these regions is illustrated in Figure 7.1. The radius and ulna are the main load bearing structures of the antebrachium. The carpal bones are arranged in two levels; distal (carpals I, II, III, & IV) and proximal (radial carpal bone, ulnar carpal bone and the accessory carpal bone). These bone make up three joint interfaces; the antebrachiocarpal joint with the radius, the middle carpal between the carpal bones, and the carpometacarpal joint with the metacarpal bones (I, II, III, IV, & V). These joints facilitate allowing extension and flexion between the metacarpals and the radius. In the metacarpals, bones III and IV bear most of the load.

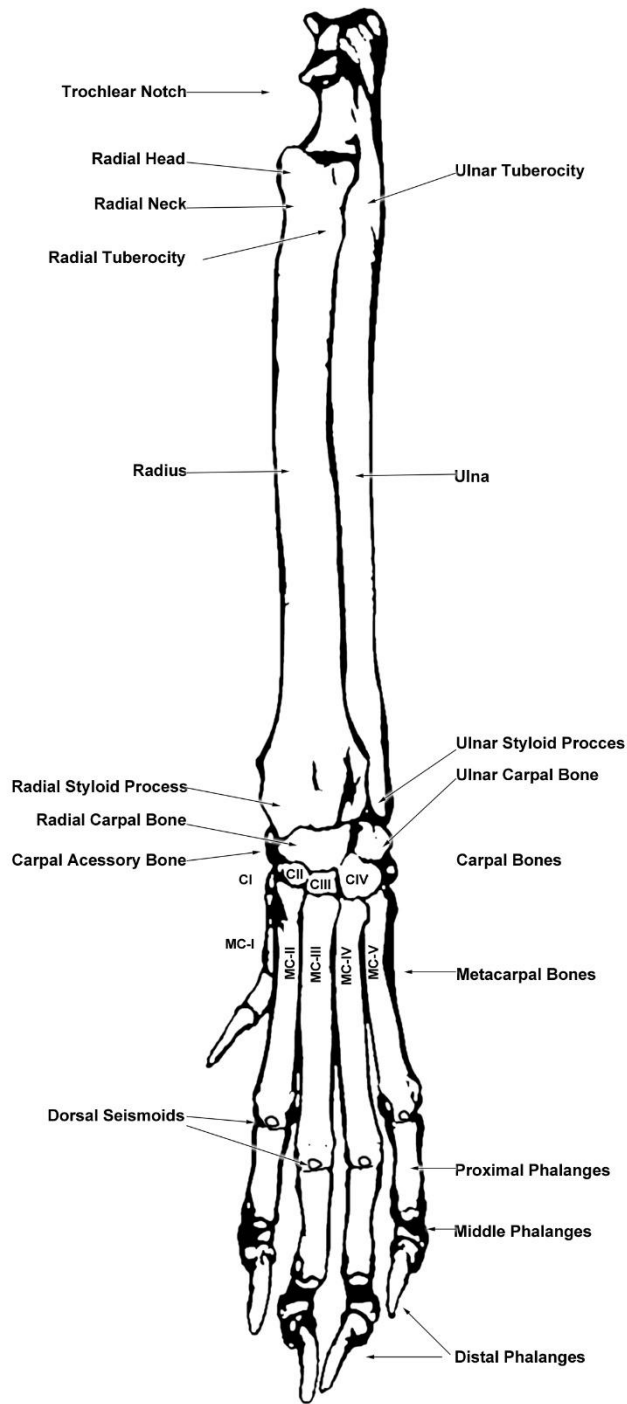


Figure 7.1: Illustration showing the bony anatomy of the canine forelimb.

7.1.2 Internal Fixation

Several bone plate configurations are currently available for limb sparing surgery. Choosing the proper constructs is important because its construct stiffness and yield points will affect the overall stability and outcome of the operated limb. Types of bone plates include the dynamic compression plate (DCP), the limited contact (low contact)-dynamic compression plate (LC-DCP), the locking compression plate (LCP), and string of pearls. Plates come in various sizes, both broad and narrow, typically designated by the size of the screw used for fixation. Special limb sparing plates are also available in both locking and conventional screw configurations (Liptak et al., 2006, Venzin et al., 2012).

Dynamic compression plates utilize eccentric countersinks that axially displace bone fragments upon screw insertion (Johnson, Houlton & Vannini, 2005). Displacements of up to 1 mm are possible in a single hole. In addition, the eccentric shape of the screw countersink allows screws to be inserted at inclined angles. Dynamic compression plates rely on friction at the bone-implant interface for providing stability. Cordey, Borgeaud, and Perren (2000) used composite beam theory to describe the relationship between screw tightness and the friction of the plate. Slippage occurs when the force exceeds the frictional force provided by the screw. However, some studies suggest that excessive plate-bone contact may contribute to cortical bone porosis after plate fixation resulting from damage to the cortical bone blood supply (Perren, 2002).

Limited contact-dynamic compression plates were developed to reduce contact between the plate and bone surface and preserve periosteal blood supply (Egol et al. 2004). However, as described in Chapter 6, recent studies have shown very little difference in the contact profile of DCP and LCDCP configurations (Field, Hearn & Caldwell, 1997). Jain et al (1998) compared the stiffness and strength of bone-plate constructs using low contact-dynamic compression plates and dynamic compression plates of various materials for fixation of canine radial osteotomies. No statistically significant difference in construct stiffness between the paired groups in the absence of the bone gap was detected. With the bone gap however, the DCP construct was stiffer than the LC-DCP construct, which were stiffer than the titanium LC-DCP construct. Results indicated the yield points of the titanium and stainless-steel LC-DCP constructs were similar, but a 59% greater yield point was found for the DCP construct compared to the stainless-steel LC-DCP construct.

The design of bone screws for internal fixation is also an important consideration. The screws provide the primary means of connection between the implant and the bone, at least until osseointegration or bone replacement follows. In the limb sparing studies reviewed, the ASIF/AO guidelines have been used. For many of the large breed dogs undergoing limb sparing this has meant using screws between 2.7mm and 4.5mm. According to ASIF/AO guidelines, the diameter of the screw used should not exceed 40% of the bone diameter (Johnson, Houlton & Vannini, 2005). For screws in the metacarpal bones, Piermattei & Flo (1997) recommend that screw diameters should not exceed 25-30% of the

bone diameter. Cortical bone screws (or cortex screws) are typically used in the diaphysis, and can engage one or both cortices, and are available in self-tapping and non-self-tapping varieties (for non-self-tapping screws, the holes must be pre-drilled and tapped). For non-locking plates the primary means of force transfer between the implant and the bone is through friction. Compression of the plate against the bone is induced by the screw. If the compression between the screw and the plate decays, rigidity is lost, and movement, non-union and failure of fixation may be the outcome (Shatzker, Horne, & Sumner-Smith, 1975).

7.1.3 Pancarpal arthrodesis

According to ASIF/AO guidelines, plates should be placed on the tension side of the bone whenever possible in order to minimize the motion between plated bone segments (Johnson, Houlton & Vannini, 2005). However, in the case of pancarpal arthrodesis, the plating is most often done on the compression surface of the metacarpal bone (Piermattei & Flo 2006). Palmar approaches have been attempted, however these tend to be more complicated, risky and prone to failure (Whitelock, Dyce, & Houlton, 1999). A dorsal approach to the radius is therefore preferred. Plates should be pre-bent to provide a 10-12° hyperextension of the carpus (Parker, Brown, & Wind, 1981). Although more recently, Liptak et al. have suggested that plastic deformation associated with pre-bending limb sparing plates may contribute to acute construct failure in an *in vitro* biomechanical test (2006). In a parallel clinical study plates were pre-bent 10°-15° (Liptak et. al 2006). In a

retrospective study of dogs with pancarpal arthrodesis using 2.7 mm or 3.5 mm bone plates, metacarpal fractures occurred in 6 out of 54 dogs. Frequency of failure was correlated to the percentage of the metacarpus covered by the plate. The results suggest that at least 50% of the third metacarpal bone be covered by the plate (Whitelock, Dyce, & Houlton, 1999). Pooya et al. suggest plate coverage of closer to 80% of the metacarpal for limb sparing with cortical allograft (2004). Pancarpal arthrodesis plates are typically secured to the third metacarpal bone, but more recently, studies have investigated new designs that are secured to both the third and the fourth metacarpals (Meeseon et al., 2012; Rothstock et al., 2012; Clark, Ferguson & Miller, 2009). These plates, manufactured by Orthomed LTD. (Halifax, West Yorkshire, England) utilize 3 pairs of 2.7 mm holes angled to improve the engagement of the screws with the metacarpal cortices.

7.2 Methods

7.2.1 Image acquisition

Five adult dogs weighing between 23.1 kg and 36.0 kg were collected after euthanasia. The dogs were euthanized at a local animal shelter for reasons unrelated to this study. Age, breed, gender, and method of euthanasia were recorded (See Appendix 1). The thoracic limbs were disarticulated at the glenohumeral joint, wrapped in saline solution (0.9% NaCl) moistened gauze, sealed in a plastic bag, and frozen at -20 °C. The limbs were later

thawed at room temperature and computed tomography imaging was performed using a helical CT (Siemens SOMATOM Sensation 64-slice configuration, Siemens Medical Solutions, Malvern, PA) with 512 x 512 resolution and 0° gantry tilt. The CT images were retro-reconstructed into 0.75 mm slices with a pixel size of 0.662 mm. An acrylic frame, shown in Figure 7.2, was fabricated to present the forelimbs at a carpal extension of 12° during scanning. Acrylic is relatively radiolucent and does not appreciably degrade scan quality.

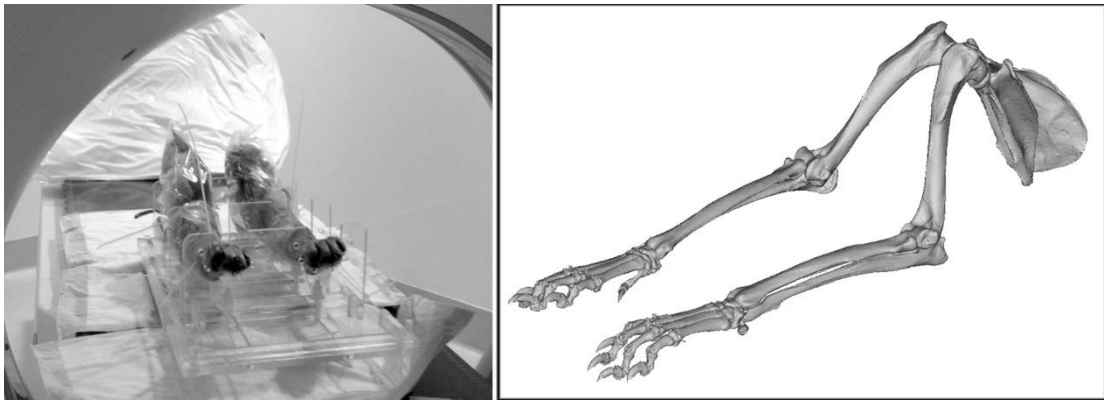


Figure 7.2: Photograph of the custom built fixture holding paired limbs with 12° carpal extension during CT scanning (left) and image of a 3D reconstruction of a scanned forelimb pair (right).

7.2.2 Patient Specific Implant Design

Mimics software (Materialise, Leuven, Belgium) was used to isolate and reconstruct the three-dimensional models of the limbs. Initial segmentation was achieved by thresholding below 226 Hounsfield units. Limbs were assigned to either the custom implant

group or the commercial implant group with a coin toss. For this study, only the limb receiving the custom implant was reconstructed with detail. Region growing isolated the limb of interest. The image masks were eroded by 1 pixel to individually segment each of the bones of the antebrachium and carpus. The segmented masks were then dilated by 1 pixel to restore the original size. Morphological closing was used to eliminate small holes in the model and open shells. Each model was remeshed to eliminate internal features and guarantee a polygonal shape quality threshold (base to height) greater than or equal to 0.7.

The design of each custom endoprosthesis followed a set of rules derived from the previous studies and available clinical data. Figure 7.3 illustrates a summary of the major process steps. For the commercial VOI plate the osseous defect is 98.0 mm, this feature was maintained in the custom device as well. However, it should be noted that the freeform nature of additive manufacturing could facilitate tighter surgical/oncological margins were they to be deemed appropriate. On the contrary, the external geometry of the graft segment was modeled after the geometry of the contralateral limb (as would likely be done in a clinical setting). Limited soft tissue coverage and relatively poor blood perfusion pointed towards minimizing the spatial disruption of these tissues (Withrow & Straw, 1996). The graft segment was populated with 5.0 mm, 30% relative density unit cells of rhombic dodecahedra (Figure 7.3-f).

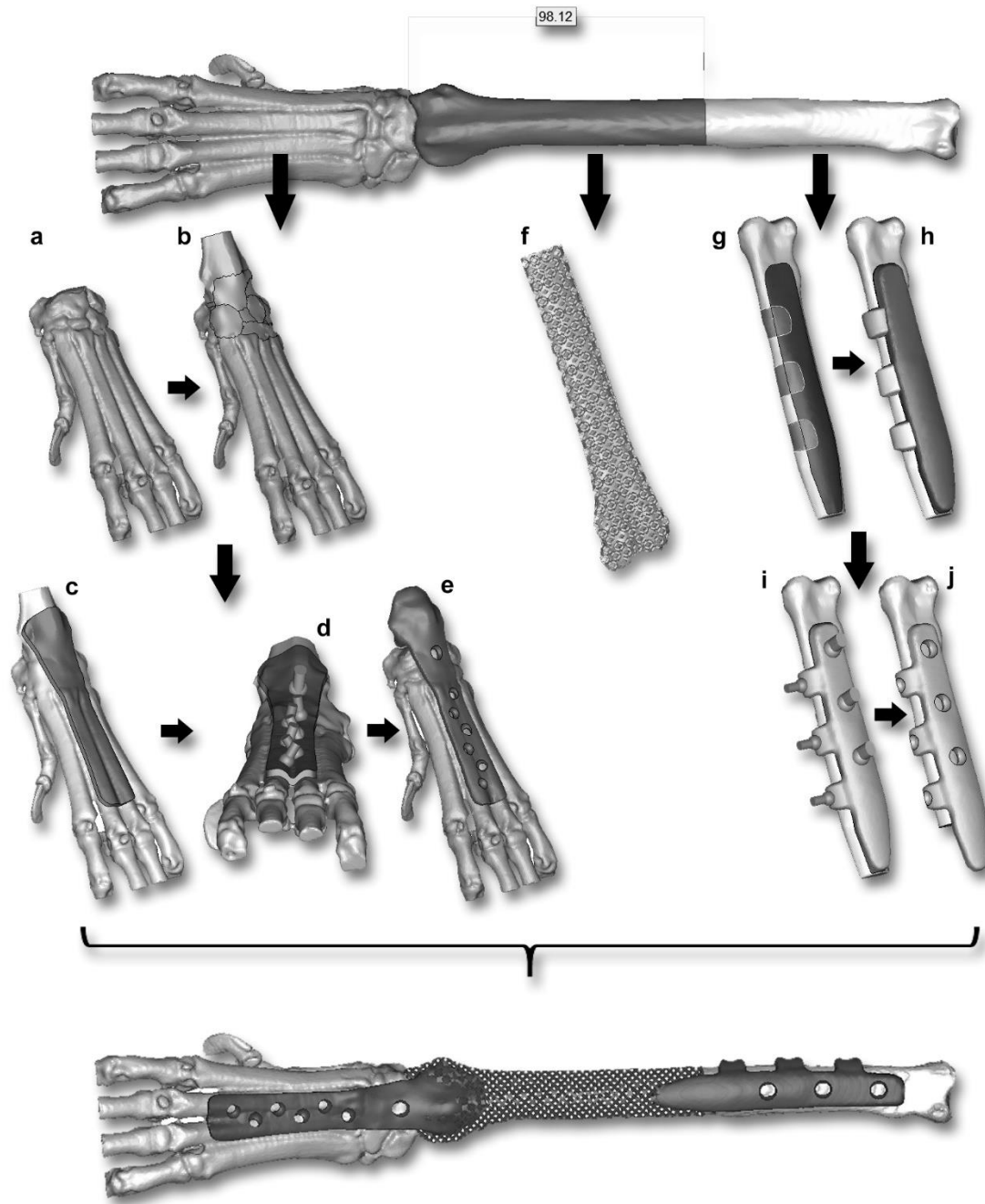


Figure 7.3: Illustration showing the process steps for the custom limb sparing endoprosthesis design.

The ventral surface of both the proximal (radial) and distal (metacarpal) plate sections were designed conformal to the bone surface. The results from the previous Chapter demonstrated increased contact area associated with conformal plates. While conformality alone did not result in an increase of stiffness as compared to standard, contoured, plates; other effects which may be realized such as improved stability and increased friction at the bone implant interface were not explicitly evaluated. Based on the results of Pooya et al. (2004), the minimum metacarpal plate coverage used here was 80%. In order to span the carpal bones and the gap at the antebrachiocarpal joint, the model surfaces were simplified. Curvature analysis (Figure 7.4) was used to identify and eliminate triangles with angles that deviate from those of nearest neighbors by a radius of curvature, 5 mm in these cases. The resulting holes were repaired using a tangential fill strategy with a 1 mm grid. The edges defined by the curvature analysis along the metacarpal also defined the medial and lateral edges of the distal plate. A smoothed curve was fit along these edges, the resultant cut surface was separated and extruded by 2.5 mm. Distally, six 2.7 mm cortical bone screw holes were located for securing the metacarpal bones. The holes were evenly spaced between the proximal head of the 4th metacarpal and a locus 8 mm proximal to the distal end of the plate. Screw holes were placed by a Boolean subtraction of the positive geometry of the countersink and hole from the plate geometry. These were initially aligned normal to the surface of the plate. The orientation and location of the screws were modeled after the OrthoMed™ pancarpal arthrodesis plate described previously. On the 3rd metacarpal bone the screws were directed medially; the distal-most screw was angled by 30°, the middle

screw was angled by 20° and the proximal-most screw was angled by 10°. In the same way the screws of the 4th metacarpal were directed laterally. The screw holes are staggered such that the distal-most hole was located on the 3rd metacarpal and the proximal-most hole is located on the 4th metacarpal. One 3.5 mm cortical bone screw was placed at the radial carpal bone.

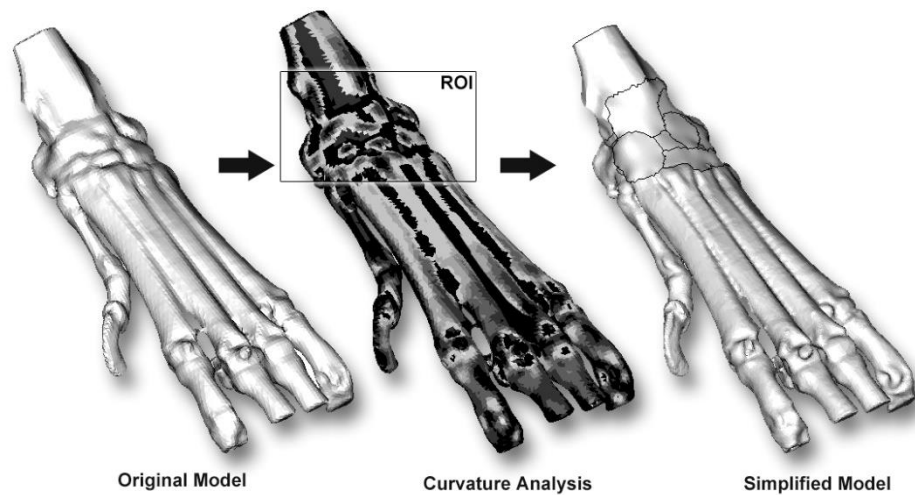


Figure 7.4: Screen capture showing the use of curvature analysis to simplify the carpal joints for plate design.

The proximal plate covered 80% of the proximal residual portion of the radius, in all cases this resulted in termination of the proximal end of the implant at the level of the radial tuberosity. Curvature analysis, with a threshold radius of 8 mm, was conducted to define the boundary path of the medial and lateral edges of the cranial portion of the proximal plate. A smoothed curve was fit to the marked triangles and the resultant surface was cut, separated and extruded by 3.5 mm (Figure 7.5).

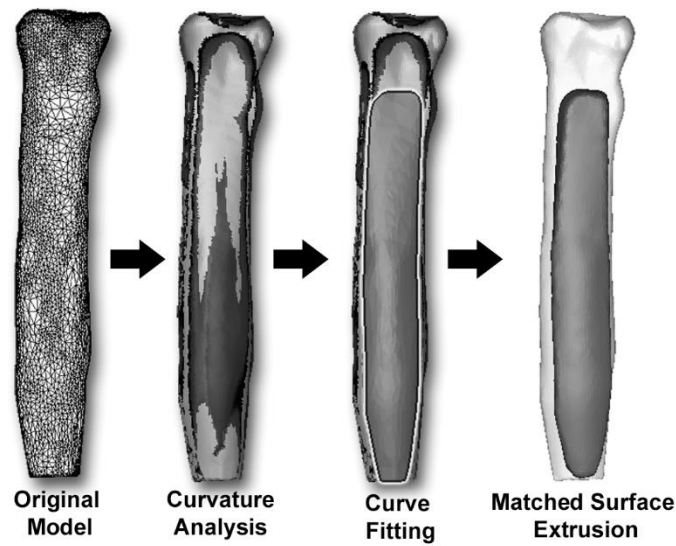


Figure 7.5: Screen capture illustrating the use of curvature analysis for defining custom plate geometry.

Six screws were located proximally. In the clinical study by Liptak et al. (2006) a minimum of five 3.5 mm or 4.5 mm cortical bone screws were placed in the proximal radius. In the custom implant, three 3.5 mm cortical bone screws were located cranially and three 2.7 mm screws were located medially since AO practices require that bone screw diameter not exceed 30% of the bone diameter. The distance between the holes was evenly spaced and the distance between the distal most hole on the proximal radius and the graft segment was 8 mm. The curves for the medial tabs were attached to the radial surface midway between the cranial screw holes. These curves were extruded by 2.5 mm and a Boolean addition was applied with the cranial plate. As Chapter 6 demonstrated, stiffness of constructs was not influenced by the presence of the medial plate in the biplanar configuration as compared to

cranial plating alone. In this design, the biplanar fixation was designed with 3 medially placed tabs connected to the edge of the cranial plate.

No precedent exists in the literature, except for the *in vitro* study presented in Chapter 6, in which the transition from solid portions to porous portions of implants is investigated. The proximal segment extends 18 mm into the mesh structure, and the distal plate extends 22 mm into the mesh structure. The outer surfaces of the radial segment were offset inward by 1.5 mm to create a solid core surrounded by the mesh structures. A 1.5 mm thick mesh layer separated the solid core from the articulating surface of the radial carpal joint.

7.2.3 Patient Specific Implant Fabrication

An Arcam model A2 EBM machine was used to fabricate the samples for these experiments. All processing parameters used were the standard and available from Arcam for Ti6Al4V (Arcam Build Control Software V3.2, SP2). The solid and mesh portions of the five implants were arranged on a build platform (190 mm x 190 mm x 10 mm) to minimize the requirement for supporting structures using Materialise Magics software. Block supporting structures, 10 mm in length, were added to the downfacing surfaces of the medial tabs and the three proximal screw holes. Additional supports connected the distal edge of the implants to the starting platform. Figure 7.6 shows the build layout, the identification of each implant was embossed on the cranial surface proximal to the last hole.

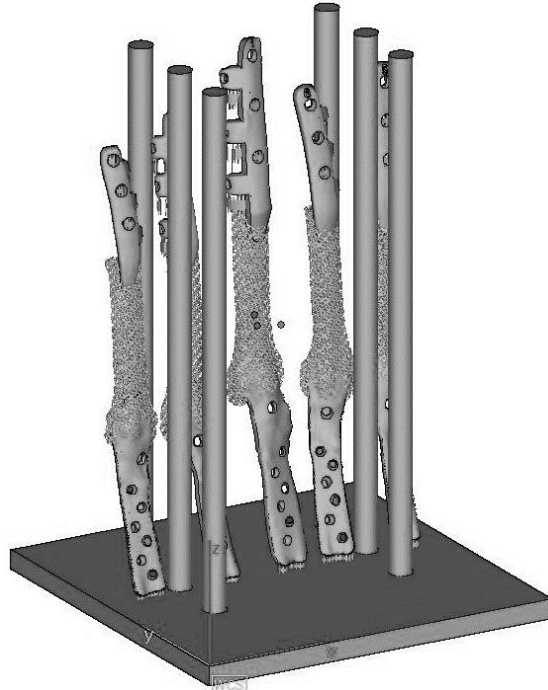


Figure 7.6: Screen capture showing the layout of the EBM build platform.

In addition, six, 12.7 mm diameter cylinders were placed in proximity to the implants; the height of which was 167 mm (5 mm taller than the tallest implant). These samples were placed to provide test coupons for material characterization. The implants were fabricated from Ti6Al4V gas atomized powder (Arcam) with a specified size distribution from 45 to 105 μm . The build required 46 hours to complete with 12 additional hours of cool-down time. Upon removal, the samples were encased in lightly sintered titanium powder that was removed by abrasive blasting using additional Ti6Al4V powder as media. Powder removal was observed by visual inspection with the aid of a white back light. Figure 7.7 shows a photograph of the samples

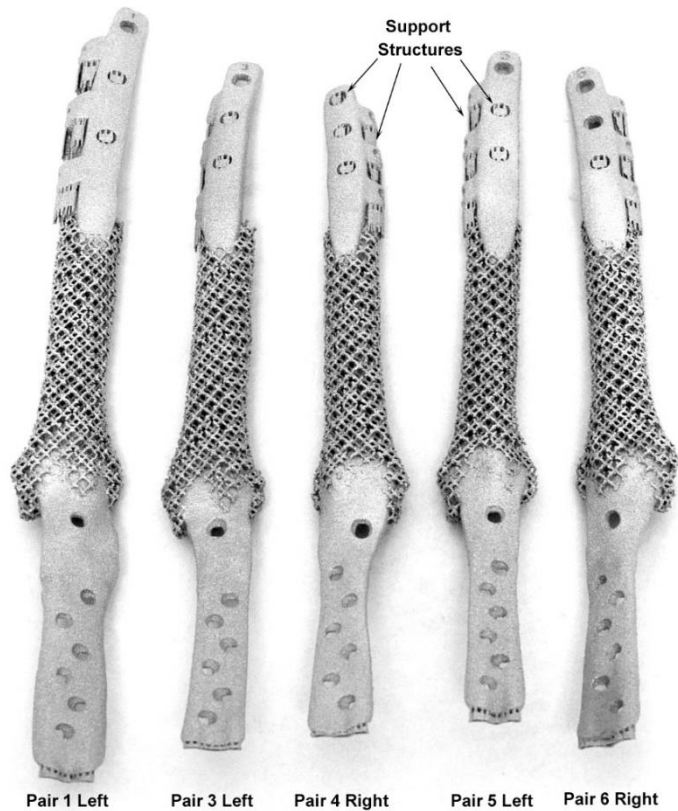


Figure 7.7: Photograph showing the five custom endoprostheses after EBM processing and powder removal.

Support structures were removed by hand. Manual surface finishing, to remove the relatively rough surface produced by the EBM was progressively achieved using a high speed finisher (Kalamazoo Industries, Kalamazoo, MI) with 80, 120, and 220 grit belts. Screw countersinks were CNC machined (Haas VF3). Surfaces were polished on a jeweler's buffing wheel with tripoli compound (Divine Brothers Corp., Utica, NY). Figure 7.8 shows a photograph of the finished implants. Figure 7.9 shows a photograph of the two implant configurations evaluated in this study.



Figure 7.1: Photograph showing the five custom endoprostheses after finishing.



Figure 7.9: Photograph showing a side-by-side comparison of the two endoprosthesis configurations evaluated in this study. The EBM fabricated custom endoprosthesis (top) and the commercial endoprosthesis (bottom).

7.2.4 Specimen preparation

Soft tissues surrounding the humerus were excised at a location approximately 35.0 mm proximal to the center of the lateral epicondyle. The ligaments of the elbow joint were left intact. The proximal head of the humerus was ostotomized at the surgical neck. Additionally, soft tissues of the paw distal to the midline of the proximal phalanges, including the digital pads, were excised. Ligamentous structures and the metacarpal pad were preserved.

Figure 7.10 shows the potting of one of the canine forelimbs. 1.5 inch nominal schedule 40 PVC pipe (48.26 mm outer diameter) was cut to a length of 200 mm. Three radial holes were drilled and threaded (M8 x 1) at a location 12 mm from one end, and

another 3 holes were located at a distance of 100 mm from the same end. Bolts threaded through these holes enabled the alignment and temporary fixation of the humerus prior to encasing the remaining volume in polyester resin compound (Bondo™, 3M corporation). The distal humerus was potted to a location 20 mm above the soft tissue resection. The test fixture, mounted and leveled on an extruded aluminum frame was used to align the potting of the paw in 3.0 inch nominal schedule 40 PVC pipe (88.9 mm outer diameter) was cut to a length of 63 mm. The pipe was initially filled with the polyester resin to a depth of 25 mm. After curing the paw was centered in the pipe, aligned with the loading axis of the fixture. A 44 N preload was applied with a hydraulic actuator and the bones of the paw were potted to the level of the proximal phalanges.

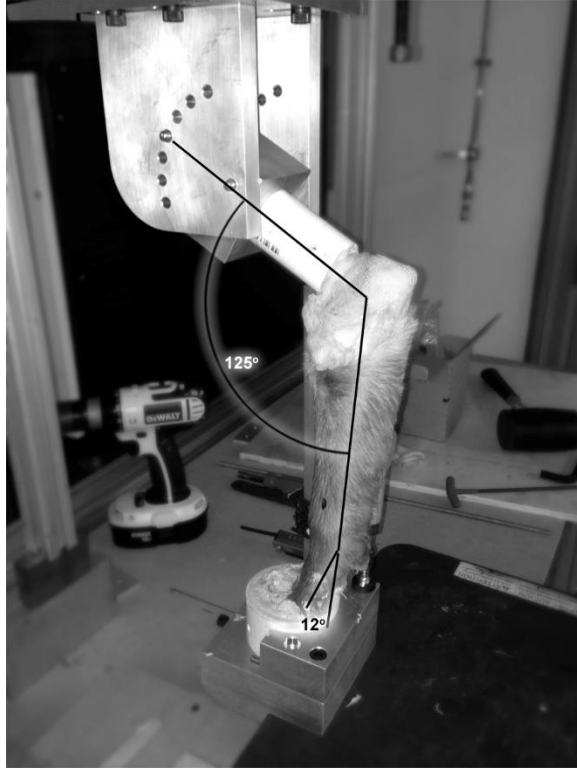


Figure 7.10: Photograph showing the use of the test fixture to align the limbs during potting.

7.2.5 Surgical placement of endoprostheses

Limb sparing surgery was carried out over two periods and was performed by a veterinary surgeon (Marcellin-Little). First, soft tissue incisions were made to expose the radius for strain gauge placement. The limbs were then subjected to pre-surgical mechanical testing, after which, the implants were placed. Limbs were thawed below room temperature for 24 hours prior to surgery. A dorsolateral incision level with the lateral side of the radius was made starting from about 40 mm distal to the elbow. At the level of the distal radius, the incision migrated dorsally following towards the centerline of the 3rd metacarpal (Figure

7.11). The extensor carpi radialis was separated from the cranial surface of the radius , but the tendons were left intact.



Figure 7.11: Photograph showing the dorsolateral incision and the surgical approach.

3D models of the custom proximal limb sparing plates (Figure 7.12) were fabricated using an Objet Connex 350 (Stratasys, Eden Prairie, IN). Using digital materials, a mixture of VeroWhite™ material mixed with Tango-Plus™. These guide plates were placed with the distal ends 98 mm proximal to the styloid process, the medial tabs provided mediolateral registration.

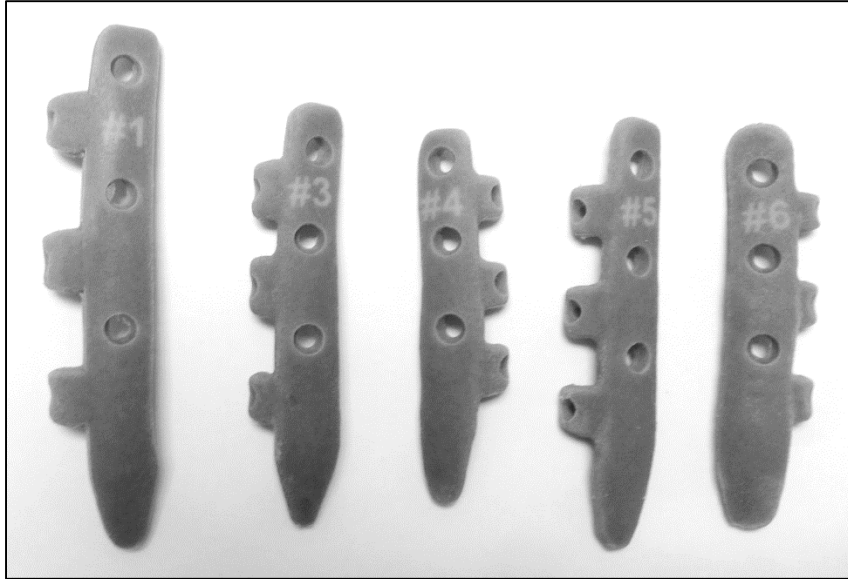


Figure 7.12: Photograph showing additively manufactured guides for strain gauge placement.

Calibrated, preassembled, 350 Ω uniaxial strain gauges (Micro-Measurements, Raleigh, NC) were applied to the cranial surface of the radius at a location 3 mm proximal to the planned osteotomy and adjacent to the lateral side of the plate (Figure 7.13). The periosteum was lightly scraped from the bone surface with a scalpel followed by swabbing for 5 seconds with Micromasurements M-Prep Conditioner A (MCA-1, Phosphoric Acid) then 5 seconds of swabbing with Micromasurements M-Prep Neutralizer (MN5A-1, Ammonia/water). Cyanoacrylate adhesive was applied to the underside of the strain gauge. Pressure was applied with a silicone rubber block for at least 15 seconds. The leads were coated with RTV silicone for protection. The cable was routed proximally, toward the elbow, under the lateral digital extensor. A strain relief loop was wrapped once around the lateral digital extensor. The 3-wire cable was then routed through a small incision in the skin behind

the elbow and terminated in an RJ45 connection. After pre-surgical mechanical testing the exposed soft tissues of the forearm were wrapped in new saline solution (0.9% NaCl) moistened gauze, sealed in plastic bags, and frozen at -20 °C.

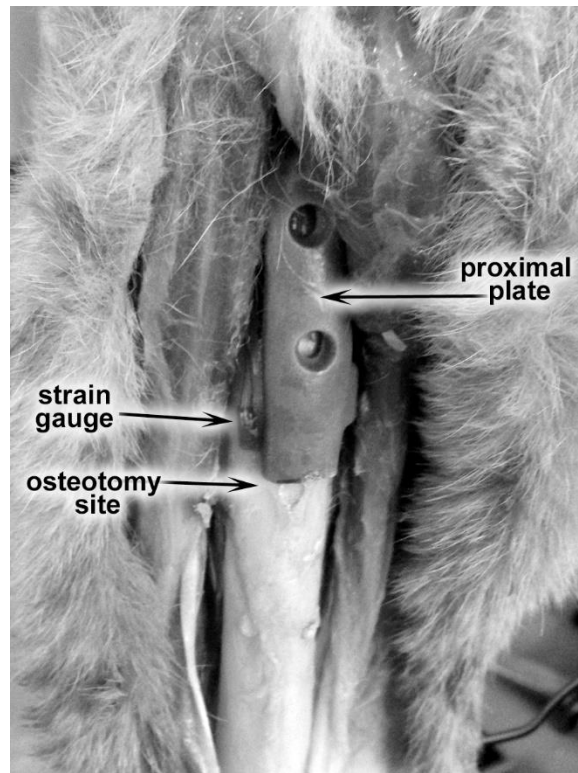


Figure 7.13: Photograph showing the placement of the uniaxial strain gauge on the dorsolateral surface proximal to the osteotomy site.

Prior to surgical placement of the limb sparing devices, the limbs were thawed at room temperature. The sequence in which implants were placed in the assigned limbs was randomized according to the table below. Limb sparing technique followed standard procedure (e.g. Withrow & Vail., 2007; LaRue et. al., 1989; Liptak et. al. 2006).

Table 7.1: Randomization schedule for the sequence of surgeries.

Surgical Sequence	Specimen	Type
1	Pair 3 Right	VOI
2	Pair 5 Right	VOI
3	Pair 5 Left	Custom
4	Pair 4 Left	VOI
5	Pair 6 Left	VOI
6	Pair 6 Right	Custom
7	Pair 1 Left	Custom
8	Pair 4 Right	Custom
9	Pair 3 Left	Custom
10	Pair 1 Right	VOI

An oscillating saw was used to osteotomize the radius perpendicular to the longitudinal axis of the bone 98 mm proximal to distal radial concavity for the commercial endoprotheses and 98 mm proximal to the styloid process for custom endoprotheses. The distal portion of the radius was removed *en bloc*. The ulna was left intact, in the biomechanical study by Liptak et. al., no difference in stiffness was associated with the presence or absence of the ulna. Cartilage was removed from the proximal surface of the radiocarpal bone with a burr. For the commercial plates, the radial defect was filled with a 98 mm stainless steel spacer fixed to a limb sparing plate (Veterinary Orthopedic Implants) with 2 machine screws. The plate was contoured to the bone surface with a plate-bending press (DePuy SynthesVet) and the distal portion of the arthrodesis plate was pre bent to provide 12° of hyperextension.

The proximal portion of the plate was applied to the cranial remnant of the radius and secured with six 3.5 mm stainless steel cortex screws (DePuy SynthesVet). The distal segment was then fixed with 2.7 mm stainless steel cortex screws (DePuy SynthesVet). A single 3.5 mm stainless steel cortex screw was placed in the radial carpal bone. The technique for placement of the custom limb sparing is nearly identical to that of the commercial endoprosthesis. However, all screws were titanium. The proximal plate was fixed cranially with three 3.5 mm titanium cortex screws obtained from the same lot (DePuy SynthesVet), and medially with three 2.7 mm titanium cortex screws (DePuy SynthesVet). The conformal plates require no pre-bending or contouring. The angle of carpal extension was 12°. Distally six 2.7 mm titanium cortex screws were placed, three each, in the 3rd and 4th metacarpal. A 3.5 mm titanium cortex screw was placed in the radial carpal bone. In all cases screw torque was limited to 2.0 Nm by using a calibrated precision torque screwdriver, adjustable in 0.1 Nm increments from 1.2-3.0 Nm, accurate to within $\pm 6\%$ (EN ISO 6789, Wera, Germany). Figure 7.14 shows a photograph of the placement of the proximal portion of the custom implant. Figure 7.15 shows a photograph of the two implant configurations after placement in a matched pair of forelimbs.



Figure 7.14: Photograph showing the placement of the proximal portion of a custom endoprosthesis.



Figure 7.15: Photographs showing the placement of commercial (top) and custom (bottom) endoprostheses immediately after surgical placement.

7.2.6 Mechanical testing of limb sparing constructs

Mechanical testing was carried out before surgical placement of implants (Figure 7.16) and after surgical placement of implants (Figure 7.17) using an ATS 1620C testing machine. ATS TestVue software (v4.22.00) recorded crosshead position and loading data from a 22,241 N capacity load cell (1210AF-5K-B) at 95 Hz. Strain data were recorded by a Micro-Measurements system 7000 data acquisition system with 8 channel DAQ card and StrainSmart software (Version 4.7.25.1161). Strain gage resistance (350 Ω), gauge factor ($2.14 \pm 0.5\%$ @ 24°C) and temperature correction factors were provided by the manufacturer and input into the system. Strain data were collected in a quarter bridge configuration with a 5 V excitation and a sampling rate of (10 Hz). A custom aluminum fixture was fabricated to present the limb for testing at varying angles of elbow flexion. The fixture was modeled after a similar design used by Liptak et.al. in the biomechanical study of limb sparing devices comparing the commercial metal endoprostheses to cortical allograft endoprostheses (2006). The potted humerus was clamped in a split housing precisely matching the outer diameter of the PVC pipe and a 0.127 mm interference. The housing was pinned to the upper frame with two ground 0.3125 inch (7.938 mm) pins, one pivot cranially and a second which facilitated adjusting the elbow flexion in 15° increments. The upper assembly was bolted to the moving crosshead of the ATS testing machine with six 3/8-24 socket head cap screws 50.8 mm in length. The pivot block was adjustable and placed such that the antebrachium was in line

with the loading axis. The distal pot was also clamped in a split housing of similar design and was mounted directly to the load cell with a 5/8-18 socket head cap screw.



Figure 7.16: Photograph of the biomechanical testing of a forelimb prior to the surgical placement of an endoprosthesis.

Loading rate dependency and fixture alignment sensitivity were investigated with a 6th pair of limbs that were not included in the study. In the studies of Liptak et. al. (2006) and Pooya et al. (2004) the loading rate was 300 N/s; to mitigate viscoelastic effects associated with such high rates and the difficulty in validating load based control, this investigation used displacement based control. No difference in stiffness was detected in loading rates ranging from 2.54 mm/min to 25.4 mm/min. Additionally, no difference in stiffness was detected between different elbow flexion angles or different humeral clamping locations (data no shown). The potted humerus was consistently placed such that the proximal end protruded 50.8 mm beyond the face of the split housing and an elbow flexion angle of 125°. For both pre-surgical and post-surgical tests the loading was applied at a rate of 25.4 mm/min to a load of 260 N and unloaded to 12 N at a rate of 127 mm/min for ten cycles. Construct stiffness was calculated from the linear least squares regression of the elastic portion of the 10th loading cycle.

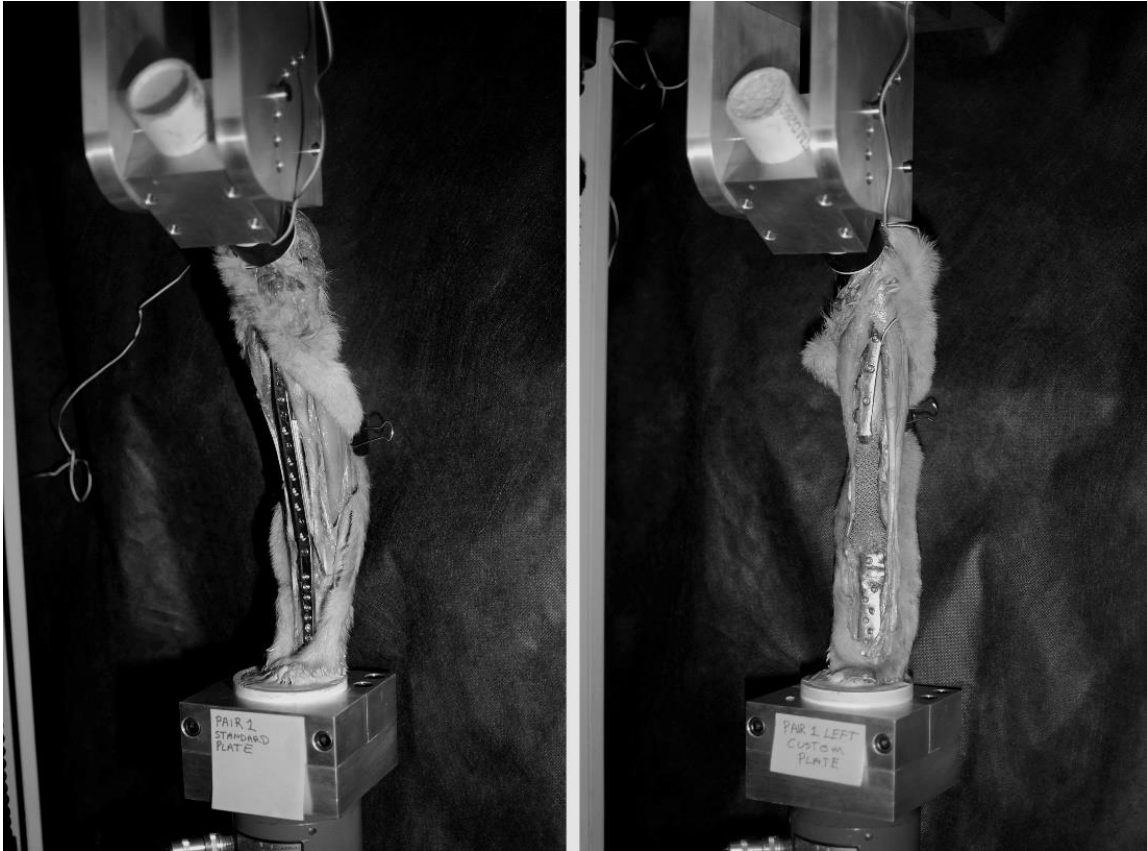


Figure 7.17: Photographs showing the biomechanical testing of forelimbs after placement of commercial (left) and custom (right) endoprostheses.

7.3 Results

7.3.1 Implant measurements

Measurements of anatomic features of paired limbs were measured from CT data prior to surgical limb sparing. These data were compared using the Wilcoxon signed rank test because of the small sample size and associated difficulties in determining the distribution of the sample population. No difference was detected in the length of paired radii, metacarpals (III & IV), or ulnae ($W=0.0313$). After reconstruction measurements of the endoprosthesis were collected, Table 7.2 highlights some of the key differences between the two endoprosthesis groups.

Table 7.2: Comparison between commercial and custom endoprostheses.

	Commercial Endoprosthesis	Custom Endoprosthesis
Material	316 Stainless Steel	Grade 5 Titanium, Ti6Al4V
Osseous Defect Length	98 mm	95 mm
Distal Screw Number	6, 2.7 mm stainless steel	6, 2.7 mm titanium
Proximal Screw Number	6, 3.5 mm stainless steel	3, 3.5 mm titanium cranially placed 3, 2.7 mm titanium medially placed
Implant Mass	164.88 ± 0.21 g	54.87±3.03
Arthrodesis Angle	12°	12°

7.3.2 Mechanical test Results

For each limb pair, the construct/limb stiffness, energy absorbed at 150 N and Strain at 150 N was recorded. Stiffness was calculated as the slope of the linear portion of the load displacement data and the energy at 150 N was calculated from the area under the normalized load – displacement plot. Paired mechanical test data were analyzed using the Wilcoxon signed rank test. Figure 7.18 shows the average stiffness for the limbs before and after surgery, for each configuration, the error bars indicate the 95% confidence interval.

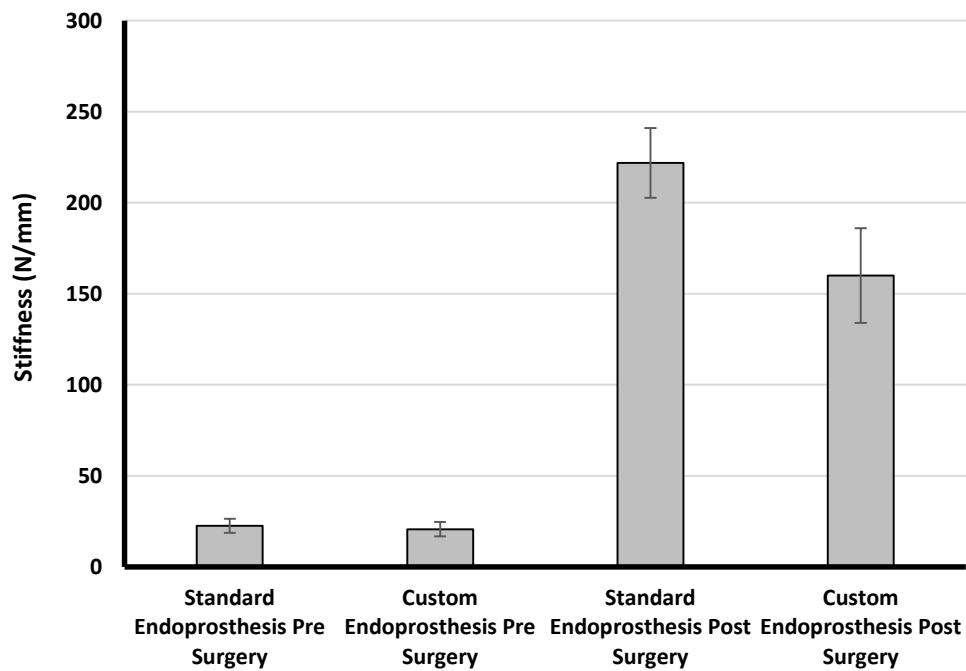


Figure 7.18: Graph showing the average stiffness of limbs before surgery and after placement of endoprostheses.

No difference in the stiffness was detected between paired intact limbs prior to surgery ($W = 0.9063$). Limbs reconstructed with the commercial and custom endoprosthesis exhibited significantly higher stiffness after surgery than before surgery ($W=0.0313$ and 0.0313 respectively). Commercial endoprostheses were significantly stiffer than custom endoprostheses ($W=0.0313$).

Figure 7.19 shows the average energy (elastic potential energy) stored in the limbs before and after surgery, for each configuration at a load of 150 N (approximately 60% of the weight of the smallest dog), the error bars indicate the 95% confidence interval.

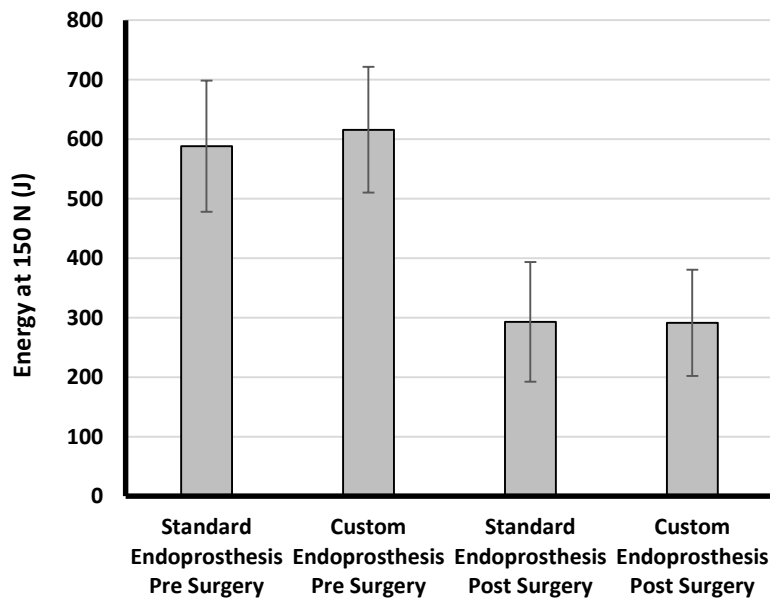


Figure 7.19: Graph showing the average elastic potential energy stored at a load of 150 N for limbs before and after placement of endoprostheses.

No difference in the stiffness was detected between paired intact limbs prior to surgery ($W = 0.6250$). Limbs reconstructed with the commercial and custom endoprostheses exhibited significantly lower stored energy after surgery ($W=0.0313$ and 0.0313 respectively). No difference in stored energy at 150 N load was detected between Commercial endoprostheses and custom endoprostheses ($W=0.500$).

Figure 7.20 shows the average measured strain at the distal portion of the radial remnant before and after surgery, for each implant configuration at a load of 150 N.

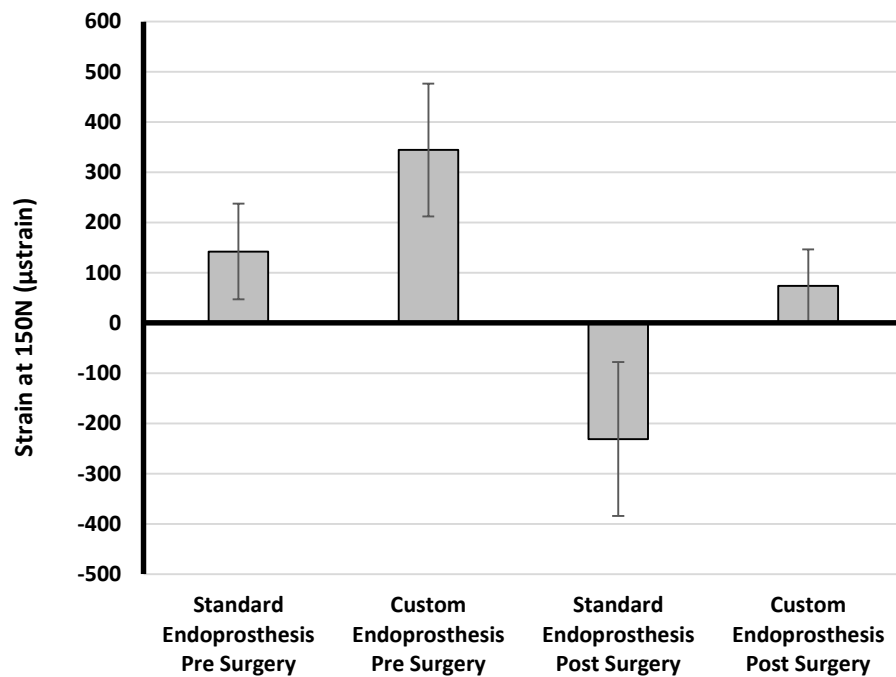


Figure 7.20: Graph showing the strain at a load of 150 N for limbs before surgery and after placement of endoprostheses.

No difference was detected in presurgical strains between limb pairs ($W=0.125$). Limbs treated with commercial endoprosthesis exhibited significantly different strains compared to presurgical strains ($W=0.0313$). While presurgical strains tended to be tensile, post surgical strains were compressive on the cranial surface of the distal portion of the radial remnant. Strains in limbs reconstructed with custom endoprostheses remained tensile, however were significantly lower than untreated limbs ($W = 0.0313$).

7.3.3 Surgical Duration

The duration of the surgeries, shown in Figure 7.21 were recorded from the start of the osteotomy to the placement of the final screw and excludes the time associated with initial incisions and closure. One way analysis of variance was used to evaluate surgical durations. The average duration of the surgeries for commercial endoprostheses was significantly longer than the average duration of the surgeries for custom endoprostheses ($p=0.0098$).

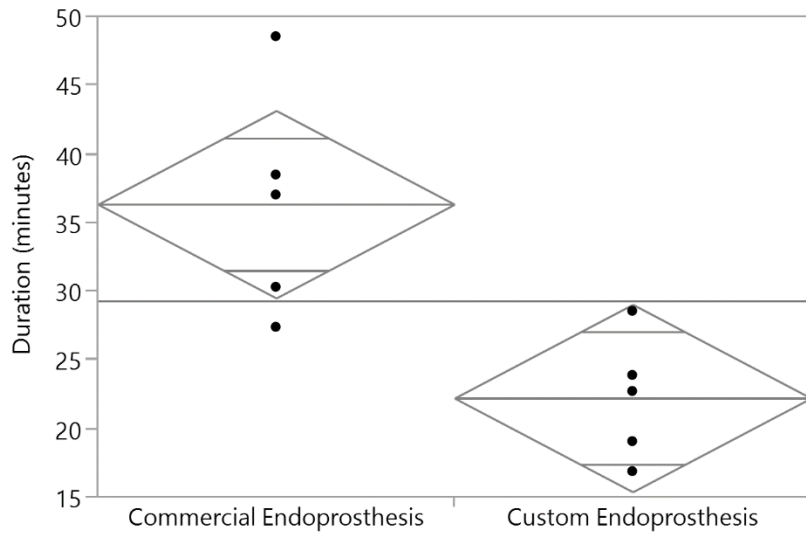


Figure 7.21: Plot showing ANOVA results comparing the duration of the surgeries for the two implant configurations evaluated.

7.4 Discussion

Current options for limb sparing in dogs have been beset with many problems, including construct loosening and failure, necrosis of the host bone, and infection. Commercially available endoprosthetic implants for limb sparing eliminate the need for bone banking facilities, and reduce the risk of infection and rejection associated with cortical allografts. However these implants are only available in standard sizes that may not be optimal for individual patients. In addition, the high stiffness of the stainless steel endoprosthesis results stress concentrations that result in stress shielding and bone resorption at the bone implant interface. The available reconstructions are also geometrically intrusive

and do not match the bone geometry. For the distal radial location, soft tissue is limited and conformity to the existing anatomy is an important consideration.

The results presented in this study suggest that the reductions in the relative density of the bulk Ti6Al4V material associated with the use of porous geometric lattice structures contributes to a loading profile that is similar to pre-surgical conditions compared to the significantly stiffer stainless steel endoprosthesis. The measured strains in both untreated limbs and limbs treated with the custom, EBM fabricated implants, were tensile on the dorsolateral bone surface. Whereas the strains measured in limbs reconstructed with the stainless steel endoprosthesis were compressive at the same location. This result, while lacking statistical power due to the small sample size, is interesting because it suggests that endoprosthetic stiffness can have a large influence on the distribution of loads encountered *in vivo*. Plating is typically applied to the side of the bone under tension, and these data hint at a possible explanation for the failures of endoprosthetic devices that have been observed clinically. Of the sample population treated with stainless steel endoprostheses in the clinical limb sparing study by Liptak et al. (2006), failures of fixation occurred in the proximal connection. Further experiments and improved methods for the collection of strain data will be required to investigate this hypothesis further.

In this study it was necessary to compare two implant configurations but it was not possible with the relatively small sample size to isolate the influence of the material stiffness from the geometric changes between the implant designs. The commercial implants are only

available in 316 stainless steel and the Ti6Al4V, CP Ti and CoCr are the only materials commercially available for the EBM process. Since the modulus of elasticity of titanium is roughly half that of stainless steel, prudence would suggest that the material plays a significant, role in construct stiffness. However, it is the precise control over geometry and relative density that additive manufacturing provides that facilitates a wide range of tailored properties below and up to full material density. Both stainless steel and titanium alloy materials have relatively good biocompatibility and corrosion resistance. Titanium has been regarded as the biomaterial of choice for endoprosthetic limb-sparing surgery because of its biocompatibility, high strength, and lower modulus of elasticity (Cordero, Munuera, & Folgueira 1994). Titanium is a material commonly used for implants that require rigid behavior and the ability to carry and transfer loads. Despite some concerns regarding vanadium content, Ti6Al4V has been widely accepted as a biocompatible material suitable for use in implants. The availability of new biocompatible metal powders such as Ti6Al7Nb may provide new opportunities for the additive manufacturing of implants. Ti6Al7Nb lacks the vanadium component that has raised health concerns.

Another important advantage associated with patient specific implants is the reduction in the duration of surgeries. In this study, the mean time required to place custom implants was 61% of the time required for commercial endoprostheses. Custom implants were conformal to the bone surfaces, features such as the medial tabs provide positive registration in multiple directions. Bending or contouring was not required for the custom

endoprostheses but was for the commercial versions. In 3 out of 5 cases the commercial plates required cutting to fit the patient (i.e. to avoid interference with the elbow or proximal phalanges). One challenge, both in the design of the implants and in the execution of the surgery was the proper orientation of the osteotomy for custom implants within the CAD space compared to the surgical approach. This problem can be addressed in part by the use of additively manufactured cutting and drilling guides such as those used by Marcellin-Little, Harrysson, & Cansizoglu for custom Chevron wedge osteotomies (2008). These types of drilling and cutting fixtures are becoming more widespread, however, in this study it was desired to keep the surgical procedure as similar as possible between the two construct types.

In this study limbs have been non-destructively tested in axial loading for ten cycles. No difference was detected in the stiffness associated with each loading cycle. Non-destructive testing provided the data necessary to compare the mechanical characteristics of the two implant configurations without compromising the reliability of constructs for use in future studies. While destructive testing may provide interesting information about the potential limits of loading, clinical failures have not been reported to be acute; rather, they appear to be the result of cyclic loading and fatigue failure. In the clinical study of Liptak et al., dogs survived for up to two years, with failures occurring at a median durations of 180 days for metal endoprostheses, and 309 days for cortical allograft endoprostheses (note that these results were not significantly different) . Based on the *in vivo* loading of the radius at a trot (Riggs, DeCamp, & Soutas-Little, 1993), 2 years equates to roughly 13 days of cyclic

testing, assuming a 2Hz loading cycle at 30%-60% body weight, which presents significant challenges for tissue preservation and ignores the influence of *in vivo* bone remodeling. The use of composite analog replicas, such as those described previously by Horn et al. (2014) may provide an immediate platform for such testing. However, as was demonstrated in Chapter 4, loading to 60% of body weight for 6 million cycles at 10 Hz was insufficient to replicate clinical implant failures suggesting that other, biologic factors, such as stress shielding, bone resorption or aseptic loosening may require closer examination.

Despite the necessary limitations of this study, the results point toward the realization of significant improvements in canine limb sparing treatment and a decreased risk of implant failure facilitated by additive manufacturing. With further investigation, the procedure may provide a viable solution for dogs with appendicular osteosarcoma, especially in cases for which amputation is not a choice. The freedom of geometric complexity and the tool-less nature of fabrication afforded by direct metal additive processes also broadens the spectrum of cases for which limb sparing will be a viable alternative to amputation.

8.0 SUMMARY AND FUTURE WORK

Primary bone cancer comprises approximately 5% of all cancer in dogs with over 8000 new cases developing each year in the United States. Osteosarcoma is the predominant form of primary bone cancer in canines most commonly developing directly above the front paw in the distal portion of the radius. Osteosarcoma is highly aggressive, metastasizing quickly to secondary sites (most commonly to the lungs); it is one of the most difficult pain states to effectively manage. Amputation of the affected limb combined with chemotherapy therefore remains the current standard of care. Amputation fully alleviates bone cancer pain and eliminates the source of the primary tumor; in many cases, dogs can tolerate amputation quite well. However, in a comparatively small subset of cases, amputation does not lead to acceptable mobility if dogs have concurrent neurologic or orthopedic disease affecting other limbs. Dogs that are not good candidates for amputation are left with inadequate alleviation of suffering. The limb sparing techniques described in Chapter 2 provide an alternative for these cases, there are no differences in survival time between dogs undergoing amputation or limb sparing surgery. However, limb sparing for the distal radial site in canines is characterized by high rates of complication such as infection and implant failure. Unfortunately the precise modes of mechanical failure are underreported in the literature but the clinical data do point towards causes such as stress shielding and fatigue failure of fixation, particularly for metal endoprostheses. This dissertation has evaluated a novel, patient specific implant design for limb sparing fabricated with direct metal additive

manufacturing processes (e.g. Electron Beam Melting). Unlike many traditional processes, additive manufacturing is not limited by tooling constraints. The resulting geometric flexibility allows fabrication of custom implants with tailored mechanical properties representative of the mechanical properties of bone, thus potentially reducing the risk of implant failure.

The experimental evaluation of custom implants presents significant new challenges to the industry. Therefore, chapters 3 and 4, focused on the development and validation of patient specific bone analog models to serve as a platform for the testing of custom implants. These analogs exhibited both intensive and extensive properties similar to the elastic properties of bone. They were produced with indirect additive processes (or rapid tooling and subsequent molding) and were fabricated relatively quickly and with readily available materials. These models only proved to be useful in the linearly elastic region and were not reliable vehicles for destructive testing. In addition, while the rapid tooling production method proved relatively fast and inexpensive compared to traditional manufacturing, experiments in Chapter 3 pointed towards the possibility of directly manufacturing similar models from CT data using material extrusion processes and a UV photopolymer matrix. This will need further development and validation but would significantly reduce costs and accelerate development of custom, additively manufactured implants. The implications would not only be limited to analog bone models, but would also be applicable for the additive manufacturing of mechanically robust and functional components.

Chapter 5 investigated the flexural properties of non-stochastic lattice structures fabricated with EBM. The rhombic dodecahedron was chosen because of its applicability to additive manufacturing. It was found that the literature focused on the fabrication of small pore sizes, typically for bone ingrowth as opposed to the tailoring of mechanical properties. However, the small scale of geometries for bone ingrowth often exceeds machine resolution resulting in both spatial and mechanical discrepancies that obviate the use of predictive models. Flexure is a more appropriate loading condition for the large segmental defects encountered limb sparing than the compressive tests cited in the literature. In Chapter 5, the relative density, and unit cell size were carefully controlled and documented. Statistical analysis indicated that the relative density, was the dominant predictor of mechanical properties presuming the manufacturability of the desired dimensions. The results also demonstrated that Ti6Al4V structures fabricated with EBM could be tailored to reliably match a wide range of cortical bone stiffness values. An important consideration that was not investigated is the fatigue properties of the EBM fabricated structures, particularly in flexure. Understanding the fatigue characteristics of such structures would have applicability in a wide variety of industries such as the aerospace or automotive sectors where the conflicting objective of reduced weight, maneuverability and fuel efficiency are balanced by the need for structural integrity.

Chapter 6 focused on quantifying the influence of many of the key benefits of additive manufacturing in the context of the mechanical performance of limb sparing implants such as conformal bone plates, multi-directional fixation and low stiffness. The results first demonstrate the ability to utilize the EBM process to fabricate complex monolithic endoprostheses for canine limb sparing with geometric features not possible with traditional processes. Conformity and plate configuration alone did not affect construct stiffness, however, the greater contact area, as measured by pressure sensitive film, may contribute to improved biologic stability and fixation. The pressure indicating film shows the interface contact only at the time of fixation, new thin film technologies may facilitate real time acquisition of pressure profiles during testing. Further, the test implants in Chapter 6 were carefully designed to isolate the effect implant features but did not consider the full potential for additive manufacturing to facilitate more complex plate designs and the associated possible improvements in stability.

This key step was undertaken in Chapter 7 which non-destructively evaluated the mechanical characteristics of paired canine thoracic limbs before and after reconstruction with either the commercially available, stainless steel, endoprosthesis or a patient specific, EBM fabricated endoprosthesis with features based upon the results of the previous chapters. Patient specific endoprostheses were geometrically similar to the original anatomy and therefore less intrusive. Custom implants were easier and faster to place, significantly reducing the duration of surgical placement and, of the parameters that were measured,

exhibited mechanical characteristics resembling untreated limbs. In addition to multiple avenues of future studies, the results of this project represent the foundation upon which future clinical trials will be planned.

However, the custom implant in this study also relies on arthrodesis of the antebrachiocarpal, and carpometacarpal joints. The distal portion of the radius is an appropriate site for limb sparing since dogs tolerate the arthrodesis at that location with acceptable limb functionality. However, arthrodeses are limited to a few anatomic locations and Lui et al. found that 20.4% of osteosarcoma cases occurred in the femur, 19.5% occurred in the humerus, 19.3% occurred in the tibia, 19.2% occurred in the radius and 4.4% occurred in the ulna (1977). In another, more recent, retrospective study, on 12 dogs, the distal radius and the proximal humerus were the most commonly affected sites at 34.9%, and 18.4% respectively (Liptak et al., 2004). Regardless of the joint involved, arthrodeses present challenges since limb function is altered with the procedure. Arthrodeses result in high stresses placed on the proximal portion of the radius and the metacarpal bones, potentially leading to mechanical complications as evidenced by the increased construct stiffness for both commercial and custom, low stiffness endoprostheses in this study. Future iterations of the patient specific implant concept should also include investigations into the feasibility of a carpal hemiarthroplasty that would maintain carpal joint motion while replacing the distal portion of the radius. Features such as attachment points for the interosseous ligaments of the antebrachiocarpal joint (e.g. dorsal radiocarpal ligament, flexor

retinoculum, superficial digital flexor, etc.) can be incorporated into complex models. The ability of additive manufacturing technologies to facilitate increases in implant complexity with little or no associated production costs may provide prove essential.

REFERENCES

- Affdl, J., & Kardos, J. (1976). The Halpin-Tsai equations: A review. *Polymer Engineering & Science*, 16(5), 344-352.
- An, Y. H., & Draughn, R. A. (2010). *Mechanical testing of bone and the bone-implant interface* CRC press.
- Ashby, M. F. (2000). *Metal foams: A design guide* Butterworth-Heinemann.
- Autefage, A., Palierne, S., Charron, C., & Swider, P. (2012). Effective mechanical properties of diaphyseal cortical bone in the canine femur. *The Veterinary Journal*, 194(2), 202-209.
- Babae, S., Jahromi, B. H., Ajdari, A., Nayeb-Hashemi, H., & Vaziri, A. (2012). Mechanical properties of open-cell rhombic dodecahedron cellular structures. *Acta Materialia*, 60(6-7), 2873-2885.
- Bagaria, V., Deshpande, S., Rasalkar, D. D., Kuthe, A., & Paunipagar, B. K. (2011). Use of rapid prototyping and three-dimensional reconstruction modeling in the management of complex fractures. *European Journal of Radiology*, 80(3), 814-820.
- Boston, S. E., Duerr, F., Bacon, N., Larue, S., Ehrhart, E. J., & Withrow, S. (2007). Intraoperative radiation for limb sparing of the distal aspect of the radius without transcarpal plating in five dogs. *Veterinary Surgery*, 36(4), 314-323.
- Bradley, G. W., McKenna, G. B., Dunn, H. K., Daniels, A. U., & Statton, W. O. (1979). Effects of flexural rigidity of plates on bone healing. *The Journal of Bone and Joint Surgery. American Volume*, 61(6A), 866-872.
- Brodey, R. S., & Abt, D. A. (1976). Results of surgical treatment of 65 dogs with osteosarcoma. *Journal of the American Veterinary Medical Association*, 168(11), 1032-1065.
- Brodey, R. S., & RISER, W. H. (1969). 7 Canine Osteosarcoma: A Clinicopathologic Study of 194 Cases. *Clinical orthopaedics and related research*, 62, 54-64.
- Buracco, P., Morello, E., Martano, M., & Vasconi, M. E. (2002). Pasteurized tumoral autograft as a novel procedure for limb sparing in the dog: A clinical report. *Veterinary Surgery*, 31(6), 525-532.

Calvert, K. L., Trumble, K. P., Webster, T. J., & Kirkpatrick, L. A. (2010). Characterization of commercial rigid polyurethane foams used as bone analogs for implant testing. *Journal of Materials Science: Materials in Medicine*, 21(5), 1453-1461.

Cansizoglu, O., Harrysson, O., Cormier, D., West, H., & Mahale, T. (2008). Properties of Ti-6Al-4V non-stochastic lattice structures fabricated via electron beam melting. *Materials Science and Engineering: A*, 492(1-2), 468-474.

Carter, D., Smith, D., Spengler, D., Daly, C., & Frankel, V. (1980). Measurement and analysis of *in vivo* bone strains on the canine radius and ulna. *Journal of Biomechanics*, 13(1), 27-38.

Cheng, X. Y., Li, S. J., Murr, L. E., Zhang, Z. B., Hao, Y. L., Yang, R., . . . Wicker, R. B. (2012). Compression deformation behavior of Ti-6Al-4V alloy with cellular structures fabricated by electron beam melting. *Journal of the Mechanical Behavior of Biomedical Materials*, 16(0), 153-162.

Chiba, K. (2006). State of the art on flow kinematics and particle orientations during composite processing. *Journal of Textile Engineering*, 52(6), 227-236.

Ciocca, L., Mazzoni, S., Fantini, M., Persiani, F., Baldissara, P., Marchetti, C., & Scotti, R. (2012). A CAD/CAM-prototyped anatomical condylar prosthesis connected to a custom-made bone plate to support a fibula free flap. *Medical & Biological Engineering & Computing*, 50(7), 743-749.

Clarke, S. P., Ferguson, J. F., & Miller, A. (2009). Clinical evaluation of pancarpal arthrodesis using a CastLess plate in 11 dogs. *Veterinary Surgery*, 38(7), 852-860.

Coleman, J. C., Hart, R. T., Owan, I., Tankano, Y., & Burr, D. B. (2002). Characterization of dynamic three-dimensional strain fields in the canine radius. *Journal of Biomechanics*, 35(12), 1677-1683.

Coomer, A., Farese, J., Milner, R., Liptak, J., Bacon, N., & Lurie, D. (2009). Radiation therapy for canine appendicular osteosarcoma. *Veterinary and Comparative Oncology*, 7(1), 15-27.

Cordey, J., Perren, S. M., & Steinemann, S. G. (2000). Stress protection due to plates: Myth or reality? A parametric analysis made using the composite beam theory. *Injury*, 31, Supplement 3(0), 1-91.

- Cormier, D., Harrysson, O., & West, H. (2004). Characterization of H13 steel produced via electron beam melting. *Rapid Prototyping Journal*, 10(1), 35-41.
- Cormier, D., Harrysson, O., Mahale, T., & West, H. (2008). Freeform fabrication of titanium aluminide via electron beam melting using prealloyed and blended powders. *Advances in Materials Science and Engineering*, 2007
- Cormier, D., West, H., Harrysson, O., & Knowlson, K. (2004). Characterization of thin walled ti-6Al-4V components produced via electron beam melting. Paper presented at the *Solid Freeform Fabrication Symposium*, 2-4.
- Cox, H. (1952). The elasticity and strength of paper and other fibrous materials. *British Journal of Applied Physics*, 3(3), 72.
- Cristofolini, L., & Viceconti, M. (2000). Mechanical validation of whole bone composite tibia models. *Journal of Biomechanics*, 33(3), 279-288.
- Crowninshield, R. D., Pedersen, D. R., & Brand, R. A. (1980). A measurement of proximal femur strain with total hip arthroplasty. *Journal of Biomechanical Engineering*, 102(3), 230. doi:10.1115/1.3149578; 10.1115/1.3149578
- Crowson, R., Folkes, M., & Bright, P. (1980). Rheology of short glass fiber-reinforced thermoplastics and its application to injection molding I. fiber motion and viscosity measurement. *Polymer Engineering & Science*, 20(14), 925-933.
- Davidson, A., Hong, A., McCarthy, S., & Stalley, P. (2005). En-bloc resection, extracorporeal irradiation, and re-implantation in limb salvage for bony malignancies. *Journal of Bone & Joint Surgery, British Volume*, 87(6), 851-857.
- de Beer, N., & Scheffer, C. (2012). Reducing subsidence risk by using rapid manufactured patient-specific intervertebral disc implants. *The Spine Journal*, 12(11), 1060-1066.
- Degna, M. T., Ehrhart, N., Feretti, A., & Buracco, P. (2000). Bone transport osteogenesis for limb salvage following resection of primary bone tumors: Experience with six cases (1991-1996). *Veterinary and Comparative Orthopaedics and Traumatology*, 13(1), 18-22.
- Dérand, P., & Hirsch, J. (2009). Virtual bending of mandibular reconstruction plates using a computer-aided design. *Journal of Oral and Maxillofacial Surgery*, 67(8), 1640-1643.

Dernell, W. S., Ehrhart, N. P., Straw, R. C., & Vail, D. M. (2007). Tumors of the skeletal system. In S. J. Withrow, & D. M. Vail (Eds.), *Withrow and macewen's small animal oncology* (pp. 540-582) Saunders Elsevier.

Dobbe, J. G., Vroemen, J. C., Strackee, S. D., & Streekstra, G. J. (2013). Patient-tailored plate for bone fixation and accurate 3D positioning in corrective osteotomy. *Medical & Biological Engineering & Computing*, *51*(1-2), 19-27.

Dunlap, J. T., Chong, A. C., Lucas, G. L., & Cooke, F. W. (2008). Structural properties of a novel design of composite analogue humeri models. *Annals of Biomedical Engineering*, *36*(11), 1922-1926.

Egol, K. A., Kubiak, E. N., Fulkerson, E., & Kummer, F. J. (2004). Biomechanics of locked plates and screws. *Journal of Orthopedic Trauma*, *18*(8), 484-493.

Ehrhart, N. (2005). Longitudinal bone transport for treatment of primary bone tumors in dogs: Technique description and outcome in 9 dogs. *Veterinary Surgery*, *34*(1), 24-34.

Field, J. R., Edmonds-Wilson, R., & Stanley, R. M. (2004). An evaluation of interface contact profiles in two low contact bone plates. *Injury*, *35*(6), 551-556.

Field, J. R., Hearn, T. C., & Caldwell, C. B. (1997). Bone plate fixation: an evaluation of interface contact area and force of the dynamic compression plate (DCP) and the limited contact-dynamic compression plate (LC-DCP) applied to cadaveric bone. *Journal of orthopaedic trauma*, *11*(5), 368-373.

Field, J. R., Hearn, T. C., & Caldwell, C. B. (1998). The influence of screw torque, object radius of curvature, mode of bone plate application and bone plate design on bone-plate interface mechanics. *Injury*, *29*(3), 233-241.

Fitzwater, K. L., Marcellin-Little, D. J., Harrysson, O. L., Osborne, J. A., & Poindexter, E. C. (2011). Evaluation of the effect of computed tomography scan protocols and freeform fabrication methods on bone biomodel accuracy. *American Journal of Veterinary Research*, *72*(9), 1178-1185.

Frigola, P., Agustsson, R., Faillace, L., Rimmer, R., Clemens, W., Henry, J., . . . Harrysson, O. (2010). Development of a CW NCRF photoinjector using solid freeform fabrication (SFF).

Gasch, E. G., Rivier, P., & Bardet, J. F. (2013). Free proximal cortical ulnar autograft for the treatment of distal radial osteosarcoma in a dog. *The Canadian Veterinary Journal*, 54(2), 162.

Gaytan, S., Murr, L., Martinez, E., Martinez, J., Machado, B., Ramirez, D., . . . Wicker, R. (2010). Comparison of microstructures and mechanical properties for solid and mesh cobalt-base alloy prototypes fabricated by electron beam melting. *Metallurgical and Materials Transactions A*, 41(12), 3216-3227.

Gibson, L. (2000). Mechanical behavior of metallic foams. *Annual Review of Materials Science*, 30(1), 191-227.

Gibson, L. J., & Ashby, M. (1982). The mechanics of three-dimensional cellular materials. *Proceedings of the Royal Society of London. A. Mathematical and Physical Sciences*, 382(1782), 43-59.

Gibson, L. J., & Ashby, M. F. (1999). *Cellular solids: Structure and properties* Cambridge university press.

Gibson, R. F. (2012). *Principles of composite material mechanics* CRC press.

Halpin, J., & Karoos, J. (1978). Strength of discontinuous reinforced composites: I. fiber reinforced composites. *Polymer Engineering & Science*, 18(6), 496-504.

Hammel, S. P., Elizabeth Pluhar, G., Novo, R. E., Bourgeault, C. A., & Wallace, L. J. (2006). Fatigue analysis of plates used for fracture stabilization in small dogs and cats. *Veterinary Surgery*, 35(6), 573-578.

Hammel, S. P., Elizabeth Pluhar, G., Novo, R. E., Bourgeault, C. A., & Wallace, L. J. (2006). Fatigue analysis of plates used for fracture stabilization in small dogs and cats. *Veterinary Surgery*, 35(6), 573-578.

Harryson, O., Cormier, D., Marcelling-Little, D., & Jajal, K. (2003). Direct fabrication of metal orthopedic implants using electron beam melting technology. Paper presented at the *Solid Freeform Fabrication Symposium Proceedings*, 439-446.

Harrysson, O. L., & Cormier, D. R. (2006). *Direct fabrication of custom orthopedic implants using electron beam melting technology* Advanced manufacturing technology for medical applications, 191-206.

Harrysson, O. L., Cansizoglu, O., Marcellin-Little, D. J., Cormier, D. R., & West II, H. A. (2008). Direct metal fabrication of titanium implants with tailored materials and mechanical properties using electron beam melting technology. *Materials Science and Engineering: C*, 28(3), 366-373.

Harrysson, O. L., Hosni, Y. A., & Nayfeh, J. F. (2007). Custom-designed orthopedic implants evaluated using finite element analysis of patient-specific computed tomography data: Femoral-component case study. *BMC Musculoskeletal Disorders*, 8(1), 91.

Haslauer, C. M., Springer, J. C., Harrysson, O. L., Lobo, E. G., Monteiro-Riviere, N. A., & Marcellin-Little, D. J. (2010). *in vitro* biocompatibility of titanium alloy discs made using direct metal fabrication. *Medical Engineering & Physics*, 32(6), 645-652.

Haug, R. H. (1993). Effect of screw number on reconstruction plating. *Oral Surgery, Oral Medicine, Oral Pathology*, 75(6), 664-668.

Heiner, A. D. (2008). Structural properties of fourth-generation composite femurs and tibias. *Journal of Biomechanics*, 41(15), 3282-3284.

Heinl, P., Körner, C., & Singer, R. F. (2008). Selective electron beam melting of cellular titanium: Mechanical properties. *Advanced Engineering Materials*, 10(9), 882-888.

Heinl, P., Müller, L., Körner, C., Singer, R. F., & Müller, F. A. (2008). Cellular Ti-6Al-4V structures with interconnected macro porosity for bone implants fabricated by selective electron beam melting. *Acta Biomaterialia*, 4(5), 1536-1544.

Heinl, P., Rottmair, A., Körner, C., & Singer, R. F. (2007). Cellular titanium by selective electron beam melting. *Advanced Engineering Materials*, 9(5), 360-364.

Hill, R. (1963). Elastic properties of reinforced solids: Some theoretical principles. *Journal of the Mechanics and Physics of Solids*, 11(5), 357-372.

Hillers, K. R., Dernell, W. S., Lafferty, M. H., Withrow, S. J., & Lana, S. E. (2005). Incidence and prognostic importance of lymph node metastases in dogs with appendicular osteosarcoma: 228 cases (1986-2003). *Journal of the American Veterinary Medical Association*, 226(8), 1364-1367.

Hodge, S. C., Degner, D., Walshaw, R., & Teunissen, B. (2011). Vascularized ulnar bone grafts for limb-sparing surgery for the treatment of distal radial osteosarcoma. *Journal of the American Animal Hospital Association*, 47(2), 98-111.

- Horn, T. J., & Harrysson, O. L. (2012). Overview of current additive manufacturing technologies and selected applications. *Science Progress*, 95(3), 255-282.
- Hrabe, N. W., Heintl, P., Flinn, B., Körner, C., & Bordia, R. K. (2011). Compression-compression fatigue of selective electron beam melted cellular titanium (Ti-6Al-4V). *Journal of Biomedical Materials Research Part B: Applied Biomaterials*, 99(2), 313-320.
- Irvine-Smith, G., & Lobetti, R. (2006). Ipsilateral vascularised ulnar transposition autograft for limb-sparing surgery of the distal radius in 2 dogs with osteosarcoma: Clinical communication. *JS Afr Vet Assoc*, 77(3), 150-154.
- Jain, R., Podworny, N., Hearn, T., Richards, R. R., & Schemitsch, E. H. (1998). A biomechanical evaluation of different plates for fixation of canine radial osteotomies. *The Journal of Trauma and Acute Care Surgery*, 44(1), 193-197.
- Jehn, C. T., Lewis, D. D., Farese, J. P., Ferrell, E. A., Conley, W. G., & Ehrhart, N. (2007). Transverse ulnar bone transport osteogenesis: A new technique for limb salvage for the treatment of distal radial osteosarcoma in dogs. *Veterinary Surgery*, 36(4), 324-334.
- Johnson, A. L., Eurell, J. A. C., & Schaeffer, D. J. (1992). Evaluation of canine cortical bone graft remodeling. *Veterinary Surgery*, 21(4), 293-298.
- Johnson, A., & Houlton, J. (2005). *AO principles of fracture management in the dog and cat* Thieme.
- Kirpensteijn, J., Steinheimer, D., Park, R., Powers, B., Straw, R., Endenburg, N., & Withrow, S. (1998). Comparison of cemented and non-cemented allografts in dogs with osteosarcoma. *Veterinary and Comparative Orthopaedics and Traumatology*, 11, 178-184.
- Kohles, S. S., Markel, M. D., Rock, M. G., Chao, E., & Vanderby, R. (1994). Mechanical evaluation of six types of reconstruction following 25, 50, and 75% resection of the proximal femur. *Journal of Orthopaedic Research*, 12(6), 834-843.
- Koptyug, A., Rännar, L., Bäckström Franzén, S., & Dérand, P. (2013). Additive manufacturing technology applications targeting practical surgery. *International Journal of Life Science and Medical Research*, 3, 15-24.
- Krishnan, S. P., Dawood, A., Richards, R., Henckel, J., & Hart, A. J. (2012). A review of rapid prototyped surgical guides for patient-specific total knee replacement. *The Journal of Bone and Joint Surgery. British Volume*, 94(11), 1457-1461. doi:10.1302/0301-620X.94B11.29350 [doi]

Kuntz, C. A., Asselin, T. L., Dernell, W. S., Powers, B. E., Straw, R. C., & Withrow, S. J. (1998). Limb salvage surgery for osteosarcoma of the proximal humerus: Outcome in 17 dogs. *Veterinary Surgery*, 27(5), 417-422.

LaRue, S. M., Withrow, S. J., Powers, B. E., Wrigley, R. H., Gillette, E. L., Schwarz, P. D., . . . Richter, S. L. (1989). Limb-sparing treatment for osteosarcoma in dogs. *Journal of the American Veterinary Medical Association*, 195(12), 1734-1744.

LaRue, S. M., Wrigley, R. H., & Powers, B. (1987). A review of the effects of radiation therapy on bone. *Veterinary Radiology*, 28(1), 17-22.

Lascelles, B. X., Dernell, W. S., Correa, M. T., Lafferty, M. H., Devitt, C. M., Kuntz, C. A., Withrow, S. J. (2005). Improved survival associated with postoperative wound infection in dogs treated with limb-salvage surgery for osteosarcoma. *Annals of Surgical Oncology*, 12(12), 1073-1083.

Li, J., Li, S., Van Blitterswijk, C., & De Groot, K. (2006). Cancellous bone from porous Ti6Al4V by multiple coating technique. *Journal of Materials Science: Materials in Medicine*, 17(2), 179-185.

Li, X., Wang, C., Zhang, W., & Li, Y. (2009). Fabrication and characterization of porous Ti6Al4V parts for biomedical applications using electron beam melting process. *Materials Letters*, 63(3-4), 403-405.

Li, X., Wang, C., Zhang, W., & Li, Y. (2009). Fabrication and characterization of porous Ti6Al4V parts for biomedical applications using electron beam melting process. *Materials Letters*, 63(3-4), 403-405.

Liggins, A., Stranart, J., Finlay, J., Rorabeck, C., & Little, E. (1992). Calibration and manipulation of data from fuji pressure-sensitive film. Paper presented at the *International Conference on Experimental Mechanics: Technology Transfer between High Tech Engineering and Biomechanics*. Limerick, Ireland: Elsevier Science Publishers BV, 61-70.

Liptak, J. M., Dernell, W. S., Ehrhart, N., Lafferty, M. H., Monteith, G. J., & Withrow, S. J. (2006). Cortical allograft and endoprosthesis for Limb-Sparing surgery in dogs with distal radial osteosarcoma: A prospective clinical comparison of two different Limb-Sparing techniques. *Veterinary Surgery*, 35(6), 518-533.

- Liptak, J. M., Dernell, W. S., Lascelles, B. D. X., Larue, S. M., Jameson, V. J., Powers, B. E., . . . Withrow, S. J. (2004). Intraoperative extracorporeal irradiation for limb sparing in 13 dogs. *Veterinary Surgery*, 33(5), 446-456.
- Liptak, J. M., Dernell, W. S., Straw, R. C., Jameson, V. J., Lafferty, M. H., Rizzo, S. A., & Withrow, S. J. (2004). Intercalary bone grafts for joint and limb preservation in 17 dogs with High-Grade malignant tumors of the diaphysis. *Veterinary Surgery*, 33(5), 457-467.
- Liptak, J. M., Dernell, W. S., Straw, R. C., Rizzo, S. A., Lafferty, M. H., & Withrow, S. J. (2004). Proximal radial and distal humeral osteosarcoma in 12 dogs. *Journal of the American Animal Hospital Association*, 40(6), 461-467.
- Liptak, J. M., Dernell, W., Ehrhart, N., & Withrow, S. (2004). Canine appendicular osteosarcoma: Diagnosis and palliative treatment. *Compendium on Continuing Education for the Practising Veterinarian-North American Edition-*, 26(3), 172-185.
- Liptak, J. M., Dernell, W., Ehrhart, N., Withrow, S., Seguin, B., Walsh, P., & Kuntz, C. (2004). Canine appendicular osteosarcoma: Curative-intent treatment. *Compendium on Continuing Education for the Practising Veterinarian-North American Edition-*, 26(3), 186-199.
- Liptak, J. M., Ehrhart, N., Santoni, B. G., & Wheeler, D. L. (2006). Cortical bone graft and endoprosthesis in the distal radius of dogs: A biomechanical comparison of two different Limb-Sparing techniques. *Veterinary Surgery*, 35(2), 150-160.
- Little, J. P., Horn, T. J., Marcellin-Little, D. J., Harrysson, O. L., & West II, H. A. (2012). Development and validation of a canine radius replica for mechanical testing of orthopedic implants. *American Journal of Veterinary Research*, 73(1), 27-33.
- Liu, S., Dorfman, H., Hurvitz, A., & Patnaik, A. (1977). Primary and secondary bone tumours in the dog. *Journal of Small Animal Practice*, 18(5), 313-326.
- Lorinson, K., Loebcke, S., Skalicky, M., Grampp, S., & Lorinson, D. (2008). Signalment differences in bone mineral content and bone mineral density in canine appendicular bones. *Vet Comp Orthop Traumatol*, 21, 147-151.
- MacDonald, T. L., & Schiller, T. D. (2010). Limb-sparing surgery using tantalum metal endoprosthesis in a dog with osteosarcoma of the distal radius. *The Canadian Veterinary Journal*, 51(5), 497.

- Manabe, J. (1993). Experimental studies on pasteurized autogenous bone graft. *Nihon Seikeigeka Gakkai Zasshi*, 67(4), 255-266.
- Marcellin-Little, D. J., & Harrysson, O. L. (2012). *Custom Total Joint Arthroplasty. Advances in Small Animal Total Joint Replacement*, 223-241.
- Marcellin-Little, D. J., Harrysson, O. L., & Cansizoglu, O. (2008). In vitro evaluation of a custom cutting jig and custom plate for canine tibial plateau leveling. *American Journal of Veterinary Research*, 69(7), 961-966.
- Marin, E., Fusi, S., Pressacco, M., Paussa, L., & Fedrizzi, L. (2010). Characterization of cellular solids in Ti6Al4V for orthopaedic implant applications: Trabecular titanium. *Journal of the Mechanical Behavior of Biomedical Materials*, 3(5), 373-381.
- Markel, M. D., Sielman, E., Rapoff, A. J., & Kohles, S. S. (1994). Mechanical properties of long bones in dogs. *American Journal of Veterinary Research*, 55(8), 1178-1183.
- Meeson, R. L., Goodship, A. E., & Arthurs, G. I. (2012). A biomechanical evaluation of a hybrid dynamic compression plate and a castless arthrodesis plate for pancarpal arthrodesis in dogs. *Veterinary Surgery*, 41(6), 738-744.
- Morello, E., Buracco, P., Martano, M., Peirone, B., Capurro, C., Valazza, A., . . . Sora, M. (2001). Bone allografts and adjuvant cisplatin for the treatment of canine appendicular osteosarcoma in 18 dogs. *Journal of Small Animal Practice*, 42(2), 61-66.
- Morello, E., Vasconi, E., Martano, M., Peirone, B., & Buracco, P. (2003). Pasteurized tumoral autograft and adjuvant chemotherapy for the treatment of canine distal radial osteosarcoma: 13 cases. *Veterinary Surgery*, 32(6), 539-544.
- Murphy, T. P., Hill, C., Kapatkin, A. S., Radin, A., Shofer, F. S., & Smith, G. K. (2001). Pullout properties of 3.5-mm AO/ASIF Self-Tapping and cortex screws in a uniform synthetic material and in canine bone. *Veterinary Surgery*, 30(3), 253-260.
- Murr, L. E., Amato, K. N., Li, S. J., Tian, Y. X., Cheng, X. Y., Gaytan, S. M., . . . Wicker, R. B. (2011). Microstructure and mechanical properties of open-cellular biomaterials prototypes for total knee replacement implants fabricated by electron beam melting. *Journal of the Mechanical Behavior of Biomedical Materials*, 4(7), 1396-1411.
- Murr, L. E., Esquivel, E. V., Quinones, S. A., Gaytan, S. M., Lopez, M. I., Martinez, E. Y., . . . Wicker, R. B. (2009). Microstructures and mechanical properties of electron beam-rapid

manufactured Ti–6Al–4V biomedical prototypes compared to wrought Ti–6Al–4V. *Materials Characterization*, 60(2), 96-105.

Murr, L. E., Gaytan, S. M., Medina, F., Lopez, H., Martinez, E., Machado, B. I., . . . Bracke, J. (2010). Next-generation biomedical implants using additive manufacturing of complex, cellular and functional mesh arrays. *Philosophical Transactions. Series A, Mathematical, Physical, and Engineering Sciences*, 368(1917), 1999-2032. doi:10.1098/rsta.2010.0010; 10.1098/rsta.2010.0010

Murr, L. E., Gaytan, S. M., Medina, F., Martinez, E., Martinez, J. L., Hernandez, D. H., . . . Wicker, R. B. (2010). Characterization of Ti–6Al–4V open cellular foams fabricated by additive manufacturing using electron beam melting. *Materials Science and Engineering: A*, 527(7–8), 1861-1868.

Murr, L., Gaytan, S., Medina, F., Lopez, H., Martinez, E., Machado, B., . . . Wicker, R. (2010). Next-generation biomedical implants using additive manufacturing of complex, cellular and functional mesh arrays. *Philosophical Transactions of the Royal Society A: Mathematical, Physical and Engineering Sciences*, 368(1917), 1999-2032.

Murr, L., Martinez, E., Gaytan, S., Ramirez, D., Machado, B., Shindo, P., . . . Ciscel, D. (2011). Microstructural architecture, microstructures, and mechanical properties for a nickel-base superalloy fabricated by electron beam melting. *Metallurgical and Materials Transactions A*, 42(11), 3491-3508.

Nairn, J. A. (1997). On the use of shear-lag methods for analysis of stress transfer in unidirectional composites. *Mechanics of Materials*, 26(2), 63-80.

Nakanishi, K., Sato, K., Sato, T., Takahashi, M., Fukaya, N., & Miura, T. (1992). Preservation of bone morphogenetic protein in heat-treated bone. *Nihon Seikeigeka Gakkai Zasshi*, 66(9), 949-955.

Paoloni, M., & Khanna, C. (2008). Translation of new cancer treatments from pet dogs to humans. *Nature Reviews Cancer*, 8(2), 147-156.

Parthasarathy, J., Starly, B., & Raman, S. (2011). A design for the additive manufacture of functionally graded porous structures with tailored mechanical properties for biomedical applications. *Journal of Manufacturing Processes*, 13(2), 160-170.

Parthasarathy, J., Starly, B., Raman, S., & Christensen, A. (2010). Mechanical evaluation of porous titanium (Ti6Al4V) structures with electron beam melting (EBM). *Journal of the Mechanical Behavior of Biomedical Materials*, 3(3), 249-259.

Peck, J. N., & Marcellin-Little, D. J. (Eds.). (2012). *Advances in small animal total joint replacement* (Vol. 5). John Wiley & Sons.

Petrovic, V., Blasco, J., Portolés, L., Morales, I., Primo, V., Atienza, C., . . . Belloch, V. (2011). A study of mechanical and biological behavior of porous Ti6Al4V fabricated on EBM. Paper presented at the *Innovative Developments in Virtual and Physical Prototyping: Proceedings of the 5th International Conference on Advanced Research in Virtual and Rapid Prototyping, Leiria, Portugal, 28 September-1 October, 2011*, 115.

Picci, P. (2007). Osteosarcoma (osteogenic sarcoma). *Orphanet J Rare Dis*, 2(6)

Piermattei, D. L., Flo, G. L., & DeCamp, C. E. (2006). *Brinker, piermattei, and flo's handbook of small animal orthopedics and fracture repair* Saunders/Elsevier.

Ponader, S., Von Wilmowsky, C., Widenmayer, M., Lutz, R., Heintl, P., Körner, C., . . . Schlegel, K. A. (2010). In vivo performance of selective electron beam-melted Ti-6Al-4V structures. *Journal of Biomedical Materials Research Part A*, 92(1), 56-62.

Pooya, H. A., Séguin, B., Mason, D. R., Walsh, P. J., Taylor, K. T., Kass, P. H., & Stover, S. M. (2004). Biomechanical comparison of cortical radial graft versus ulnar transposition graft Limb-Sparing techniques for the distal radial site in dogs. *Veterinary Surgery*, 33(4), 301-308.

Razi, H., Checa, S., Schaser, K., & Duda, G. N. (2012). Shaping scaffold structures in rapid manufacturing implants: A modeling approach toward mechano-biologically optimized configurations for large bone defect. *Journal of Biomedical Materials Research Part B: Applied Biomaterials*, 100(7), 1736-1745.

Renwick, A., & Scurrall, E. (2008). Orthogonal bone plate stabilization for limb-sparing surgery. *Vet Comp Orthop Traumatol*, 21(3), 294-301.

Ricalde, P., Caccamese, J., Norby, C., Posnick, J. C., Hartman, M. J., & von Fraunhofer, J. A. (2008). Strength analysis of 6 resorbable implant systems: Does heating affect the stress-strain curve? *Journal of Oral and Maxillofacial Surgery*, 66(12), 2493-2497.

Rothstock, S., Kowaleski, M. P., Boudrieau, R. J., Beale, B. S., Piras, A., Ryan, M., ... & Brianza, S. (2012). Biomechanical and computational evaluation of two loading transfer concepts for pancarpal arthrodesis in dogs. *American journal of veterinary research*, 73(11), 1687-1695.

Rovesti, G. L., Bascucci, M., Schmidt, K., & Marcellin-Little, D. J. (2002). Limb sparing using a double Bone-Transport technique for treatment of a distal tibial osteosarcoma in a dog. *Veterinary Surgery*, 31(1), 70-77.

Rubin, C. T., & Lanyon, L. E. (1982). Limb mechanics as a function of speed and gait: A study of functional strains in the radius and tibia of horse and dog. *Journal of Experimental Biology*, 101(1), 187-211.

Ruedi, T. P., & Murphy, W. M. (2007). *AO principles of fracture management* Ao Publishing.

Safdar, A., He, H., Wei, L., Snis, A., & de Paz, Luis E Chavez. (2012). Effect of process parameters settings and thickness on surface roughness of EBM produced ti-6Al-4V. *Rapid Prototyping Journal*, 18(5), 401-408.

Sanadi, A., & Piggott, M. (1985). Interfacial effects in carbon-epoxies. *Journal of Materials Science*, 20(2), 421-430.

Schatzker, J. (2005). Principles of internal fixation. *The rationale of operative fracture care* (pp. 3-31) Springer.

Schatzker, J., Horne, J. G., & SumnerSmith, G. (1975). The effect of movement on the holding power of screws in bone. *Clinical Orthopedics and Related Research*, 11, 257-262.

Séguin, B., Walsh, P. J., Mason, D. R., Wisner, E. R., Parmenter, J. L., & Dernell, W. S. (2003). Use of an ipsilateral vascularized ulnar transposition autograft for Limb-Sparing surgery of the distal radius in dogs: An anatomic and clinical study. *Veterinary Surgery*, 32(1), 69-79.

Selvarajah, G. T., & Kirpensteijn, J. (2010). Prognostic and predictive biomarkers of canine osteosarcoma. *The Veterinary Journal*, 185(1), 28-35.

Straw, R. C., & Withrow, S. J. (1996). Limb-sparing surgery versus amputation for dogs with bone tumors. *The Veterinary Clinics of North America. Small Animal Practice*, 26(1), 135-143.

Straw, R., Powers, B., Withrow, S., Cooper, M., & Turner, A. (1992). The effect of intramedullary polymethylmethacrylate on healing of intercalary cortical allografts in a canine model. *Journal of Orthopaedic Research*, 10(3), 434-439.

- Sumner, D. R., Turner, T. M., & Galante, J. O. (1988). Symmetry of the canine femur: Implications for experimental sample size requirements. *Journal of Orthopaedic Research*, 6(5), 758-765.
- Szentimrey, D., Fowler, D., Johnston, G., & Wilkinson, A. (1995). Transplantation of the canine distal ulna as a free vascularized bone graft. *Veterinary Surgery*, 24(3), 215-225.
- Szivek, J. A., Thompson, J. D., & Benjamin, J. B. (1995). Characterization of three formulations of a synthetic foam as models for a range of human cancellous bone types. *Journal of Applied Biomaterials*, 6(2), 125-128.
- Szivek, J., & Gealer, R. (1991). Technical note. comparison of the deformation response of synthetic and cadaveric femora during simulated one-legged stance. *Journal of Applied Biomaterials*, 2(4), 277-280.
- Ta, H. T., Dass, C. R., Choong, P. F., & Dunstan, D. E. (2009). Osteosarcoma treatment: State of the art. *Cancer and Metastasis Reviews*, 28(1-2), 247-263.
- Taniguchi, N. (1989). The energy-beam processing of materials.
- Thomsen, P., Malmström, J., Emanuelsson, L., Rene, M., & Snis, A. (2009). Electron beam-melted, free-form-fabricated titanium alloy implants: Material surface characterization and early bone response in rabbits. *Journal of Biomedical Materials Research Part B: Applied Biomaterials*, 90(1), 35-44.
- Thrall, D. E., Withrow, S. J., Powers, B. E., Straw, R. C., Page, R. L., Heidner, G. L., . . . DeYoung, D. J. (1990). Radiotherapy prior to cortical allograft limb sparing in dogs with osteosarcoma: A dose response assay. *International Journal of Radiation Oncology* Biology* Physics*, 18(6), 1351-1357.
- Vandenbroucke, B., & Kruth, J. (2007). Selective laser melting of biocompatible metals for rapid manufacturing of medical parts. *Rapid Prototyping Journal*, 13(4), 196-203.
- Venzin, C., Grundmann, S., & Montavon, M. (2012). Endoprosthesis (EN) in frontlimb-sparing surgery for distal radial tumours in the dog: Preliminary results. *Schweizer Archiv Für Tierheilkunde*, 154(8), 337-343.
- Wallace, M. K., Boudrieau, R. J., Hyodo, K., & Torzilli, P. A. (1992). Mechanical evaluation of three methods of plating distal radial osteotomies. *Veterinary Surgery*, 21(2), 99-106.

- Weese, J. (2008). A review of post-operative infections in veterinary orthopaedic surgery. *Veterinary and Comparative Orthopaedics and Traumatology*, 21(2), 99.
- Weiner, S., & Wagner, H. D. (1998). The material bone: Structure-mechanical function relations. *Annual Review of Materials Science*, 28(1), 271-298.
- Wheeler, D. L., & Enneking, W. F. (2005). Allograft bone decreases in strength in vivo over time. *Clinical Orthopaedics and Related Research*, 435, 36-42.
- Whitelock, R. G., Dyce, J., & Houlton, J. E. (1999). Metacarpal fractures associated with pancarpal arthrodesis in dogs. *Veterinary Surgery*, 28(1), 25-30.
- Wieding, J., Jonitz, A., & Bader, R. (2012). The effect of structural design on mechanical properties and cellular response of additive manufactured titanium scaffolds. *Materials*, 5(8), 1336-1347.
- Wieding, J., Souffrant, R., Mittelmeier, W., & Bader, R. (2013). Finite element analysis on the biomechanical stability of open porous titanium scaffolds for large segmental bone defects under physiological load conditions. *Medical Engineering & Physics*, 35(4), 422-432.
- Williams, C. B., Cochran, J. K., & Rosen, D. W. (2011). Additive manufacturing of metallic cellular materials via three-dimensional printing. *The International Journal of Advanced Manufacturing Technology*, 53(1-4), 231-239.
- Withrow, S. J., Dernell, W. S., Jameson, V. J., Powers, B. E., Johnson, J. L., & Brekke, J. H. (2004). Biodegradable cisplatin polymer in limb-sparing surgery for canine osteosarcoma. *Annals of Surgical Oncology*, 11(7), 705-713.
- Withrow, S. J., Powers, B. E., Straw, R. C., & Wilkins, R. M. (1991). Comparative aspects of osteosarcoma. dog versus man. *Clinical Orthopaedics and Related Research*, 270, 159-168.
- Xiong, Y., Zhao, Y. F., Xing, S. X., Du, Q. Y., Sun, H. Z., Wang, Z. M., . . . Wang, A. M. (2010). Comparison of interface contact profiles of a new minimum contact locking compression plate and the limited contact dynamic compression plate. *International Orthopaedics*, 34(5), 715-718.
- Yang, L., Cormier, D., West, H., Harrysson, O., & Knowlson, K. (2012). Non-stochastic Ti-6Al-4V foam structures with negative poisson's ratio. *Materials Science and Engineering: A*, 558(0), 579-585.

Yang, L., Harrysson, O., West, H., & Cormier, D. (2012). Compressive properties of Ti–6Al–4V auxetic mesh structures made by electron beam melting. *Acta Materialia*, 60(8), 3370-3379.

Yang, L., Harrysson, O., West, H., & Cormier, D. (2012). Compressive properties of Ti–6Al–4V auxetic mesh structures made by electron beam melting. *Acta Materialia*, 60(8), 3370-3379.

Zak, G., Haberer, M., Park, C., & Benhabib, B. (2000). Mechanical properties of short-fibre layered composites: Prediction and experiment. *Rapid Prototyping Journal*, 6(2), 107-118.

Zdero, R., Elfallah, K., Olsen, M., & Schemitsch, E. H. (2009). Cortical screw purchase in synthetic and human femurs. *Journal of Biomechanical Engineering*, 131(9)

Zhou, L., Shang, H., He, L., Bo, B., Liu, G., Liu, Y., & Zhao, J. (2010). Accurate reconstruction of discontinuous mandible using a reverse engineering/computer-aided design/rapid prototyping technique: A preliminary clinical study. *Journal of Oral and Maxillofacial Surgery*, 68(9), 2115-2121.

Zou, C., Zhang, E., Li, M., & Zeng, S. (2008). Preparation, microstructure and mechanical properties of porous titanium sintered by ti fibres. *Journal of Materials Science: Materials in Medicine*, 19(1), 401-405.

APPENDICIES

Appendix 1: Lists of cadavers

Table A1: List of Cadavers used in Chapter 3 and Chapter 4 experiments.

	Type	Weight (Kg)	Sex	Age	Date Euthanized	Method Used	Shelter
Dog 01	White	26.14	Male	Young Adult	6/27/2007	Lethal Injection	Harnett County
Dog 02	Black	29.32	Male	Older Adult	6/28/2007	Lethal Injection	Harnett County
Dog 03	Tan Boxer	46.59	Female	Adult	6/29/2007	Lethal Injection	Harnett County
Dog 04*	Black/Tan Rottweiler	39.77	Female	Adult	7/5/2007	Lethal Injection	Harnett County
Dog 05	Black	26.82	Male	Young Adult	7/18/2007	Lethal Injection	Harnett County
Dog 06	Tan Pitbull	24.95	Female		8/2/2007	Lethal Injection	Harnett County
Dog 07	Tan Pitbull Mix	37.27	Female		9/6/2007	Lethal Injection	Harnett County
Dog 08	Black/Tan Rottweiler	29.55	Male (Neut)		9/12/2007	Lethal Injection	Harnett County
Dog 09	Tan	34.09	Male	Adult	9/20/2007	Lethal Injection	Harnett County
Dog 10	Tan	20.55	Female	2.5 yrs	11/14/2007	Lethal Injection	Harnett County
Dog 11	Black/White Pitbull	23.85	Male	Young Adult	3/5/2008	Lethal Injection	Harnett County
Dog 12	Black Lab X	19.54	Female	Young Adult	3/6/2008	Lethal Injection	Harnett County
Dog 13	Tricolor Hound	19.84	Female	Adult	3/7/2008	Lethal Injection	Harnett County
Dog 14	Lab X	27.36	Female	Young Adult	4/16/2008	Lethal Injection	Harnett County
Dog 15	Lab X	25.68	Male	Adult	4/17/2008	Lethal Injection	Harnett County
Dog 16	Rottweiler	32.95	Male	Young Adult	4/18/2008	Lethal Injection	Harnett County

Table A2: List of Cadavers used in Chapter 7.

	Type	Weight (Kg)	Sex	Age	Date Euthanized	Method Used	Shelter
20140111-1	German Shepherd (white)	31.4	Male intact	Adult	04/11/14	Lethal injection	Pending
20140111-4	Shepherd	32.0	Male intact	Adult	04/11/14	Lethal injection	Pending
20140111-5	Lab x	23.4	Male intact	Adult	04/11/14	Lethal injection	Pending
20140307-1	Shepherd	23.2	Female	Adult	3/7/14	Lethal injection	JCAS
20140307-2	Shepherd x	36.0	Male intact	Adult	3/7/14	Lethal injection	JCAS

Appendix 2: Derivations

Derivation of Equation 6.1:

Equation 6.1 describes the moment of inertia of the ovoid cross section used for the geometry of the segmental defect repair in the craniocaudal bending direction. As such, the general form for the moment of inertia for a given body about the x axis for area, A, within that body is often expressed as:

$$I_x = \int y^2 dA$$

This can be derived as the summation of an ellipse evaluated from $0 - \pi/2$ and a circle from $\pi/2$ to π . So that;

$$I_x = \int_0^r \int_0^{\pi/2} y^2 r d\theta dr + \int_0^r \int_{\pi/2}^{\pi} y^2 r d\theta dr$$

First we evaluate the ellipse, (I_{xa}) In Cartesian coordinates of x and y an ellipse of radius a (in x) and radius b (in y) is defined as:

$$1 = \frac{x^2}{a^2} + \frac{y^2}{b^2} \Rightarrow x = \frac{a}{b} \sqrt{b^2 - y^2}$$

Therefore:

$$I_{xa} = \int_0^b \int_{-x}^x y^2 dx dy = \int_0^b [y^2 x]_{-x}^x dy = \int_0^b y^2 (2x) dy$$

Substituting x:

$$I_{x_a} = \int_0^b 2y^2 \frac{a}{b} \sqrt{b^2 - y^2} dy$$

Letting $y = b \sin \theta$ and $dy = b \cos \theta d\theta$, where $y = [0, b] \rightarrow \theta = [0, \pi/2]$ and $b = r$

$$I_{x_a} = \int_0^{\pi/2} 2(r \sin \theta)^2 \frac{a}{r} \sqrt{r^2 - (r \sin \theta)^2} r \cos \theta d\theta$$

$$I_{x_a} = \int_0^{\pi/2} 2r^3 a \sin^2 \theta \cos^2 \theta d\theta$$

By identities:

$$I_{x_a} = \int_0^{\pi/2} \frac{r^3 a}{2} \sin^2 2\theta d\theta$$

$$I_{x_a} = \frac{r^3 a}{8} \int_0^{\pi/2} \frac{1 - \cos 4\theta}{2} d4\theta$$

$$I_{x_a} = \frac{r^3 a}{8} \int_0^{\pi/2} \frac{1 - \cos 4\theta}{2} d4\theta$$

$$I_{x_a} = \frac{r^3 a}{16} [4\theta - \sin 4\theta]_0^{\pi/2}$$

$$I_{x_a} = \frac{r^3 a}{16} (2\pi - \sin 2\pi)$$

$$I_{x_a} = \frac{\pi r^3 a}{8}$$

For the circular component of the ovoid moment of inertia (I_{x_c}) from $\pi/2$ to π

Letting $y=r \sin \theta$ and $dA=r d\theta dr$,

$$I_{x_a} = 2 \int_0^r \int_{\frac{\pi}{2}}^{\pi} r \sin^2 \theta r d\theta dr$$

$$I_{x_a} = 2 \int_0^r \int_{\frac{\pi}{2}}^{\pi} r^3 \left(\frac{1 - \cos 2\theta}{2} \right) \left(\frac{1}{2} \right) d2\theta dr$$

$$I_{x_a} = 2 \int_0^r \frac{r^3}{4} [2\theta - \sin 2\theta]_{\frac{\pi}{2}}^{\pi} dr$$

$$I_{x_a} = 2 \int_0^r \frac{\pi r^3}{4} dr$$

$$I_{x_a} = \left[\frac{\pi r^4}{8} \right]_0^r$$

$$I_{x_a} = \frac{\pi r^4}{8}$$

Combining:

$$I_x = \frac{\pi r^4}{8} + \frac{\pi r^3 a}{8}$$

$$I_x = \frac{\pi}{8} (r^4 + r^3 a)$$